Title	Design of Optical Near-eye See-through Display
Authors(s)	Zhou, Yao
Publication date	2023
Publication information	Zhou, Yao. “Design of Optical Near-Eye See-through Display.” University College Dublin. School of Mechanical and Materials Engineering, 2023.
Publisher	University College Dublin. School of Mechanical and Materials Engineering
Item record/more information	http://hdl.handle.net/10197/29511

Design of Optical Near-eye See-through Display

by

Yao Zhou, BSc, MSc

The thesis is submitted to University College Dublin
In fulfilment of the requirements for the degree of

DOCTOR OF PHILOSOPHY

IN

NATIONAL UNIVERSITY OF IRELAND,
UNIVERSITY COLLEGE DUBLIN,
COLLEGE OF ENGINEERING & ARCHITECTURE,
SCHOOL OF MECHANICAL & MATERIALS ENGINEERING.

Supervisor:
Prof. Fengzhou Fang

Co-supervisor:
Assistant Prof. Jufan Zhang

December 2022

Contents

Abbreviations

AR	augmented reality
VR	virtual reality
HMD	head mounted display
FOV	field of view
DOF	depth of field
ERF	eye relief
EPD	exit pupil diameter
PBS	polarized beam splitter
OLED	organic light-emitting diode
QLED	quantum dot light-emitting diode
LCOS	liquid crystal on silicon
VAC	vergence accommodation conflicts
PWM	pulse width modulation
RGB	red-green-blue
SLM	spatial light modulator
IPD	interpupillary distance

Abstract

The Metaverse is a digital living space built by human beings for an extended experience beyond the real world. It is a virtual world in nature that maps, transcends, and reacts with the real world, with a new social system. The Metaverse is highly immersive and interactive such that people can socialize, learn, play, live and work, just as they do in the real world. Augmented reality (AR) is an important medium to support the Metaverse by connecting the virtual world and the real world.

The optical imaging module is a key component of AR display, providing the users with a clear digitalized image or video that can be superimposed on a realistic external view. For AR, the main requirements on the optical module include a large field of view (FOV), large pupil exit, clear display, small size, light weight, and a small shift in the centre of gravity. Although there have been significant advances in AR displays in the last decade, better optical performance and more compact hardware structures are still being pursued as a long-term goal. This is also a major barrier that obstructs the wide uptake of AR devices in the consumer market, as it is still quite challenging to make a satisfactory balance between the system compactness and optical display performance.

Based on the requirements mentioned above, this thesis presents an in-depth study of near-eye see-through displays and proposes some innovative research outputs on both the optical system design and AR application mode. The main contents are as follows:

This thesis starts with the motivation for carrying out this project, followed by a comprehensive literature review. The identified challenges in this area underpin the objectives presented in Chapter 1. In Chapter 2, based on the characteristics of human eyes, the main design requirements and performance indicators of AR imaging systems are analysed. By comparing the mainstream AR display technologies, the geometrical waveguide is considered as the most promising solution in virtue of its 85% transparency, large FOV over 50°, large eye relief around 20mm, large eye box, smaller size, and lightweight. In Chapter 3, based on the requirements of the AR display system, we develop a one-dimensional geometrical waveguide with 72º FOV and two-dimensional geometrical waveguide with 69° horizontal FOV and 56° vertical FOV. The illumination uniformity can reach 83% after optimization. Stray lights causing ghost images

are systematically discussed and tailored solutions are presented which suppress the stray light to under 1% as proven by simulations. Another major barrier for AR display, vergence accommodation conflicts are discussed in Chapter 4. A dual-layer waveguide design is proposed to achieve depth changing with 34° FOV to mitigate the dizziness caused by vergence accommodation conflicts in long time use. The angular uniformity of the intensity across the exit pupil is more than 70%. Another varifocal geometrical waveguide is also developed and evaluated by the illumination of different depths. Manufacturing of geometrical waveguide is discussed in Chapter 5. Manufacturing is a major obstacle for widespread uptake of such a promising solution. Besides, the evaluation indicators, tolerance and characterization methods of each step are analysed and proposed. Finally, based on the study of near-eye see-through display, a fast positioning and calibration system combining waveguide and micro-lens array is proposed to improve the depth accuracy of 3D imaging. The system could filter out a useful object from complex background or in poor lighting condition, and scope targeted information rapidly. It can also calibrate the synthesized images by plenoptic cameras.

Statement of Original Authorship

I hereby declare that this thesis submitted for the Ph.D. degree is my work and effort and that it has not been submitted anywhere for any reward. I further declare that where other sources of information have been used, they have been acknowledged by means of a comprehensive list of references.

Acknowledgment

Upon the completion of this thesis, I am grateful to those who have offered me encouragement and support during my Ph.D. study.

First and foremost, I sincerely appreciate the consistent supervision and encouragement of my supervisor, Professor Fengzhou Fang. His profound insight, thoughtful and thorough guidance taught me so much that they are engraved on my heart. Also, my sincere thanks go to co-supervisor Assistant Professor Jufan Zhang, who has offered me numerous valuable comments and suggestions with incomparable patience and encouraged me profoundly throughout my Ph.D. study. Without their painstaking teaching and insightful advice, the completion of this thesis would have been impossible.

Secondly, I would like to present my thanks to one of my special colleagues Dr. Yue Zhang from whom I get tremendous help and technical support. What is more, I am particularly grateful to my colleague Mingyue Shen whose accompany, and care gave me great psychological comfort. Many thanks to my friend He Liu for her time to help to balance my study and life. Besides, I would like to express the most heartfelt gratitude to all MNMT-Dublin members and friends who have provided me with great help and support.

Lastly, my thanks would go to my beloved parents and grandparents for their loving consideration and great confidence in me all through these years. Only with their selfless support, concern, and love, can I overcome those difficulties and pursue my study till now. Their loving considerations and help are the source of my strength. Last but not least, acknowledgements are extended to Science Foundation Ireland (SFI) and the School of Mechanical and Materials Engineering for their financial support.

List of publications

Journal paper

Zhou, Yao, Jufan Zhang, and Fengzhou Fang. "Advances in the design of optical see-through displays." *Advanced Optical Technologies* 9, no. 4 (2020): 167-186. (Chapter 1/Chapter 2)

Zhou, Yao, Jufan Zhang, and Fengzhou Fang. "Stray light analysis and design optimization of geometrical waveguide." *Advanced Optical Technologies* 10, no. 1 (2021): 71-79. (Chapter 3)

Zhou, Yao, Jufan Zhang, and Fengzhou Fang. "Design of a large field-of-view two-dimensional geometrical waveguide." *Results in Optics* 5 (2021): 100147. (Chapter 3/Chapter 4)

Zhou, Yao, Jufan Zhang, and Fengzhou Fang. "Vergence-accommodation conflict in optical see-through display: Review and prospect." *Results in Optics* 5 (2021): 100160. (Chapter 4)

Zhou, Yao, Jufan Zhang, and Fengzhou Fang. "Design of a dual-focal geometrical waveguide near-eye see-through display." *Optics & Laser Technology* 156 (2022): 108546. (Chapter 4)

Zhou, Yao, Jufan Zhang, and Fengzhou Fang. "Design of the varifocal and multifocal optical near-eye see-through display." *Optik* 270 (2022): 169942. (Chapter 4)

Zhang, Jufan, Yao Zhou, and Fengzhou Fang. " Depth error correction for plenoptic cameras based on an innovative AR system combining geometrical waveguide and micro-lens array." *Optics and Lasers in Engineering* (OLEN-D-22-02004). 2022 (accepted) (Chapter 6)

Conference paper

Yao Zhou, Fengzhou Fang, and Jufan Zhang. " Design of a hybrid total-internal-reflection collimator." *AETS&nanoMan2022*, 30.08-01.09 (2022). (Chapter 3)

Book chapter

Zhang, Jufan, Yao Zhou, and Fengzhou Fang. "Advancements in Optical See-through Near-Eye Display." In *Advances in Virtual Reality*. IntechOpen, 2022. (Chapter 1/Chapter 2)

List of Tables

List of Figures

Chapter 1 Introduction

1.1 Background

Augmented reality (AR) "seamlessly" integrates the information from the real world and virtual world. This burgeoning technology can blend virtual information into the real world by 3D immersive simulations and then superimpose human senses, such as olfactory and haptic stimulation, enabling a sensory impression beyond reality [1]. The real environment and virtual objects are superimposed on the same screen or space in real time, through specially designed devices such as a helmet-mounted display or AR glasses that combine the real world with computer graphics.

Augmented reality technology converges multimedia, three-dimensional (3D) modeling, real-time video display and control, multi-sensor fusion, real-time tracking and registration, scene fusion and other new techniques. Augmented reality provides the information which is different from what humans can perceive with fewer dimensions.

In general, there are two definitions of augmented reality. One proposed by Ronald Azuma in 1997 is that augmented reality included three aspects: virtual and reality integration, instant interaction and 3D markers [2]. The other is Milgram's reality-virtuality continuum proposed by Paul Milgram and Fumio Kishino in 1994 [3]. They take the real environment and the virtual environment as two ends of a continuous system, and what is in the middle is called mixed reality. In theory, AR is in proximity to the real environment, while augmented virtuality (VR) is closer to the virtual environment as is shown in Figure 1.1.

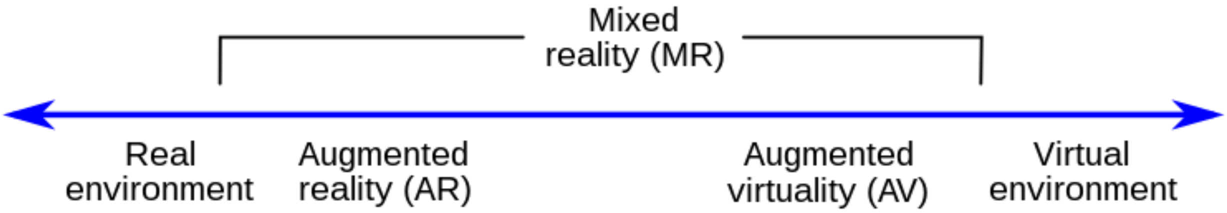

Figure 1. 1 Mixed reality among augmented reality and virtual reality.

Various techniques are developed to enhance the users' experience and cognitive level, wherein imaging systems are the fundamental to the AR technology. Optical near-eye see-through display is the key component, through which the virtual information is presented on the real environment. Different from the panel displays, near-eye see-through displays are wearable and close to human eyes. They can be categorized into two types, i.e., optical see-through systems and video see-through systems. For the optical see-through display shown in Figure 1.2 (a), the visual information is projected by a light source and displayed in front of the eyes by a transparent optical element without blocking the view to the real world. In the case of video see-through display, as is shown in Figure 1.2 (b), it captures the real-world information with video cameras mounted on the head gear, and projects the digital content to observers on an opaque display [4].

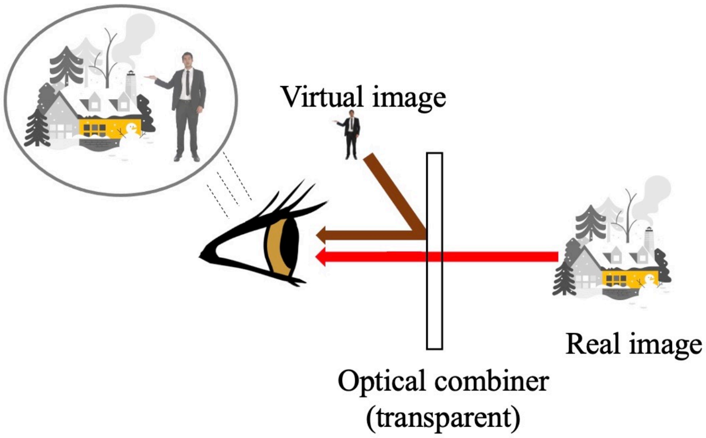

(a) Schematic diagram of optical see-through

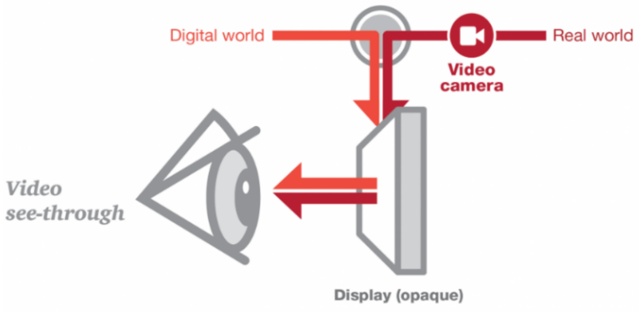

(b) Schematic diagram of video see-through

Figure 1. 2 Schematic diagram of near-eye see-through display [5]

The optical part consisting of various optical elements is the most important part in the whole system. However, traditional optical elements cannot meet the demands of such high-end applications. Consequently, the capability of optical elements has received considerable attentions, as well as the optical technologies that are used to achieve the field combining functionality.

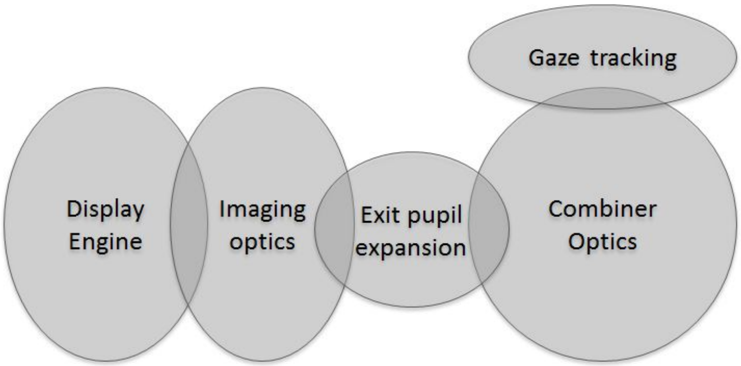

Figure 1. 3 Optical building blocks of an augmented reality headset system [6]

Figure 1.3 illustrates the building blocks of an optical see-through display. The display is where images are formed and then transferred to form the pupil through an optical combiner. The building blocks in the optical see-through display are designed to obtain images, exit pupil expansion and combiner functions synchronically, to accomplish the expected function. As the essential part, the optical element is the bridge to connect human, the virtual world and the real world. There are many technical parameters to determine the optical performance of AR devices, including the form factor, the eye box, and the field-of-view (FOV). To provide a better user experience, compact optical elements with large FOV, large eye relief, high-resolution, and lightweight are becoming inexorable tendencies [7-12].

Compared with traditional bulkier displays, like digital screen display, the optical see-through display is more socially acceptable due to its excellent wearability and compatibility to mobile applications. The requirements of complicated optical performance induce complex demands on optical designs which drives the development of on/off-axis optics, freeform optics, diffractive waveguide, and geometrical waveguide. Among these, waveguide technology has more advantages over the others and strong potential to dominate relevant applications. However, due to technical challenges, such as shifting focus and decreased chromatic aberration, there is a vast gap between the theoretical model and practical products.

1.2 Development and applications of AR displays

The earliest near-eye see-through display concept emerged during the World War I for a helmet-mounted display around 1915 to 1917 [13, 14]. However, limited by the development of technology, the first AR system was 1940s, which only developed in the gunsight in military applications, especially in the condition of bad visibility. The gunsight was projected in front of the pilots [15]. The first AR system didn't have promising performance in fulfilling the users' requirements due to the large weight, limited eye freedom, risk of force loading on pilots' faces, etc. In 1961, the world's first see-through head-mounted AR system was devised, which employed the conventional cathode ray tube (CRT) display, and the source is an electronic magazine for imaging. The success of this system also inspired the research and development of a lighter device because it was suspended to the ceiling, the pioneering part in the work is to reduce the device weight and loading pressure on people's head [16]. In 1972, the hybrid combination system of lenses and hologram, based on diffractive and refractive optics was introduced, which offered a new optical design for the optical display elements [17, 18]. Despite the continuous technical innovation in AR, the inveterate disadvantage of the AR applications was its large keystone distortion since it came out.

In 1980'ies, the concept of head-mounted display (HMD) for pilots' training in commercial aviation was proposed. In the same year, the Eye Tap was invented, including the computer, the camera, and the projector, which allowed users to see the virtual data and the real environment at the same time. In 1984, the first visual coupling system was invented, which connected pilots to aircraft with a half-mirror optical combiner. In 1986, the first modern military HMD, the DASH GEN III, was designed, which provided a collimated image by a spherical visor. The second modern HMDs reaching 20-degree FOV was developed by Elbit system which is limited by the monocular system. The third modern HMD can reach the FOV up to 40-degree [14, 19]. In 1968, a headset with two CRTs from the ceiling was built. In 1997, three characteristics of AR were defined, 1) real and virtual objects in a real (3-D) environment, 2) running interactively and in real time, 3) aligning real and virtual objects with each other, which contribute to the future development of artificial intelligence and machine learning [20]. The freeform prism was first applied into the HMD in 1998 [21]. ARQuake, the first outdoor mobile AR game was developed in 2000 which represented a milestone of AR development. In the following years, optical see-through displays developed so fast that more and more products were released while some mobile applications were even prevailing. In 2013, Google released the wearable optical head-mounted display (OHMD), namely Google Glass, which is a glass-type device employing see-through technology based on polarization gratings [15]. In 2014, Holographic waveguide structure was presented, for which optical transmission of visible light can reach 85%. The technology makes the system more compact. In 2015, the first commercial holographic waveguide product, HoloLens was released by Microsoft, which reached a new phase of "mixed reality (MR)". MR combines the VR and AR to realise more immersive and diverse interactions between the real world and virtual world [22]. In 2016, Meta 2 was developed, which applies the off-axis optics. Then Magic Leap One applying two-layer diffractive waveguides, released in 2018, solving the dizzy problem to some extent. Microsoft Hololens 2 was released in February 2019, which achieved an FOV of 52 degrees. In the same year, LetinAR released the pinhole display, which applied light field technology to achieve varifocal depth with 22 degrees FOV. Figure 1.4 shows the main history of optical technologies for AR display.

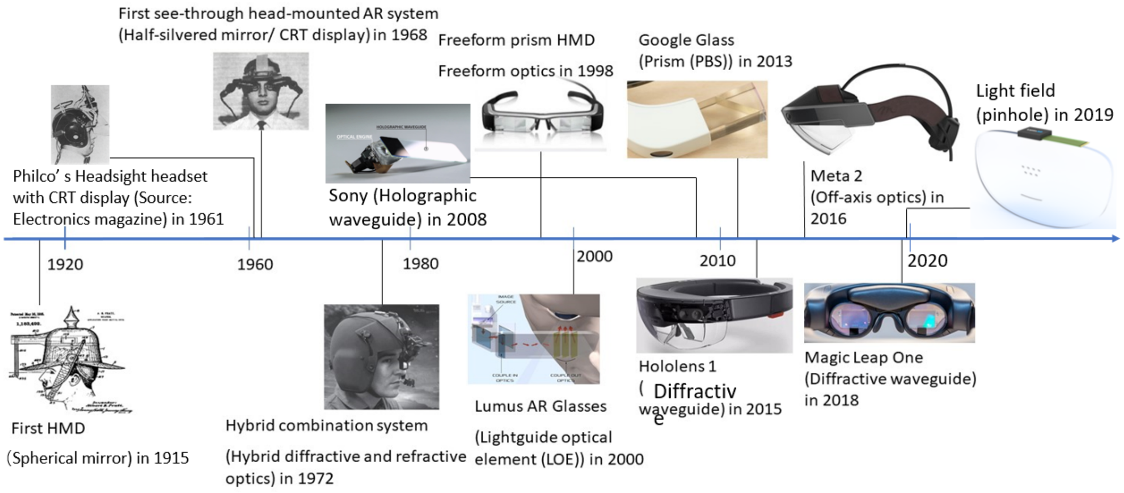

Figure 1. 4 Highlights of development of optical technologies for AR [11, 23-28]

With the progress of AR technology, AR is increasingly used in various industries, such as education, training, medical care, design, advertising, etc. AR has injected new vitality into education with its rich interactivity. Compared with stuffy paper books, AR combines text and dynamic 3D images together, which provides an immersive experience and facilitates a quicker understanding of the knowledge. AR enhances the clarity and intuitiveness and perceptual impact of real situations, making situational learning more friendly, dynamic, and natural [1, 29-31]. For example, for training on medical and clinical treatment, the application of AR makes the esoteric and profound medical theories more lively and concrete, which greatly improves learning efficiency and outcomes, especially in minimally invasive surgery [32-35]. In tourism, such as museums, AR provides virtual text, pictures, videos, and other information for the introduction and description of exhibits. AR has also been applied for restoring and displaying cultural relics by virtually filling up the incomplete part, which brings an immersive feeling to tourists [36, 37]. In addition, in the manufacturing industry, based on smart AR glasses, data collection and process investigation are carried out through the AR cloud to provide visual information for the technical support team, therefore realizing expert-level remote assistance. This truly makes the communication of industrial issues more direct, accurate, efficient through visualized way, and eliminates the risk of unavailability of qualified experts in the field for urgent problems, and significantly saves cost and time. AR helps abandon complicated work manuals, flowcharts, walkie-talkies, etc., and completely liberates the hands of workers/operators [38]. Pilots can also use HMD to observe navigation information and even warning information about the potential risks. The Synthetic Training Environment based on AR systems helps users be trained in a more immersive way, by placing them in a more physically and psychologically stressful simulated combat zone [39-41]. For entertainment, AR is applied to create interactive games, like racetracks and basketball rivalry games, for which the camera can track the locations or even the body language to give a more accurate response [42-44].In the field of AR hardware, it can be divided into three parts based on upstream components, midstream modules, and downstream machines, as shown in Figure 1.5. The following picture is a good illustration of the industry chain composition. Most components and modules are already commercially available. The battery, storage and the imaging optical module are precisely the areas being pursued in the hope of improving performance by research institutes and commercial companies. The imaging optics module is a very important part in AR systems, which directly determines the virtual imaging effect. There is a long history of development and technology iteration in the imaging optical module. On the strength of the continuous contribution from involved organizations, AR is moving forward from the accumulation of patents to the breakthrough of technical difficulties, now stepping into the construction of the industrial chain.

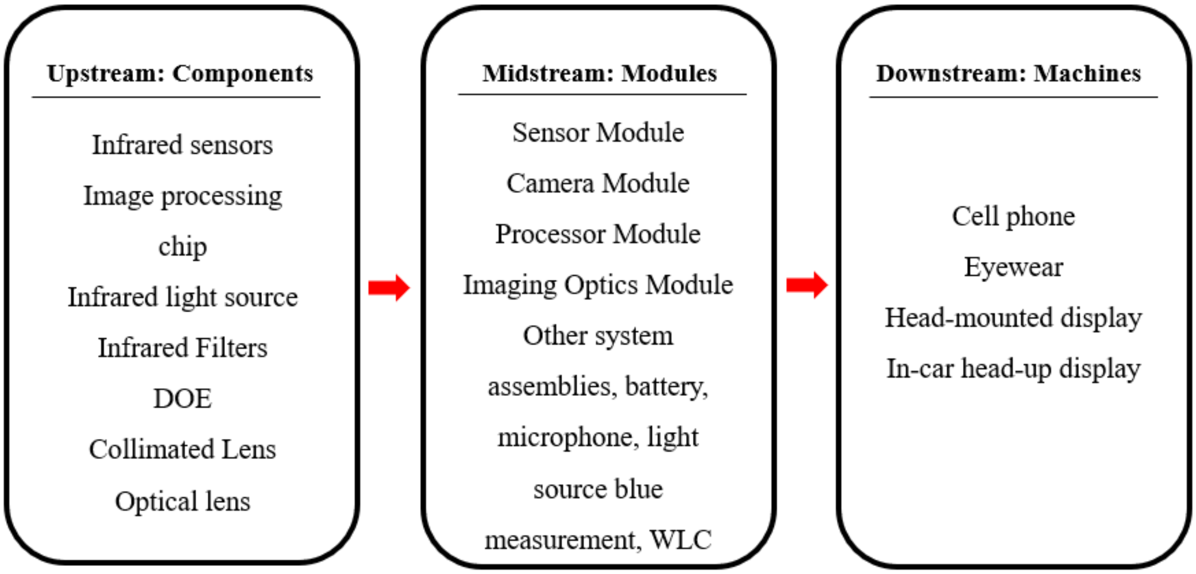

Figure 1. 5 Illustration of the industry chain composition in AR hardware system

1.3 Challenges

The optical imaging module is recognized as the key element of optical see-through displays. For better wearability and human perceptual capabilities, there is still a long way to achieve perfect optical performance. There are three main challenges to be solved on optical performance and vergence–accommodation conflicts, which will be briefly discussed in detail below.

1.3.1 Optical performance

The optical imaging module and the screen determine the optical performance of the system. The optical imaging module is designed to expand the exit pupil and provide proper FOV to enhance the immersive feeling. The eye box and eye relief have reciprocal influences on the FOV [45]. The design of the imaging system is crucial to reach a consensus on a quantifiable and measurable optical specification that meets the requirements. Thus, the design of the optical imaging module determines the optical performance to a large extent. The projector is also a crucial part of the AR system to manipulate the brightness and contrast of the virtual images. Brightness refers to how much light appears in the virtual image displayed by the optical system and high brightness guarantees users to have clear vision in a direct sunlight environment. Low brightness is one of the major challenges faced by the existing AR devices. It was reported that HoloLens and DAQRI Smart Glasses reach brightness of about 300 nits, and Magic Leap One reaches brightness of about 200 nits [46, 47]. The brightness of most AR devices on the market is only applicable for indoor use, and challenging to use outdoors. To alleviate this problem, some AR headsets use optical means to block ambient incoming light or use dyed lenses to improve the relative brightness of the optical module, however this method has a drawback of reducing the light transmission rate correspondingly. Light transmission refers to how much ambient light can be received by the human eye through the optics. The ideal light transmission rate is 100%, but it is impossible to achieve this rate with existing AR technology. Low light transmission rate may meet requirements of consumers-oriented products, but it is insufficient to complete missions in many professional application scenarios, because the light transmission rate has a great impact on operational safety. For existing mainstream AR devices, HoloLens is known to have a light transmission rate of about 40%; Magic Leap One has a light transmission rate of about 15%; Nreal model shown in early 2019 has a light transmission rate of about 25% [48-51]. Although the human eye can adapt to the lower light transmission rate of AR glasses, it would degrade to be imperceptible in dark working environment [52, 53].

1.3.2 Chromatic aberration

In light-transmissive AR devices, the display part usually consists of virtual images (waveguide or semi-reverse semi-transmissive, etc.), external light shields, additional optical module protectors, etc. Although some of them help to enhance the optical display, they inevitably affect the real-world light to some extent which leads to the distortion and deformation of the real-world view. Consequently, AR not only loses resolution during optical propagation, but may also cause image distortion. For example, a rectangle projected by the display will look slightly different in shape compared to the view from human eyes. If the degree of distortion is relatively large, it may cause local resolution degradation. Image distortion is usually ignored by AR devices compared with some other major issues. Image distortion can be solved during rendering by display calibration, and it does not require much additional processing power. In some cases, it is even possible to "mask" the distortion by reducing the field of view. The refractive index of the optical element is related to the wavelength of light, and therefore also has a variety of different focal lengths depending on the light color. This also occurs in cameras and can usually be compensated by combining multiple lenses of different glasses, but this approach is not suitable for AR glasses/headsets due to size and weight considerations. Therefore, chromatic aberration remains an unresolved problem for most AR systems [54-56].

All optical systems have problems caused by chromatic aberration (dispersion), but the resolution of the human eye is the baseline of the system. No matter how much the stray lights or the dispersion is, the color and the brightness of the light source must be excellent, which is the first step of the imaging. In the process of designing and simulating the film layer of the waveguide for different color lights, researchers should try to minimize the color difference (dispersion) to the human eye [57, 58]. Besides, the ghost image is also one server problem of AR devices as shown in Figure 1.6. The precise coating of multiple different reflective surfaces is a highly demanding process, prone to stray lights ghosting [59]. Stray light is the primary cause of ghost images in AR devices.

Figure 1. 6 Ghost images of augmented reality device [60]

1.3.3 Vergence–accommodation conflicts

Considering the stereoscopic imaging mechanism of the human vision, only when the display meets the requirements of psychological perception and the physiological perception at the same time, it can be defined as a satisfactory display. The psychological perception can be achieved by affine, occlusion, shadow, texture, and prior knowledge to define whether it is near or far and the three-dimensional shape of the objects in images. The latency between the real and the virtual image makes the observer feel dizzy, which can be solved by software. The psychological perception can be met by existing designs. However, the speed of industrialization approaching physiological perception is restricted.

There are three basic elements in the physiological perception as shown in Figure 1.7: 1) Binocular parallax; 2) Motion parallax and 3) Accommodation and vergence. While the first two have had solutions, the accommodation and vergence have not been solved yet.

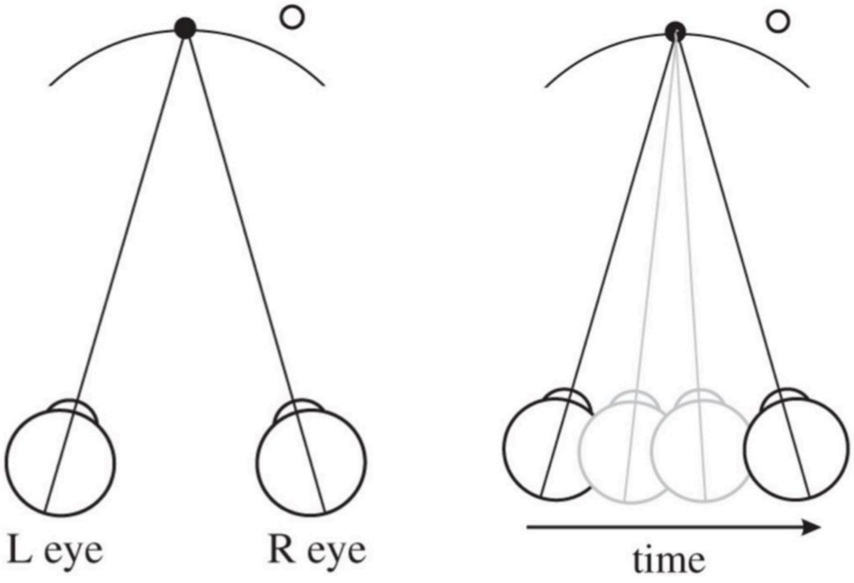

(a) Binocular disparity (b) Motion parallax

Figure 1. 7 The illumination of the viewing parallax. (a) Binocular disparity, (b) Motion parallax [61]

Vergence–accommodation conflicts (VAC) help eyes to shift focus between far and near objects. Focusing far objects makes the ciliary muscle relax while focusing near objects makes the muscle contracted [62-64]. For example, observers can lift one finger and make sure there are far trees and near finger in observer's field of view. When you focus the near finger, the far trees would be blurred. On the contrary, the nearby finger is blurred. Most optical designs in optical see-through displays have the problem of identical VAC. In the displayed images, no matter near or far objects they are all displayed in one plane, the ciliary muscle does not change at all, which obeys the physiological perception. Thus, observers feel dizzy when they wear the displays for a long time [65, 66].

Based on the above discussion, it is clear that one more display plane means one more dimension. Thus, in order to solve the VAC problem, increasing the display layers to simulate several different depths to get higher visual quality of displayed images can possibly work. [67]. Adding any more dimension in the plenoptic function may make great progress in the images displayed. For the evaluation of this solution, several methods can be applied, such as subjective user studies [62], oculomotor responses measurement [68], physiological fatigue indicators measurement [69], brain activity measurements via tools such as EEG or fMRI [70, 71].

The sliding optics is the first solution to VAC. A lens was placed between the see-through display and the exit lenses to change the optical depth [72]. Deformable membrane mirrors were then proposed, the deformations of which could be controlled by a pneumatic system. Curvature values and maximum displacement of the deformable membrane mirrors are crucial to the eye relief [73]. In addition to the aforementioned technique issues, the existing product also cannot meet lightweight requirements of the system. The actual production manufacturing should also be improved to get closer to the design for actual deployment in practical applications.

1.4 Objectives

The optical structure of AR glasses determines the final imaging effect. The main cost of AR glasses is the optical display module carried inside the glasses. Basically, the performance of the optical system determines the imaging effect of AR glasses. To address the major challenges mentioned above and provide a better user experience, this thesis aims at developing a novel near-eye see-through display system with slimmer structure, reduced weight and better imaging performance. The aim of this thesis is to get through the whole process of AR glasses from design, analysis, optimization to manufacturing. This thesis analyses and breaks the bottleneck from the point of design to design the geometrical waveguide model with high optical properties, and provides a complete manufacturing process and characterization method from the point of manufacturing. Thus, the objectives are summarized as the following.

(1) Develop one dimensional and two-dimensional geometrical waveguides to achieve large FOV, large eye relief and large eye box, with superior structural compactness and weight over exiting optical solutions.

(2) Analyse the causes of stray light and propose tailored solutions regarding both optical design and manufacturing to control the generation of ghost images.

(3) Develop multifocal and varifocal near-eye see-through solutions to mitigate VAC.

(4) Develop innovative application model based on AR mechanism.

Based on the above objectives, the technical route is planned as follows.

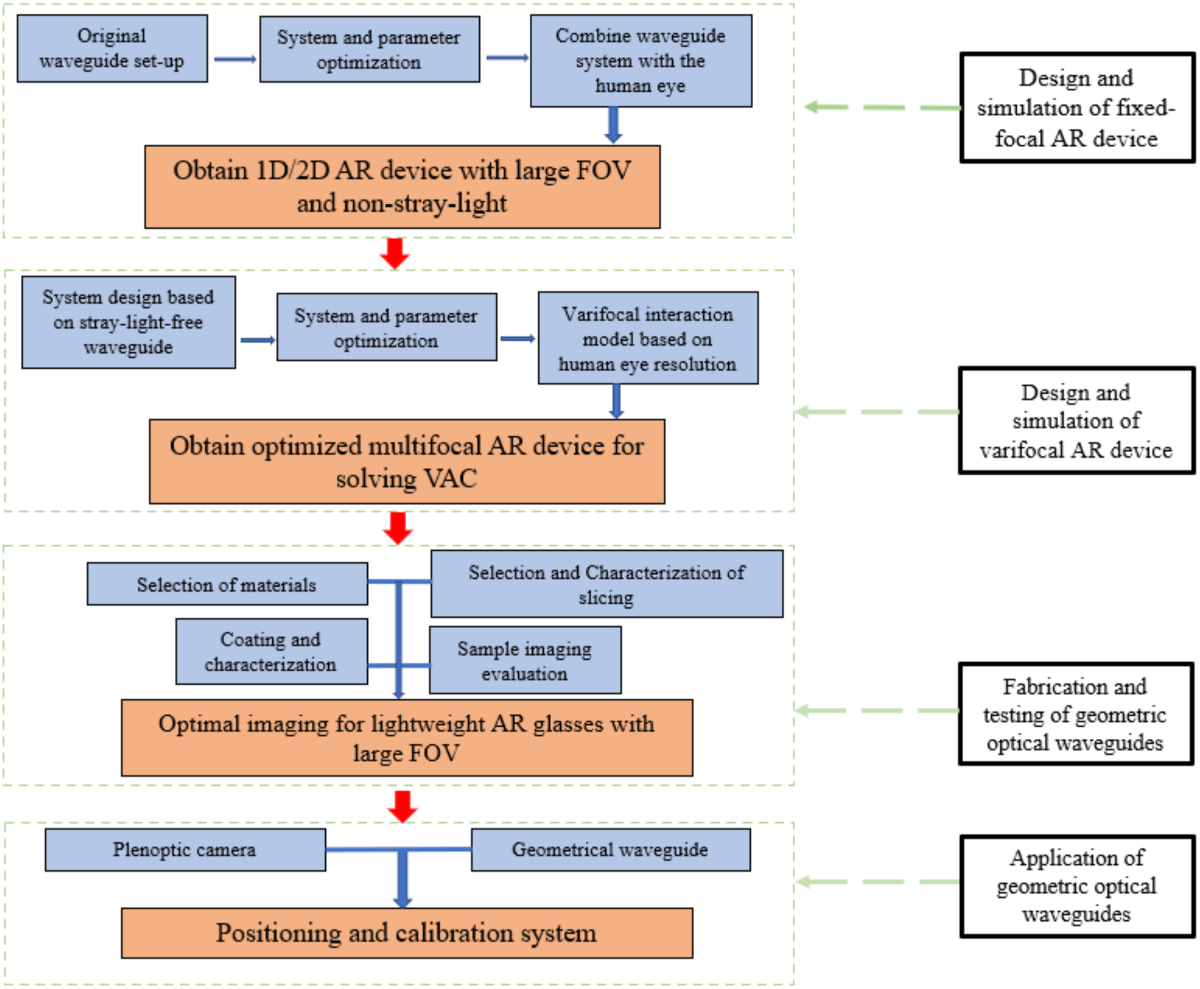

Figure 1. 8 The specific technical route

Chapter 2 Development of augmented reality

2.1 Human vision

Human eyes are the receivers of AR display, which is the core of the whole optical imaging system and the destination of projected images. Therefore, it is essential to understand the functions that AR optical systems can achieve when designing the optics of such visual instruments. For example, if an AR optical system is required to identify a target of a designated size or to perform a designated precision measurement or to exhibit a designated performance, the light transmitted through the optical system must ensure that the eye can recognize the details in the received image. Otherwise, the designed imaging system would fail to bring expected vision. Based on the visual requirements of human eyes, the assessment parameters of the designed imaging module can be determined.

2.1.1 Physiological structure of the human eye

Light acts on the visual organ, makes its sensory cells excited, and the information is processed by the visual nervous system to produce vision. Through vision, humans can perceive the size, light and shade, color, movement of external objects, and various information. At least 80% of our external information is obtained through vision, which is the most important sense for humans. The human eye of which the structure is shown as Figure 2.1, including the cornea, iris, aqueous humor, vitreous, retina, and optic nerve. The path of vision formation is: light -- > cornea -- > pupil -- > lens (refracting light) -- > vitreous (fixing eyeball) -- > retina (forming object image) -- > optic nerve (transmitting visual information) -- > visual center of brain (forming vision).

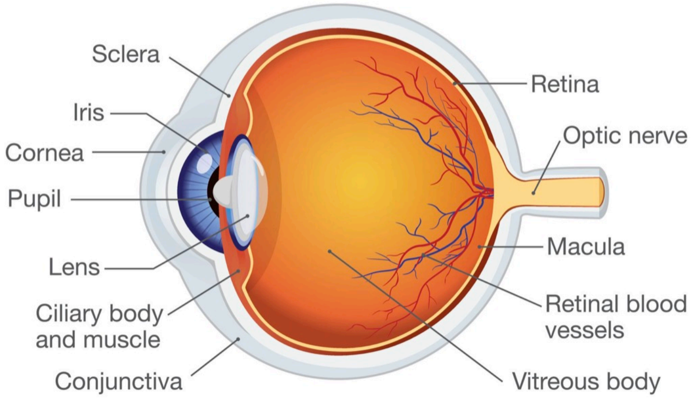

Figure 2. 1 The structure of the human eye [74]

Functionally, the eyeball can be divided into a refractive system and a photoreceptor system. The transparent cornea, aqueous humor, lens and vitreous constitute the refractive system, and the retina is the photosensitive system. The study of receiving light is very similar to that of a camera, including the ability to control the amount of incoming light, to bend light into focus, and to present external images, as shown in Table 2.1 below. The refractive system limits and determines the assessment parameters of the designed system. For example, the cornea and the pupil limit the FOV, eye relief and eye box. Only virtual images from a proper eye relief range can be processed by human eyes. Longer or shorter eye relief affects human eye to receive whole virtual images. The photoreceptor system determines the threshold value of the illumination or brightness uniformity.

Table 2. 1 The relationship between eye and camera

Eye	**Function**	**Camera**
Cornea/Aqueous humor	Converge light from the target	Focusing lens
Lens	Finely focused	Second lens
Hyaloid canal	Refraction	Camera obscura
Pupil	Change depth and flux	Aperture
Retina	Optical signal to electrical signal	CCD/CMOS sensor
Optic nerve	Data transfer	Signal output

The human eye's binocular viewing angle limit is about 150 degrees vertically and 230 degrees horizontally, as shown in Figure 2.2. If all the screens are within this viewing angle, it will give us a sense of immersion. In fact, human vision in 10 degrees is a sensitive area, 10 to 20 degrees can correctly identify information, 20 to 30 degrees is more sensitive to dynamic things. When the vertical perspective of the image is 20 degrees, the horizontal perspective of 36 degrees, there will be a very good visual immersion, and it will not cause eyestrain by the frequent rotation of eyes.

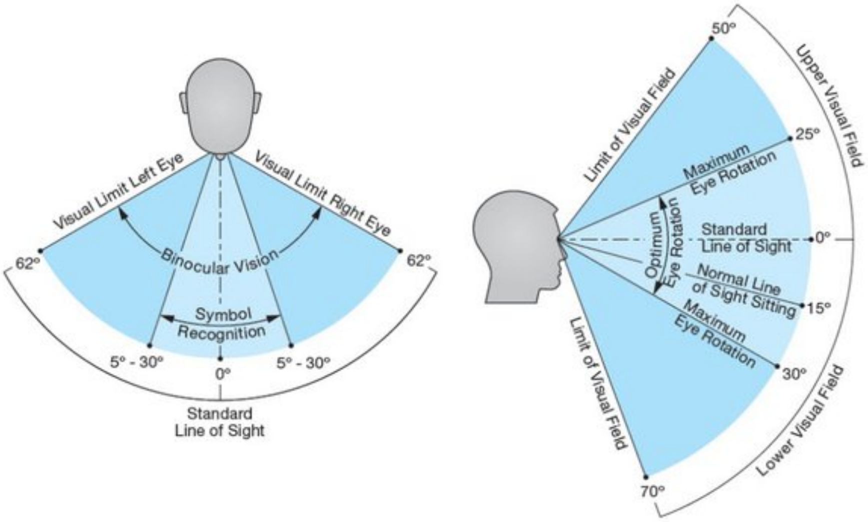

Figure 2. 2 Horizontal and Vertical FOV for binocular view [75]

2.1.2 Optical model of the human eye

Over 150 years, dozens of papers concerning models of the human eye have been published. These models range from a simplified version of the human eye consisting of only one refractive plane to a complex model of the human eye consisting of more than 4000 refractive planes. Some models have a gradient refractive index lens, some have two or more homogeneous lamellar structures to represent the gradient of refractive index, and some have only a uniform refractive index lens.

A one-size-fits-all human eye model for any situation does not exist. And it does not mean that a more complex human eye model is better. For example, using a model that includes a gradient refractive index lens that does not provide more valid information than a uniform refractive index lens model is not necessary at all - because such a model can significantly slow down the computation of large amounts of light in optimized or non-sequential modes as shown in Figure 2.3 In general, only a very simple spherical model is needed for single-wavelength near-axis calculations as shown in Figure 2.4. A representative simplified model for near-axis calculations can consist of a refractive surface with a diopter of 60 and a refractive index of 4/3. This model is particularly useful for calculating retinal imaging dimensions. Since the node is 5.55 mm from the surface, the image size of an object with a known position, size, or field of view on the image plane can be easily derived by projecting light at 16.67 mm. This near-axis model has an error of about a few percentage points when calculating a 10° FOV. Thus, the imaging module should be designed and optimized based on the eye model. The receiver of the imaging module should be consistent with the characteristics of the human eyes as far as possible for the stray lights or illumination analysis.

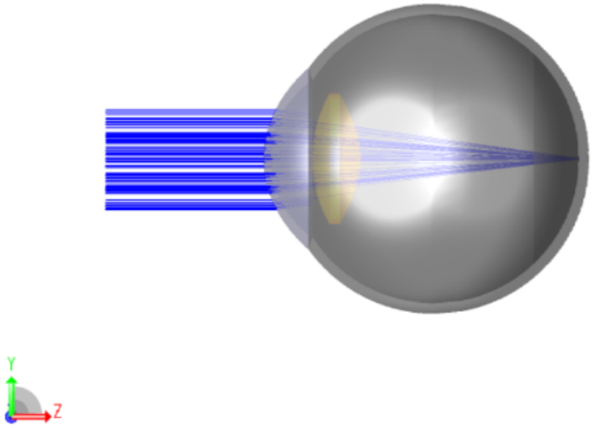

Figure 2. 3 Non-sequential modes of eye model [76]

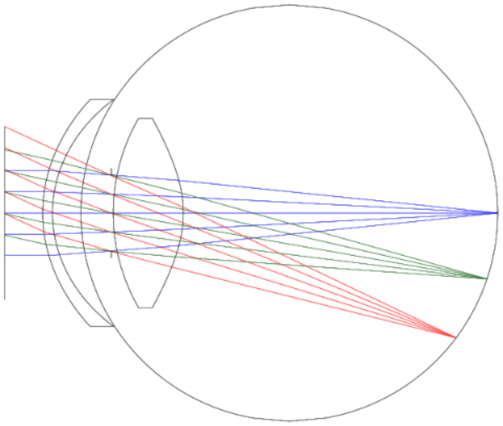

Figure 2. 4 Sequence pattern model of Eye Retinal Object.zmx in Zemax [77]

2.2 Projector system

Performance of the projector directly affects the imaging quality of the virtual images. There are some critical parameters assessing the performance of projector screen, such as the pixel, resolution, pixel per inch (PPI), and contrast. The pictures on the projector screen are made of millions of pixels. Each pixel is composed of three-color pixels, including red, green, and blue (RGB). The variety of colorful pictures is projected by adjusting RGB. Resolution is the number of pixels. PPI is the number of pixels per inch on the screen. The higher the PPI, the smaller the pixel size, and the sharper it is. Screen contrast refers to the ratio between the brightness of black and white. The higher the contrast, the brighter and more colorful the images.

2.2.1 Liquid-crystal display

A liquid-crystal display (LCD) is a flat-panel display technology commonly applied in televisions and computers. The first mass-produced LCD panel technology is twisted nematic (TN). As shown in Figure 2.5, when there is no electric field on the liquid crystal modules, the molecules in the LCD cell twist by 90 degrees. When the light from the environment and backlight passes through the first polarizer, the light is polarized and distorted by the liquid crystal molecular layer. When it reaches the second polarizer, it is blocked. Thus, the viewer observes the black screen. When there is an electric field applied to the liquid crystal molecules, they unravel. When polarized light reaches the liquid crystal molecular layer, the light transmits directly without distortion. When it reaches the second polarizer, it can pass through equivalently, and the observed screen is bright. The electric field rather than the current makes the technology consume less power. By controlling the voltage, the deflection angle of the liquid crystal layer can be adjusted, and the brightness of each sub-pixel of RGB can be controlled respectively. By changing the brightness ratio, all colors can be realized by mixing RGB in different proportions. Due to the liquid crystal molecules can't close completely, LCD is not capable of showing pure black. LCD technology has the great advantage of being light, thin and low power consumption [78-80]. However, its drawbacks include slow response time (especially at low temperatures), limited viewing angles, and backlighting requirements.

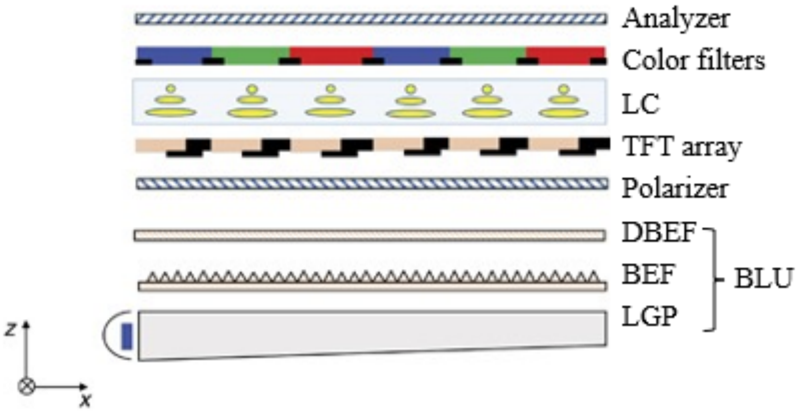

Figure 2. 5 Working principle of LCD [78]

2.2.2 OLED

A single Organic light-emitting diode (OLED) is a pixel, thus there are millions of OLED dots on the screen. As shown in Figure 2.6, there is an organic light-emitting layer between these two electrodes. When the positive and negative electrodes crush in the organic material, the light emits. Each pixel of an OLED is composed of three sub-pixels, RGB, which light up when power is on. The brightness of each sub-pixel can be controlled by adjusting the voltage. The brightness of the three colors can be mixed in different proportions to show the desired color. Except OLED lights themselves, no backlight source is needed, and each pixel can independently control the switch, enabling pixel-level light control. Compared with the LCD, OLED can provide pure black, and achieve no light leakage and perfect contrast. Besides, OLED screens have very short response times when switching between colors, with almost no drag. OLED screens are much thinner than LCD screens and can be bent considerably. OLED screens consume relatively little power by switching on and off independently for each pixel. However, the working life of OLED is shorter than LCD by aging and burning problems due to the self-light principle. Moreover, there is an obvious strobe in low brightness, resulting in visual fatigue by pulse-width modulation (PWM) dimming [81, 82]. Epson is using their own OLED for AR glasses and SONY's OLED is applied for Nreal glasses.

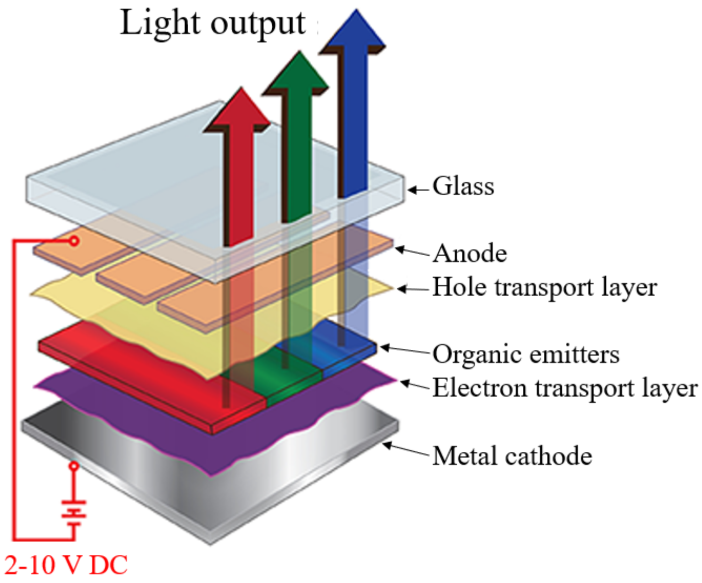

Figure 2. 6 Working principle of OLED [83]

2.2.3 QLED

Quantum-dot light-emitting diode (QLED) works based on the principle of quantum dots, which is to place quantum dots on a flat surface of a display and then use a control circuit to display the pictures, as shown in Figure 2.7. Quantum dots (QDS) have excellent optical properties, including continuously tunable peak positions of whole-spectrum luminescence, high color purity, and good stability, which are excellent luminescence and photoelectric materials. QLED display is built on these special properties of QDS to achieve high performance and low cost. Compared with OLED, QLED can provide higher brightness and a wider spectrum, and the size is flexible with longer lifetime [84-86]. However, OLED has more advantages in no light leakage, shorter response time, and wider visible view. Besides, OLEDs can provide a purer black display, better contrast, lighter and thinner, less power consuming, and performs better at night.

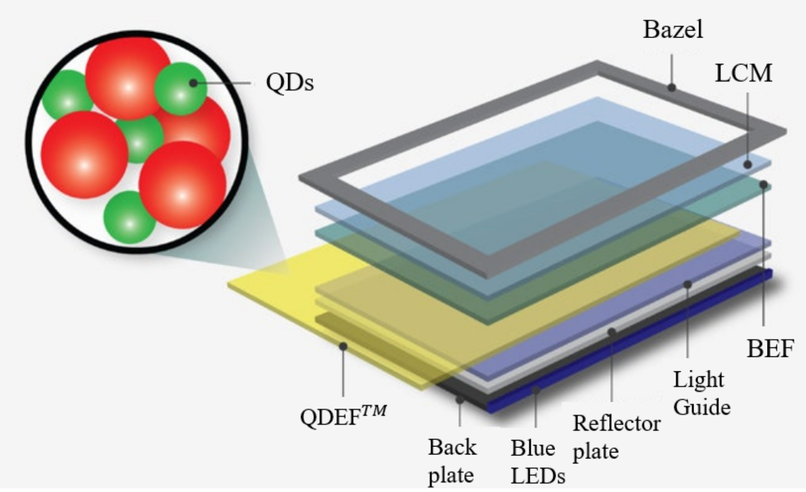

Figure 2. 7 Working principle of QLED [86]

2.2.4 LCOS

Liquid Crystal on Silicon (LCOS) is a new reflective display technology combining LCD and CMOS integrated circuit. The birefringence characteristic of the liquid crystal molecule itself is applied for the light controlling. And the polarization of the incident light is modulated by the switch of the circuit to promote the rotation of the liquid crystal molecule. As shown in Figure 2.8, when the applied voltage of the LCD layer pixel is zero, the input light does not enter the projection light path and there is no light output, that is, the pixel presents a dark state. When there is an applied voltage in the pixel, the bright is state, so the image is displayed on the screen.

The voltage applied at both ends of the pixel will affect the optical performance of the liquid crystal molecule, and then determine the grey scale of the pixel. Its advantage is that it is mature and cheap, and its pixel density is relatively high, and the overall energy rate is also relatively high [87, 88]. Its disadvantages mainly lie in its relatively low contrast, especially at large incident angles, and it must be used in conjunction with polarized beam splitter (PBS), which limits the miniaturization process of the overall optical system, and it cannot work at low temperature [87, 89, 90]. Mini Glass and Magic Leap use LCOS for the AR glasses.

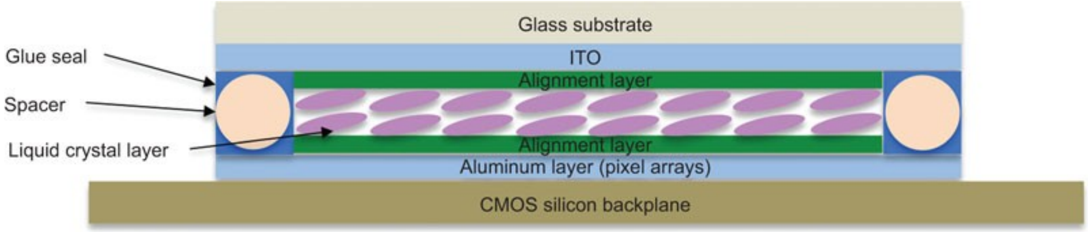

Figure 2. 8 Working principle of LCOS [87]

2.2.5 Comparison

Table 2.2 shows the performance comparison among the above projector technologies. However, the state of the art cannot achieve ideal performance for optimal imaging quality in the optical see-through near-eye display. That is the one of the reasons why the virtual image of AR display requires high light efficiency and high transparency for imaging module. Table 2.3 shows the performance gap between the ideal condition and the current craft of AR display. When the imaging module is designed, the specification of the light source should be consistent with the current craft, because the illumination and the brightness of the projector affects the final imaging quality. There is still a long way to go for perfect match between projector and imaging module.

Table 2. 2 Comparison among existing projector technologies [91, 92]

	LCD	OLED	QLED	LCOS
Substrate	Glass	Glass/polymer	Glass	Glass
Material of luminescent layer	LED/CCFL	Organic light emitting material	Quantum dot luminescent materials	LED/CCFL
Polaroid	Line polaroid*2	Circular polaroid	Line polaroid*2	Line polaroid*2
Backlight module	Yes	No	Yes	Yes
Color filter	Yes	No	Yes	Yes
Light panel	Yes	No	Yes	Yes
Emitting principle	Backlight (inactive)	Organic layer(active)	QD (inactive)	Backlight (inactive)
Contrast	>10000:1	>1000000:1	>1000000:1	>1500:1
Angle of visibility	<150°, chromatic aberration	~180°, no aberration	~180°, no aberration	~180°, no aberration
Power consumption	High	Low	Low	High
Thickness	>1.2mm	<1.5mm	<1.5mm	>1.2mm
Service life	Long	Short	Short	Long
Cost	Low	High	High	Low
Mobile phone screen	Yes	Yes	Yes	No
Flat-panel screen	Yes	Yes	Yes	Yes
Working temperature	20°C~60°C	-40°C~80°C	40°C~80°C	None
Impact on environment	Small	Big	Small	Small
TFT needed for each pixel	1	2	1	1
Toxic potentials	No	Yes	No	No
Spatial color uniformity	Great	Good	Great	Good
Light propagation	Transmission	Transmission	Transmission	Birefringence

Table 2. 3 Performance gap [93, 94]

Key Merits	Ideal	Status quo
Brightness	$10^5 \sim 10^6$ nits	10^4nits
Contrast Ratio (ANSI)	>300:1	<100:1
Refresh rate	>75Hz	60Hz
Resolution	>60 pixel/DEG	30 pixel/DEG
Power consumption	<50mW	100mW
Endurance	-55℃~100℃	-10℃~60℃
Form factor	Driver integrated, panel no larger than screen	Panel about 2*screen area
Emitting angle	Comply with exit pupil	Lambertian

2.3 Assessment parameters of AR imaging system

The user experience is related to image quality and wearable ability of the device. Thus, the optical design and optical elements are crucial to the system performance. For different application scenarios and users, diverse demands rise which requires customized optical design. It is hard to identify which specific parameter is the most important one, the expected applications of this field are always the decisive factor in the optical design. However, all of these assessment parameters should be determined by the visual requirements of human eyes and the comfort standard of wearable device. The parameters include:

Field of view (FOV) It refers to the solid angle between the outline of the object observed by the human eye and the line connecting the center of the pupil of the human eye. FOV includes the vertical field of view, horizontal field of view, and diagonal field of view, as shown in Figure 2.2 [95]. The size of a person's retina is limited, so the corresponding viewing range of the human eye is also limited. The FOV is the major indicator that many developers are concerned with primarily.

Eye relief Eye relief of an optical display represents the distance from the exit pupil area to the optical combiner within which the user's eye can obtain a full view and clear images. Most near-eye displays need binoculars or monocular with a minimum of 16mm eye relief [96]. It is an important parameter to evaluate comfort level.

Eye box Eye box is defined by the space within which the images can be effectively viewable. Therefore, images within the eye box can be observed in both angular and lateral movements of the human eye. It's how far off center your eye can be and still see through the scope properly. Within the eye box area, the observer at any position can reach the entire FOV. Exceeding this area may result in distorted images, incorrect color rendering, or even no content [97]. A larger eye box allows the user to have greater freedom on head movement to observe the whole visual image.

Distortion Lens distortion is a general term for the inherent perspective distortion of optical lenses, that is, the distortion caused by perspective. There are three kinds of distortions including pincushion distortion, barrel distortion, and linear distortion. Pincushion distortion is a phenomenon caused by the lens "shrinking" the picture toward the center. Barrel distortion is a barrel-shaped expansion caused by the physical properties of the lens and the combined structure of the lens. Linear distortion is defined as a change in amplitude or phase with no new frequencies added [98-100].

Stray light For the optical imaging system, any undesired light that propagates to the detector can be defined as stray light. Due to the multiple optical elements and complex architecture used in an integrated display system, stray light may be induced by diffraction, unwanted reflection, and scattering. Theoretically, stray light has a veto effect on optical systems. If the stray light affects the imaging quality, all ray paths should be traced back to the receiver for defects shooting. However, stray light cannot be completely eliminated, but can only be suppressed to a certain extent [101, 102]. Supposing that stray light is controlled within an imperceptible range by human eyes, or within some acceptable or permissible extent defined by users, it is regarded as the completion of stray light suppression.

Brightness and transmittance Brightness refers to the amount of light in the virtual image displayed by the optical system. Enough brightness allows users to see the image clearly in direct sunlight. It is also one of the major challenges faced by current AR devices. The brightness of most existing AR devices can be only used indoors. In order to alleviate this problem, some AR headsets use optical designs such as birdbath to block ambient light or use tinted lenses to improve the relative brightness of the optical module, but the associated adverse effect is reduced light transmittance. Light transmittance refers to how much ambient light the human eye can receive through the optical element [103-106]. The ideal light transmittance is 100% although it is still difficult for the existing AR devices to achieve. Lower light transmittance may be acceptable to consumers for some specific application scenarios in entertainment, but it is generally unacceptable in many professional/industrial application scenarios because light transmittance has a great impact on users' safety.

Resolution and contrast Resolution refers to the number of pixels a display can cover, and the optimal display resolution should be close to or slightly higher than the limits of human vision. There is no official definition or measurement of contrast or contrast ratio, for the user experience, it's a perception, a display's property to produce both bright and dark pixels. With low contrast, bright content and dark content will not be displayed correctly. In the optical perspective AR display system, dark or black color is hard to render, so high transparency areas may appear dark color in low contrast. Thereby, the brighter the AR display is, the higher the requirement for contrast is. For AR display, the color perceived by human eyes is also related to the real environment background superimposed by the virtual image. As with contrast, pixels vary in color quality depending on where they are on the display [107, 108]. For example, the same pixel color may look different on the left and right sides of the display with distinct image patterns, as well as depending on the location of the user's pupils.

Vergence accommodation conflicts There are two main reasons for vertigo: (1) conflicts between binocular parallax and accommodation on visual perception; (2) the conflict between motion perception and visual perception [45, 109-113]. The display system mainly focuses on solving the accommodation problem.

Size and weight Size is one of the biggest challenges of the see-through near-eye display. Larger FOV and eye box always mean bigger size and weight at the same time. The larger size usually implies inconvenience to wear and tends to block sight. Besides, there is a limit to the amount of weight that the human ear, bridge of the nose, and top of the head can hold.

Delay All virtual images are produced by the projectors, it affects the conflicts between motion perception and visual perception. Thus, the response time of hardware is very important for the reaction of the human brain and eye. An imaging delay of fewer than 5 milliseconds is generally considered benign for optical perspective systems. A longer delay would cause dizziness. It is mainly determined by the response time of projector.

IPD Interpupillary distance (IPD) is the distance between the pupils of your eyes measured from center to center when your eyes are focused on infinity. IPD varies from person to person, and is also smaller when looking at something nearby. The same term also applies to the distance between the centers of a binocular's exit pupils.

2.4 Comparison of AR display technologies

2.4.1 On-axis optics

Birdbath design is a typical on-axis optical system, which combines a spherical mirror and a beam splitter for a simple design and low cost. Most commercial AR glasses adopt this optical solution. However, the primary disadvantage of the birdbath design is light loss. The transmissive light and reflective light passing through is Lr x Lt. For example, if the transmissive percentage is 58% and the reflective percentage is 38% (with 4% total loss), the passing light is only around 22% (0.58*0.38) [114]. Google Glass employs a kind of alternative method using a polarized beam splitter, which is one of the birdbath architectures, as shown in Figure 2.9. Polarized beam splitter (PBS) is the simplest optical design used to split light beam from the light source, which is basically a cube glass. PBS, based on the crystal birefringence of the natural materials or the polarization selectivity of the multiple layers, usually provides high extinction ratios and a wide angular bandwidth in order to get high-resolution images [25]. When the PBS is applied in the HMD or AR glasses, a cube PBS is placed in front of the intended sight. PBS is easy to integrate with 0° of incidence (AOI) with no beam shift. The optical path of reflective light is the same as the optical path of the transmitted light. Based on the imaging principle, there would be double images or ghost images if the entrance angle is not 45°. Due to the polarized system, the maximum light throughput from the real world is no more than 45%. Furthermore, such design is bulky and heavy, and not friendly to larger FOV. Besides, the polarization beam splitting film has a high requirement on the selected light angle, and the light outside the range does not have a good effect on beam splitting. Hence, the angle of the light in the system should be controlled strictly within the range, which causes a low FOV range of 15°. PBS can hardly get colorful and sharp images, with wide frequency spectrum and a large paraxial range. Besides, the FOV of the prism display technology is greatly limited [26].

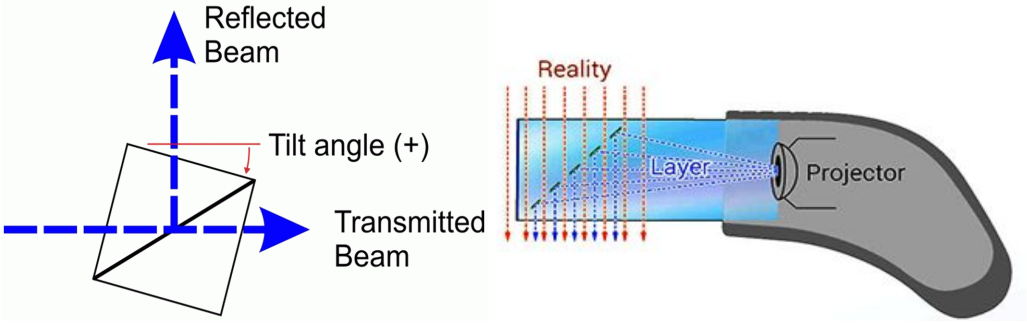

(a) (b)

Figure 2. 9 Beam splitter (a) the principle of PBS, (b) the schematic diagram of Google Glass [2, 115]

According to the law of etendue, a diagram is given to correlate the interpupillary distance, and the combiner thickness is limited by the law, as shown in Figure 2.10. Considering the manufacturing difficulties and the wearability, the optical design should be in the gray window. When applying the birdbath architectures, larger interpupillary distance (IPD) always means thicker optical elements. When applying the waveguide, it can be noticed that the thickness of the waveguide keeps constant with increased eye box, because waveguide design folds and resituates the FOV and lossless transmits the light by TIR. However, for the waveguide design, higher FOV means longer lateral size.

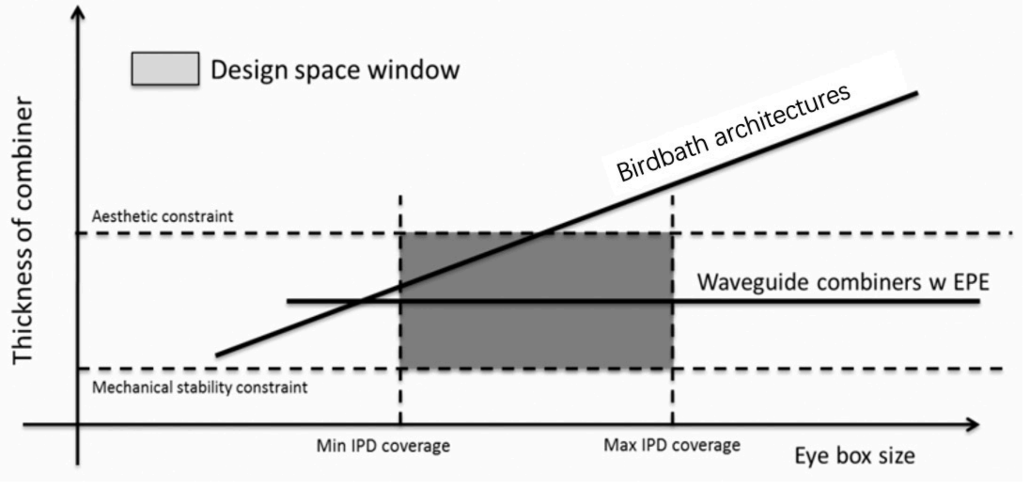

Figure 2. 10 Typical design space for specific interpupillary distance (IPD) coverage and ID requirements [6]

2.4.2 Off-axis optics

The off-axis optical system is a kind of system in which the optical axis of the aperture does not coincide with the mechanical center of the aperture. Meta 2 is the representative of commercial off-axis AR products in that the display is not perfectly perpendicular to the combiner, which is a binocular display. Actually, it also applies the plate beam splitter as shown in Figure 2.11. It is much lighter than the cube PBS and can achieve higher FOV (Meta 2 achieves 90 degrees FOV). However, the transmitted light has beam shift, and the 45 degrees AOI requires an additional alignment time.

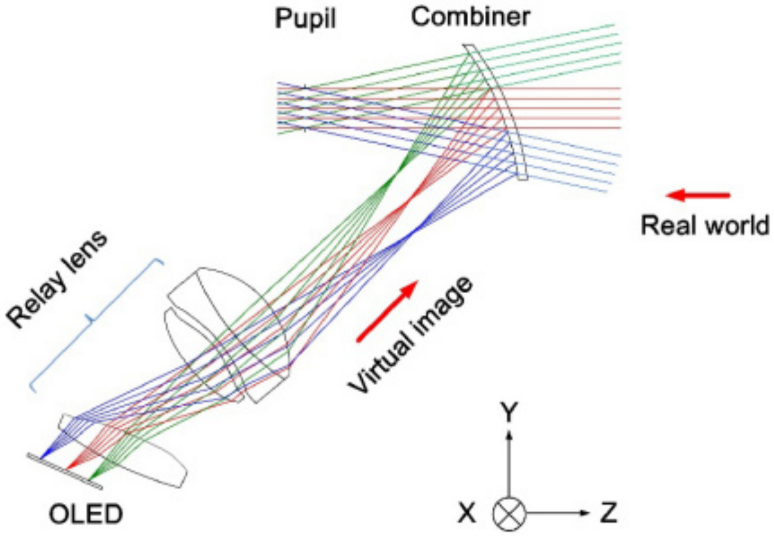

Figure 2. 11 The principle of off-axis system [33]

Compared with the coaxial system, the off-axis system can reach a wider FOV. It was measured that the Meta 2 pass 60% light and reflect 40% light. It manifests this design generates 3 to 4 times brighter images than other AR devices with the same display [116]. It also reduces the curvature hybrid. However, off-axis optical system usually contains many optical elements, which means larger size and heavier weight, so not suitable for long time use.

2.4.3 Freeform optics

Freeform is defined as any non-rotationally symmetric surface, which is very different from spherical and aspherical geometry. Freeform lenses can enable unique optical performance, such as low f-number, large eye relief, and wide FOV. One possible form of freeform optics is the eccentric use of rotating symmetrical lens, thus accommodating off-axis ranges. There are three main ways to describe free-form surfaces, including NURBS, XY polynomials, and radial basis function representation. The use of freeform optics reduces the number of components in an optical system, resulting in a smaller, lighter, and more efficient system [117, 118].

Olympus Corporation was the first to apply the freeform prism into the HMD in 1998 [21, 119]. In 2009, a combination of a wedge-shaped freeform prism and a freeform lens is designed, where it has a diagonal FOV of 53.5° and an f/# of 1.875, with an 8mm exit pupil diameter and an 18.25mm eye relief as shown in Figure 2.12. Until 2010s, mainstream systems started to integrate freeform optics into production, especially in VR and AR HMDs. For HMDs, a compact form with high optical performance, high resolution, large field-of-view (FOV) and good image quality are needed. This was significantly enabled by freeform surfaces with an additional corrector element [120].

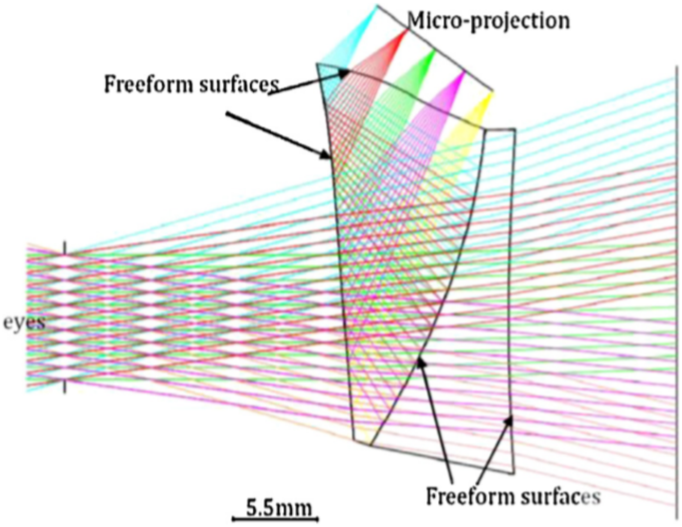

Figure 2. 12 Optical simulation of FFS prism [121]

Differing from the on/off-axis optics, the image detector is just placed at one side of the element because the freeform prism can fold the optical path into one single element [122-125]. Overall, the unique freeform optical design combines the imaging and the HMD eyepiece to achieve better display without auxiliary devices. The biggest advantage of freeform surfaces is that they can achieve very good imaging quality due to their special geometry and a high degree of freedom. However, compared with the traditional symmetric lens, the optical design and manufacturing process from freeform surfaces are more complex and demanding

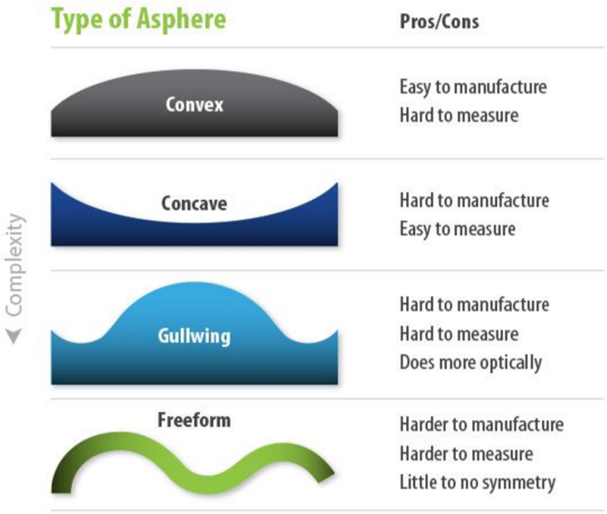

Figure 2. 13 Different types of surface (pros and cons) [126]

2.4.4 Optical waveguide

Waveguide structure has been applied in many fields, such as optical communication and optoelectronics. Optical waveguide is an optically transparent medium that guides the propagation of light waves or electromagnetic waves in it. Different from the metal-enclosed waveguide, optical waveguide is total internal reflection (TIR) on the interface with different refractive index in a limited area. Figure 2.14 shows the basic structure of the fiber optical waveguide for illustration. The refractive index of core (transmitter) is higher than that of the cladding (reflector) [127-129]. Any light with incident angle larger than the critical angle can be totally internally reflected within the waveguide where the critical angle is the angle of incidence when the angle of refraction is 90°. The light must travel from an optically more dense medium to an optically less dense medium. The light passing through the optical fiber have negligble loss in light quantity and can be emitted to the receiver. The materials of the core and cladding influence the reflective index, which determines the critical angle. Thus, the materials and refractive index influence the angle of incident light. The number of the transmitting light is limited. However, the wavelength has no effect on the transmission due to the TIR.

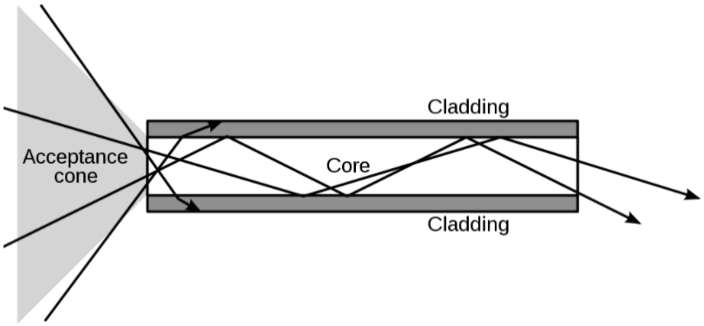

Figure 2. 14 Layout of the fibre/waveguide [127]

To obtain the three-dimensional (3D) images and better see-through optical performance, researchers proposed that waveguide could be applied replacing the half mirror of HMD. Recently, more and more companies applied the optical waveguide in the design of new optical see-through displays, such as Lumus, LingXi, Mircosoft, Waveoptics, etc. The FOV of previous generations of products were too small because of the paraxial approximation in optical design. The light near the optical axis has high efficiency and the light far from the optical axis may have quality differences. Waveguide technology bypasses the paraxial approximation problem. Optical waveguide structures are thin, which makes the optical system small and lightweight to bring more favorable wearability. It is a promising optical solution to satisfy the large eye box, enough eye relief and large FOV. In contemporary HMD systems, several waveguide methods are used for AR applications: reflective, polarized, diffractive and holographic waveguides.

1) Diffractive waveguide

Diffractive waveguides are currently widely used in the optical see-through display. The incident light wave is collimated into the waveguide with a certain angle through the first slanted grating (in-coupler). After passing through the waveguide, it would finally extract the pupil through the second slanted grating (out-coupler). The diffractive optical element (DOE) is the couple-in and couple-out part of the system as shown in Figure 2.15 [15]. DOE waveguide is thin, light and has high light transmission (usually higher than 89%), which enhances wearability.

The diffractive waveguide, also called a surface relief waveguide, was patented and first commercialized by Nokia. The transparent AR system Vuzix produced by Nokia and Microsoft Holographic Lens applies the diffractive waveguide, which has low-resolution for the transferred light information. Magic Leap aimed to use the laser as light source, the principle of which is the same as the DOE waveguide. The application of nanometer beam sources can reduce some defects, but cannot eliminate, such as flares for the capturing light from the real world. Additionally, they applied the multilayers optical waveguide to solve part of the Vergence–Accommodation Conflicts (VAC).

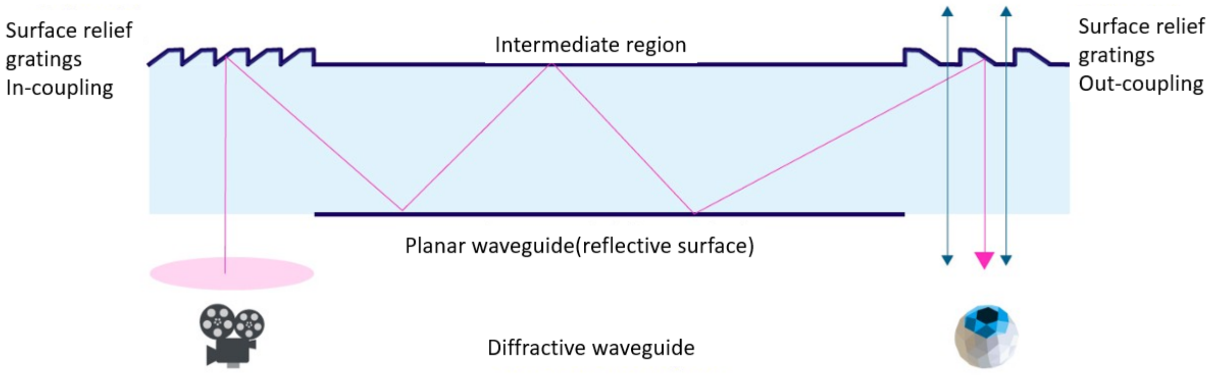

Figure 2. 15 The schematic of the diffractive waveguide[130]

Diffraction grating observation can blur and distort the image of the real world, and the waveguide would soften/blur the virtual image (not all light can pass through the waveguide). There are two undeniable problems for DOE waveguides. One is the rainbow effect of the diffraction grating, and the other is the darkening of the real world. The rainbow effect is due to the diffraction effect. The diffractive waveguide has a common problem that the blue and blue-green color shifts in image as consequence of the rainbow effect. Meanwhile, the optical efficiency of the waveguide is too low. Only a small part of the light can be seen by human eyes. It is estimated that diffractive waveguide blocks about 85% of the light. Different from the prisms, diffractive gratings diffract the light into a series of diffractive orders as shown in Figure 2.16. Only one of these orders is of the essence when using the diffractive waveguide, with the rest of the light being lost, resulting in reduced contrast of the whole system when those orders bounce back in the optical system. If the angle of the incident light is too large for the in-coupler, the light cannot be diffracted/coupled into the waveguide. The function of the grating is influenced by the angle and spacing of the orders of the grating, which also affects the transmission of visible light from the real world [131-133].

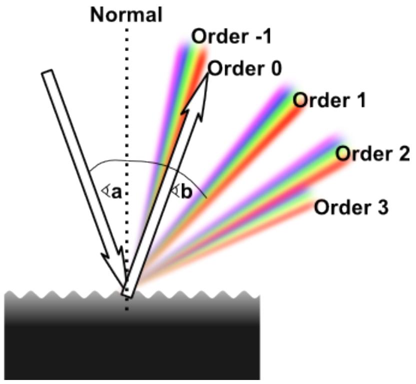

Figure 2. 16 Diffraction grating [134]

The molding and UV-replication processes are applied for the mass production but the high cost is still an obstacle for consumer products [135-138]. Meanwhile, nano-imprint master manufacturing stage is widely applied because the cost can be controlled and the yield rates are suitable for the commercial production [120, 139].

2) Holographic waveguide

Holographic waveguide display is developed with the maturity of holographic imaging technology. This technique was developed in 1990s by Kaiser optical system [140]. Holographic optical element includes a lens, filter, beam splitter and diffraction grating. Holographic technique is applied to record and reproduce the real three-dimensional image of the object using interference and diffraction principles. [7, 23, 141-143].

The principle of the holographic waveguide is total internal reflection and diffraction as shown in Figure 2.18. The system is composed of a microdisplay, a holographic grating and slab waveguide. Holographic grating is a film, the principle of which is similar with that used in the diffractive waveguide. They are all used as the in-couplers and out-couplers. The light wave from the projector goes through the collimating lens, becoming the parallel light beam and then reflected into the in-coupler. The transmission direction of the light in the waveguide will be altered by the diffraction effect of the holographic. When the light beam arrives at the out-coupler, the condition of TIR is destroyed and hence the light is transmitted out of the waveguide to reach human eyes, projecting images on the retina.

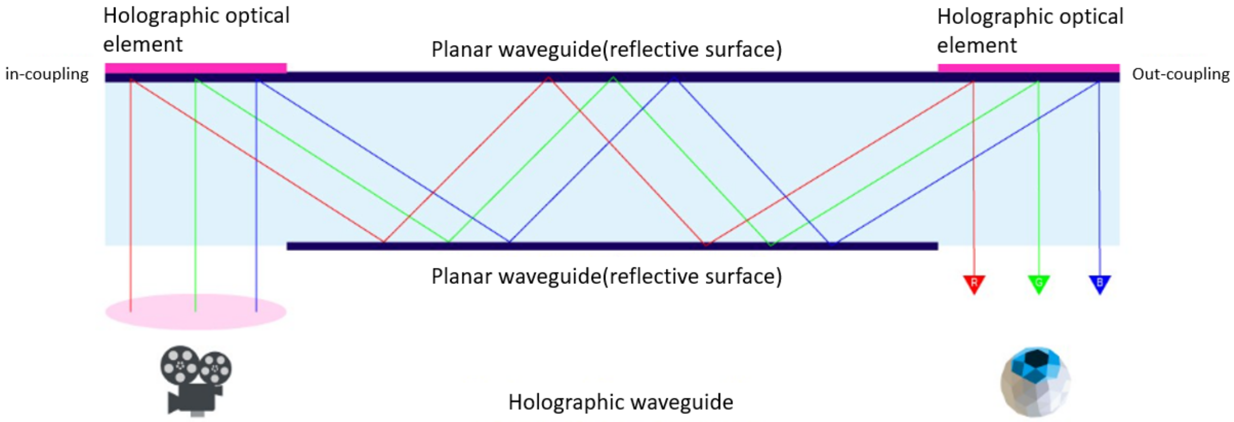

Figure 2. 17 Schematic of the holographic waveguide [130]

There are two kinds of holographic waveguides, one applies the transmission hologram, another applies the reflection hologram as shown in Figure 2.18. The spectral bandwidth of reflection hologram is narrower and the angular selectivity of it is narrower than the transmission hologram. Wider angular bandwidth allows larger FOV, while narrower spectral bandwidth allows broader spectral source, which helps eliminate the color crosstalk problem. Thus, reflective hologram is more widely used in holographic waveguide in AR HMDs [120].

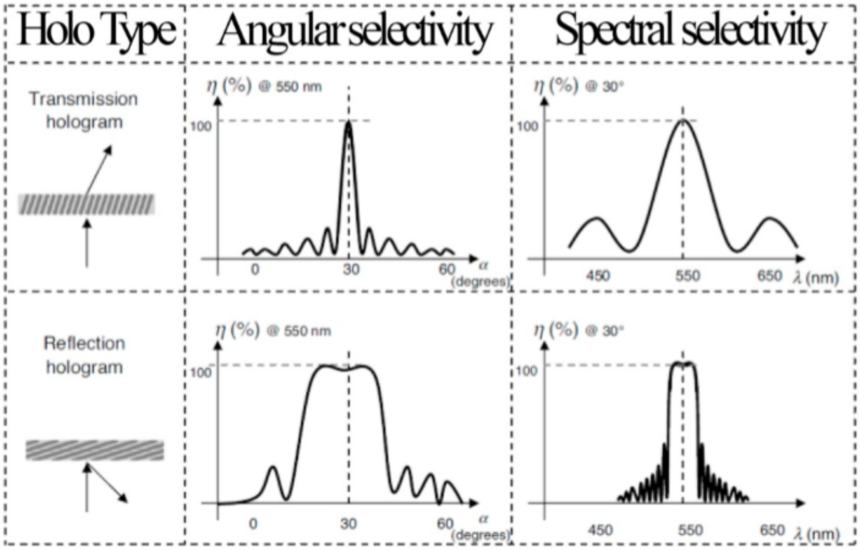

Figure 2. 18 Angular selectivity and spectral selectivity of transmission and reflection holograms [144]

The diffraction efficiency of the same color fluctuates depending on the incident angle, resulting in a different proportion of red, green, and blue light across the entire field of view (FOV), which is called the rainbow effect. This is caused by the inherent physical characteristics of diffraction gratings, and the color uniformity problem can only be optimized but not completely eliminated by design. Besides, the optical efficiency of the diffractive elements is very low, with nearly 85% of the projected light blocked, so only a small part can reach the human eyes. As a result, usually, an extra shading lens is needed for the observer to see the virtual images clearly and the contrast of the whole system is also reduced.

3) Geometrical waveguide

The geometrical waveguide is employed by Epson and Lumus. The reflective coating film is used as the in/out-coupler for the light propagating. The light is totally internally reflected by the in-coupler and bounces within the waveguide. When the light hits the out-coupler, part of the light is reflected out of the waveguide towards the eye while another part transmits through it for further propagating to the next out-coupler, as shown in Figure 2.19. The partially reflected mirror array (PRMA) expands the exit pupil and achieves uniform light for virtual images. Since the light will be reflected out from each out-coupler which makes the light density arriving at each out-coupler distinct, each of the out-couplers in the array needs a different reflection and transmission ratio (R/T) to ensure that the amount of light coupled out within the whole range of the eye pupil is uniform. The wavelength will not affect the imaging quality, but the R/T ratio would result in fringes in light and dark. The PRMA replicates the pupil to increase the total exit pupil area, however, it reduces the amount of light at each exit pupil area. Thus, the efficiency of the geometrical waveguide is less than that of conventional optical systems. It is complicated in manufacturing of geometrical waveguide, which presents rigorous requirements to each step of the process chain for high precision, usually at the micro and nano scale. Figure 2.20 shows the position of the projector and the waveguide, and how the light beam travels in the system. For the projector and the waveguide, they can be manufactured by common optical materials. This technology provides high brightness, compact and lightweight optical see-through display.

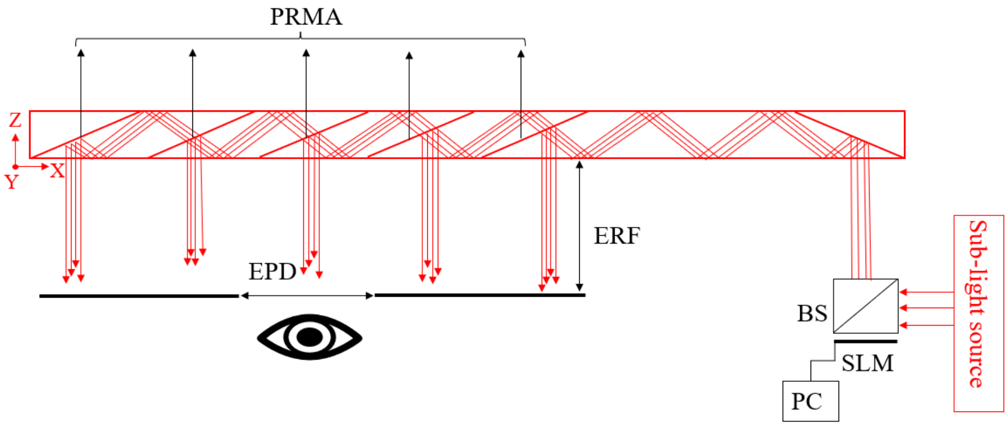

Figure 2. 19 Schematic of the geometrical waveguide

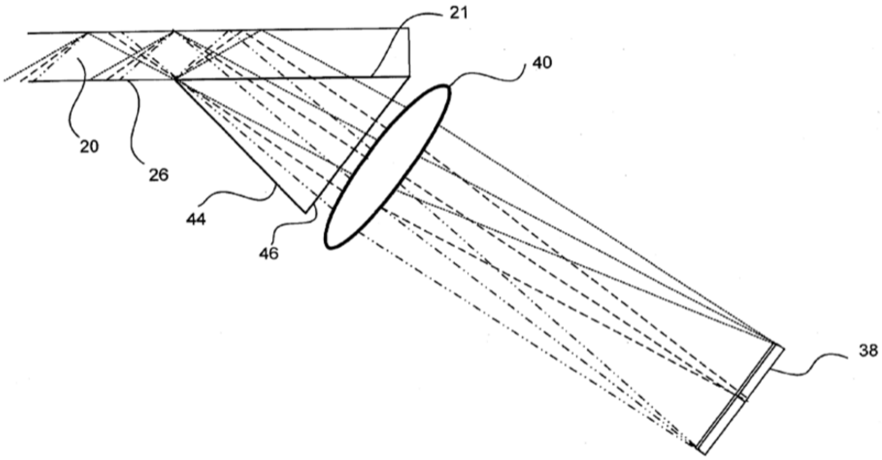

Figure 2. 20 The light beam travels in the system, betweeen the projector and the waveguide [145]

Compared with all above technologies, geometrical waveguide has great advantages in thickness, FOV, eye box, light efficiency and size. Based on the imaging principle of geometrical waveguide, the trade-off process of the parameters is crucial to reach better physical performance. The stray light should also be supressed to reach better optical performance.

GodView, a company which is focusing on AR/MR core optical modules and smart glasses application demand solutions, released the world's first resin arrayed geometrical waveguide as shown in Figure 2.21. Different from the glass material diffractive waveguide, the GodView resin array optical waveguide technology can produce new nano-resin materials with lower cost and higher plasticity. It liberates from the bottlenecks of glass material, such as the manufacturing difficulty, low portability, weight, fragility and safety. At the same time, it has better performance than glass material regarding FOV and transmittance, which greatly reduces the cost and improves the optical performance and productivity of lens. The thickness of GodView resin array optical waveguide is around 1.3-2.0 mm, which is thin and it solves the problem of atomization caused by temperature difference. Lightweight and strength of resin materials can also provide the property of anti-fall performance and safety. This is the key reason why GodView resin array optical waveguide lenses have attracted significant attention [25, 146, 147]

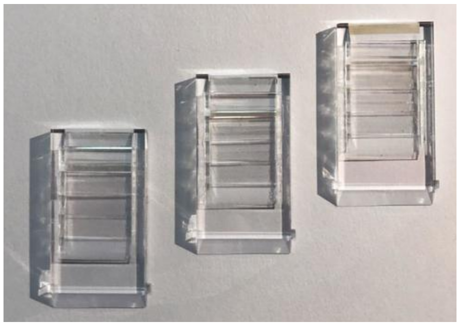

Figure 2. 21 The resin materials applied in the waveguide by GodView [148]

Comparison of waveguide technologies

As discussed above, the optical waveguide is one of the most promising technologies for the optical see-through display. Table 2.4 compares geometrical waveguide and diffractive waveguide.

Table 2. 4 Commercially available waveguide see-through displays [149]

Waveguide Category	Geometrical waveguide	Diffractive waveguide
Representatives	Lumus, Lingxi, Lochn,etc.	Microsoft, Magic Leap, Digilens, Waveoptics, etc.
Optical element	Transflective film array: glass or plastic with thin film coating	Surface relief grating (SRG), volumetric holographic grating (VHG)or holographic optical element (HOE)
Input	Reflective film	SRG, VHG
Output	Transflective film array	SRG, VHG
Largest FOV	65°	55°
Eye relief	~20mm	~20mm
Eye box	15mm*5mm	12mm*13mm
Thickness	~2mm	~3mm
Transparency	>80%	>35%
Imaging effect	Ghost images, fringes	Rainbow effect, color dispersion
Light efficiency	10%-15%	2%-5%
Manufacturing method	Conventional optics, coating, stacking, slicing, etc.	Microfabrication in semiconductor foundry, nanoimprint, holographic laser interferometry
MP	Hard	Easy

1) Transparency

As shown in Table 2.4 compared with the diffractive waveguide, the transparency of geometrical waveguide is much higher. The diffraction gratings soften or blur the virtual images. If more lights from the real world are reflected into observer's eye, the observer would not see the virtual image clearly. It is defined as waveguide glow when it is out of focus reflections. The contrast and resolution of the images is lower when in larger bright environment. The image of Magic Leap is even blurrier than HoloLens.

2) Color issue

The DOE and HOE are based on the diffractive theory. Diffractive grating has both angular selectivity and wavelength seletivity. For the angular selectivity, the transmission of the light is determined by the light frequency, and the diffractive intensity is influenced by the incident angle of the light beam, as shown in Figure 2.22. The diffractive light cannot be seen at a diverged viewpoint, which intrinsically limits the FOV.

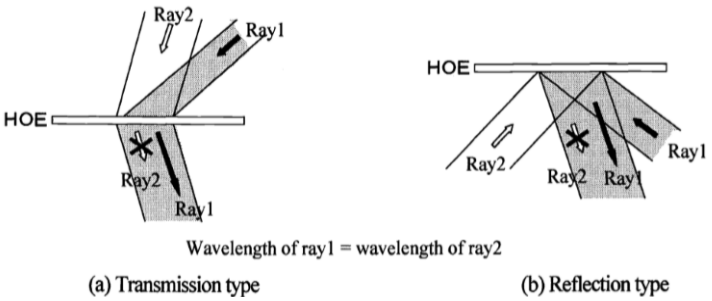

Figure 2. 22 Basic principle of angular selectivity of DOE/HOE [23]

Another side effect is the rainbow effect, which is due to the fact that the holographic grating can only diffract single wavelength, which there should be three colors (RGB) sandwiched together, meaning that each of which needed to be exposed by a laser in a special direction. If single wavelength is slightly diffracted by another color grating, there will be color "cross-talk". Although this can be corrected by software, the nuance of color sensitive can still be noticed [150]. As shown in Figure 2.22, HoloLens stacked RGB waveguides with slanted sub-wavelength gratings (SRGs) acting as couple-in and couple-out for lights transmission and reflection. The Microsoft holographic lens can block 60% of the light but can penetrate 2.67 times more real light than the diffractive waveguide.

However, for geometrical waveguide, no matter the reflective waveguide or polarized waveguide, they have no grating color issue. The largest problem of the geometrical waveguide is the uneven strips because of the foldding and unfoldding of the images. Precision manufacuring is the main method to resolve the strips problem. Thus, the image quality of geometrical waveguide could be higher than the diffractive waveguide.

3) Light energy utilization

The light energy utilization of the geometrical waveguide is much higher than the diffractive waveguide. Due to the way of the couple-in, when the light enter the coupler, the DOE/HOE influences and blocks some lights to reduce the light energy.

4) Eye box and FOV

The eye box and FOV are pertinent to the optical design. Diffractive waveguide and goemetrical waveguide both apply the waveguide TIR. Thus, there is no big difference between there two waveguides.

Based on the above discussion, it can be seen that the geometrical waveguide is more promising in the future development.

2.4.5 Comparison of mainstream AR display technologies

Among the above technologies, geometrical waveguide is confirmed to possess best optical properties potentially as shown in Table 2.5 [26, 115, 145, 151].

Table 2. 5 Comparison of some mainstream AR display technologies [149, 152]

Technology	Prism	Freeform	Birdbath	Diffractive waveguide	Geometrical waveguide
Represent Products	Google Glass	EPSON BT-35E	NedAR AR180120	Microsoft Hololens 2/ WaveOptics	LUMUS OE-50/ LingxiAR 2D-1
Difficulty in manufacturing	Weak	Medium	Medium	Strong	Strong
Thickness	>10mm	>10mm	>8mm	<2mm	<2mm
FOV	~55°	~30°	30°~50°	>40°	>40°
Transparency	~50%	~50%	<50%	>80%	>90%
Efficiency	10%~20%	30%~50%	10%~15%	0.3%~1%	>15%
Size	Large	Large	Small	Small	Small
Projector screen	LCoS	LCoS/Micro-OLED	Micro-OLED	DLP/Micro-LED	LCoS/Miceo-OLED/Micro-LED
Weakness	Large volume	Thick	Thick, low brightness	Rainbow effect, low efficiency	Hard manufacturing

As compared in Table 2.4 and Table 2.5, the waveguide technology performs much better in thickness, transparency, and size, which directly affect the lightweight requirement and immersive feeling. However, compared with the manufacturing of conventional technologies, waveguide technology has more complex manufacturing process. Complicated manufacturing increases the difficulty of the product yield. Only by meeting the commercial standards of lightweight can products be applied to more scenarios more flexibly. Overall, waveguide technology is the most promising method in AR devices, and geometrical waveguide can achieve better optical performance than diffractive waveguide.

2.5 LightTools process

LightTools is a professional optical simulation software commonly used to design and optimize optical systems. The LightTools Core Module provides graphical 3D solid modeling functionality and interactive optical ray tracing for creating and visualizing optical and opto-me-chemical systems, including the capability to specific properties for materials and optical surfaces. LightTools enables designers to simulate and analyze light as it traverses the optical and mechanical components in a model. Includes state-of-the-art Monte Carlo ray tracing for accurate predictions of intensity, luminance, and illuminance throughout the model, as well as powerful illumination analysis capabilities. It automatically improves the performance of virtually any type of illumination system. Full integration with the LightTools 3D solid modeling environment ensures practical, realistic solutions in a fraction of the time it would take to accomplish manually. In this thesis, we mainly applied advanced design module, illumination module, stray light analysis module and optimization module. Here is the basic flow of optical simulation using LightTools:

1) Create the model: Use the tools in LightTools to create the geometry and materials of the optical system.

2) Set the light source: Select the appropriate light source type and set the light source properties, such as light intensity and wavelength.

3) Add materials: Add appropriate optical materials such as glass, metal or plastic to different parts of the model.

4) Define boundary conditions: Set appropriate boundary conditions on the surface of the model, such as reflection, transmission or absorption.

5) Run simulation: Run optical simulation and collect data by selecting appropriate simulation Settings.

6) Analysis results: Use the analysis tools in LightTools to evaluate the performance of the optical system, such as light intensity, spot size, and transmission efficiency.

7) Optimization model: Optimize the optical system according to the simulation results, such as changing the position of the light source, changing the shape of the optical element or changing the optical material.

8) Export results: Export simulation results into graphs or data files for further analysis or use.

The process of stray light simulation module in Chapter 3/Chapter 4/ Chapter 5 can be concluded as:

1） Ray path analysis that visually identifies stray light issues and summarizes energy flux and total power

2） Receiver data filtering for multiple analyses from a single simulation

3） Aim areas for efficient analysis of stray light in systems

4）CAD import and export to leverage existing data

2.6 Summary

For optical see-through display systems, there are many important parameters in evaluating the display performance. To achieve the high brightness required for AR display, the choice of both projector and optical combiner is very important. Generally, there is no universal display solution that can satisfy various application scenarios. AR display systems are an integration of projector, optical combiners, digital processing unit, power source, etc, which requires to work synergistically to suit different AR system specifications.

The requirements of the human eye visual system provide quantitative standards for AR displays and point to the main issues that need to be addressed in current AR head-mounted displays, such as resolution, field of view, display brightness, convergence-adjustment conflict, and volume size. The larger the field of view, the higher the display brightness, the bulkier the display device becomes. The convergence-adjustment conflict is generally resolved by changing the display plane distance or providing different display planes. Optical combiners combine virtual objects with real scenery and determine the display brightness of AR head-mounted displays. Geometrical waveguides have better imaging quality, high efficiency, and larger size. Although the size of the grating waveguide combiner is small, the display brightness is insufficient, and the grating diffraction tends to make the brightness distribution and color distribution nonuniform. Under the contemporary technology level, how to find the delicate balance between the field of view and display brightness and other indicators is crucial for AR devices. With the development of micro-projector, optical imaging technology and digital processing, the future AR head-mounted display will certainly be more compact and comfortable and would be competent to diversified application scenarios for various applications.

Chapter 3 Design and optimization of geometrical waveguide

Waveguide technology has great prospects of development in optical see-through near-eye displays with larger field of view, lower thickness and lighter weight than other conventional optical technologies. However, the stray light is usually inevitable in current optical design and manufacturing, causing a poor imaging quality. In this chapter, the principle and structures of stray light generation in 1D and 2D model are analysed, and the causes are discussed by non-sequential ray-tracing with mass precision calculation. These designed models perform much better than prior models in optical performance.

3.1 Design of 1D geometrical waveguide

For the geometrical waveguide, as shown in Figure 3.1(a), the visual information is projected by a light source, then collimated and coupled into waveguide. The projected light is totally reflected by the in-coupler. The light can be totally reflected internally within two edges of waveguide component and coupled out to observer’s eyes until it transfers to out-coupler, partially reflective mirror array (PRMA), which break the TIR condition. The geometrical waveguide works as an entrance pupil expander, as shown in Figure 3.1(b). The PRMA should keep the uniformity of the illumination to human eyes. This property of the waveguide has great advantages in optimizing the design and appearance of the headset. However, several exit pupils increase the total area of exit pupil, which decrease the luminous flux at each exit pupil. The optical efficiency of the waveguide is low, and a powerful projector is required.

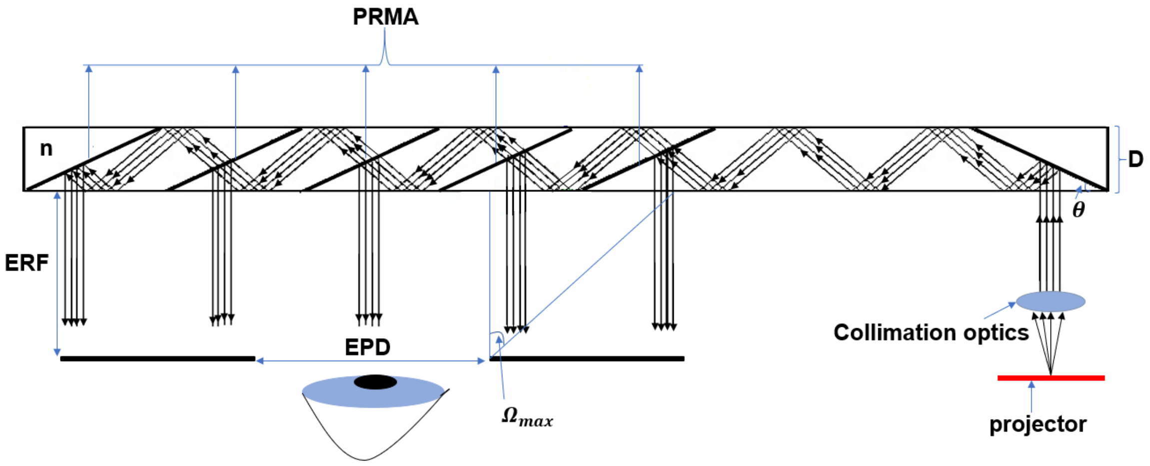

(a) Schematic diagram of the geometrical waveguide near-eye display

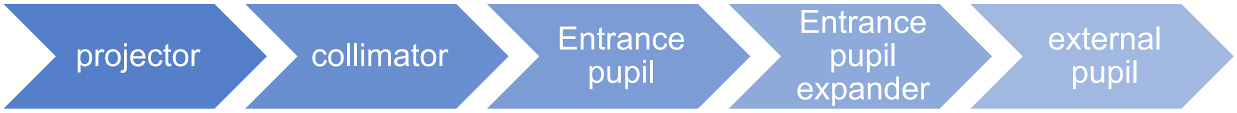

(b) The process of the system

Figure 3. 1 The geometrical waveguide system

Figure 3.1(a) shows the schematic diagram of the geometrical waveguide near-eye display, where n is the refractive index of the base material, D is the thickness of the waveguide, θ is the angle between the edge of waveguide and in-coupler. The angle between the out-coupler and the edge of the waveguide is also θ. There are 5 mirrors (out-couplers) in the waveguide. The maximum field angle along the direction of entrance pupil expander (EPD) can be defined as Eq. (3.1). EPD is the best observation area on the exit pupil plane.

$$\tan \Omega_{max} = \frac{\frac{N*D}{\tan\theta} - EPD}{2ERF} \tag{3.1}$$

where the N is the number of PRMA. The FOV of the waveguide is expressed by Eq. (3.2).

$$FOV = 2\ \tan^{-1} \frac{\frac{N*D}{\tan\theta} - EPD}{2ERF} \tag{3.2}$$

The lights transfer inside by TIR, which means the lights inside angle with the edge ω_2 (shown in Fig. 3.4) must be larger than the critical angle θ_c and satisfy the following formula:

$$\theta_c = \sin^{-1}\left(\frac{1}{n}\right) \tag{3.3}$$

$$\omega_2 = 2\theta - \omega_1 > \theta_c \tag{3.4}$$

where ω_1 is the refractive angle of the light along the entrance pupil expansion in the waveguide. Any angle lower than the critical angle cannot be totally-internally-reflected (TIR) within the waveguide. In engineering optics, the refractive index of air is often regarded as 1. Thus,

$$\theta > \frac{\sin^{-1}\left(\frac{1}{n}\right) + \omega_1}{2} \tag{3.5}$$

From the above, it is obtained that larger refractive index of the substrate results in larger FOV when keeping the other variables constant. The whole length of the waveguide cannot be too long, as expressed in Eq. (3.6). Usually, the maximum length is set as L_{whole}, which is set for the waveguide before reaching the out-couplers.

$$L_{whole} = \frac{N*D}{\tan\theta} + \frac{m*D}{\tan(2\theta-\omega_1)} \tag{3.6}$$

where m is the number of reflections of the light before reaching the first out-coupler. Hence, it is derived below:

$$m < \left(\frac{L_{whole}}{D} - \frac{N}{\tan\theta}\right) * \ \tan(2\theta-\omega_1) \tag{3.7}$$

To increase the range of eye moving, the exit pupil diameter (EPD) is usually 10mm. ERF is set to 20mm to satisfy the observers with glasses. People pursue large FOV, according to Eq. (3.2), the larger D, the smaller θ, smaller EPD and ERF could reach the larger FOV. However, in practise, larger FOV, thinner waveguide and bigger EPD and ERF are all expected. Thus, the parameters selection is a trade-off process depending on specific application focus.

3.2 Design of 2D geometrical waveguide

The schematic diagram of 2D geometrical waveguide system is shown in Figure 3.2, which is the orthogonal combination of a horizontal waveguide and a vertical waveguide. Both waveguides have in-coupler and out-coupler elements. The information is projected from the projector, then collimated and transferred into the vertical waveguide. The light is coupled into the middle of the vertical waveguide and transfer upwards and downwards simultaneously. Partial light transfers through the in-coupler and directly couples out into the horizontal waveguide, while the other part propagates by TIR for the vertical expanding and then couples out to the horizontal waveguide when light meeting the out-couplers (partially reflective mirrors array). Similarly, horizontal waveguide works in the same way as that of vertical waveguide. After horizontal expanding, the light arrives at observers' eye pupil. The specific way of two-dimensional expanding has great advantages in optimizing the design and appearance of the near-eye display. However, several exit pupils of the 2D waveguide increase the total area of exit pupil of the system, which decrease the luminous flux at each exit pupil. Thus, a high-performance projector is required to increase the optical efficiency of the waveguide. The waveguide works in expanding the exit pupil from projector. The pupil could intercept the complete image information from a certain plane, which could be transmitted to the retina by a lens. The light from the out-couplers produces a sub-exit-pupil array. Since the light rays exit at the same angle, light from any two or more adjacent out-couplers can converge to a single point in the eye's lens to form an image. The human eye can observe whole FOV in the eye box (any places, which could receive the entire light from the out-couplers to form an entire image).

Therefore, the light from the same angle would theoretically cover one visual cell, like a pixel in the image sensor, without any double shadows or ghost images. If the gap between the out-couplers is beyond the eye resolution 60”, double shadows or image gap would be observed by human eye. The design could obey the visual requirements as discussed in Chapter 2.1.

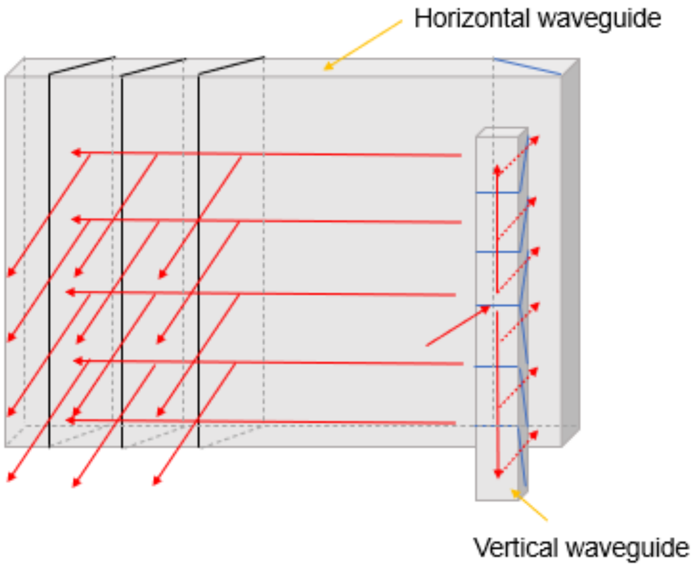

Figure 3. 2 Configuration of two-dimensional geometrical waveguide.

3.2.1 Horizontal waveguide

Figure 3.3 shows the schematic diagram of the horizontal geometrical waveguide. Entrance pupil expander (EPD) is the best observation area on the Fourier plane. The FOV of the horizontal waveguide is defined as Eq. (3.8).

$$FOV_{horizontal} = 2\tan^{-1}\frac{\frac{N*D}{\tan\theta} - EPD}{2ERF} \tag{3.8}$$

$$\mathrm{EPD}_{\mathrm{horizonal}} = \frac{\mathrm{N*D}}{\tan\theta} \tag{3.9}$$

where D is the thickness of the waveguide, θ is the angle between the edge of waveguide and in-coupler equal to the angle between the out-coupler and the edge of the waveguide, N is the number of out-couplers in the waveguide. Eq. (3.9) is the horizontal eye box of the model.

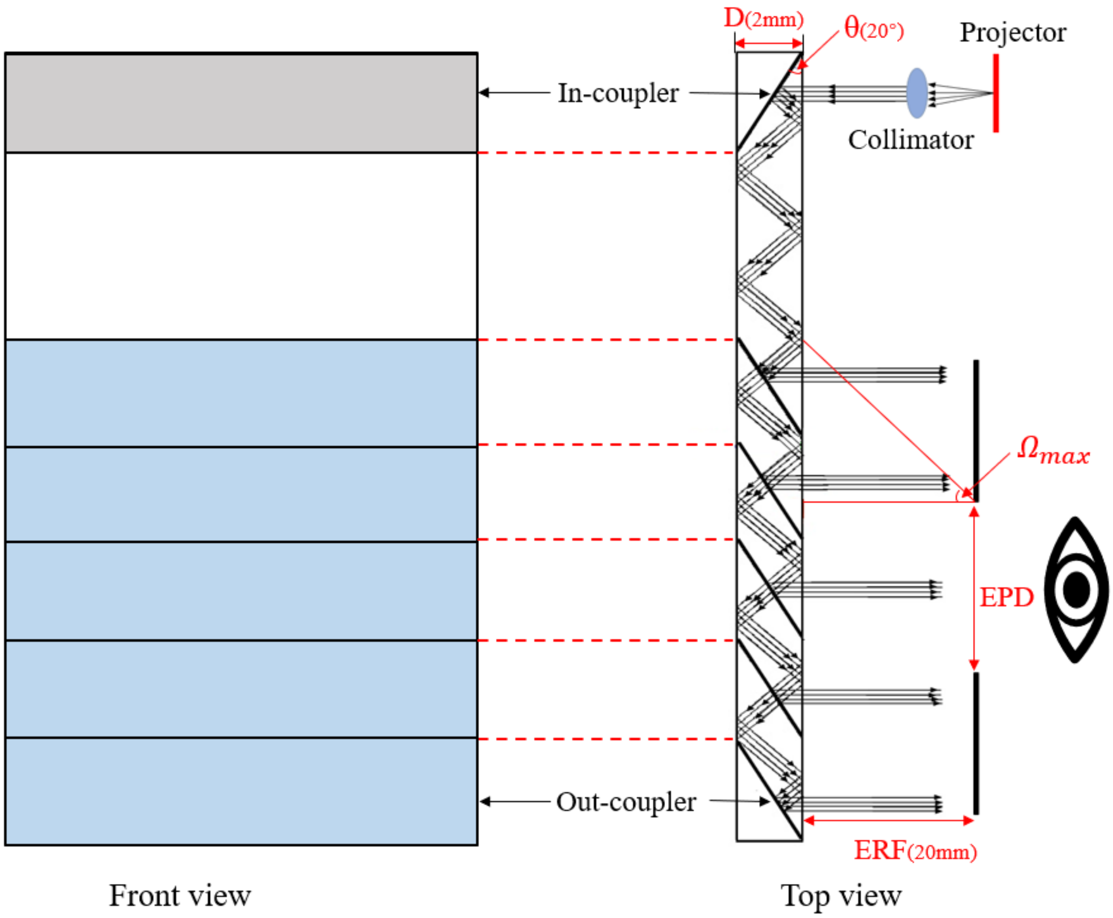

Figure 3. 3 Configuration of horizontal waveguide.

The light propagates by TIR, thus, the transferring angle with the edge ω_2 (shown in Figure 3.4) must be larger than the critical angle θ_c (any angle smaller than the critical angle cannot be totally internal reflected within the waveguide) which must satisfy Eq. (3.10).

$$\omega_2 = 2\theta - \omega_1 > \theta_c = \sin^{-1}\left(\frac{1}{n_1}\right) \tag{3.10}$$

where ω_1 is the entrance angle of the light along the entrance pupil expansion in the waveguide, n_1 is the refractive index of the substrate material. Any angle ω_2, which is lower than the critical angle cannot propagate with TIR within the waveguide. Thus, θ is derived as the following.

$$\theta > \frac{\sin^{-1}\left(\frac{1}{n_1}\right)+\omega_1}{2} \tag{3.11}$$

From the above equation, it is obtained that the larger refractive index of the substrate results in larger FOV when keeping the other variables constant. The exit pupil diameter (EPD) is set as 10 mm and ERF is set to be 20 mm to give the observers more flexibility. According to Eq.

(3.8), the larger D, the smaller θ, smaller EPD and ERF could result in the larger FOV. Larger FOV, thinner waveguide, bigger EPD and ERF are expected at the same time in practical application. However, the parameter selection is a trade-off depending on the specific requirements of the application.

The length of the waveguide should meet ergonomic principle, as expressed in Eq. (3.12).

$$L_{wavegudie} = \frac{N*D}{\tan\theta} + m*D*\tan\omega_2 \tag{3.12}$$

where m is the number of reflections of the light before reaching the first out-coupler. Hence, it is derived below:

$$m < \frac{\frac{L_{waveguide}}{D} - \frac{N}{\tan\theta}}{\tan\omega_2} \tag{3.13}$$

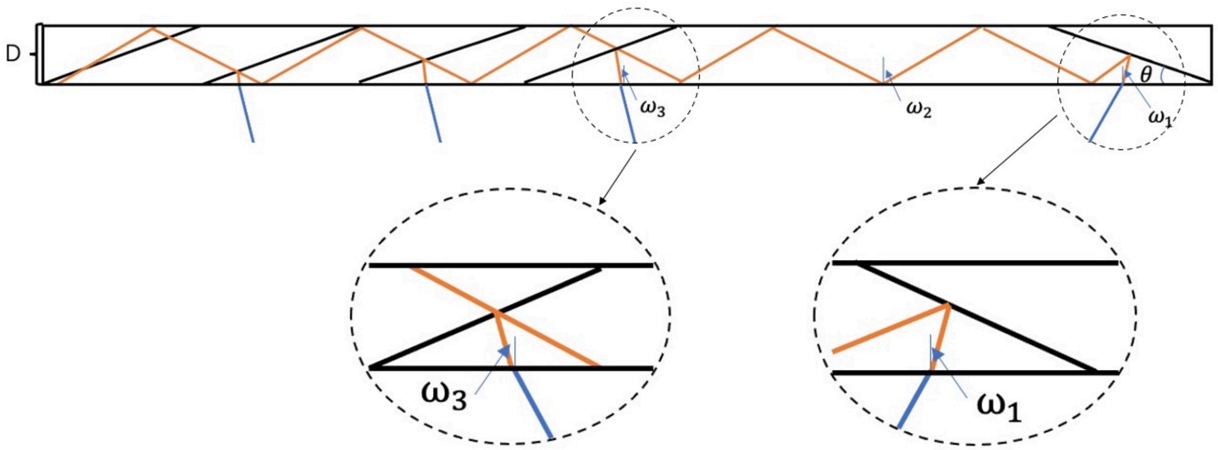

Figure 3. 4 The included transferring angle in the horizontal waveguide

3.2.2 Vertical waveguide

The vertical waveguide is designed based on the parameters of the horizontal waveguide to match the eye pupil, as shown in Figure 3.5(a). The projector is set in the middle point of the vertical waveguide to reduce the total travelling distance so as to reduce the stray lights. Figure 3.5(b) is the back view and (c) is the side view of the vertical waveguide. When the light transfers to the in-couplers of vertical waveguide, partial light continues transferring with the original direction and couples out of the substrate, and the other part of light is reflected and couples to the substrate by TIR and continues to travel to the other out-couplers. Therefore, for each out-coupler, a part of the light is coupled out to horizontal waveguide and the other part transfers to next out-coupler except the last one with total reflection. The out-couplers are designed with different coating films to achieve different reflection/transmission ratios. The coating characteristics on different out-couplers should ensure that the coupled-out light is evenly distributed on every out-coupler.

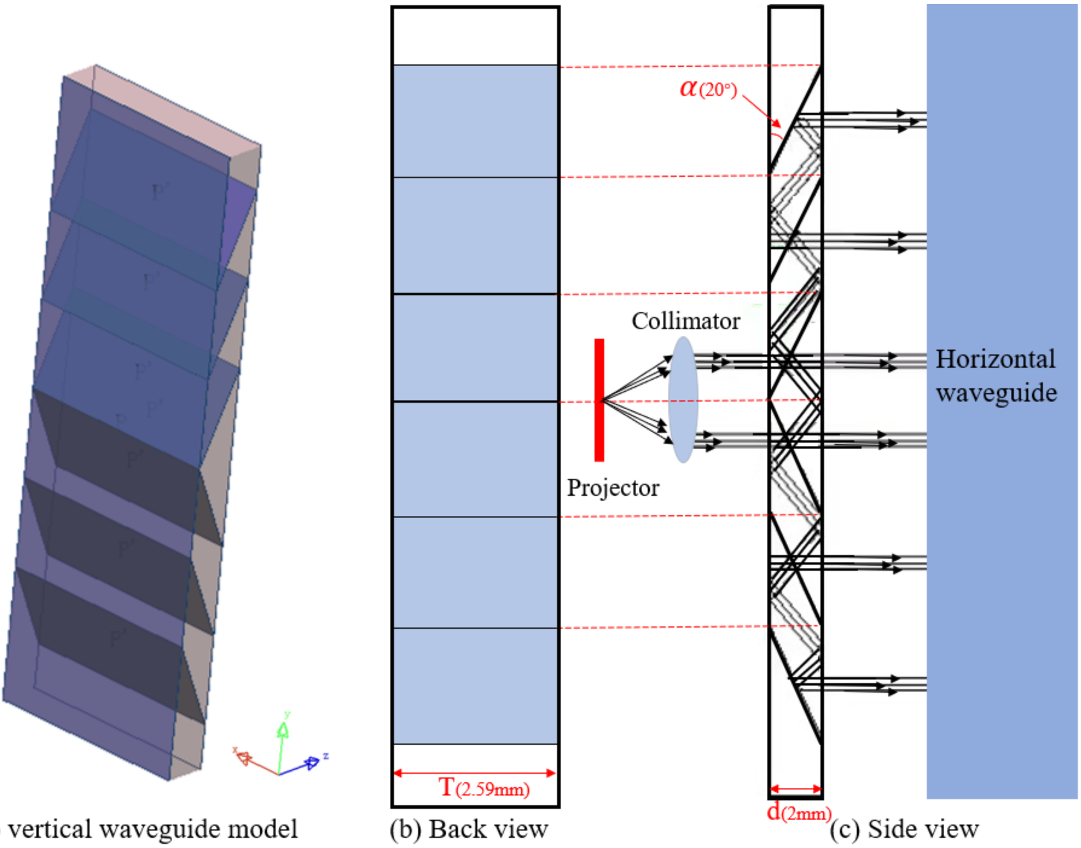

(a) vertical waveguide model (b) Back view (c) Side view

Figure 3. 5 Configuration of vertical waveguide.

The light is expanded by vertical waveguide in vertical direction, the FOV is also expanded correspondingly. If the light from the projector is directed perpendicular to the vertical waveguide, the FOV can be calculated as

$$FOV_{vertical} = 2\tan^{-1}\frac{\frac{M*d}{\tan\alpha} - EPD}{2ERF} \tag{3.14}$$

$$\mathrm{EPD}_{\mathrm{vertical}} = \frac{\mathrm{M*d}}{\tan\alpha} \tag{3.15}$$

where M is the number of the couplers and d is the thickness of the vertical waveguide.

3.3 Analysis and suppression of stray light

3.3.1 Causes of stray light generation

The waveguide works in expanding the light information from projector. The pupil plane of the system is the exit pupil plane of the virtual image. The pupil could intercept the complete image information from this plane, which could be transmitted to retina by lens. Therefore, the light from the same angle will cover one exit pupil area, without any double shadows or ghost images [12].

According to the geometry of the waveguide, the pupil is expanded by PRMA. In this process, some unwanted ghost images would occur due to the inconsistency (error in geometric position) of the out-couplers of the waveguide, so stray light would be generated by these inevitable reflections. The contrast, modulation transfer function (MTF) and sharpness of the image would be greatly reduced by stray light and energy distribution of the image plane would undergo a significant change. Severely, the target image would be annihilated in the background stray light. The stray light would become stronger when FOV increases in the direction of entrance expansion. The ghost image in the edge is more obvious than it in the centre. There are several cases of the stray light. The first case is caused by twice reflection at the in-coupler, as shown in Figure 3.6(a). All light just need to be reflected once by in-coupler and the second reflection change the original direction of the normal lights and cause stray light. The first case usually happens when

$$\omega_1 < \pi/2 - 3\theta \tag{3.16}$$

The second case is caused by twice reflection by one out-coupler, as shown in Figure 3.6(b). All light should be coupled out to observer's eye by once reflection at out-coupler. But some light may not break the TIR condition after the first reflection at the out-coupler and hit the same out-coupler again. In this case, the lights may not transfer in the expected direction and become stray light. The second case happens when

$$\omega_1 < 3\theta - \pi/2 \tag{3.17}$$

As shown in Figure 3.6(a), the first case may also cause the second case at the edge of the waveguide. The third case and the fourth case are both caused by reflection at the back of the out-coupler, as shown in Figure 3.6(c) and (d) respectively. For ideal design, all light, no matter from projector or from real world, should pass through the back of out-couplers. But the lights reflected on the back of the out-coupler still transfer within the waveguide and then may be coupled out to observer after once or twice reflected by the next out-coupler (once reflection by next out-coupler in Figure 3.6(c), twice reflection in Figure 3.6(d).

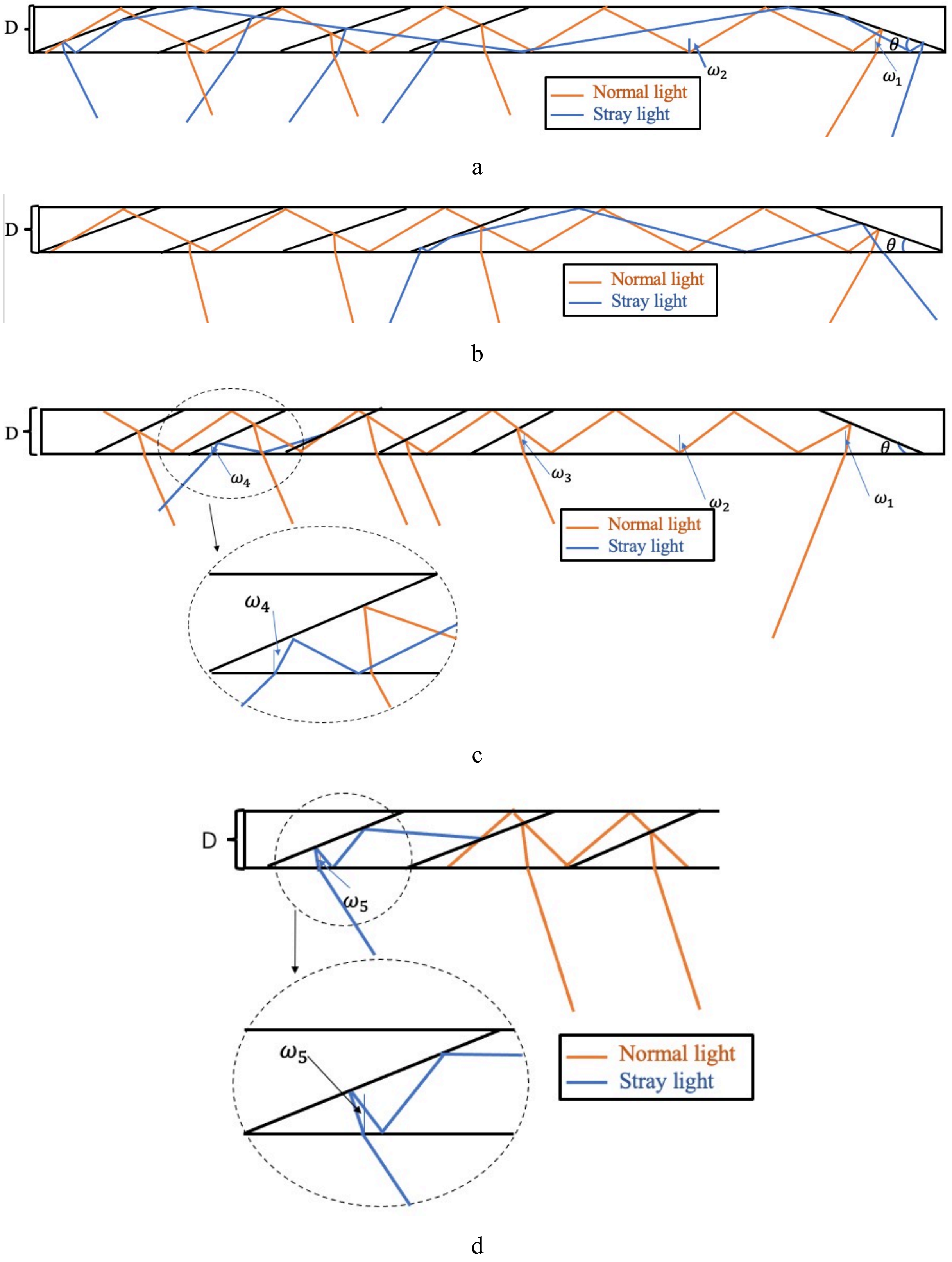

Figure 3. 6 Stray lights in geometrical waveguide (a) twice reflection at in-coupler; (b) twice reflection at out-coupler; (c) and (d) lights are reflected by the back of out-coupler.

From Figure 3.6(c) and Eq. (3.4), the angle of normal light along the expansion direction before it passes through the waveguide ω_3 can be derived as

$$\omega_3 = \omega_1 \tag{3.18}$$

The angle of third and fourth cases of stray light along the expansion direction before it passes through the waveguide ω_4 and ω_5 can be derived as

$$\omega_4 = \pi - 6\theta + \omega_1, \tag{3.19}$$

$$\omega_5 = 6\theta - 3\pi/2 + \omega_1, \tag{3.20}$$

which happens when

$$\omega_1 < 4\theta - \pi/2 \text{ (third case)}, \tag{3.21}$$

$$\omega_1 > 4\theta - \pi/2 \text{ (fourth case)}. \tag{3.22}$$

From above, stray light can be summarized as shown in Figure 3.7. When θ and ω_1 are set up, the kinds of stray light would be determined. Then the stray light can be solved in a targeted manner. Green line is first case stray light, blue line is second case stray light area, red line is third stray light area and the black line is the fourth case of stray light.

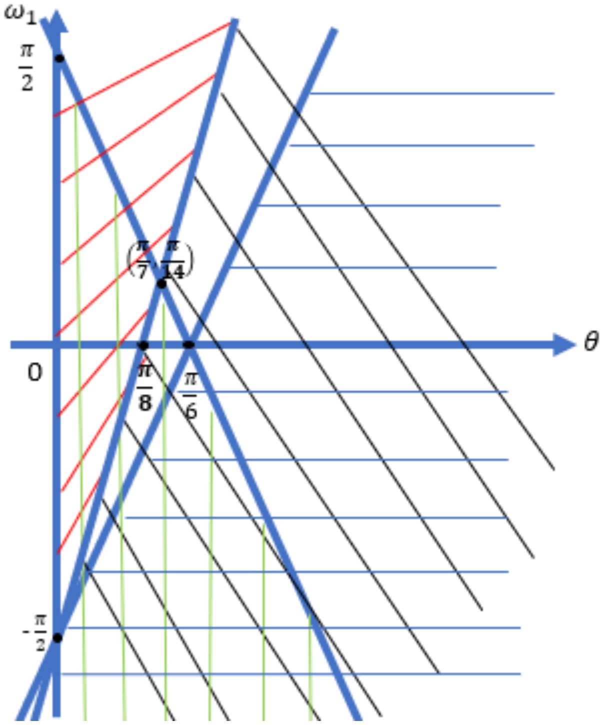

Figure 3. 7 All kinds of stray light (green line is 1st stray light, blue line is 2nd stray light, red line is 3rd stray light and black line is 4th stray light).

3.3.2 Stray light suppressing of 1D geometrical waveguide

To suppress the first case of stray light, a part of the in-coupler Y could be removed, or the edge of the waveguide X could be blocked, which shows the critical condition as seen in Figure 3.8. The light hits the edge of the in-coupler after it's reflected by in-coupler. X and Y part can be expressed as:

$$Y = \frac{D}{\sin\theta} - \frac{2D\sin(2\theta - w_1)}{\cos(w_1 - \theta)} \tag{3.23}$$

$$X = \frac{Y\cos(w_1 + \theta)}{\cos\omega_1} \tag{3.24}$$

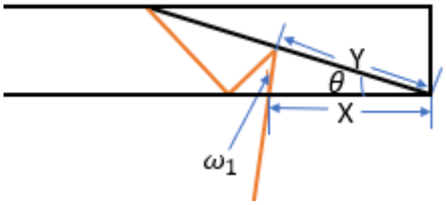

Figure 3. 8 Suppression of first stray light

For the second case of stray light, the abnormal light would be suppressed when first stray light was eliminated, and the angle meets Eq. (3.16) and Eq. (3.17).

The suppression of the third and fourth conditions mainly rely on the coating of the out-coupler. Stray light is caused by the convergence of real light rays, which is reflected from the back of the out-couplers, usually normal light passing through even times on the working surface. For optical imaging systems, stray light increases the noise on the image surface and decreases the contrast of the image. The normal light hits the back side of the out-couple surface in a large angle with the out-coupler and the stray light hits the surface in a small angle with the surface. Thus, the coating film can be designed to weaken the reflection of the beam with large incident angle as much as possible and divide the light of small incident angle in a certain proportion, so as to expand the field of view.

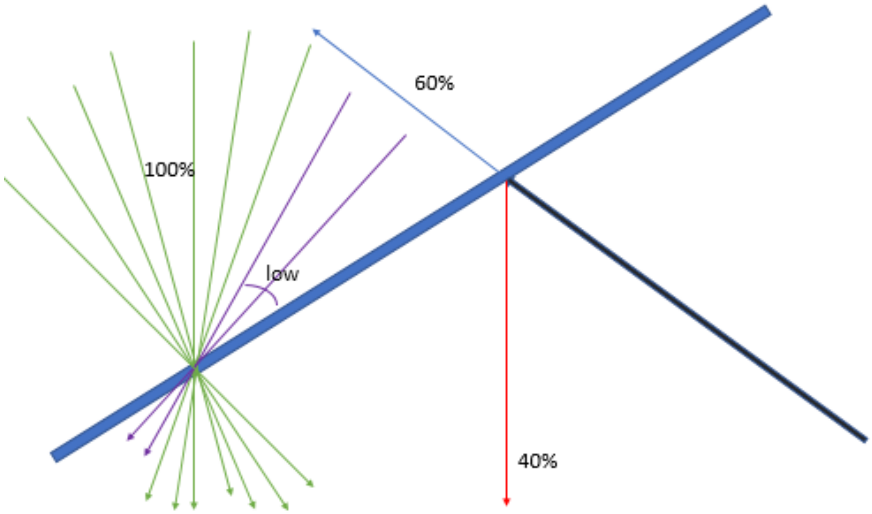

Figure 3. 9 Selection of the coating film on out-coupler (red line is reflected light, blue line is transmitted light, green line is totally transmitted light and purple line is transmitted light with very low percentage).

As shown in Figure 3.9, the light from one side can be reflected by the film while a part of which could be transmitted through the film, where the reflection and transmission ratio is different on every film. The light from the other side can totally transmits through the film. The selection of coating materials should consider such issues as the low absorption rate in the required band, the matching level between the coating layer and the incident medium, and the refractive index of the substrate material.

Besides, if the stray light in the third and fourth conditions can be transmitted out of EPD, they can be ignored, as shown in Eq. (3.25) and Eq. (3.26).

$$L_{Stray} = ERF * \tan[\sin^{-1}(n_1 * \sin\omega_4)] \geq EPD \tag{3.25}$$

$$L_{Stray} = ERF * \tan[\sin^{-1}(n_1 * \sin\omega_5)] \geq EPD \tag{3.26}$$

from which, the ω_4 and ω_5 could be derived to suppress these two conditions.

Besides the stray light in the waveguide system, there are some situations of stray light caused by manufacturing. The errors in manufacturing break the original light path and cause stray lights. As shown in Figure 3.10, the manufactured waveguide has a parallelism tolerance between two edges, which is noted by angle Δ. After the light hits the waveguide edge with some error, it continues to transmit in the wrong way. Whenever the light hits the error edge, the transmission deviates more from the normal angle [14].

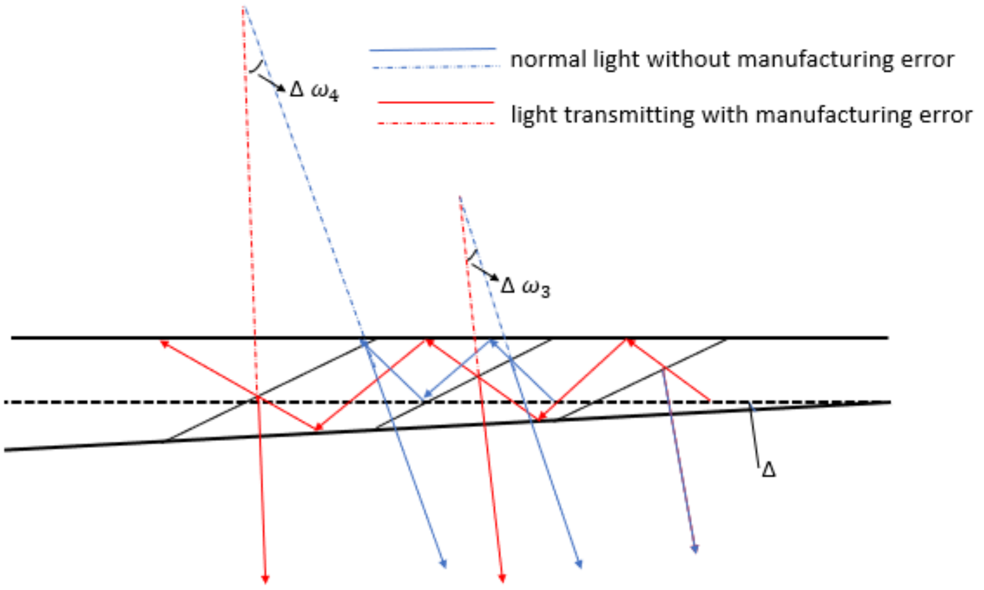

Figure 3. 10 Stray light caused by manufacturing error at substrate of waveguide.

Eq. (3.27) expresses the angle error before the light through-out the waveguide along the normal direction.

$$\Delta\omega_3=2\Delta$$

$$\Delta\omega_4=3\Delta$$

$$\Delta\omega_5=4\Delta$$

$$\vdots$$

$$\vdots$$

$$\Delta\omega_{q-1}=q*\Delta. \tag{3.27}$$

where the q is the number of hits of light at the error edge of waveguide.

As the angular resolution of the human eye is 60″ [153]， the manufacturing error could be accepted if the largest angle error is below 60″. Any angle beyond this would cause ghost images.

$$\sin^{-1}[n * \sin(q * \Delta)] < 60'' \tag{3.28}$$

$$\Delta < \frac{\sin^{-1}\left[\frac{\sin 60''}{n}\right]}{q} \tag{3.29}$$

The length of waveguide and the number of the out-coupler determine q. Thus, only when the manufacturing tolerance meets Eq. (3.29), observers could get the virtual information with no ghost image.

The same light is coupled out by PRMA in parallel. The parallelism of the out-couplers is crucial. If the parallelism tolerance of out-couplers is beyond some permittable value, the light transmitted deviates from the normal angle, as shown in Figure 3.11. There are two kinds of parallelism errors, larger or smaller than the right angle.

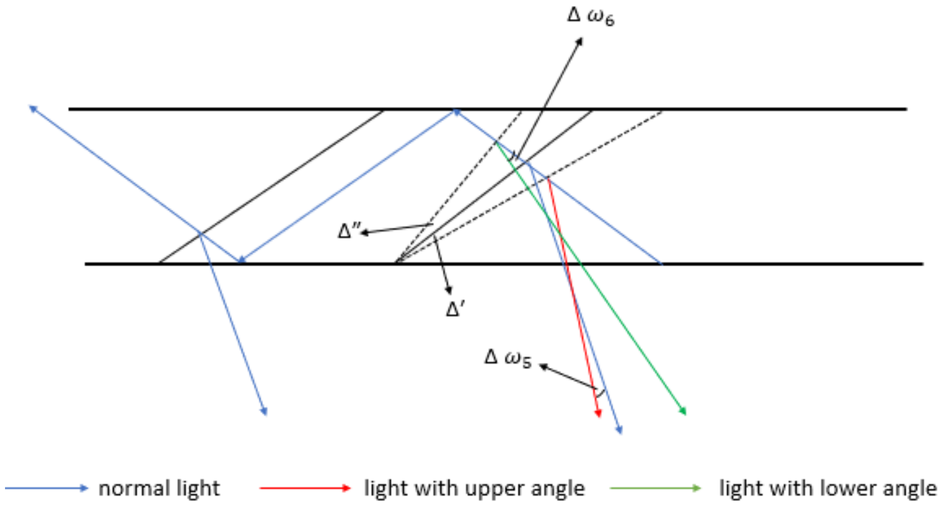

Figure 3. 11 Stray light from the manufacturing at out-coupler of waveguide.

Eq. (3.30) express the parallelism error in upper and lower angle from the normal angle.

$$\Delta\omega_5 = 2\ \Delta'$$
$$\Delta\omega_6 = 2\ \Delta'' \tag{3.30}$$

where Δ′ is lower angle and Δ″ is the upper angle.

$$\sin^{-1}[n * \sin(\Delta\omega_5 \text{or} \Delta\omega_6)] < 60'' \tag{3.31}$$

$$\Delta' \text{or}\ \Delta'' < \frac{\sin^{-1}\left[\frac{\sin 60''}{n}\right]}{2} \tag{3.32}$$

When the manufacturing error meets Eq. (3.32), the virtual information could be seen completely with no ghost image.

3.3.3 Stray light suppressing of 2D geometrical waveguide

The light from the projector is expanded along two axes, which can be expressed as a vector presentation. Thus, all propagating light can be divided into two directions. Based on the ray-tracing process, the stray light can also be divided into vertical and horizontal directions and the propagation path of all stray light can be traced for analysis.

A) Stray light in vertical direction

The light expands the pupil by a partially reflective mirror array (PRMA). The light which transfers into the vertical waveguide should be reflected once by the in-coupler and bounce within the waveguide by TIR. However, it is possible for the light not to exactly follow its designed pathway and cause stray light due to the errors caused by manufacturing and assembly. In this expanding process, ghost images would occur by the inconsistency of the angle of the vertical waveguide. There are four types of stray light occurring in the vertical waveguide as shown in Figure 3.12, which is half of the whole vertical waveguide, because the vertical waveguide can be regarded as axially symmetry. The light propagates upwards and downwards in the vertical direction after being incident at the coupler in the middle of the vertical waveguide. The upper and lower parts are symmetrical, so one direction is taken for consideration in this study.

The first case is from twice reflection at the in-coupler, as shown in Figure 3.12(a). The second reflection changes the original travel direction and cause stray light. The second case is induced by twice reflection by the out-coupler, shown in Figure 3.12(b). The first hit at the out-coupler can still totally internally reflect inside, which deviates from the excepted direction. On the front of the out-coupler, partial lights can be reflected by the out-couplers and partially lights can transmit through the out-couplers. However, the coating may not strictly meet this selection requirement and cause stray light. Thus, the third and fourth cases are both caused by unwanted reflection at the back of the out-couplers, as shown in Figure 3.12(c) and Figure 3.12(d). All light should transmit through the out-couplers from the back of the vertical waveguide in an ideal design. The angles of above stray light along the expansion direction before coupling out of the vertical waveguide can be derived as

$$\varphi_2 = 2\alpha - \varphi_1 \text{ (stray light 1: } \varphi_1 < \pi/2 - 3\alpha) \tag{3.33}$$

$$\varphi_3 = 6\alpha + \varphi_1 - \pi \text{ (stray light 2: } \varphi_1 < \pi/2 - 3\alpha) \tag{3.34}$$

$$\varphi_4 = \pi - 2\alpha - \varphi_1 \text{ (stray light 3: } \varphi_1 < 4\alpha - \pi/2) \tag{3.35}$$

$$\varphi_5 = \varphi_1 \text{ (stray light 4: } \varphi_1 < 4\alpha - \pi/2) \tag{3.36}$$

where φ_1 is the angle of TIR, φ_2 is the reflection angle of the light along the entrance pupil expansion in the vertical waveguide, φ_3 is the angle of second case of stray light along the expansion direction before coupling out of the vertical waveguide, φ_4 and φ_5 are the angles of the third and fourth cases of stray light along the expansion direction before they pass through the vertical waveguide.

When the φ_1 meet Eq. (3.33), the first stray light would occur. When it meets Eq. (3.34), the second stray light is caused. The third and fourth stray light would occur when it meets the Eq. (3.35) and Eq. (3.36).

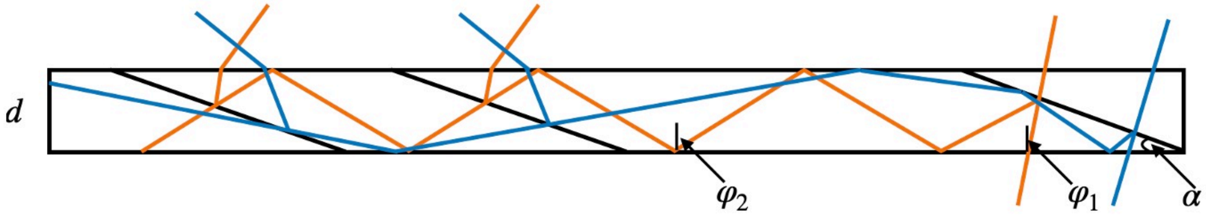

(a)

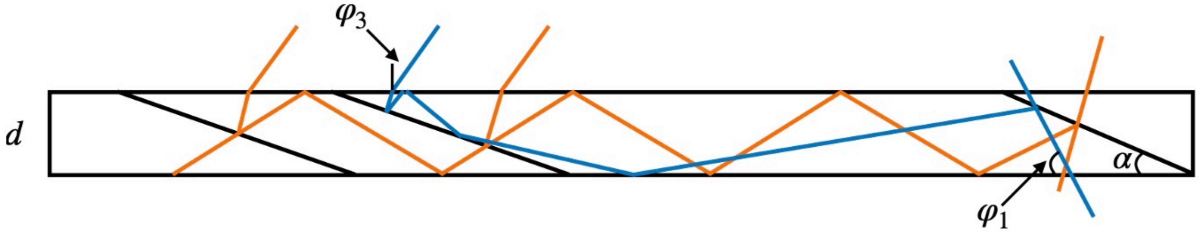

(b)

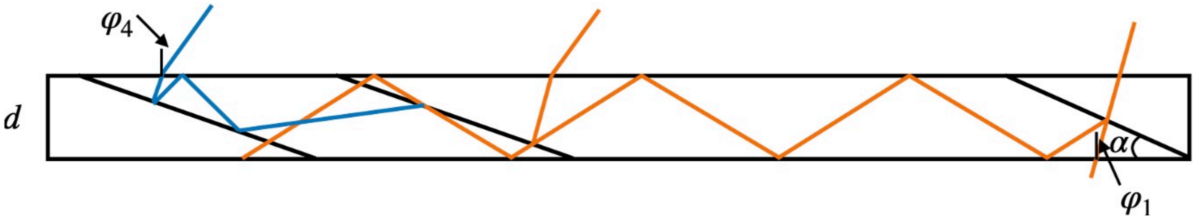

(c)

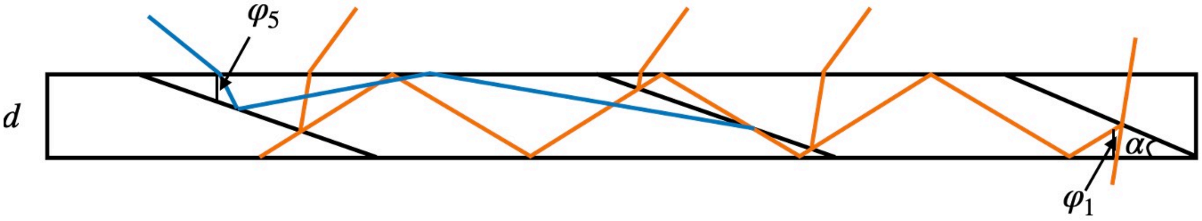

(d)

Figure 3. 12 Stray light in partial vertical geometrical waveguide (a) twice reflection at in-coupler; (b) twice reflection at out-coupler; (c) and (d) lights are reflected by the back of out-coupler. Orange line is normal light and blue line is stray light.

Above four cases of stray light would continue transferring to the horizontal waveguide. The angle changes of the stray light caused in vertical direction would not affect the angle in horizontal direction. As shown in Figure 3.13(c), the black line is original light, and the red line is stray light with an angle error on vertical direction. Although the red line and the black line seem overlapped from the top view shown in Figure 3.13(a), there is actually an angle between them as shown in Figure 3.13(b). When the light transfers to coupler in the horizontal waveguide, the red line is decomposed into two components, one is along the direction of the black line, which will not affect the normal reflection, but the other component does not coincide with the propagation direction of the black line. The red line produces a propagation path in another direction in the three-dimensional space. The propagation has no angle change in horizontal direction; thus, it is not stray light in this propagation direction. Thus, the stray light from vertical waveguide will not produce stray light in horizontal waveguide. The two components of the vector do not affect each other. As shown in simulation result Figure 3.14, the black line is normal light and the red line is stray light, causing ghost images. The stray light in vertical direction has no effect on horizontal direction but produce a displacement on vertical direction when light propagates in horizontal waveguide.

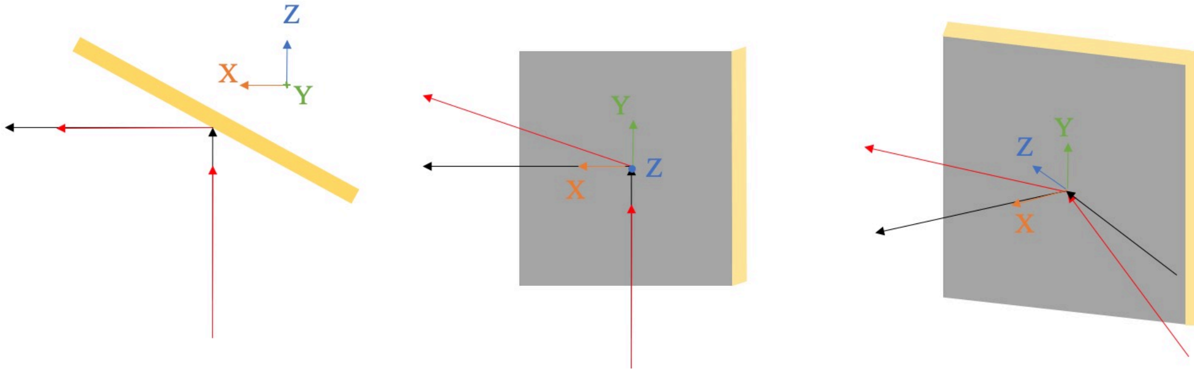

(a) Top view (horizontal view) (b) Front view (vertical view) (c) Side view

Figure 3. 13 The stray light from vertical waveguide is reflected by the in-coupler in horizontal waveguide.

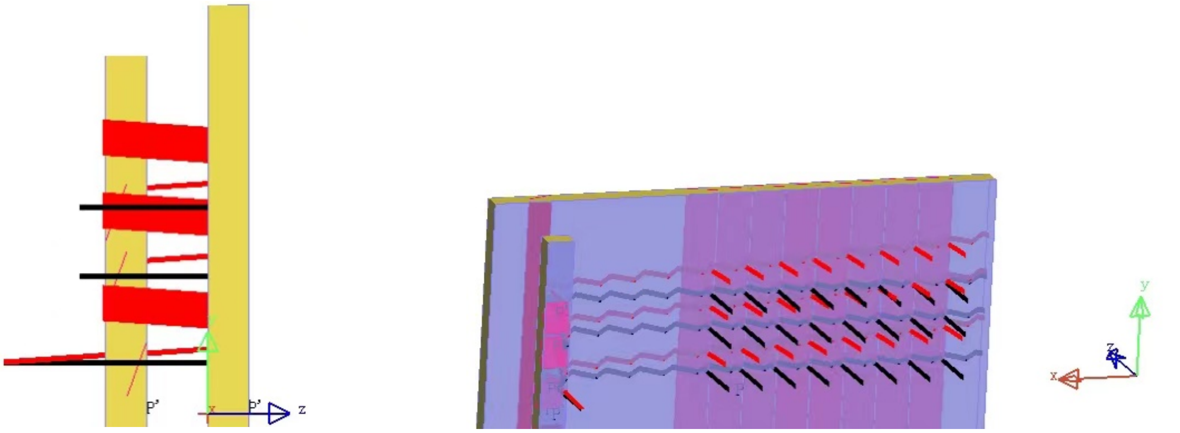

(a) Side view (b) Back view

Figure 3. 14 Comparison of stray light and normal light in vertical direction, (a) side view and (b) back view. The black line is normal light and the red line is stray light.

The vertical FOV is expanded by vertical waveguide. However, the displacement from the stray light in vertical waveguide affect the real vertical FOV of the system. As shown in Figure 3.15, the vertical displacement can be derived as

$$d_3 = d_1 \tan\beta \tag{3.37}$$

$$n_2 \sin\varphi = n_3 \sin\beta = n_1 \sin\gamma \tag{3.38}$$

$$d_4 = 2s \tan\gamma \tag{3.39}$$

where d_1 is the average distance of the gap between vertical waveguide and horizontal waveguide, d_3 is the vertical displacement of the stray light in the gap, d_4 is the vertical displacement of stray light in horizontal waveguide, n_1 is refractive index of horizontal waveguide, n_2 is the refractive index of vertical waveguide, n_3 is the refractive index of gap material, s is a vertical distance vector, β is the transmission angle in the gap along the vertical waveguide which also equals to the coupler-out angle at the horizontal waveguide, γ is the transmission angle in horizontal waveguide.

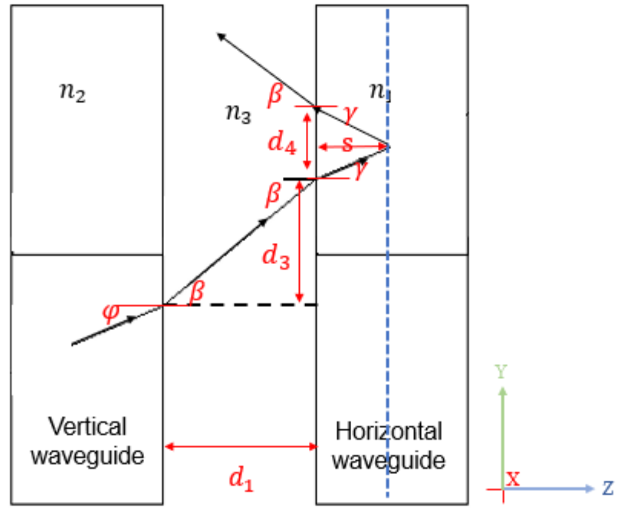

Figure 3. 15 Side view of the vertical angle change of light from vertical waveguide to horizontal waveguide

As shown in Figure 3.13, the stray light from vertical waveguide does not produce stray light displacement in horizontal vector in horizontal waveguide. Thus, the displacement (one component of the stray light in vertical direction) and the deviation angle change the light path which would be coupled out into human eyes and cause ghost images. Thus, the angle of stray light will be affected by β and it is restricted by the resolution of human eyes [154].

B) Stray light in horizontal direction

If there is an angle change with perpendicular in horizontal direction (along x-axis), the angle of the light changes is as shown in Figure 3.16. The displacement at the gap can be derived as

$$\mathrm{d}_2 = \mathrm{d}_1 \tan\delta \tag{3.40}$$

$$\mathrm{n}_2 \sin\epsilon = \mathrm{n}_3 \sin\delta = \mathrm{n}_1 \sin\omega_1 \tag{3.41}$$

where ϵ is the angle error in vertical waveguide from projector in horizontal direction, δ is the horizontal angle change in the gap material, ω_1 is the horizontal incident angle in horizontal waveguide.

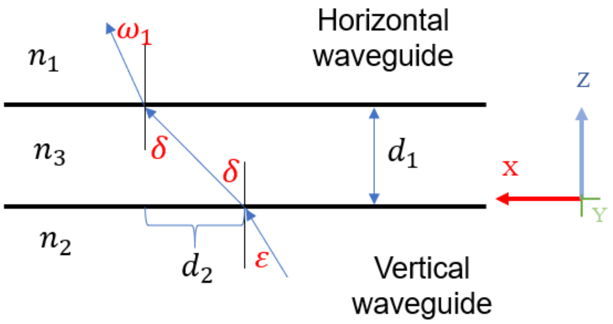

Figure 3. 16 Top view of the horizontal angle change of light from vertical waveguide to horizontal waveguide

The incident angle ω_1 may cause the stray light in the system, as shown in Figure 3.6. There are also four cases of stray light in the horizontal direction, which is the same as the stray light in 1D waveguide. Figure 3.17 shows the comparison of stray light and normal imaging light in horizontal direction. The upper side is stray light and the lower side is normal light. The stray light in the horizontal direction has no effect on vertical direction but causes worse image quality as shown in Figure 3.18(b).

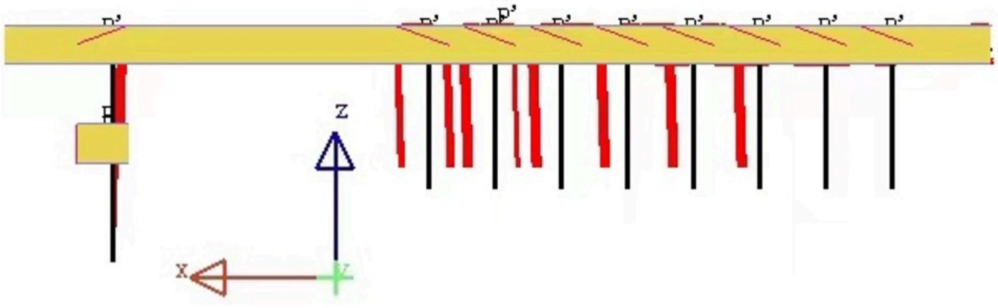

(a) Top view

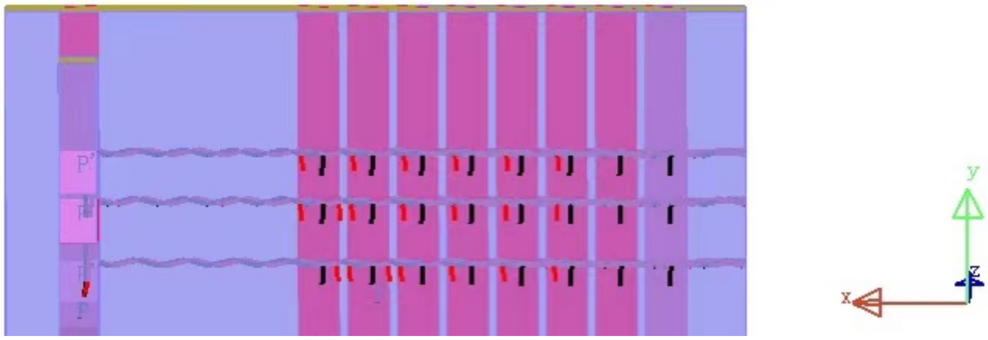

(b) Back view

Figure 3. 17 Comparison of stray light and normal light in horizontal direction, (a) is top view and (b) is back view. The black line is normal light and the red line is stray light.

From Figure 3.6 and Eq. (3.18), the angle of normal light along the expansion direction before it passes through the waveguide ω_3 can be derived as

$$\omega_3 = -\omega_1 \tag{3.42}$$

The angle of third and fourth cases of stray light along the expansion direction before it passes through the waveguide ω_4 and ω_5 can be derived as

$$\omega_4 = \pi - 6\theta + \omega_1 \tag{3.43}$$

$$\omega_5 = 6\theta - 3\pi/2 + \omega_1 \tag{3.44}$$

which happens when

$$\omega_1 < 4\theta - \pi/2 \text{ (third case)} \tag{3.45}$$

$$\omega_1 > 4\theta - \pi/2 \text{ (fourth case)} \tag{3.46}$$

The resolution is related to the brightness and contrast of the observed object. According to actual statistics, the angle resolution of the eye is between 50"-120", and it is generally 60" under good lighting conditions [155]. Therefore, in this optical system, it is necessary to ensure that the output image can reach a better resolution than that of the eye [154]. If the angle error of the stray light is below 60″, there will be less ghost images perceived, as shown in Eq. (3.47)

$$\sin^{-1}\left[n_1 * \sin\left(\omega_{\text{stray light}} \text{ or } \beta\right)\right] < 60'' \tag{3.47}$$

The stray light in the above two directions can be suppressed by the same methods. The suppression methods consist of angle design as above and coating-selection design, which have been discussed in Chapter 3.3.2 [156]. Besides, the manufacturing tolerances in substrates and couplers have also been analyzed in detail. There are two situations of stray light caused by manufacturing inaccuracy discussed in Chapter 3.3.2.

The stray light cases and suppression conditions of 1D and 2D waveguide can be conclude as Table 3.1

Table 3. 1 Stray light and suppression conditions

	1D waveguide	2D waveguide		Suppression method
		Horizontal	Vertical	
1st case	Twice reflection at in-coupler	Twice reflection at in-coupler	Twice reflection at in-coupler	Limit the entrance angle and position
2nd case	Twice reflection by out-coupler	Twice reflection by out-coupler	Twice reflection by out-coupler	Limit the entrance angle
3rd case	One reflection at out-coupler after one reflection at the back of out-coupler	One reflection at out-coupler after one reflection at the back of out-coupler	One reflection at out-coupler after one reflection at the back of out-coupler	Coating method and material selection; Limit the angle to couple the light out of EPD
4th case	Twice reflection at out-coupler after one reflection at the back of out-coupler	Twice reflection at out-coupler after one reflection at the back of out-coupler	Twice reflection at out-coupler after one reflection at the back of out-coupler	Coating method and material selection; Limit the angle to couple the light out of EPD

3.4 Simulation and optimization of 1D geometrical waveguide

The parameter selection is a trade-off process depending on the application. The optimization process for the designed waveguide model can be concluded as:

1. Determine the design objectives and performance parameters, such as the resolution, brightness, chroma and contrast of the optical system that you want to optimize.

2. Build the original model and do basic testing. Create a 3D model in LightTools, including various optical components. Test the model to determine its basic performance and shortcomings.

3. Define the optimization variables and ranges and set the optimization template. In LightTools, you can define parameters and ranges that can be adjusted and turn them into optimizable variables. You can then save it as an optimized template for later use.

4. Optimize modeling parameters. Use the optimization function and template in LightTools to automatically adjust parameters and find optimized solutions. This part requires trial and error and adjustment to find the best solution.

5. Validate the results of the optimization and validate the determined design with more detailed tests. For example, MATLAB or other simulation software can be used to measure performance parameters to confirm optimized results.

6. Modify the design and repeat the optimization process. Depending on the test results, the design may need to be fine-tuned to optimize more performance parameters.

7. Output final design. Finally, after determining the optimization, you can export the final LightTools design for manufacturing or use in a project. In summary, the LightTools optimization process requires trial and error and fine-tuning to expect the best results.

According to the above analysis, to provide a smaller thickness and larger FOV of a wearable geometrical waveguide, the parameters in the design are listed in Table 3.2. Based on the above parameters, the FOV can be calculated as 72° from Eq. (3.34).

Table 3. 2 Parameters of the geometrical waveguide

n	ω_1	θ	N	D (mm)	EPD (mm)	ERF (mm)
>1.66	0°	20	8	2	10	20

In order to eliminate the overlapping image, the in-coupler should be designed as shown in Figure 3.18. The reflective surfaces are adjacent to each other, and eyes will extract the full image from the exit pupil plane. Thus, there will be no holes of the projected image by the non-overlap surfaces. The out-coupler design affects the FOV. The active part of out-coupler can be expressed as

$$a=\frac{2D\sin(2\theta-w_1)}{\cos(w_1-\theta)} \tag{3.48}$$

and the FOV of new designed system can be derived as

$$\mathrm{FOV}_{\mathrm{design}} = 2\tan^{-1}\frac{N*2D\tan(2\theta-\omega_1)-\mathrm{EPD}}{2\mathrm{ERF}} \tag{3.49}$$

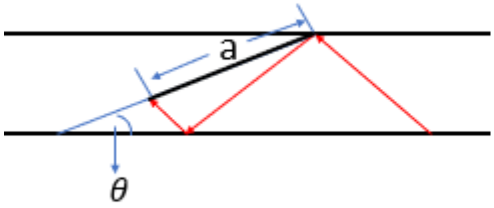

Figure 3. 18 Active part of out-coupler

The light coupled out from the out-couplers should be uniform. Thus, the illumination from each out-coupler should be the same. Taking 8 out-couplers as an example, the ratio of transmittance and reflectance of the film on every out-coupler should follow table 3.3 to make sure the uniformity of the illuminance.

Table 3. 3 The ratio of transmittance and reflectance under visible wavelength [157]

Out-coupler	1st	2nd	3rd	4th	5th	6th	7th	8th
Reflectance	25%	30%	35%	40%	45%	50%	55%	60%
Transmittance	75%	70%	65%	60%	55%	50%	45%	40%

Based on the above, the schematic diagram of the optimized geometrical waveguide is shown in Figure 3.19. The wavelength of the light source is 550nm with a 2.3mm×10mm area. The luminous flux is 679.55 Lumen with uniform angle distribution and volume distribution.

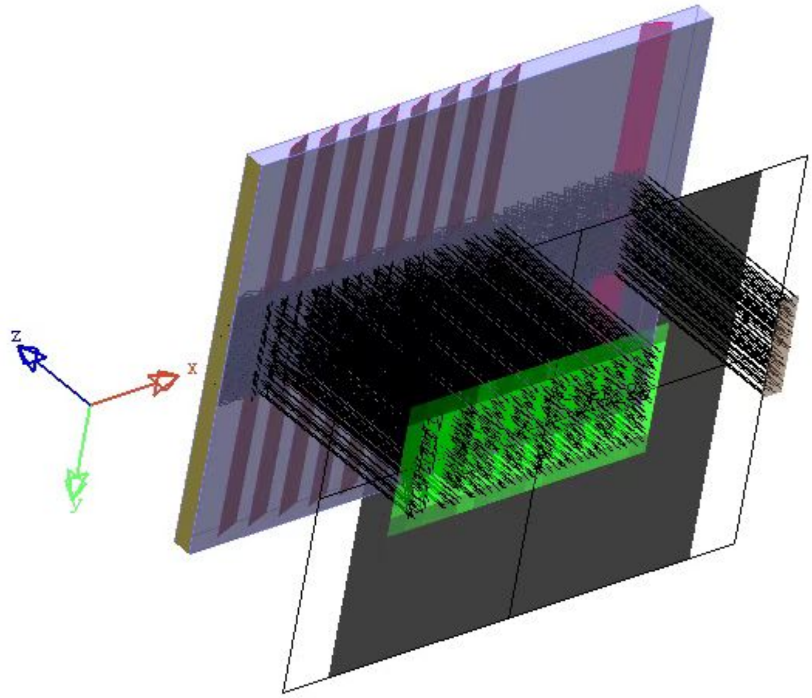

Figure 3. 19 Schematic diagram of the optimized geometrical waveguide.

Figure 3.20(a) shows the illuminance of the waveguide with no optimization for the coating at the exit pupil of the system. Because the coating tolerance ±5% is added for the reflectance ratio, the illumination received is ununiform. The light is unevenly distributed, the field loss occurs at the edge of the out-couplers, which causes ghost images, as designed in Table 3.2. Figure 3.20 (b) shows the illuminance of the optimized geometrical waveguide with the same light source at the exit pupil. One variable on reflectance is added based on the original ratio, the optimized reflectance ratio is received as 23%, 27%, 34%, 40%, 45%, 51%, 57%, and 62%. From the LightTools ray-tracing analysis, the light distribution is uniform, and the stray light is greatly suppressed. The projected light is expanded several times by the folding and unfolding process. The gap between the blocks of the image is below the resolution of human eyes. The Figure 3.21 shows the angular distribution of the optimized system, which effectively suppress the stray lights and expands the field-of-view of the system.

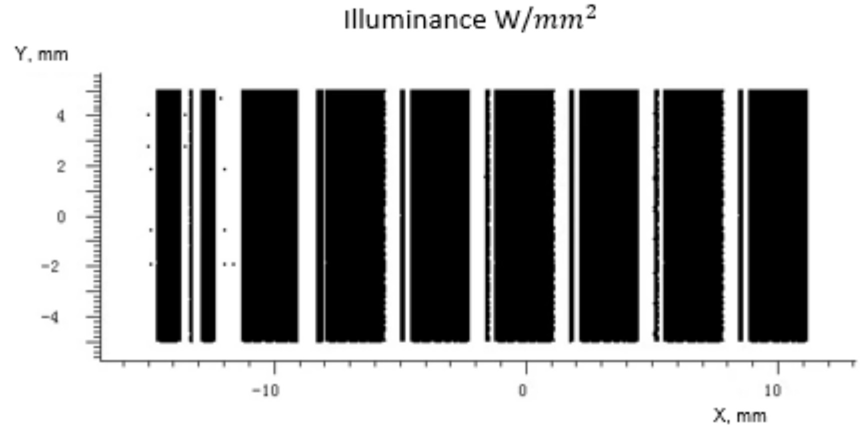

(a) illuminance with stray light

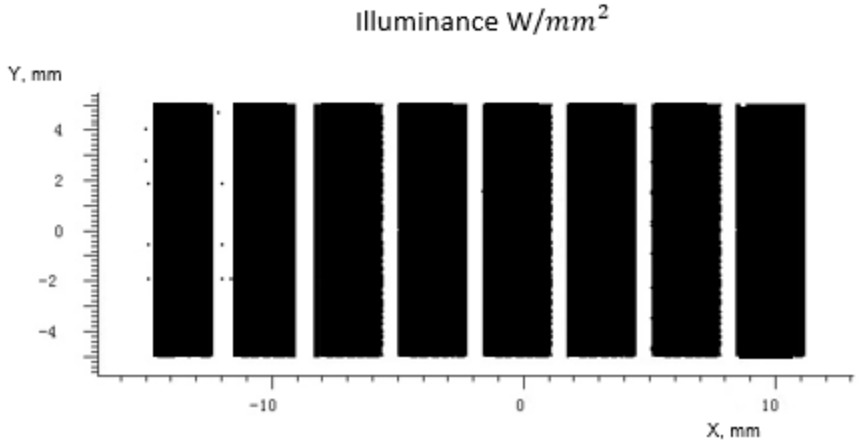

(b) illuminance without stray light

Figure 3. 20 Scatterer distribution diagram of illuminance, (1) is the illuminance with stray light and (2) is light illuminance without stray light, the unit is W/mm^2.

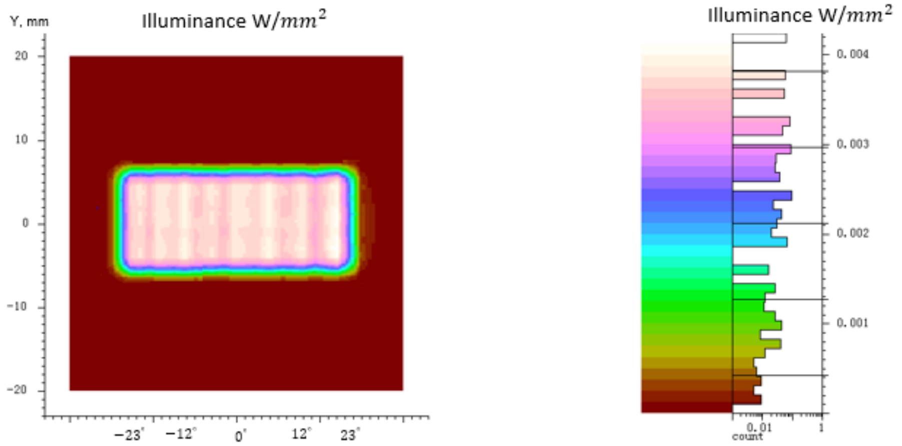

Figure 3. 21 The angular distribution of the optimized system, the unit is W/mm^2.

3.5 Simulation and optimization of 2D geometrical waveguide

The length and the position of the couplers are designed based on the above analysis as shown in Figure 3.22.

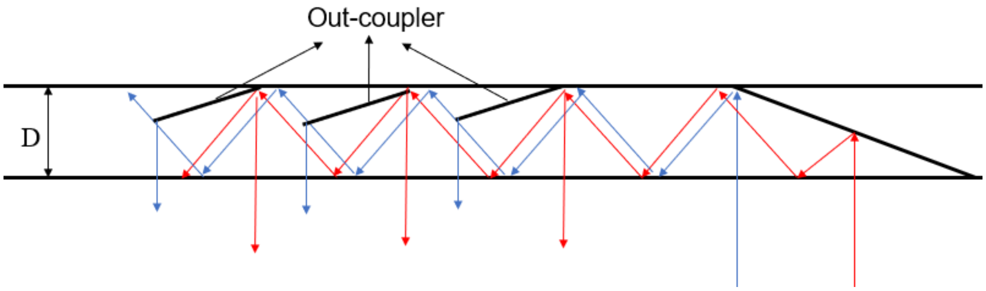

(a) out-coupler design in horizontal waveguide

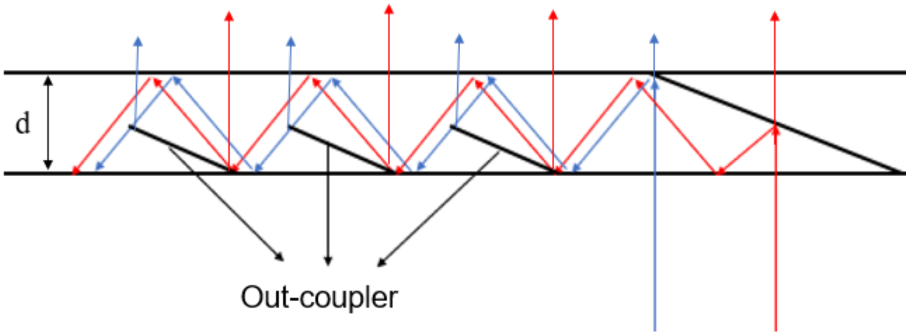

(b) partially coupler design in vertical waveguide

Figure 3. 22 The position design of the couplers in geometrical waveguide.

The pupil plane is at the exit pupil of the virtual imaging, and the pupil will extract the full image from this plane. Light in the same angle from different out-coupler will be focused on the same pixel (viewable unit) with overlapping images. There will be no gap or holes on the observed images. To make sure the expansion resolution of these two waveguides matches with each other based on the eye-observation requirements, the optimized parameters for the two-dimensional geometrical waveguide are set as listed in Table 3.4. Based on Eq. (3.8) and Eq. (3.14), the horizontal FOV can be derived as 69° and vertical FOV can reach 56°.

Table 3. 4 Parameters of the combined waveguide

	n	ω_1/ φ_1/ ϵ	θ/ α	N/M	D (mm)	Eye box (mm)	FOV
Horizontal waveguide	>1.66	0°	20°	8	2	22.6	69
Vertical waveguide	>1.66	0°	20°	6	2	26	56

The coatings on the couplers should have a specific ratio of transmittance and reflectance to present uniform illuminance of the virtual information from the projector. The ratio in horizontal waveguide is listed in Table 3.5, while the ratio of the vertical waveguide is listed in Table 3.6. The material of the glue should have good stability and high transparency, which would affect the light efficiency of the system. The refractive index of the glue should be the same as the refractive index of the substrate material at 1.69±0.02. Within this range, the stray light would not cause a ghost image based on the resolution of the eye. Otherwise, ghost images will be produced. The methods discussed in Section 3.4 can be used to suppress these stray light [156]. Besides, the layer of the glue should be uniform, otherwise, there will be parallelism errors between two edges of the substrate or between out-couplers like in Figure 3.10 and Figure 3.11.

Table 3. 5 The ratio of transmittance and reflectance in horizontal waveguide

Out-coupler	1st	2nd	3rd	4th	5th	6th	7th	8th
Reflectance	11.0%	12.5%	14.3%	16.7%	20.0%	25.0%	33.0%	50.0%
Transmittance	89.0%	87.5%	85.7%	83.3%	80.0%	75.0%	67.0%	50.0%

Table 3. 6 The ratio of transmittance and reflectance in vertical waveguide

coupler	1st	2nd	3rd
Reflectance	25%	33%	50%
Transmittance	75%	67%	50%

Based on the above discussion, the schematic diagram of the optimized 2D geometrical waveguide is shown in Figure 3.24. The light source is divided into two parts, each of which is reflected by the in-couplers of the vertical waveguide towards the upper or lower direction. From this model, the illuminance of the optimized model at the exit pupil can be obtained as shown in Figure 3.25. Illuminance is a measure of how much the incident light illuminates a surface and it is a physical quantity that reflects the intensity of light. It is vital to check that the distribution is sufficiently uniform. The detector is placed at 20mm eye relief position to simulate the position of the human eye. The virtual images should be smaller than the size of the horizontal and vertical couplers, which is 2.76mm *2.76mm. The light source is 2mm*2mm area and the light at the exit pupil is expanded multiple times. The total luminous flux is 679.55 Lumen, 1W, and the wavelength is 550nm. The light from light source is perfectly collimated, including 25,000 rays. Human eyes are most sensitive to electromagnetic waves with a wavelength of about 555nm. The angular distribution and the volume distribution are uniforms. However, because of the manufacturing restrictions, the coating model at normal spectral characteristics (The thickness of the coating film is based on the R/T ratio, and the uniformity error is set at 1% and the surface roughness is set at Ra 2nm) is set and the loss of the projector/collimator is set under 0.2dB. In practice, if the condition of collimation is not ideal, the light cause no ghost images when the angular resolution of stray light is below the resolution of human eyes. Figure 3.24 (a) shows the illuminance at the exit pupil in X-axis and Y-axis and (b) is the illumination distribution across the exit pupil at above parameters. It can be concluded that the light distribution after expansion by horizontal waveguide and vertical waveguide is uniform after suppressing the stray light. The size of the projector could match the size of in-coupler in vertical waveguide. The fluctuations shown in Figure 3.24 (a) are caused by the coating, because in practice it is difficult to realize the ideally uniform distribution of the output light. There are some slight light spots shown in Figure 3.24 (b) due to the loss of the collimator, the slight uncollimated light would cause some stray lights on the receiver.

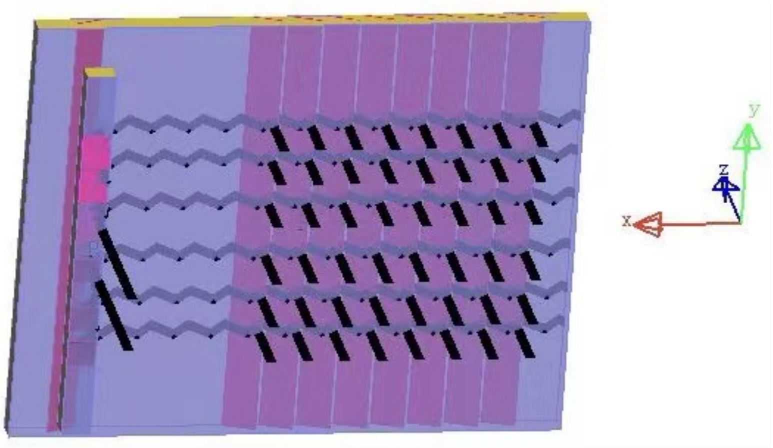

Figure 3. 23 Schematic diagram of the optimized 2-D geometrical waveguide.

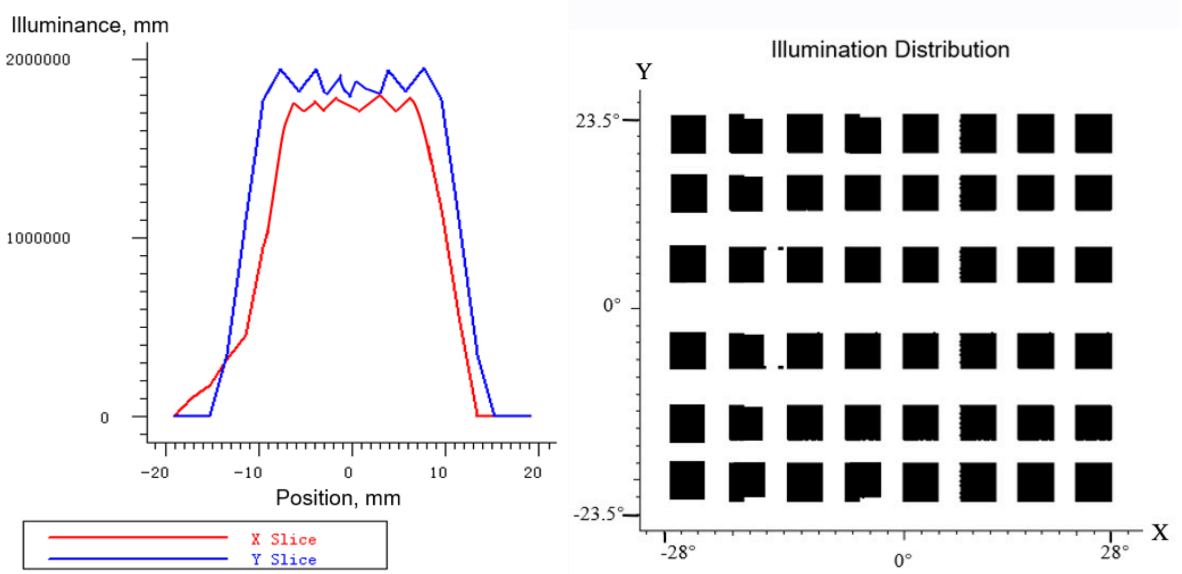

(a) Illuminance at the exit pupil (b) Illumination distribution at the exit pupil

Figure 3. 24 The illuminance of the system at the exit pupil.

There is no need to express the color of each frequency separately when we deal with colors. The three primary colors of red, green, and blue (RGB) are added in different proportions to synthesize to produce color vision. The frequency and wavelength of the light satisfy the relationship:

$$\lambda = \frac{\nu}{f} \tag{3.50}$$

$$\nu = \frac{c}{n} \tag{3.51}$$

where ν is the propagation speed, unit is m/s; λ is wavelength, unit is m; and f is the frequency of the light, the unit is Hertz (Hz), c is the speed of light in vacuum and n is the refractive index of material at the wavelength, lambda. Figure 3.26 shows simulation results for a light source with different wavelength. Figure 3.26, (a) is the simulation of red light, (b) is the simulation of green light, (c) is the simulation of blue light and (d) is the simulation of RGB color model. The wavelength of the light source is slightly affected by the waveguide although it is totally geometrical propagation. Due to the dispersion and absorption curve, blue light will be much likely absorbed than the other one, and lead to a yellowing effect. The reflection/transmission coefficient of the out-coupler is also related to the wavelength and will lead to color modification according to the position of the out-coupler. Thus, the quality of the coating on the out-couplers is vital to the image quality.

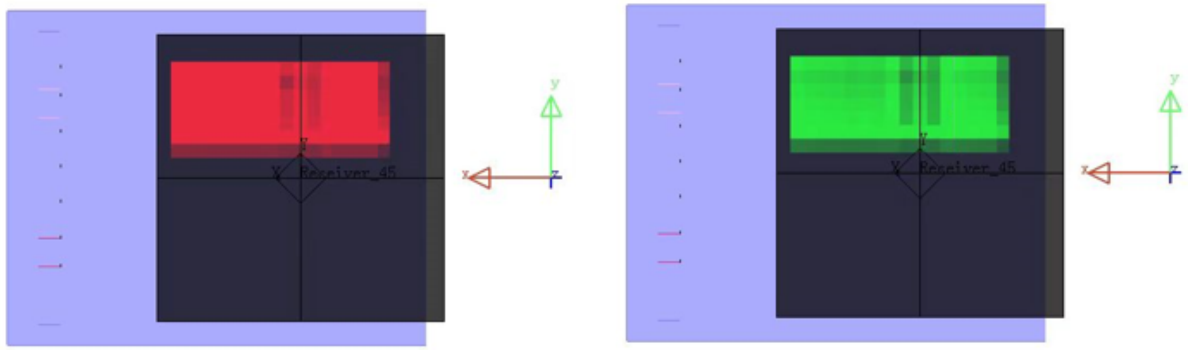

(a) Red light (620-750nm)

(b) Green light (495-570nm)

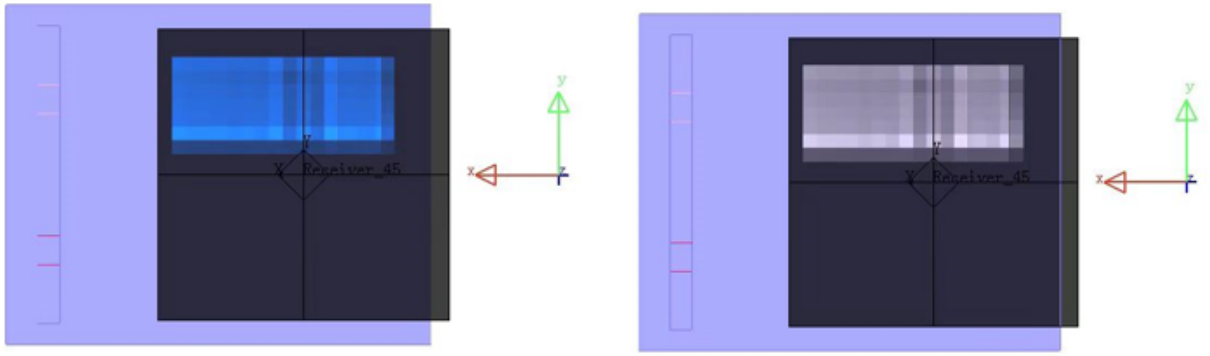

(c) Blue light (450-475nm)

(d) RGB

Figure 3. 25 Simulation results of light with different wavelength

3.6 Design and optimization of hybrid collimator

AR display has strict criteria on the brightness and uniformity of the projector due to the virtual imaging method. After optimizing the illumination uniformity of the waveguide, the illumination uniformity and the brightness uniformity of the projector also affect the performance and quality of virtual images. Thus, the secondary light distribution of the light source is essential for the illuminating system. Secondary light distribution is a critical issue for the light distribution and output efficiency of LED to get a high energy efficiency and uniform illumination system together. The reflective cup and normal lens are applied in the LED light source design. Freeform illumination system is capable of adjusting the beam angle and shaping the light spot based on a more compact structure, which has been extensively employed in the design and manufacturing process of the illuminating system.

Driving benefits from the compact structures, the TIR lenses have been successfully applied to direct the light internal beams to a particular point or plane in practical applications, such as LED illuminating systems. The freeform surfaces could manipulate beams of light at different angles to maintain approximate magnification simultaneously as they pass through the principal axis, which minimizes the aberration. To build the collimating model, the relationship between angle and surface form parameters of the projector system is determined based on the ray tracing model, and the relationship between system volume and system parameters is confirmed. In compliance with the correlations, the performance of the alignment system can be accurately evaluated, while the correlation between freeform lens parameters and system performance could be assessed, and the designed function can be realized.

3.6.1 Model design

The volume, uniformity of illumination, and energy utilization of the projector system have a direct effect on the quality of the virtual images from the AR system. Therefore, the secondary light distribution of the light source in the AR system is significant. The secondary light distribution system works as shown in Figure 3.27.

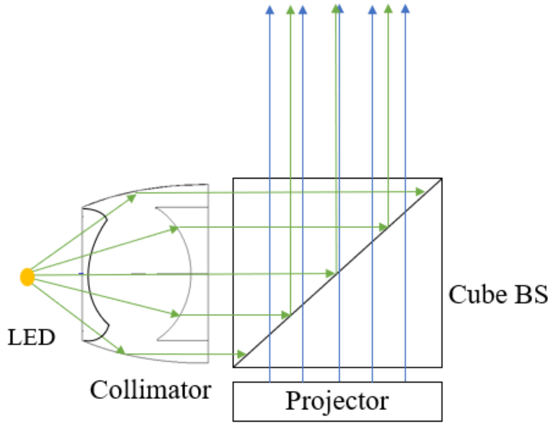

Figure 3. 26 Diagram of secondary light distribution for projector

The light from the LED is directed and collimated to the cube beam splitter (BS), together with the light information from the projector to increase the uniformity of the virtual images. The TIR collimator is a rotationally symmetric structure, and the profile structure is shown in Figure 3.28. The collimator consists of three parts: the conicoid (i.e., the paraboloid), the spherical surface, and the lens. The light path is divided into two parts, the edge part to the conic surface and the central part passing through the freeform lens. The LED is set at the point, which is the focal point of the parabola, the center of the sphere, and the focal point of the lens. The light passes through the spherical surface with no angle change. When the light transfers to the paraboloid surface, it is totally internally reflected out of the collimator parallel to the x-axis. The light is perpendicular to the interface, thus there is no angle change when the light couple out of the lens.

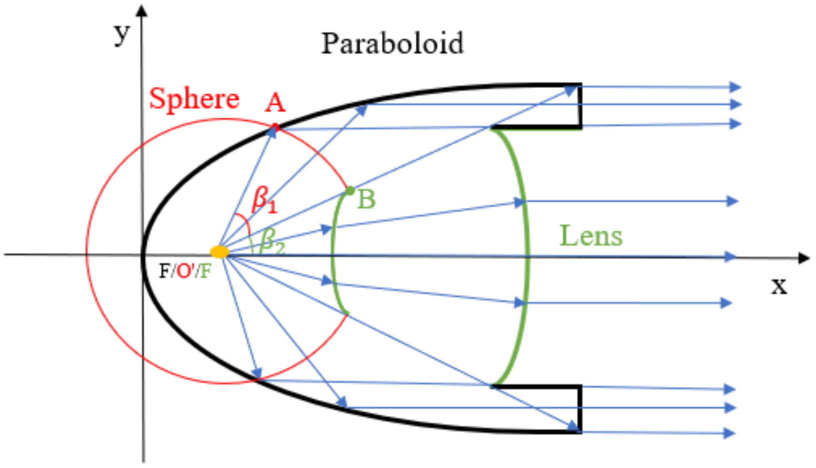

Figure 3. 27 Profile structure of the TIR collimator

As shown in Figure 3.28, the angle of light transfer to the paraboloid is β_1. The light from the focal point is projected out of the lens also in parallel, the angle of which is β_2. The half-angle of the divergence of the light source is β_1+β_2.

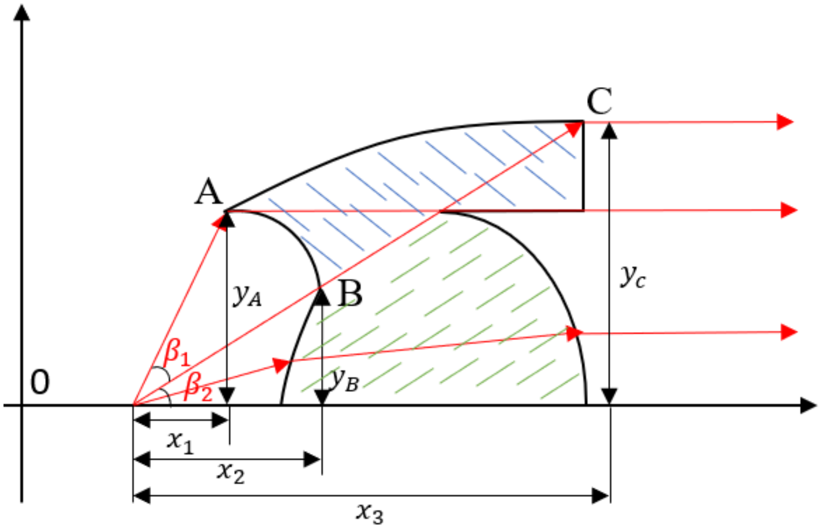

Figure 3. 28 Diagram of the diameter length dimension

The equation of even degree aspheric surface of the rotationally symmetric structure is

$$z = \frac{cr^2}{1+\sqrt{1-(1+k)c^2r^2}} + a_1r^2 + a_2r^4 + a_3r^6 + a_4r^8 + a_5r^{10} + \cdots \tag{3.52}$$

where $z = \frac{cr^2}{1+\sqrt{1-(1+k)c^2r^2}}$ is the quadric equation of datum, c is the curvature of the vertex of the aspheric surface, r is radial coordinate, which is the distance from any point on the aspheric surface to the optical axis, k is constant of the conic, $\Delta z = a_1r^2 + a_2r^4 + a_3r^6 + a_4r^8 + a_5r^{10} + \cdots$ is an offset of the aspherical surface from a reference conic. The equation of the cross profile of the paraboloid, which is a conic, can be derived as

$$y^2 = 2px \tag{3.53}$$

The coordinate of the focal point is $\left(\frac{p}{2}, 0\right)$. The coordinate of intersection point A between the sphere and paraboloid can be derived as

$$\mathrm{x_A} = \frac{\mathrm{p}}{2} + \mathrm{x_1} = \frac{\mathrm{p}}{2} + \frac{\mathrm{p}}{\tan(\beta_1 + \beta_2)^2} + \frac{\mathrm{p}}{\tan(\beta_1 + \beta_2)}\sqrt{\frac{1}{\tan(\beta_1 + \beta_2)^2} + 1} \tag{3.54}$$

$$\mathrm{y_A} = \frac{\mathrm{p}}{\tan(\beta_1 + \beta_2)} + \mathrm{p}\sqrt{\frac{1}{\tan(\beta_1 + \beta_2)^2}} \tag{3.55}$$

Thus, the diameter of the collimator entrance is $\frac{2\mathrm{p}}{\tan(\beta_1+\beta_2)} + 2\mathrm{p}\sqrt{\frac{1}{\tan(\beta_1+\beta_2)^2} + 1}$. The sphere can be described as

$$\mathrm{y_B} = \mathrm{p}\sqrt{\frac{\frac{2}{\tan^2\beta_2} + 2\sqrt{\frac{1}{\tan 4\beta_2} + \frac{1}{\tan^2\beta_2}} +}{2\sqrt{\tan^2\beta_2 + 1} + \tan^2\beta_2 + 3}} \tag{3.56}$$

$$\mathrm{x_B} = \mathrm{x_2} + \frac{\mathrm{p}}{2} = \frac{\mathrm{y_B}}{\tan\beta_2} + \frac{\mathrm{p}}{2}$$

The endpoint of the paraboloid is C, which determines the length of the TIR collimator. Thus, the point C can be derived as

$$\mathrm{y_c} = \frac{\mathrm{p}}{\tan\beta_2} + \mathrm{p}\sqrt{\frac{1}{\tan{\beta_2}^2} + 1} \tag{3.57}$$

$$\mathrm{y_c} = \frac{\mathrm{p}}{2} + \mathrm{x_3} = \frac{\mathrm{p}}{2} + \frac{\mathrm{p}}{\tan\beta_2} + \mathrm{p}\sqrt{\frac{1}{\tan{\beta_2}^2} + 1} \tag{3.58}$$

Thus, the length of the collimator is

$$\mathrm{L_{collimator}} = \mathrm{x_3} - \mathrm{x_1} = \frac{\mathrm{p}}{\tan\beta_2} + \mathrm{p}\sqrt{\frac{1}{\tan{\beta_2}^2} + 1} - \frac{\mathrm{p}}{\tan(\beta_1 + \beta_2)^2} - \frac{\mathrm{p}}{\tan(\beta_1 + \beta_2)}\sqrt{\frac{1}{\tan(\beta_1 + \beta_2)^2} + 1} \tag{3.59}$$

From the above formula, the basic parameters of the TIR collimator can be calculated to construct the initial structural model. Besides, the volumetric model can also be constructed as below.

For the central part of the freeform structure, the detailed diagram of designing the freeform TIR lens has been described in Figure 3.30 by Zhao,et al [158]. The association between light source position and collimating lens should be determined first. The vector of the tangent direction on the lens surface is obtained by the principle of geometric optics. Then, the two-dimensional surface of the freeform lens can be constructed by the value of the vector in the tangent direction. The designed freeform lens can be obtained by rotating the 2D surface shape around the optical axis.

The light from the LED is collimated to the optical axis after passing through the freeform surface. As shown in Figure 3.31, Q is one point on the freeform surface, the red line is the light path. The relationship between these parameters can be derived as

$$\mathrm{i} - \theta_1 = \frac{\pi}{2} - \theta_2 \tag{3.60}$$

$$\alpha = \frac{\pi}{2} - \mathrm{i} + \theta_1 \tag{3.61}$$

where θ_1 is incident angle and θ_2 is exit angle. Besides,

$$\mathrm{n} \sin \theta_1 = \sin \theta_2 \tag{3.62}$$

where n is the refractive index of the collimator and assuming the refractive index is 1. Thus,

$$\theta_1 = \tan^{-1}\left(\frac{\cos \mathrm{i}}{\mathrm{n} - \sin \mathrm{i}}\right) \tag{3.63}$$

$$\alpha = \frac{\pi}{2} - \mathrm{i} + \tan^{-1}\left(\frac{\cos \mathrm{i}}{\mathrm{n} - \sin \mathrm{i}}\right) \tag{3.64}$$

The vector in any direction of Q can be obtained. As shown in Figure 3.32, it is a conceptual mapping from a point light source to a freeform surface (Q) to a set of target points ($\mathrm{y_n}$). The surface normal ($\mathrm{Q_n}$) is set to send the incident light to the corresponding target point. The surface profile is generated by B-spline function surface interpolation, which is typical freeform surface.

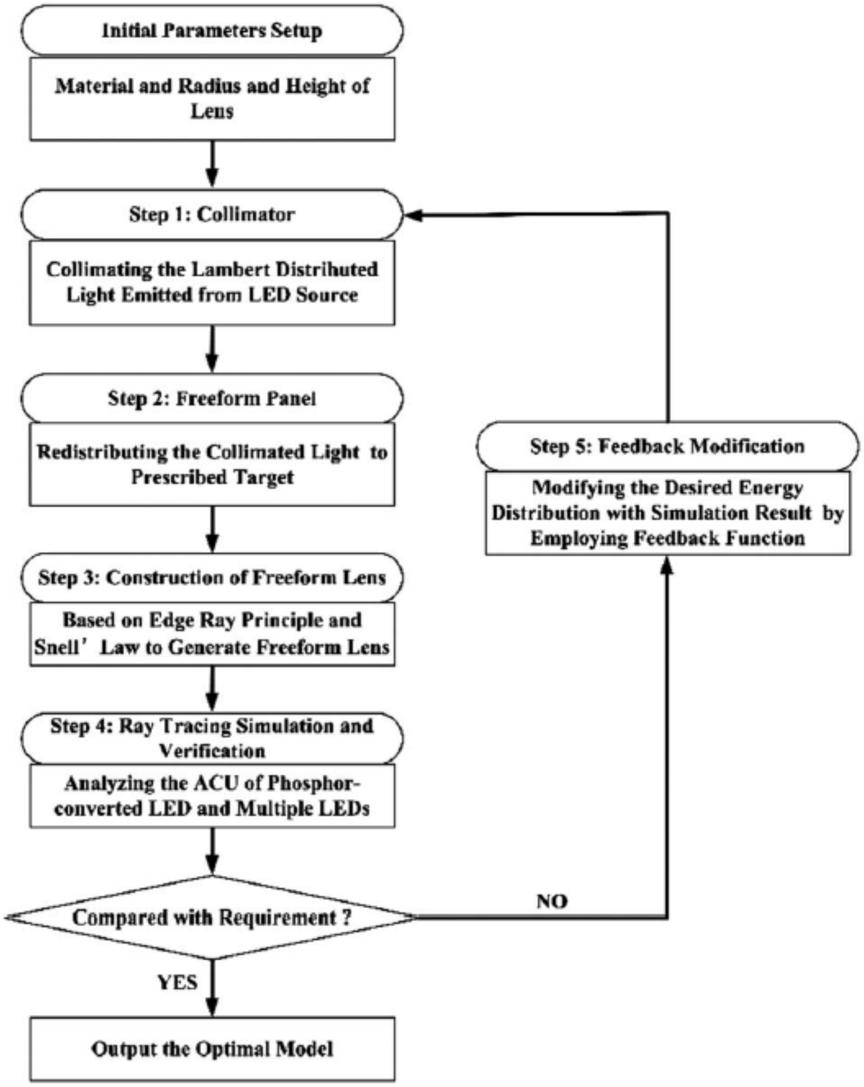

Figure 3. 29 Diagram of the design method of freeform TIR lens.

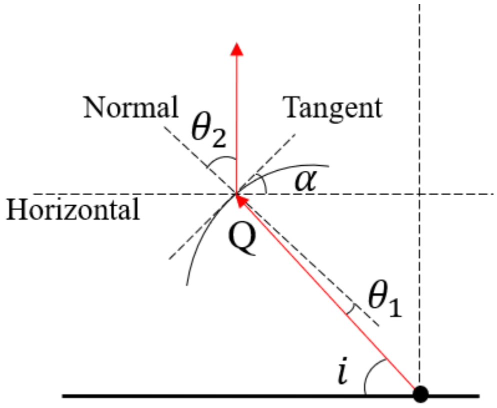

Figure 3. 30 Geometrical analysis of the freeform surface

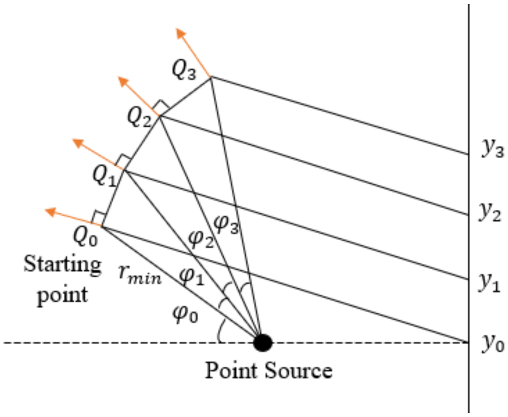

Figure 3. 31 Calculation method for freeform surface

3.6.2 Simulation and optimization of designed collimator

Under the synergy effect of the central freeform optical lens part and the edge part of the TIR optical element, the collimation of the light source can be realized. The size of the LED is 1mm*1mm, the effect of which can be negligible to the illumination. The material of the collimator is polymethyl methacrylate (PMMA). The refractive index n=1.49 at 555 nm wavelength. Thus, the critical angle δ of the TIR is around 45°.

$$\delta_{\text{critical angle}} = \sin^{-1}\frac{1}{n} \tag{3.65}$$

Based on Eq. (3.52) to Eq. (3.54), the surface data of the central part can be calculated and optimized as discussed above. The diameter of the entrance side of the system is 15mm, and the diameter of the exit side of the system is 29mm. The length of the system is around 18.3mm. The divergence angle of LED is around 120°. The conceived collimator model is shown in Figure 3.33.

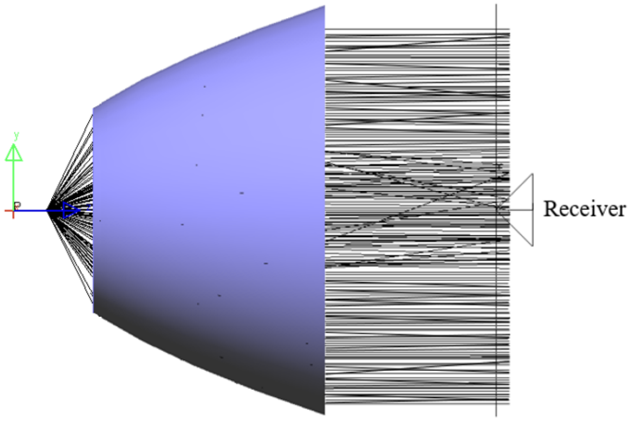

Figure 3. 32 Simulation of the light path of the TIR collimator

LightTools can automatically optimize the system with variables for the curvature of the intermediate lens. The design has a good illumination uniformity on the receiver plane, as shown in Figure 3.34. The illumination uniformity of the system is over 94% and the luminous flux utilization rate is over 91%, which are proved as shown in Figure 3.35. The uniformity of the system [159] can be derived as

$$\mathrm{U} = \frac{\mathrm{U}_{\mathrm{max}} - \mathrm{U}_{\mathrm{min}}}{\mathrm{U}_{\mathrm{max}} + \mathrm{U}_{\mathrm{min}}} \times 100\% \tag{3.66}$$

where $\mathrm{U}_{\mathrm{max}}$ is the maximum illumination and $\mathrm{U}_{\mathrm{min}}$ is the minimum illumination of the system. The light utilization rate of the system [160] is

$$\mathrm{E}_{\mathrm{uniform}} = \frac{\mathrm{E}_{\mathrm{min}}}{\mathrm{E}_{\mathrm{max}}} \times 100\% \tag{3.67}$$

where $\mathrm{E}_{\mathrm{min}}$ is the minimum light energy and $\mathrm{E}_{\mathrm{max}}$ is the maximum light energy across the whole field. The system would reduce the resolution of the image; thus, there is a trade-off process between uniformity and the resolution of the virtual images. The coefficients of the equation fitted by the discrete data points are set as discrete variables, and the initial structure is optimized using the collimation optimization function in the LightTools. Figure 3.35(a) is the illumination distribution before optimization and (b) is the uniform distribution after optimization by variables on LightTools.

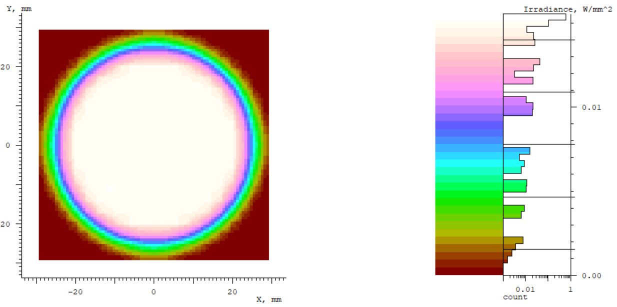

Figure 3. 33 Scatter chart of the illumination of the TIR collimator

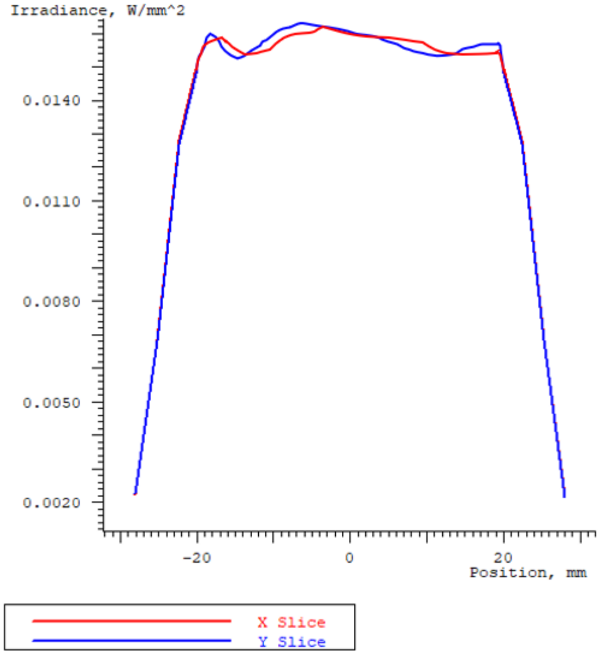

(a)Illumination distribution before optimization

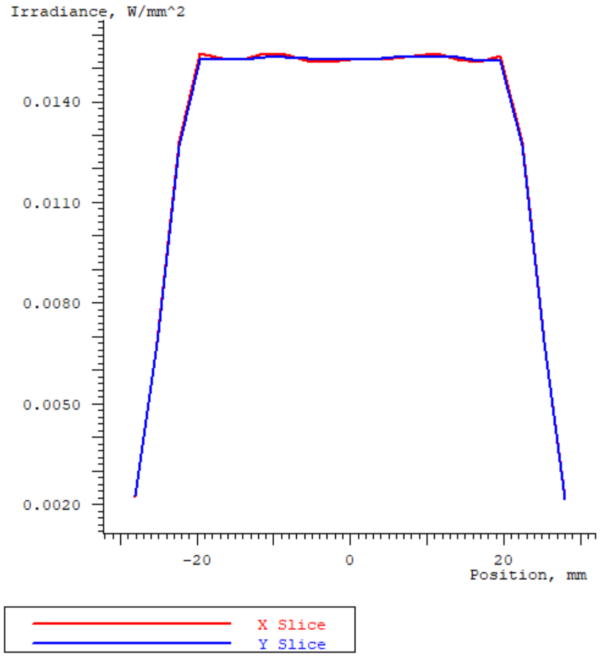

(b)Illumination distribution after optimization

Figure 3. 34 Line chart of the illumination of the TIR collimator

3.7 Summary

In this Chapter, one-dimensional geometrical waveguide is designed, and the simulation results show the achieved specifications of the 72º FOV and 22mm×23mm eye box. A 2-dimensional geometrical waveguide is then developed which realizes 69° horizontal FOV and 56° vertical FOV, along with 22.6mm×26mm eye box. The illumination uniformity of the 2D design could reach 83% after optimization. Stray light causing ghost images are suppressed under 1% by the presented tailored solution. A hybrid collimator combining freeform optics and TIR technology is designed and optimized to achieve a high illumination uniformity and brightness uniformity of projector, for improved quality of virtual images. The simulation demonstrates that illumination uniformity of the collimator system is over 94% and the luminous flux utilization rate is over 91%. The proper match between the projector and waveguide system could reach better optical performance and image quality.

Chapter 4 Analysis and mitigation of vergence accommodation conflicts

4.1 Analysis of vergence accommodation conflicts

Most conventional stereoscopic 3D displays have inherent VAC problem because they simulate the perception of 3D images by the psychological perception from 2D images, which is not real stereoscopic images. Thus, it is necessary to provide great depth and stereo design for the AR system. VAC is a long-lasting problem in stereoscopic displays. To reproduce the real world visually, the light field needs to be studied, which is a vector function to describe the collection of the light in space [161]. A plenoptic function P $(x, y, z, \theta, \phi, \lambda, t)$ for monocular vision is a mathematical model to represent the light field containing 7 dimensions, as shown in Figure 4.1 [162-164]. Light can enter the human eye at different points and at different angles. (x, y, z) represents the position coordinates of the human eye in three-dimensional space. (θ, ϕ) represents the azimuthal angle and polar angle of the light entering the human eye. The meanings of θ and ϕ have been swapped compared to the physics convention. Each ray has a different color, which can be expressed by the wavelength (λ) of the light. The light information, such as coordinates and energy, entering the human eye would change over time (t). The light field describes the collection of rays with the human eye as the center. The reflectance light field also has 7 dimensions, which is the light collection at the center of a luminous object due to the reversible light path [165-168]. Collecting and displaying the light field is vital to reproduce the real-world images. Light field display is a promising approach to solving VAC problem [169-171].

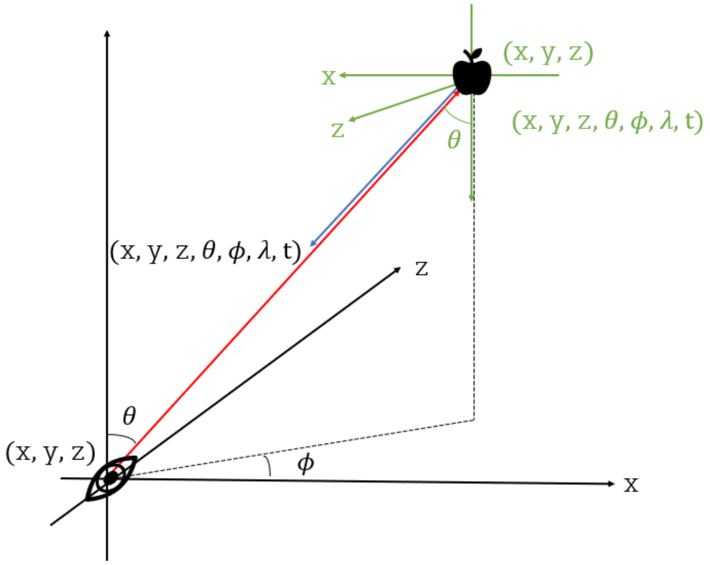

Figure 4. 1 Plenopic field and reflectance field in one space

There are two main reasons for vertigo, including: (1) the conflict between motion perception and visual perception; (2) conflicts between binocular parallax and accommodation of visual perception [172, 173]. The perception of human vision of a three-dimensional environment can be divided into psychological perception and physiological perception. The psychological perception is mainly through affine, occlusion, light and shadow, texture, prior knowledge [174-176]. From these aspects, 3D images can be generated. When looking at a certain point, human eyes rotate, and the diopter of the lens is changed so that the point of view falls on the corresponding position on the retina, thus, the object can be seen clearly. When looking at a near object, human eyes usually look inward, and when looking at a far object, the axis of sight diverges a little, which causes visual convergence as shown in Figure 4.2 [177, 178]. There are also differences in observed view of the same object from different angles, and the brain perceives the stereoscopic image based on these differences [179]. The light information from each eye is slightly different on the retina. The brain accepts the light signals from both eyes to judge distances and rotate eyes correspondingly to response to these differences. Convergence and divergence are unique eye movements as these are the only eye movements that are not conjugate thus are termed deconjugate [180].

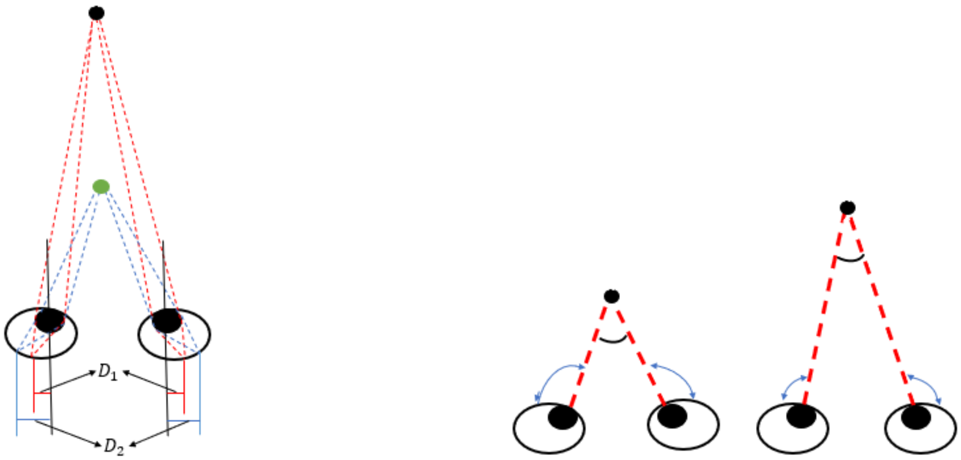

（1）Binocular parallax （2）Binocular convergence

Figure 4. 2 Physiological visual information.

Besides, the physiological perception of stereoscopic vision mainly includes binocular parallax, moving parallax and blurred focus [181-183]. Two different objects at different distance to human eyes, although they move same distance, it cause different visual effect to human perception, which is motion parallax. Whether it is the movement of the object or the movement of the subject, it will cause a change in the imaging position of the observed object on the retina. Motion parallax refers to the difference in movement direction and speed of objects when the line of light moves laterally in the field of view. When doing relative displacement, the near objects seem to move faster, and the far objects seem to move more slowly. Motion parallax can also be judged by calculating the speed at which the retinal image position changes. When the two cues of motion and binocular parallax work at the same time, binocular parallax have more influence on depth perception. Besides, the relationship between motion and binocular parallax is not a linear superposition, but are dependent on each other [184, 185]. The 3D movie can already achieve the motion parallax for an immersive feeling. Furthermore, human eyes change the shape of the lens to adjust the position of focus by ciliary muscle, and it does very quickly. When looking at real objects, in addition to visual convergence adjustment, there is a need to adjust the refractive of the light at different distances, so that the light can be focused on the retina to form a clear image. This process of focusing the lens on the object is called accommodation as shown in Figure 4.3 (a). When focusing on any point, the other two points will be vague for perception. As Figure 4.3 (b) illustrates, when eyes focus on the far bus for clear vision, the near cat would be blurred; when eyes focus on the near cat for clear imaging, the far bus is vague for perception. In a natural viewing environment, the interaction between adjustment and convergence provides comfortable and clear binocular vision. Due to the certain depth of field of the lens, a certain degree of adjustment error is allowed. To keep the image clear, the error needs to be controlled within ±0.25 diopter [66, 186, 187]. The pupil can respond to light and shade and then adjust the light acceptance. Only a very small area of the retina is used to identify light information. This area, called the macula, is about 6-7mm in diameter, and it is very sensitive and has very high resolution in the dynamic range of light and shade, grayscale, and color scale.

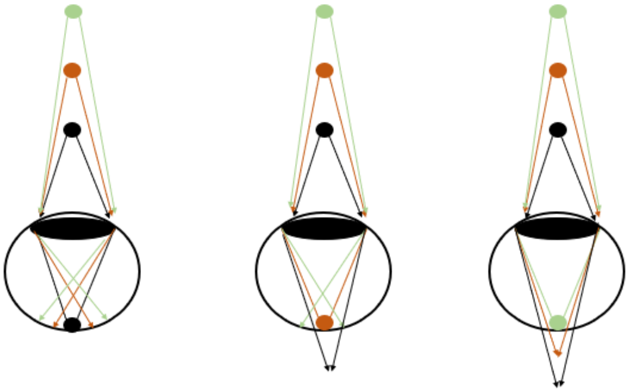

（a）Accommodation at different distance

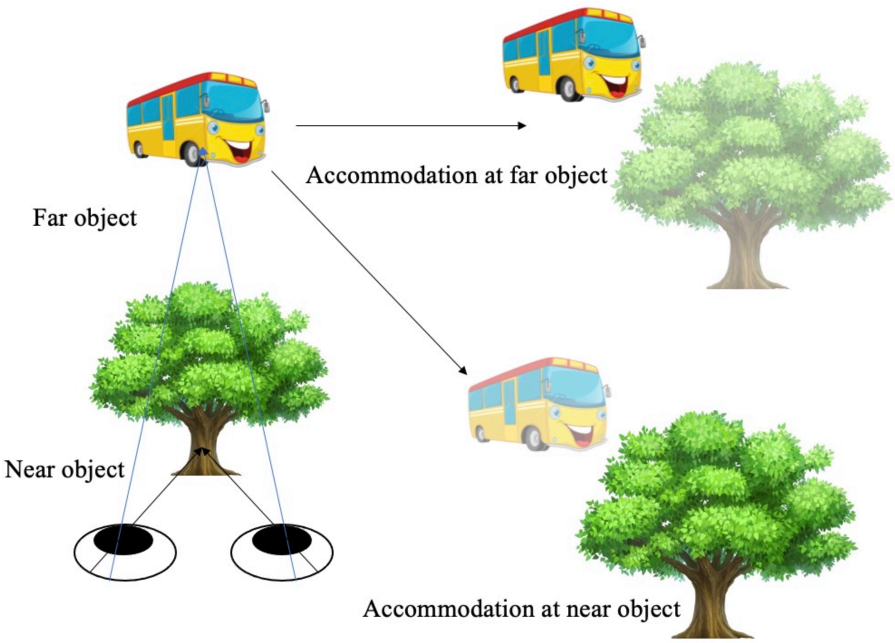

（b）view the real objects

Figure 4. 3 Physiological visual information (accommodation).

Visual comfort is one of the main criteria for stereoscopic image experience quality. Current devices display images, which are taken from different angles of the same object through the left and right sides, and the offset of the image seen by both eyes represent a stereoscopic perception. However, the light emitted by the screen has no depth information, and the focus of the eyes is fixed on the screen. Therefore, the adjustment of the focus of the eyes is not matched with this depth perception, resulting in VAC [188-190]. At present, with the development of display technology, display devices can provide more and more abundant visual perception information. According to the visual information that can be presented, the display devices can be divided into 4 levels, as shown in Figure 4.4 [66, 179, 191-193]. The pupil and the lens of the eye do not change when humans look at the 2D images. Accommodation is an unsolved problem for AR/VR systems. The current technologies are aiming to increase the layers of the image plane as much as possible. As the number of layers of the image increases, the VAC issue would be reduced. When the number of imaging layers reaches a certain number, the human eye can no longer clearly feel the VAC [194, 195].

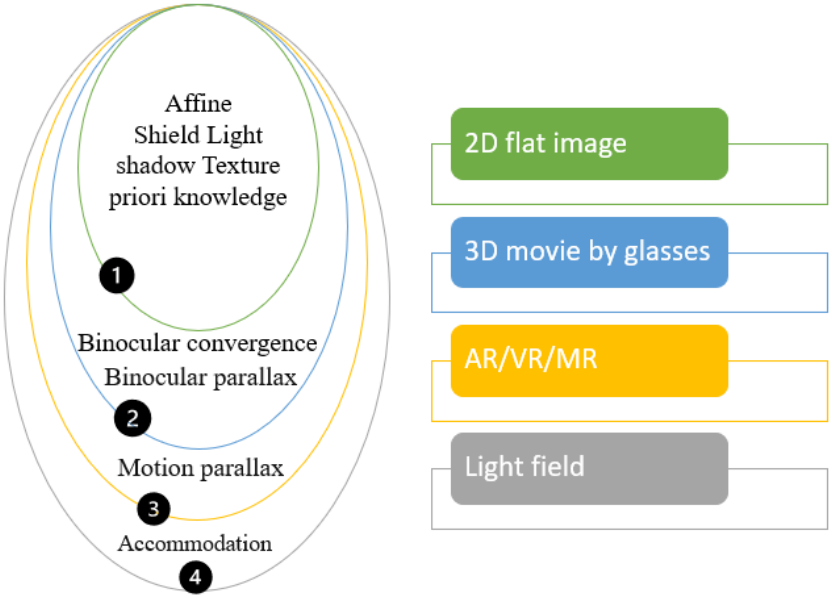

Figure 4. 4 Classification of display devices [179]

4.2 Comparisons of state-of-the-art technologies in solving VAC

Some methods have been presented to suppress the VAC problem for the optical display with depth perception. Dunn et al. provided a deformable membrane mirror system, with 100° FOV and 300ms switching depth from 20cm to infinity [73, 196]. Liu et al. developed an addressable lens system, with 24° FOV and 74ms switching depth from 8D to infinity to match the vergence [197]. Kaan et al. proposed a method of applying diffusing holographic screen and a sliding optics for 55°- 63° FOV and 410ms switching time from 5D to infinity [198]. Hua et al. showed a compact time-complexed multiplane display using freeform optics and microscopic integral imaging method, spanning the depth range from 40cm to 5cm [199]. Klug et al. published a patent including two layers of RGB grating lightguide to form two depths of images [200]. Lee et al. demonstrated a 3D display consisting of two display modules, a waveguide, and a holographic lens, reaching 38°× 19° FOV. Yuki et al. presented a novel design with deep depth of field (DoF) by pinhole arrays [201]. Andrew et al. demonstrated a method combining pinlight arrays and spatial light modulators (SLM), which reached 110° FOV [202]. To render a true 3D image, these technologies can be concluded into three categories: (1) varifocal display; (2) multifocal display and (3) light-field display. Table 4.1 compares different kinds of accommodation-solving displays [111, 190, 203-211].

Table 4. 1 Comparison of VAC-solving displays [7, 73, 122, 197].

	Display technology	Focus mechanism	Focal plane	Eye box	Latency	Form factor	Stray light	Technology
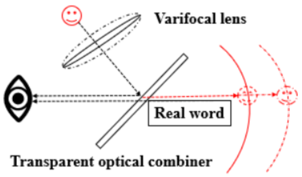 	Varifocal see-through display	Varifocal	According to the diopter of the lens	Large	Yes	Less bulky	Yes	Deformable membrane mirror, addressable focal play displays…
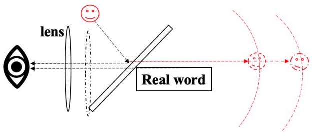 					Yes			The sliding optics
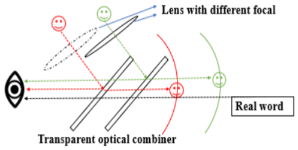 	Multifocal see-through display	Multifocal	According to the numbers of the display /light source	Large	No	Bulky	Yes	Waveguide and holographic combination systems
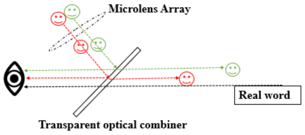 					No			Integral imaging display
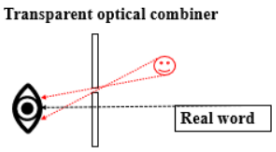 	Pinhole /Pinlight see-through display	Light field	Several planes	Small	No	Thin	No	Pinhole mirror, pinlight arrays…
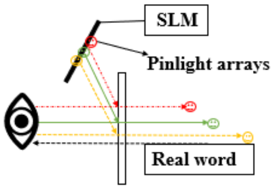 								

4.2.1 Varifocal design

A varifocal display consisting of a varifocal image plane with high angular resolution is a solution for the accommodation problem. Some technologies have been applied for varifocal displays, such as deformable membrane mirrors, addressable focal planes, the sliding optics and so on. Dunn et al. proposed a monocular varifocal mechanism based on the deformable membrane mirror system, as shown in Figure 4.5 [73]. The virtual images are reflected by a deformable membrane mirror to human eyes, in which the mirror works as a spherical concave reflective surface. The focal distances change based on the mirror curvature. The diagonal FOV could reach 100° with fast depth switching (from 20cm to infinity within 300ms) [196]. Figure 4.6 shows the experimental result of viewing the focus of near and far soda cans and the virtual teapot. However, the display can only present the virtual image at a single depth every time. It is hard to get multiple focus properties across the entire FOV. Thus, the depth of virtual objects must be computed and determined by the gaze tracker in advance [212, 213]. Besides, the response time of 300ms also causes latency, and the image resolution still needs to be improved.

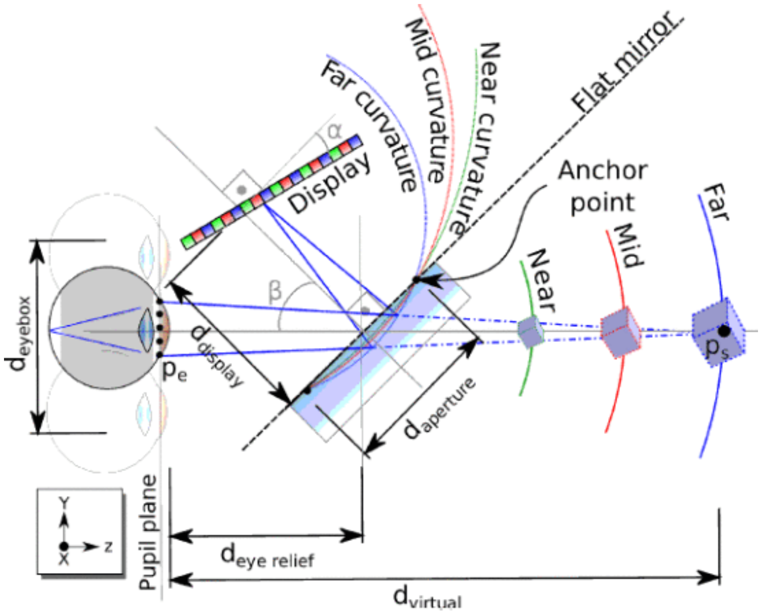

Figure 4. 5 Layout of varifocal display with deformable membrane mirror [73].

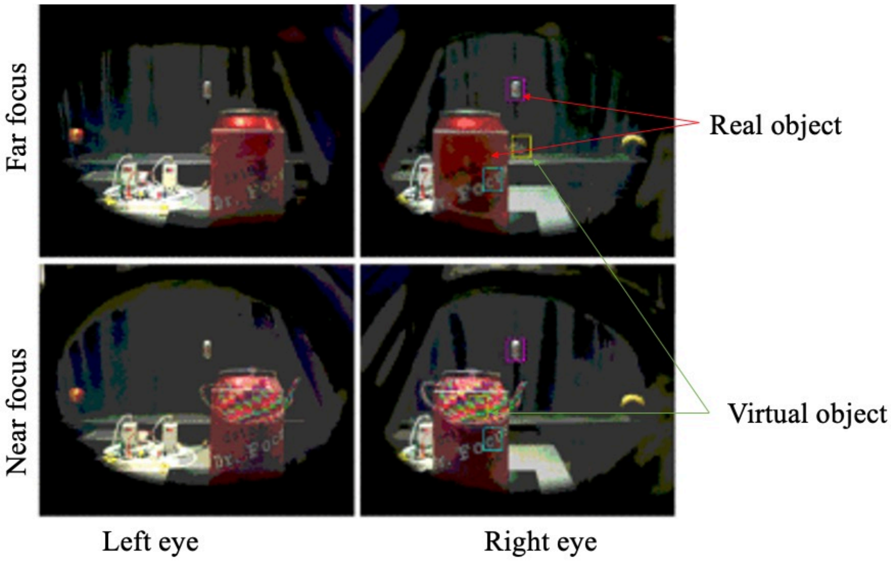

Figure 4. 6 Viewing result of deformable membrane mirrors [73].

Liu et al. presented an optical see-through display with addressable focal planes based on the electrowetting phenomenon of a liquid lens, as shown in Figure 4.7 [197]. The liquid lens for accommodation consists of two optical power, one is variable from -5 to 20 diopter and the other one is constant, which present the intermediate image. The spherical mirror would relay the intermediate image and transfer it to human eyes. When the variable power changes from high power I to low power II, the accommodation cue moves from far I” to near II”. Figure 4.8 shows the experimental result with a focus distance from 40cm to 100cm away from the viewer. The two cups are real objects and the coke is a virtual image. The left cap is placed at far distance and the right cup is placed at near distance. The distance of virtual image cola can be changed. Figure 4.8 (a) and (b) is the depth at 40cm, and Figure 4. 8(c) and (d) is the depth at 100cm. And Figure 4.8 (a) and (d) simulated the focus at 40cm, Figure 4.8(b) and (c) simulated the focus at 100cm. However, the distance of the virtual image should also be pre-programmed. The diopter of the lens is changed by the voltage, which causes some latency.

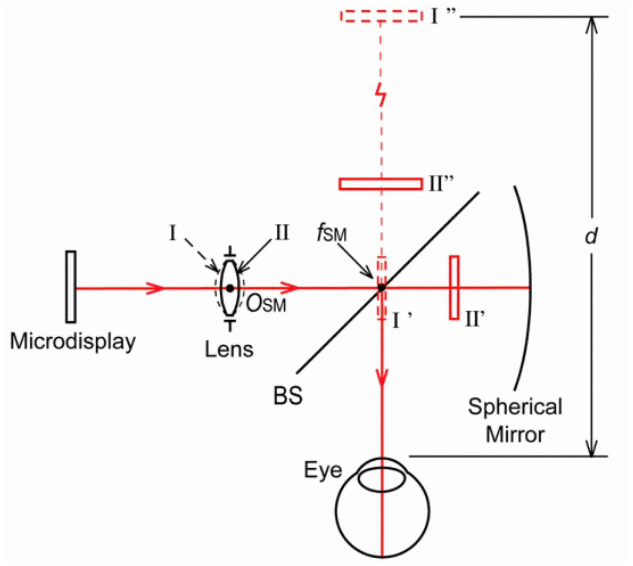

Figure 4. 7 Schematics of the optical see-through display with addressable focal plane [197].

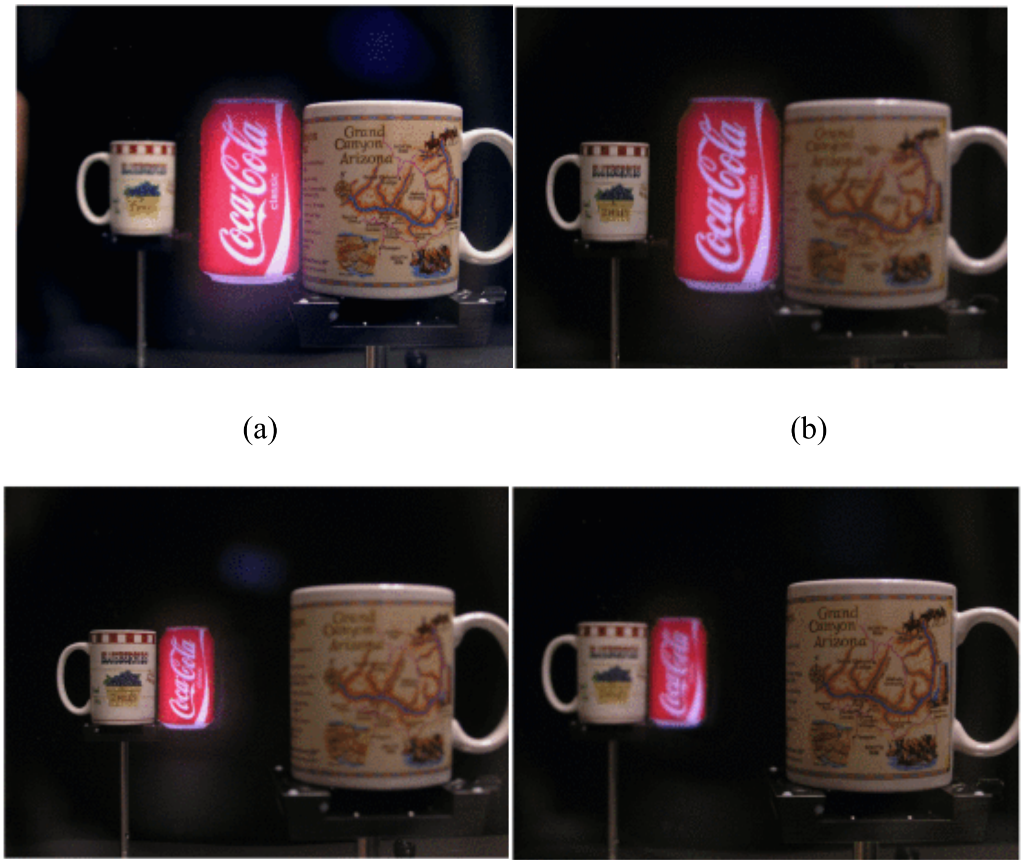

(a) (b)

(c) (d)

Figure 4. 8 The test result of optical see-through display with addressable focal plane. (a) and (d) simulated the focus at 40cm, (b) and (c) simulated the focus at 100cm. Coke can is the virtual image [197].

Kaan et al. proposed a varifocal near-eye display with desired depth to match the vergence by a sliding curved beam combiner on axis, as shown in Figure 4.9 [198]. In this design, the virtual images were formed as intermediate images by the oasis screen (one-way diffusing holographic screen), then relayed to the curved beam combiner and finally transferred to human eyes. It provided symmetric monocular FOV 55° to 63°. The size of the virtual image is limited by the structure of the curved beam combiner. The focal plane can be dynamically moved by changing the geometry and the position of the screen along the optical axis of the system. Figure 4.10 shows the compact prototype and the brightness achieved at eye position by this design. The light engine must be connected to a computer for the real-time virtual light programming, therefore, the system is somewhat bulky for wearable use [214, 215].

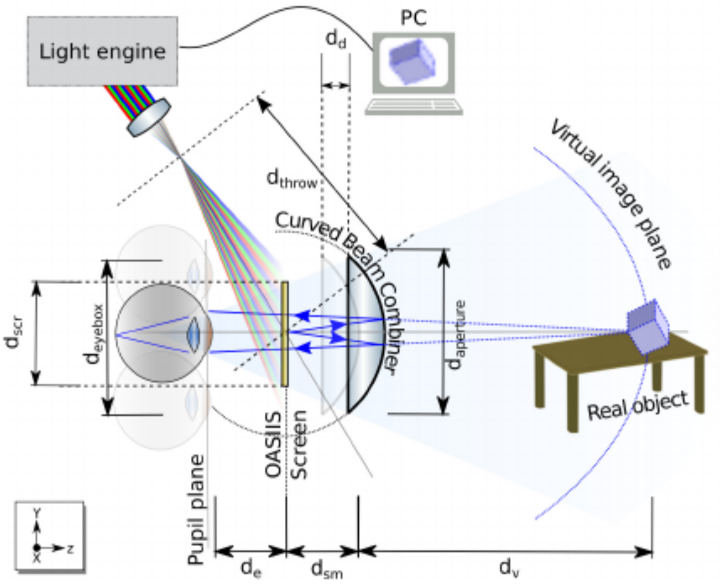

Figure 4. 9 Varifocal display with sliding optics [198].

Figure 4. 10 Layout of the design and daylight photo taken from the eye position [198].

4.2.2 Multifocal design

Hua et al. presented an innovative approach to optical see through HMD designs by combining the recent advancement of freeform optical technology and microscopic integral imaging (micro-InI) method, as shown in Figure 4.11 [199]. Each of the set of 2D elemental images represents a different perspective of the 3D scene, projected by the projector. Then each elemental image transfers to a spatially incoherent image when they pass through the microlens array and built a perception of 3D images. By means of the freeform optics, the 3D scene is relayed to human eyes without blocking the images from the real world. The FOV of this proof-of-concept prototype is around 40° and the depth range is over 4 meters. Figure 4.12 shows the experimental results at 4m and 30cm depth. Snellen chart is placed at 4 m and the grating target is placed at 30cm away from the observer. The number ‘3’ is much clearer in Figure 4.12(a) than the letter ‘D’, as 3 is projected at 4m, while the ‘D’ is projected at 30cm. The resolution of the projector and the virtual images quality still have space to be further improved. The FOV and latency also need to be optimized [121, 216, 217].

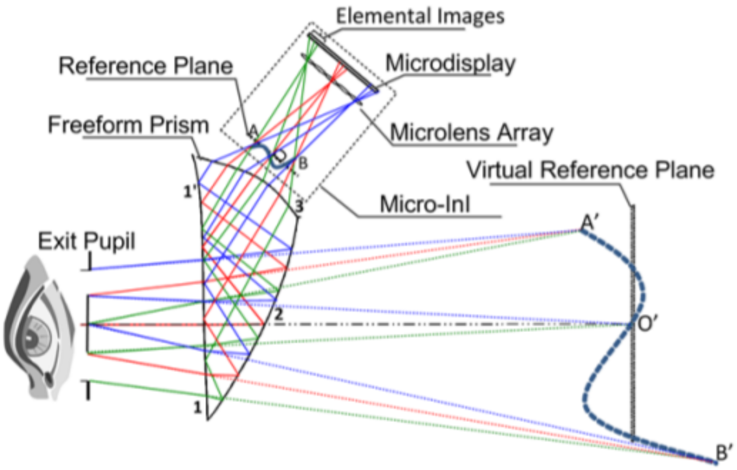

Figure 4. 11 Schematic design of OST-HMD using freeform optics and micro-InI [199].

(a) (b)

Figure 4. 12 Experimental results. (a) is reconstructed image at the 4m depth and (b) is the reconstructed image at 30cm depth [199].

Klug et al. published a patent including a fiber scanning display, a combination system and the lightguide element, shown in Figure 4.13 [200]. The light source includes two sub-light sources. When the light transfers to the gratings on the lightguide system, they are coupled into the lightguide. The lightguide has two RGB elements, which are used to increase the number of spatially separated lights. RGB reduces the cross-walk of each color [218-220]. When the light transfer to the out-couplers, two groups of sub-lights are coupled out as different sub-pupils to human eyes, including two depth planes. However, diffraction gratings, or holograms cause chromatic aberrations which cannot be eliminated and decrease the light efficiency. It needs very high-resolution display [221-223]. 6 layers lightguide also increases the size and weight of the whole system.

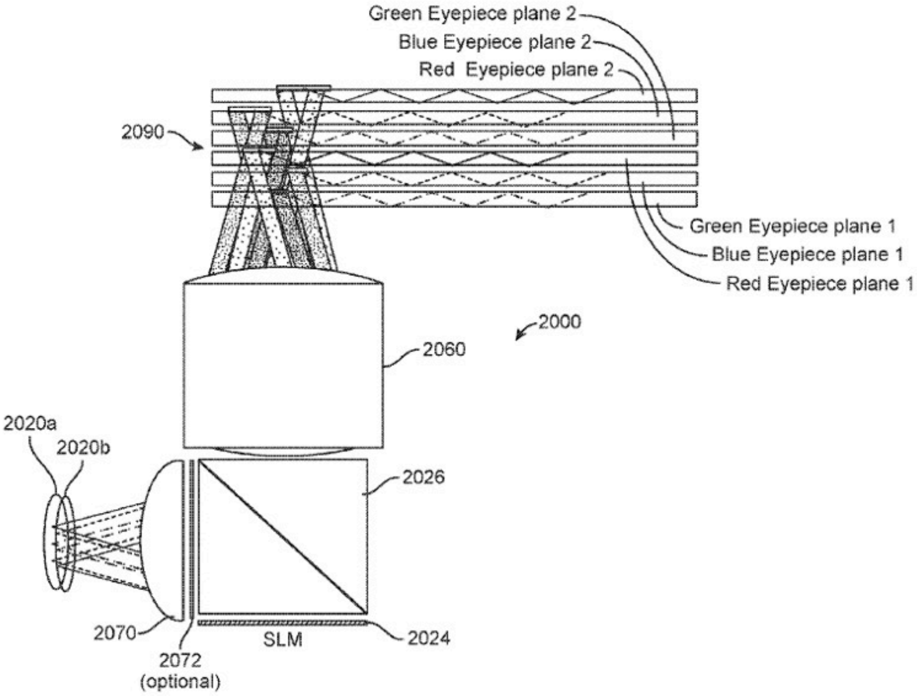

Figure 4. 13 Schematic design of the application [200].

4.2.3 Light field design

Yuki et al. proposed an optical see-through display with a deep depth of field using pinhole polarizing plates as shown in Figure 4.14 [201]. The light from the projector is vertically polarized and reflected by the beam splitter. Only when the polarized horizontal light passing through the pinhole can it transfer to human eyes, most of the light is blocked by the plate. The light from the real world can pass through the system. However, the light efficiency is decreased when the light passes through the polarizing plate and beam splitter. The FOV and the DoF are limited by the pinhole size [201, 224]. PinMR™ technology released by LetinAR uses the pinhole effect for the expandable FOV and the extended DoF [225]. The LetinAR system is based on pin mirrors embedded in a transparent substrate. These small mirrors are tilted at about 45° to send the image into the viewer's eye. Typically, they are flat but their diameter is small enough (pin-head size) so they act as a pinhole camera and provide a large depth of field. The optical design of the pin mirrors is application dependent. In addition to a flat mirror design, it can also be a freeform curved mirror which can both fold the light path and focus the light to provide the virtual image to the viewer. The advantage of a freeform mirror is that it can have a larger diameter and therefore higher efficiency and still have a very large depth of field. Flat or curved mirrors are so small and so close to the eye that the mirrors themselves are not seen – only the image generated by the mirrors is visible. The lenses with the embedded mirrors are essentially see-through to the real world, with the mirrors themselves interfering very little with the outside view. Figure 4.15 shows the images from LetinAR glasses with a diagonal 41° FOV. However, pinhole technology has a high requirement on the distance between the glasses and human eyes, so the eye relief is significantly limited.

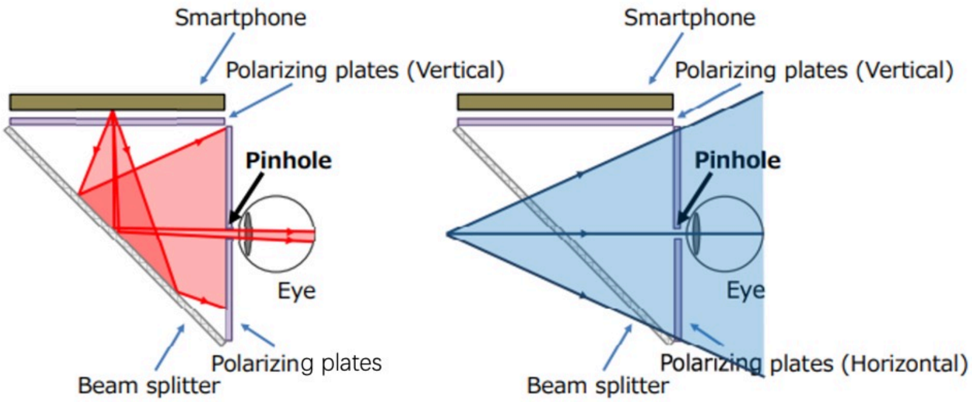

(a) (b)

Figure 4. 14 Mechanism of pinhole technology. (a) Red lines are from the projector. Most lines are locked by the polarizing plate and only the light passing through the pinhole can transfer to human eyes. (b) Blue lines are the light from real world [201].

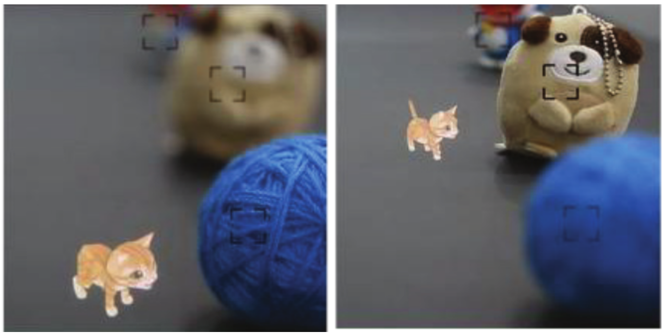

Figure 4. 15 Images of LetinAR glasses [225].

Maimone et al. presented a defocused point light array display as shown in Figure 4.16 [202]. The pinlight technology is composed of point sources. The point light sources are coded by a spatial light modulator (SLM) to form miniature see-through projectors with a specific angle. The sub-images are rearranged by the software for different accommodation depths by controlling sub-pinlight. Eye tracking is employed to maximize depth resolution. It could reach 110° FOV [226, 227]. Pinlight technology has high requirements for the SLM system and the combination of each pinlight, which has a direct impact on the projected image quality.

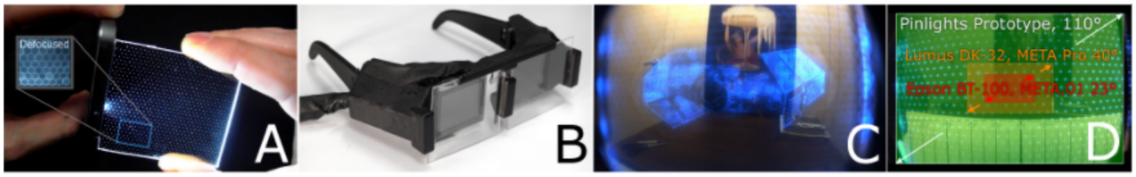

Figure 4. 16 Pinlight displays. (a) is the array of pinlight source. (b) is the prototype consisting of pinlight arrays and SLM. (c) is the images from the glasses. (d) shows the 110° FOV[202].

4.2.4 Comparison and prospect

The VAC is a significant ergonomic issue for the near-eye see-through display, which relates to the fatigue and dizziness of viewers. The VAC is the result of a single or limited depth plane of virtual images, so all the above potential solutions work on increasing the depths of the display, as shown in Table 4.1. Ideally, different focal lengths for each pixel for the virtual images should be chosen. The experimental systems listed in Table 4.1 are mainly trying to solve the VAC problem through this direction. However, all these systems can only adjust the focal length simply to improve the depth perception to approach the principle of human eyes. Hence, there is still a long way to go for commercial applications. Compared with the varifocal and multifocal displays, the thickness of light field display is thinner. Besides, the pinlight and pinhole display have less stray light because there are fewer optical elements for the light to pass through, thereby, the light efficiency is much higher than the other two kinds of technologies. However, the pinhole structure limits the eye box and eye relief due to its' inherent working mechanism. Varifocal and multifocal displays can be employed to achieve larger eye box and eye relief. For the varifocal display, if there is an extra lens, such as addressable focal plans and deformable membrane mirror, would result in significant distortion. There is a trade-off process between the diopter selection of the lens and the distortion level. Besides, as the diopter of the lens is switched by a controller, there must be some latency during the process.

Asthenopia prediction algorithms based on the adjustment mechanism of convergence have also been continuously developed in recent years. From the initial reliance on parallax statistical analysis, it has been developed to consider defocus blur and adjust the dynamic process of convergence. Most such solutions could reach ideal FOV and DoF providing an immersive feeling, but they still depend on the algorithm and the software precoding system [228]. They alter the depth of the virtual images to match viewers' comfortable focus area and distance, however, they are still limited by the programming, environment, latency and refresh rate, which is not suitable for all observers and environments. To solve the problem, the most effective method is to connect the hardware to gaze tracking, user and environment tracking [229]. Gaze tracking makes the virtual images closer to the human eyes, thus the software could simulate the real-time virtual images suitable for vision [230-233]. Besides, user and environment tracking are crucial for the immersive feeling for customers [2]. Although some efforts are made through both hardware and software, the stereoscopic fatigue has more influence factors, such as cognitive fatigue. The processing of visual information needs to pass through the optic nerve and the complex cerebral cortical pathways. The non-natural viewing conditions of stereoscopic displays may increase a load of stereoscopic information processing, resulting in overload and cognitive fatigue. There are several non-invasive technologies to measure the activity of the brain, such as functional magnetic resonance imaging (fMRI), electroencephalogram (EEG) and functional near-infrared spectroscopy (FNIRS), which are related to the neurology [234-238]. Researchers conducted tests on the relationship between the autonomic nervous system (ANS) and the non-invasive technologies [239-243]. The results show that the non-invasive technologies help significantly in reducing the stereoscopic fatigue.

While no single technology can solve the VAC problem completely, the integration of different means has become a major development trend of near-eye see-through displays. However, due to some technical barriers such as near-eye display and perceptual interaction, the development of the end market will take time. It is predicted that the field of near-eye see-through display will see a large space for imagination in the form of terminal products, software, content, and applications in the next decade.

4.3 Design and optimization of 2.5D geometrical waveguide

4.3.1 System design

Seriously limited by the component thickness, most stereoscopic displays can only realize one focal plane. Although waveguides can support thinner designs, by now only very limited designs have succeeded in achieving two focal planes by the diffractive waveguide. Due to the inherent working mechanism based on the RGB structure, the thickness of the diffractive waveguide component is relatively larger than that of the geometrical waveguide. Herein, a dual-layer geometrical waveguide design is proposed to offer a two-focal depth display with the thinner structure shown in Figure 4.17. The light source consists of two sub-light sources, each of which aims to form sub-pupils. The lights from the two sub-lights are separated from each other and they are perfectly collimated. The SLM encodes and combines the two sub-light beams with every image data by passing through the beam splitter. SLM is a kind of device that can transform information into one-dimensional or two-dimensional optical data to change the amplitude, phase, and polarization of spatial light distribution under the control of time-varying electrical drive signals or other signals. The visual information is collimated and coupled into the waveguide by the in-coupler. The light can be internally reflected in total within the waveguide and coupled out to the next optical element until it transfers to the partially reflective mirror array (PRMA), which breaks the condition of TIR. The light from waveguide A is presented at infinity for human eyes. The fixed-focal lens between the two waveguides fixes the focal point to approximately 100mm from the waveguide B (GWB) surface. A compensation lens in front of waveguide B is added to counteract the aberration caused by the fixed-focal lens, so the real-world information will not change significantly. Then the light is coupled into the corresponding geometrical waveguide and coupled out to human eyes to generate the combined (virtual & real) images, as shown in Figure 4.18. The virtual images are displayed at different depths to reduce the vergence accommodation conflict and generate an immersive feeling. In this process, the waveguide is only responsible for transmitting the light. Under normal circumstances, it does not do any work on the image itself (such as zooming in and out, etc.). Besides, it extends the images in a certain direction, such as 1D, 2D or 3D, to make the images acquired in a larger spatial area. This method achieves larger FOV, eye box and eye relief, and reduces the form factor. Compared with the multi-layer diffractive waveguide, there is no rainbow effect in the geometrical waveguide and the light efficiency is higher, as well as smaller component thickness.

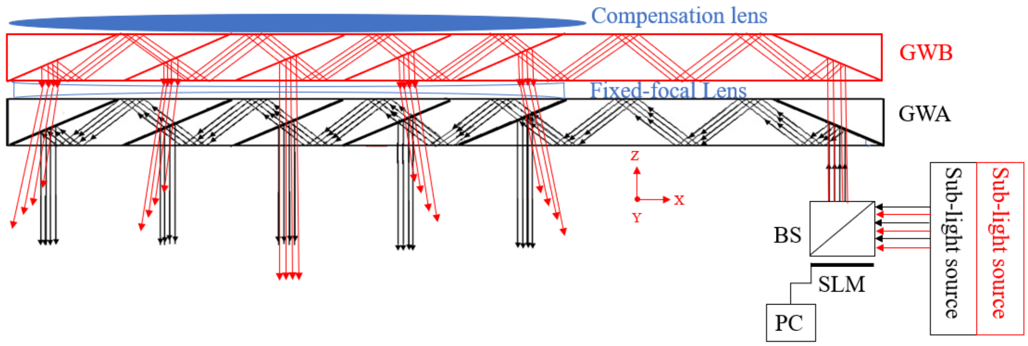

Figure 4. 17 Design of the dual-layer geometrical waveguide.

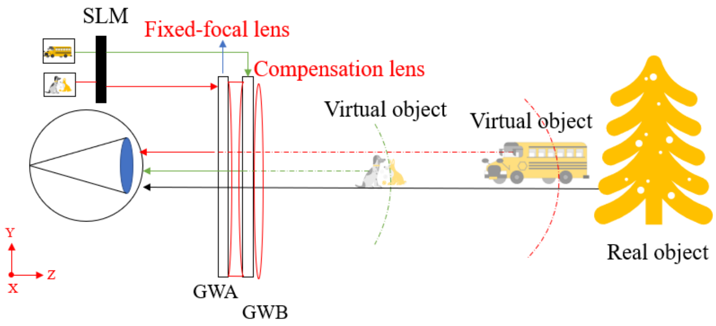

Figure 4. 18 Virtual images at different depths without blocking the information from the real world.

Waveguides require the images entering them to be focused on infinity. The fixed-focal lens works to change the focus of the virtual images. After the parallel incident light passes through the fixed-focal lens, the reverse extension line of its divergent light intersects at a point, which is the virtual focus of the concave lens. Thus, the virtual images will be presented at this focal point as shown in Figure 4.19. Due to the refraction of light, the image formed by the actual object through a thin concave lens is always an upright and reduced virtual image. There is also a lens added in front of the waveguide B to offset these effects, so real-world focus and magnification will not change.

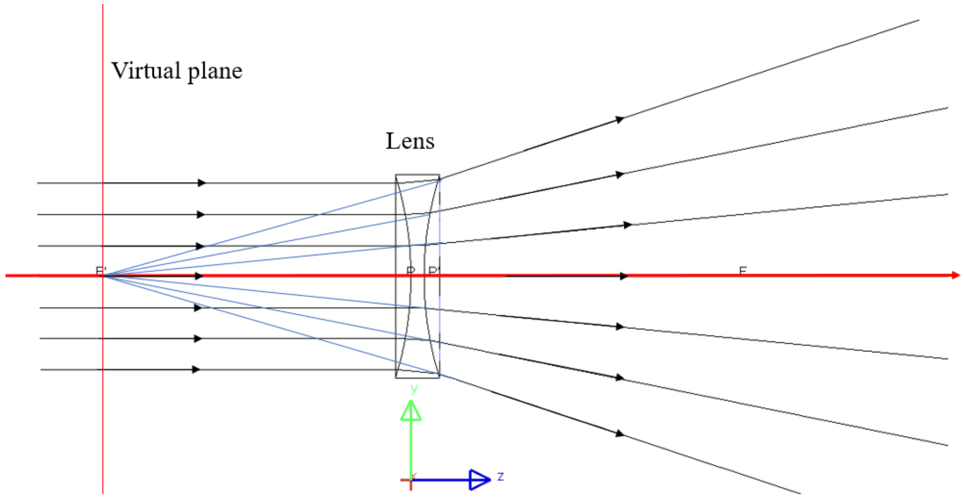

Figure 4. 19 The virtual focal plane of the lens is used to change the depth of virtual images.

The dual-layer geometrical waveguide is shown in Figure 4.20. The light from projector is projected to waveguide A and B respectively. Each layer has its light path. θ_A, d_A, n_A and α_A are the angle between the coupler and edge, thickness, refractive index, and entrance angle of the waveguide A. θ_B, d_B, n_B and α_B are the angle between coupler and edge, thickness, refractive index, and entrance angle of the waveguide B. The distance between A and B is d_g.

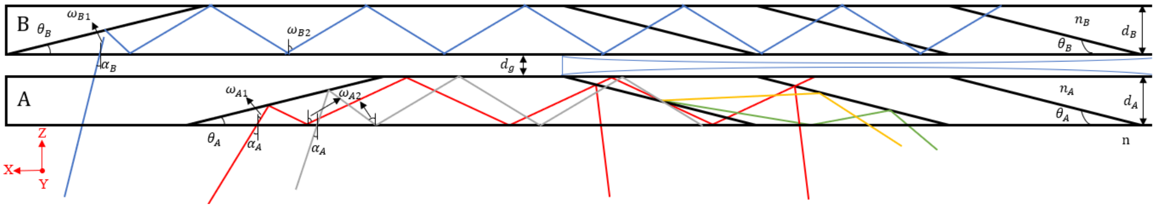

Figure 4. 20 Schematic of the dual-layer geometrical waveguide

Thus, the angle along the z-axis inside the waveguide can be derived as

$$\omega_{A1} = \frac{n}{n_A} \sin \alpha_A \tag{4.1}$$

$$\omega_{B1} = \frac{n}{n_B} \sin \alpha_B \tag{4.2}$$

where n is the refractive index of air. And ω_{A1} and ω_{B1} must be larger than the critical angle to meet the requirement of TIR, which are given as

$$\omega_{A2} = 2\theta_A + \omega_{A1} > \theta_{CA} = \sin^{-1}\left(\frac{1}{n_A}\right) \tag{4.3}$$

$$\omega_{B2} = 2\theta_B + \omega_{B1} > \theta_{CB} = \sin^{-1}\left(\frac{1}{n_B}\right) \tag{4.4}$$

where θ_{CA} and θ_{CB} are the critical angles in waveguide A and B respectively. The angles of light within the waveguide should also satisfy the condition that the angle of TIR should be larger than the critical angle. Based on the above equations, the relationship between entrance angle, critical angle and reflection angle can be described as shown in Figure 4.21, Ideally, when the light points fall onto the blue surface, light can realize TIR without stray light being produced. Any light points falling out of the blue surface cannot transfer as required within the waveguide or produce stray light as discussed in more detail below.

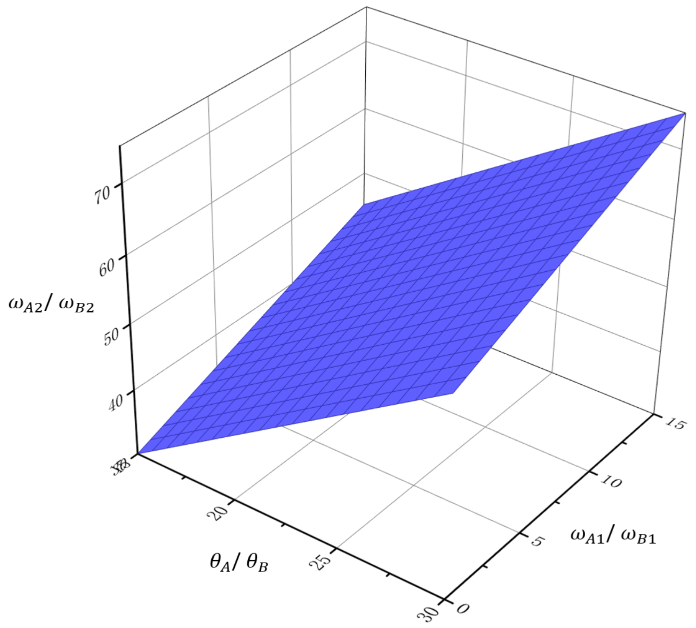

Figure 4. 21 Relationship between entrance angle, critical angle and reflection angle in the waveguide

Thus, the angles between the couplers and the edge of the waveguide should satisfy

$$\theta_A > \frac{\theta_{CA} - \omega_{A1}}{2} \tag{4.5}$$

$$\theta_B > \frac{\theta_{CB} - \omega_{B1}}{2} \tag{4.6}$$

The angles of the maximum field (half FOV) along the z-axis can be derived as

$$\Omega_{\mathrm{maxA}} = \tan^{-1}\left(\frac{\frac{d_A \times M}{\tan\theta_A} - \mathrm{EPD}}{2\mathrm{ERF}}\right) \tag{4.7}$$

$$\Omega_{\mathrm{maxB}} = \tan^{-1}\left(\frac{\frac{d_A \times N}{\tan\theta_B} - \mathrm{EPD}}{2\left(\mathrm{ERF} + d_A + d_g\right)}\right) \tag{4.8}$$

where M is the number of out-couplers in waveguide A and N is the number of out-couplers in waveguide B.

4.3.2 Stray light analysis and elimination

Considering the above angle restrictions, the entrance angle along the z-axis inside the waveguide is derived and restricted by

$$\theta_{CA} - 2\theta_A < \omega_{A1} < \theta_A \tag{4.9}$$

$$\theta_{CB} - 2\theta_B < \omega_{B1} < \theta_B \tag{4.10}$$

$$\omega_{A1} < \frac{\pi}{2} - 3\theta_A \tag{4.11}$$

$$\omega_{B1} < \frac{\pi}{2} - 3\theta_B \tag{4.12}$$

Besides, the first hit point at the in-coupler is also restricted as shown in Figure 4.22, which takes waveguide A as an example. If the hit point is not within a certain distance, TIR will not occur. After finding the critical point at the in-coupler, the working distance q at the in-coupler can be derived at

$$q = \frac{2d_A \times \sin\omega_{A1}}{\cos(\omega_{A1} - \theta_A)} \tag{4.13}$$

Hence, the first hit point on the in-coupler should satisfy

$$\frac{d_A}{\sin\theta_A} - \frac{2d_A \times \sin\omega_{A1}}{\cos(\omega_{A1} - \theta_A)} < l < \frac{d_A}{\sin\theta_A} \tag{4.14}$$

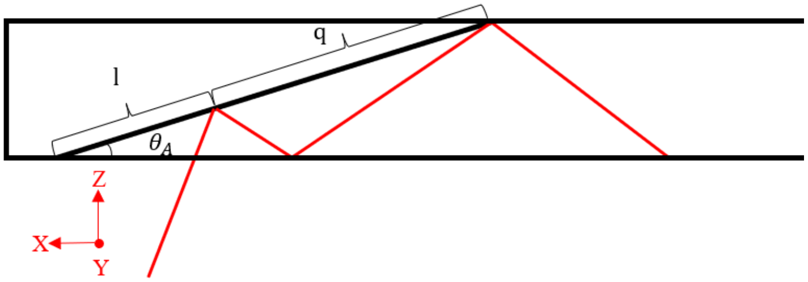

Figure 4. 22 Constraints of the in-coupler

As all rays hit the out-coupler from the direction of the z-axis, part is reflected, and part is transmitted. However, some rays hit the backside of the our-couplers and are reflected as stray light as shown in Figure 4.20. Taking waveguide A as an example, the red line and gray line are the normal light transmitted within the waveguide. When the rays are reflected by the backside of the out-couplers, the stray light is produced as a green line and yellow line. The stray light will produce ghost images. Thus, the exit angle inside the waveguide can be derived as

when $\omega_{A1} > \frac{\pi}{2} - 4\theta_A$,

$$\omega_{\mathrm{out\,green}} = \pi - 6\theta_A - \omega_{A1} \tag{4.15}$$

when $\omega_{A1} \leq \frac{\pi}{2} - 4\theta_A$,

$$\omega_{\mathrm{out\,yellow}} = 2\theta_A + \omega_{A1} \tag{4.16}$$

The angle of yellow stray light is much larger than the angle of the maximum field along the z-axis, so it has no influence on ghost images, which can be ignored. Based on Equation (4. 9)-(4.16), the relationship between the exit angle of the green light and the basic angles of light within the waveguide is shown in Figure 4.23. For rays on the blue surface, light can realize TIR without stray light being produced. When rays fall out of the blue surface, TIR may not be achieved, causing stray light.

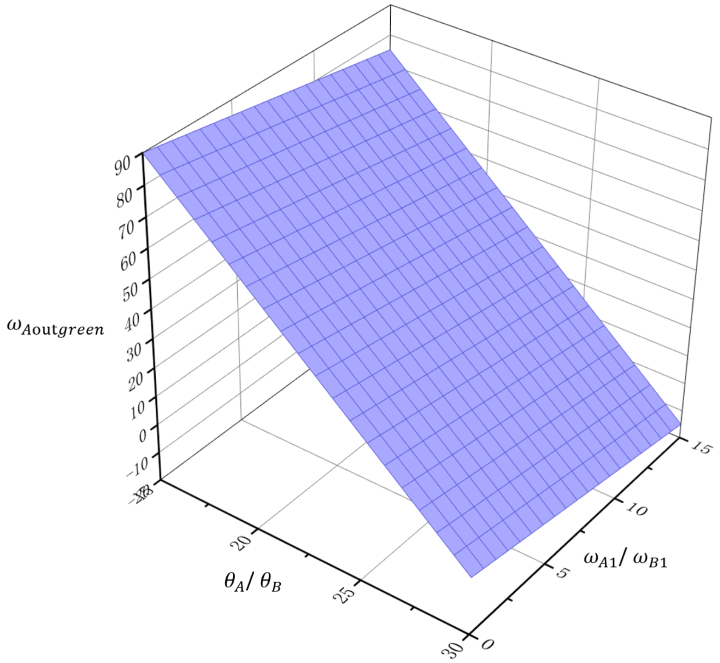

Figure 4. 23 The relationship between the exit angle and the angles of light within the waveguide.

To eliminate the stray light indicated by the green line, the following equation must be satisfied

$$\frac{d_A}{\tan\theta_A} + \mathrm{ERF}\tan[\sin^{-1}(n_A \times \omega_{\mathrm{out}})] \geq \mathrm{EPD} \tag{4.17}$$

$$\omega_{A1} \leq 6\theta_A - \frac{1}{n_A}\sin\left(\tan^{-1}\frac{\mathrm{EPD} - \frac{d_A}{\tan\theta_A}}{\mathrm{ERF}}\right) - \pi \tag{4.18}$$

Similarly, the stray light in waveguide B should satisfy

$$\frac{\mathrm{ERF}+\mathrm{d_g}+\mathrm{d_A}}{\tan\theta_\mathrm{B}}+\mathrm{ERF}\tan[\sin^{-1}(\mathrm{n_B}\times\omega_\mathrm{out})]\geq\mathrm{EPD} \tag{4.19}$$

$$\omega_\mathrm{B1}\leq 6\theta_\mathrm{B}-\frac{1}{\mathrm{n_B}}\sin\left(\tan^{-1}\frac{\mathrm{EPD}-\frac{\mathrm{d_A}}{\tan\theta_\mathrm{A}}}{\mathrm{ERF}+\mathrm{d_g}+\mathrm{d_A}}\right)-\pi \tag{4.20}$$

Crosstalk stray light is from waveguide B to waveguide A and is reflected by the backside of the out-couplers in waveguide A as shown in Figure 4.24. The exit angle of normal light from the waveguide B is the same as the entrance angle ω_B1. The influence of the fixed-focal lens on changing the angle of the light is negligible as the distance $\mathrm{d_g}$ is too short to cause a perceptible variation in the light path from waveguide B to waveguide A. The exit angle of the crosstalk stray light can be derived as

$$\omega_\mathrm{out}=4\theta_\mathrm{A}+\omega_\mathrm{BA}-\frac{\pi}{2} \tag{4.21}$$

$$\omega_\mathrm{BA}=\sin^{-1}\left(\frac{\mathrm{n_B}\times\sin\omega_\mathrm{B1}}{\mathrm{n_A}}\right) \tag{4.22}$$

where ω_BA is the entrance angle concerning the z-axis within the waveguide A, and it must satisfy

$$\frac{\mathrm{d_A}}{\tan\theta_\mathrm{A}}+\mathrm{ERF}\tan[\sin^{-1}(\mathrm{n_A}\times\omega_\mathrm{out})]\geq\mathrm{EPD} \tag{4.23}$$

$$\frac{1}{\mathrm{n_A}}\sin\left[\tan^{-1}\left(\frac{\mathrm{EPD}-\frac{\mathrm{d_A}}{\tan\theta_\mathrm{A}}}{\mathrm{ERF}}\right)\right]\leq\omega_\mathrm{BA}\leq\frac{\pi}{2}-2\theta_\mathrm{A}-\sin^{-1}\frac{1}{\mathrm{n_A}} \tag{4.24}$$

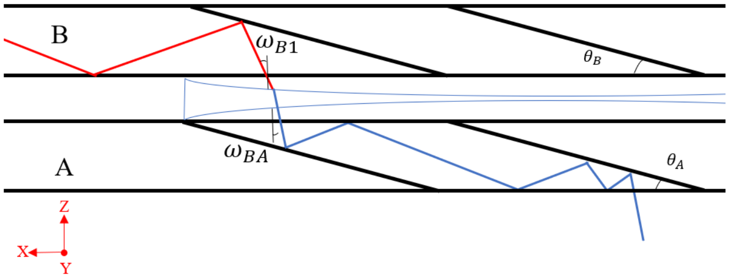

Figure 4. 24 Crosstalk of waveguide A and waveguide B

4.3.3 Numerical analysis, optimization, and verification

Glass is usually used for the waveguide substrate, which has a higher refractive index compared with resin, good coating resistance, and can withstand various semiconductor etching processes. The high refractive index means that the total internal reflection angle is smaller. A smaller TIR angle can give more flexibility to accommodate a wider range of light transmission angles, which means that the FOV will also be larger. As discussed above, parameter selection is a total trade-off process. The dual-layer waveguide design is built and simulated by non-sequential ray tracing. The parameters of the model are shown in Table 4.2. The gap d_g between waveguide A and waveguide B is set at 0.8 mm, and the thickness of each waveguide is 2.000 ± 0.005mm; thus, the total thickness of the dual-layer waveguide is around 5.6 mm. The eye relief is set at 20 mm and the eye box is 38.46 mm in the horizontal direction. The FOV along the X-axis is 35°. The material of glue should have good stability and high transparency, which affects the light efficiency of the system. The refractive index of the glue should be the same as the refractive index of the substrate material at 1.68 ± 0.02 based on the tolerance analysis. Besides, the tolerance of the thickness and parallelism of the two sides of waveguide and the out-couplers have already been analysed based on the 60″human eyes resolution in Chapter 3.3[156, 244].

Table 4. 2 Parameters of the dual-layer waveguide.

	$n_A \& n_B$	$\theta_A \& \theta_B$	N & M	$d_A \& d_B$(mm)	Eye box (mm)	ERF (mm)	FOV
Waveguide A	> 1.66	20°	7	2	38.46	20	35°
Waveguide B	> 1.66	20°	7	2	38.46	22.8	35°
Combined				4.8	38.46	20	35°

Based on the geometrical parameters in Table 4.2, the illumination distribution from the dual-layer waveguide can be simulated using LightTools. Illumination describes the measurement of the amount of light falling onto (illuminating) and spreading over the receiver (human eyes). Illumination also correlates with how humans perceive the brightness of an illuminated area. The density contrast can be calculated by

$$E = \frac{I_{max} - I_{min}}{I_{max} + I_{min}} \tag{4.25}$$

where I_{max} and I_{min} are the maximum and minimum illumination at the receiver fields. Waveguide A and waveguide B have the same numbers of out-couplers. The reflectance of the coatings on the out-couplers follows

$$R_i = (1 - R_i) \times R_{i+1} \tag{4.26}$$

where i is the serial number of the out-couplers and i+1 is the number of coating reflectance on next out-coupler.

A volume cuboid light source was set to 1-watt radiometric power. The angular surface distribution and volumetric distribution are set to be uniform and collimated. However, stray light reduce the illumination of the virtual image' uniformity as mentioned above. As these stray light are all located outside of the exit pupil area, it reduces the energy density from the desire lights. As the result, the illumination is severely influenced and becomes nonuniform. The illumination distribution is in Figure 4.25.

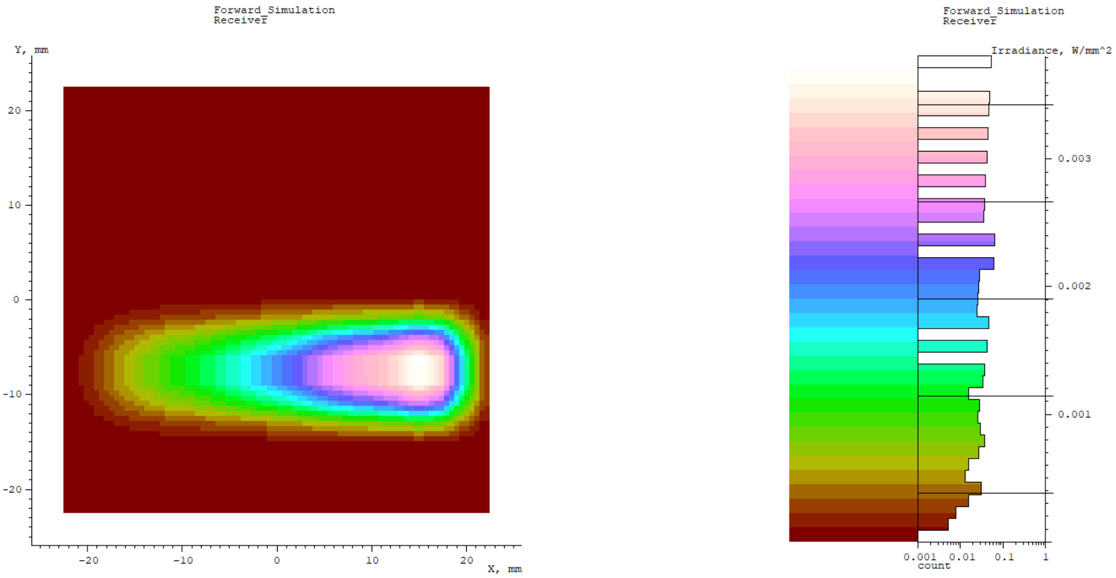

Figure 4. 25 Illumination distribution simulation with no optimization.

To ensure the uniform illumination at eye position, the reflectance of the coatings on each out-couple needs to be carefully calculated and set with acceptable tolerance during manufacturing. The illumination variance of the model is proposed as

$$\sigma_{illumination} = \sqrt{\frac{\sum_i (E_i - E_{ave})^2}{i}} \tag{4.27}$$

Where i is the number of illumination chart, $\mathrm{E_i}$ is the illumination at $\mathrm{x_i} * \mathrm{y_i}$ field as shown in Figure 4.26. $\mathrm{E_{ave}}$ is the average illumination at eye position. Illumination variance can reflect the degree of dispersion of the illumination. The absolute average illumination of the simulation data can be proposed as

$$\mathrm{E}_{\overline{\mathrm{ave}}} = \frac{\sum_{\mathrm{i}}(\mathrm{E_i} \times \mathrm{x_i y_i})}{\sum_{\mathrm{i}} \mathrm{x_i y_i}} \tag{4.28}$$

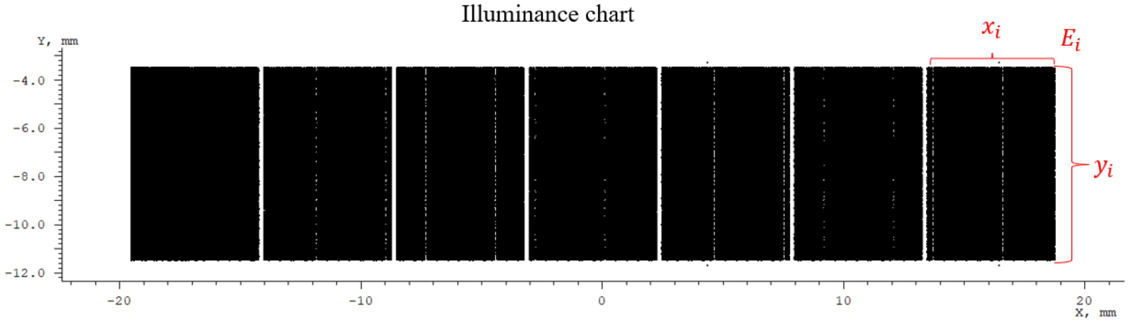

Figure 4. 26 Illumination chart of one layer waveguide.

Absolute average illumination is the average illumination relating to each exit pupil. Thus, the correction ratio of the reflectance is proposed as

$$\nabla_{\mathrm{reflectence}} = \frac{\mathrm{E}_{\overline{\mathrm{ave}}}}{\mathrm{E_{ave}}} \times \mathrm{R_i} \tag{4.29}$$

By the merit function optimization of the LightTools, the ratio of the reflectance on each out-coupler is optimized for the uniform exit pupil and the optimized illumination is shown as the raster chart of the illumination display in Figure 4.27 and the colors represent the irradiance at the exit pupil.

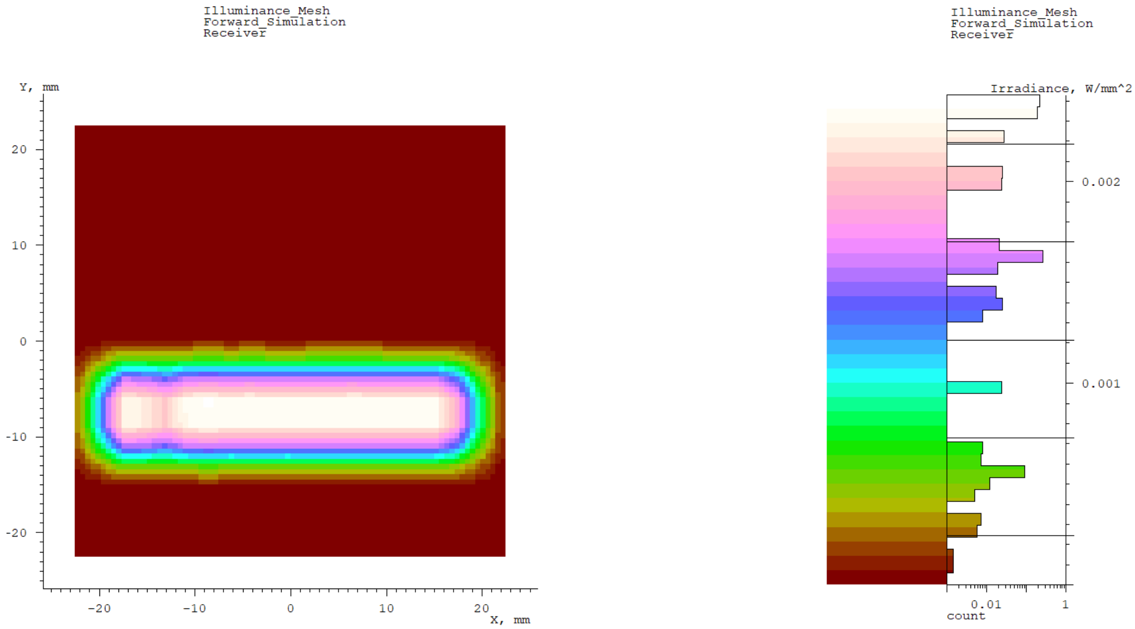

Figure 4. 27 Optimized illumination simulation distribution

The coating on each out-coupler should have a specific ratio of transmittance and reflectance to present uniform illumination of the virtual information from the projector. The R/T ratios of each out-coupler for both waveguides are shown in Table 4.3 which designs 7 out-couplers. The two waveguides are all optimized as above. The light path of the combined system works as shown in Figure 4.28. The pupil diameter of the human eye is generally 2-5 mm. The combined system enlarges the eye box to 38.46 mm, which enables the observation of the virtual images in a larger spatial area. The receiver is set at a 20 mm exit position to simulate the human eyes' distance. The light tracing of illumination distribution throughout the entire FOV is shown in Figure 4.29. The level line represents the illumination energy, and the energy is very uniform in the pupil area. The illumination uniformity can be calculated as

$$U_0 = {}^{E_{min}}\!/_{E_{ave}} \tag{4.30}$$

where E_{min} is the minimum illumination value, which is calculated based on the point-by-point calculation. The more uniform the light distribution, the better the illumination and the more comfortable the visual experience. The closer the uniformity of illumination approaches 1, the better imaging quality can be obtained. According to lighting standard GB 50034-2004, the lighting of indoor work areas should achieve an illumination uniformity of 0.7 or higher on the work surface [245, 246]. The illumination uniformity of this combined model is around 0.83.

Table 4. 3 The ratio of transmittance and reflectance of out-couplers

	1st	2nd	3rd	4th	5th	6th	7th
Transmission	89.0	87.5	85.7	83.3	80.0	75.0	67.0
Reflection	11.0	12.5	14.3	16.7	20.0	25.0	33.0

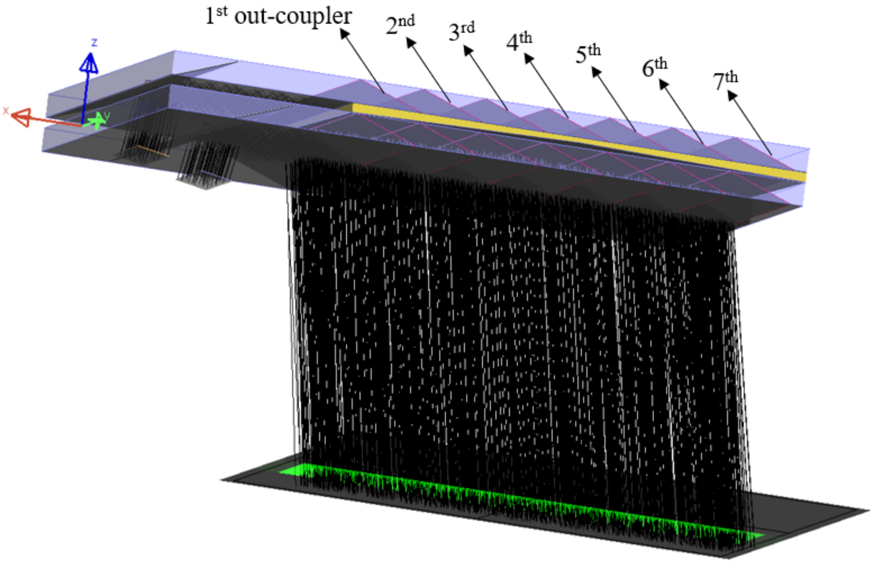

Figure 4. 28 Schematic model of the dual-layer geometrical waveguide.

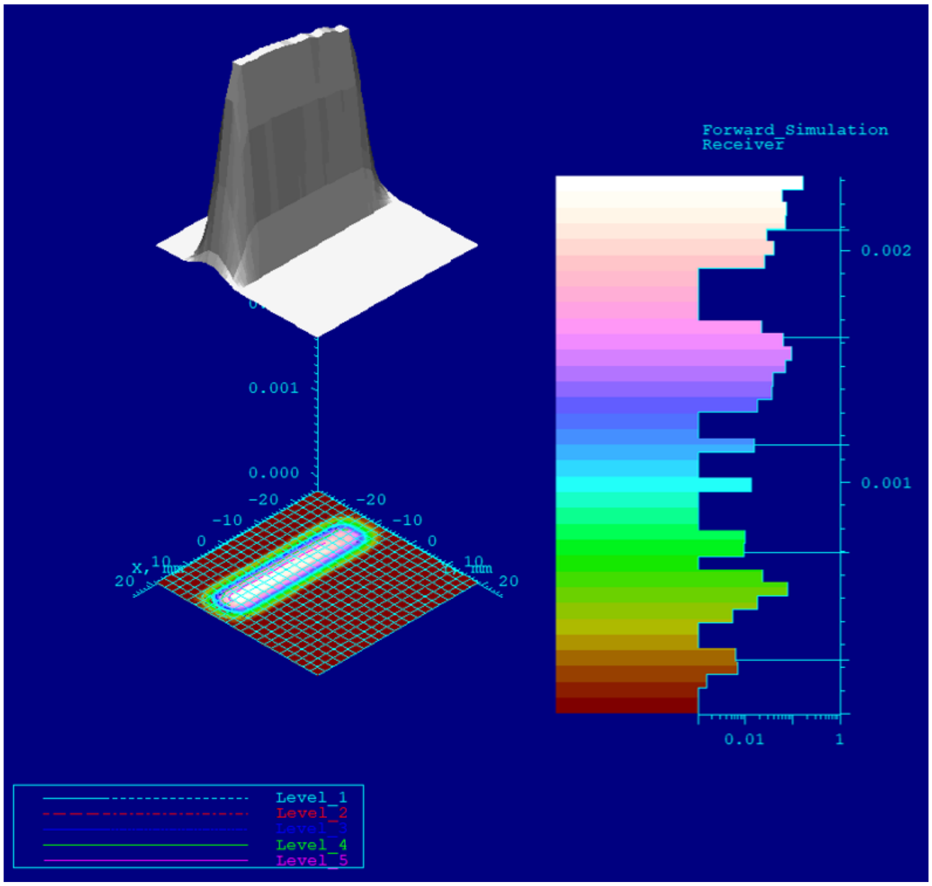

Figure 4. 29 Illumination distribution in the entire FOV.

To quantitatively analyse the intensity uniformity over the dual-layer system, the system automatically sampled 19 test points of the intensity distribution uniformity across the angle of the exit pupil, as shown in Figure 4.30. Test points are set automatically according to the illumination values and uniformity. The simulation result is shown in Figure 4.31. From the simulation, the total photometric flux is 0.11 W. Except for the discrepancy at the marginal field, the angular uniformity of the intensity across the exit pupil is more than 70%. The illumination uniformity can also be improved as below.

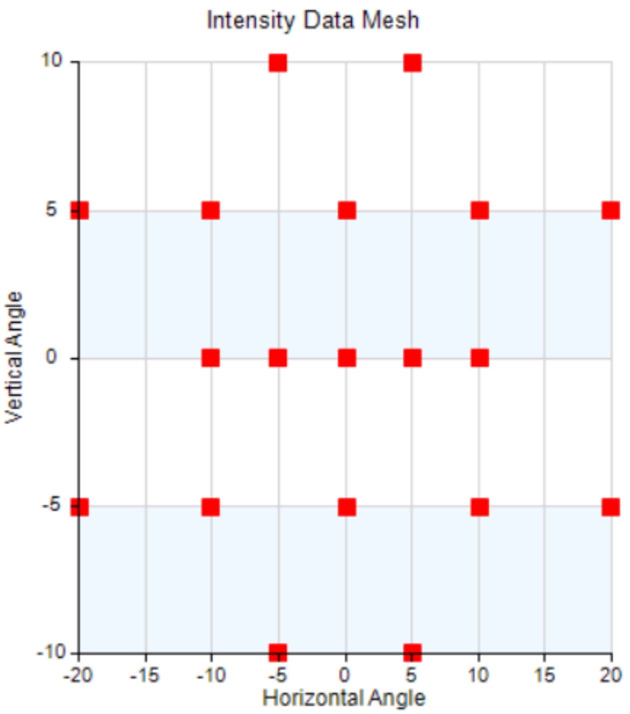

Figure 4. 30 Test points of the intensity field.

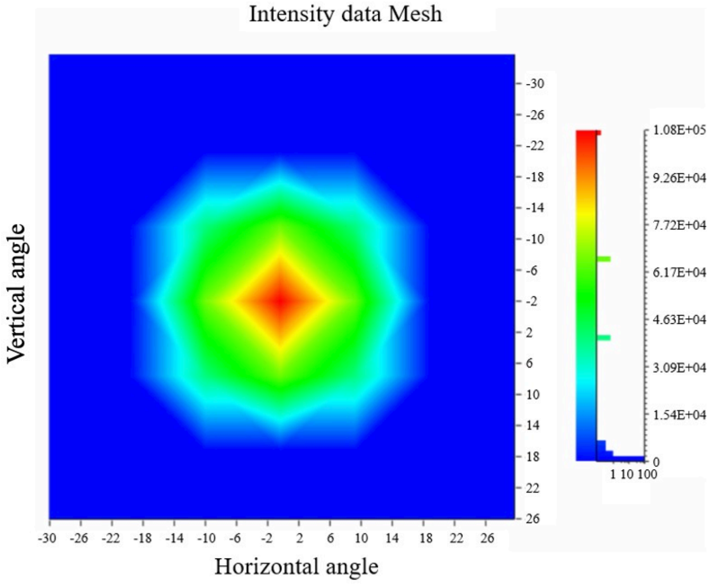

Figure 4. 31 Intensity uniformity across the exit pupil.

The light from waveguide A and waveguide B have the same flux. But the exit angles of light from waveguide A and waveguide B are different, so they have different irradiance. Based on the equation of irradiance

$$\mathrm{E} = \frac{\mathrm{d}\Phi}{\mathrm{dS}} \tag{4.31}$$

where Φ is the total flux from the waveguide and S is the area of the illuminating surface. There is a divergence angle of the light passing through the fixed-focal lens from waveguide B; thus, the illuminating surface on the receiver from waveguide A and waveguide B are different.

$$\frac{\mathrm{E_A}}{\mathrm{E_B}} = \frac{\mathrm{dS_B}}{\mathrm{dS_A}} \tag{4.32}$$

The surface area can also be described as

$$\frac{\mathrm{S_B}}{\mathrm{S_A}} = \frac{\pi \mathrm{r_B}^2}{\pi \mathrm{r_A}^2} \tag{4.33}$$

where $\mathrm{r_B}$ is the equivalent radius of the surface at the receiver from waveguide B and where $\mathrm{r_A}$ is the approximate radius of the surface at the receiver from waveguide A. The distance from the waveguide to the receiver is ERF. The light from waveguide B passes through the fixed-focal lens and divergence a little and the reverse extension line of the exit light converges at the focal point F. The divergence angle is α. $\mathrm{r_1}$ is the radius of the lens and $\mathrm{r_2}$ is the radius of the illuminating surface, as shown in Figure 4.32. It can be derived as the following

$$\frac{\mathrm{r_2}}{\mathrm{r_1}} = \frac{\mathrm{ERF + f}}{\mathrm{f}} \approx \frac{\mathrm{r_B}}{\mathrm{r_A}} \tag{4.34}$$

$$\tan \alpha = \frac{\mathrm{r_1}}{\mathrm{f}} \tag{4.35}$$

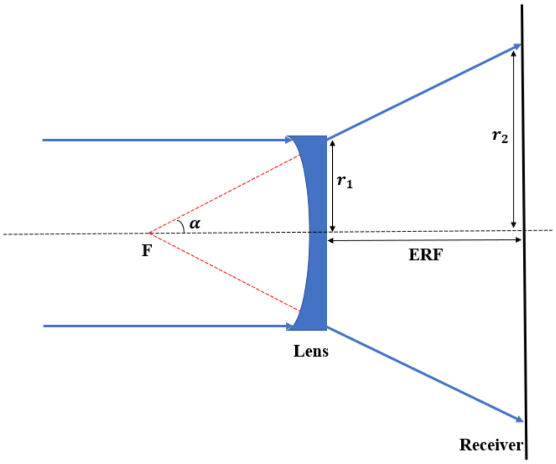

Figure 4. 32 Irradiance from the light source at a point to a surface.

The light from waveguide A and waveguide B has nearly the same distance to exit pupil and the same angle α (the thickness of waveguide A in the ERF of waveguide B can be negligible), so the relationship between irradiance ratio can be derived as

$$\frac{E_A}{E_B} = \frac{d\left[\frac{(\mathrm{ERF} + f) * r_1}{f}\right]^2}{d{r_1}^2} \tag{4.36}$$

The irradiance from waveguide A and waveguide B are simulated as shown in Figure 4.33. the average intensity from the simulation can be obtained. The fixed-focal lens is 40 mm in height and 40mm in width with 100 mm focal length. Based on the numerical aperture of the lens, the dispersion angle can be calculated as 11.31° on a single side. The exit angle of light from waveguide B at 22.62° is larger than it from waveguide A (0°). The average irradiance from the simulation in Figure 4.33 satisfies the Eq. (4.36) within the limit of error.

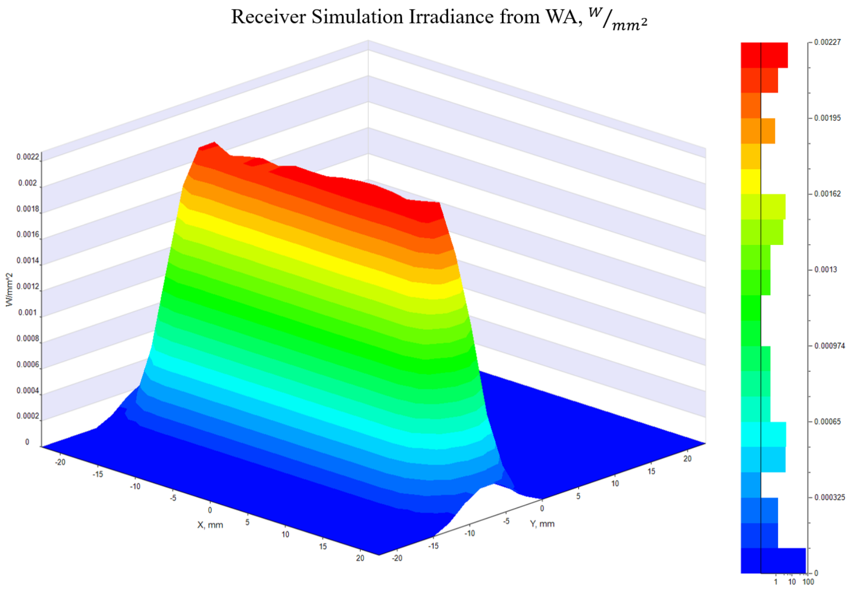
Receiver Simulation Irradiance from WA, $^{W}/_{mm^2}$

(a) LumViewer irradiance from waveguide A at the exit pupil

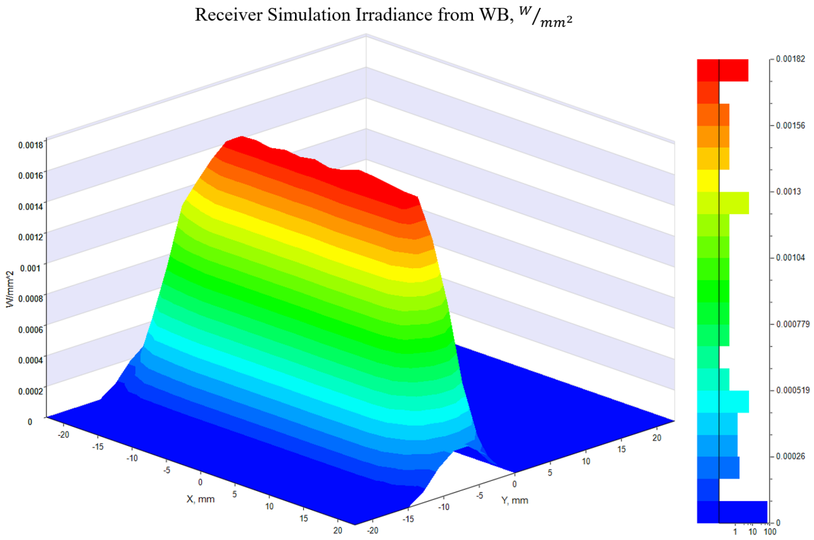

(b) LumViewer irradiance from waveguide B at the exit pupil

Figure 4. 33 LumViewer irradiance from each waveguide at the exit pupil.

The FOV of the system is around 35°. After suppressing the stray light using methods in Chapter 3. Figure 4.34 shows the light tracing results of the system at 0°, ±10° and ±17°. There are obvious stray light in the field of -17°, -10° and 10°. Stray light outside of the exit pupil can be ignored. Under the threshold value $0.001\mathrm{W/mm}^2$ on LightTools, the energy of the largest stray light at 10° is less than 1.5% of the exit pupil energy.

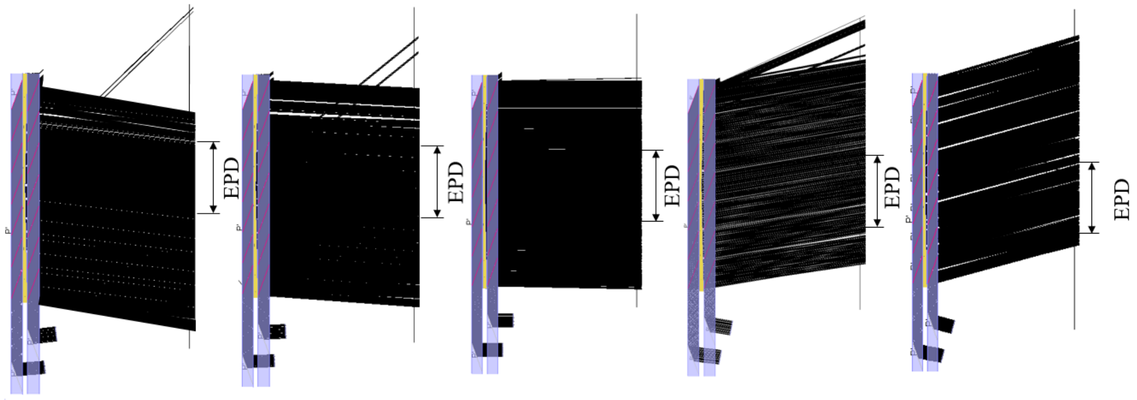

(a) (b) (c) (d) (e)

Figure 4. 34 Light path tracing result in the field of (a) -17°, (b) -10°, (c) 0°, (d) 10°, (e) 17°. EPD is 11.5mm.

4.3.4 Varifocal design

Based on the above dual-focal display design, a concept design of a varifocal display is proposed as shown in Figure 4.35. Waveguide A can project the light at infinity and the light from waveguide B can be displayed at different depths controlled by the varifocal liquid lens. The lens between the two waveguides is a liquid lens, which can achieve changeable curvature, as shown in Figure 4.36. The liquid lens is controlled by the computer to shift through a wide range of focal lengths of the virtual images. Liquid lenses are mechanically or electrically controlled cells containing optical-grade liquid. When a current or voltage is applied to a liquid lens cell, the shape of the cell changes. This change occurs within milliseconds and causes the optical power, and therefore focal length and working distance, to shift. Besides, the size of the liquid lens should match the length of the exit pupil. At present, the diopter of the lens released by Lemnis can achieve 4.5 D, which can shift the focus display from 22 cm to infinity. The liquid lens is mainly applied in VR glasses now. Hopefully, this technology can be applied soon when the response time, size and complexity of integration are improved.

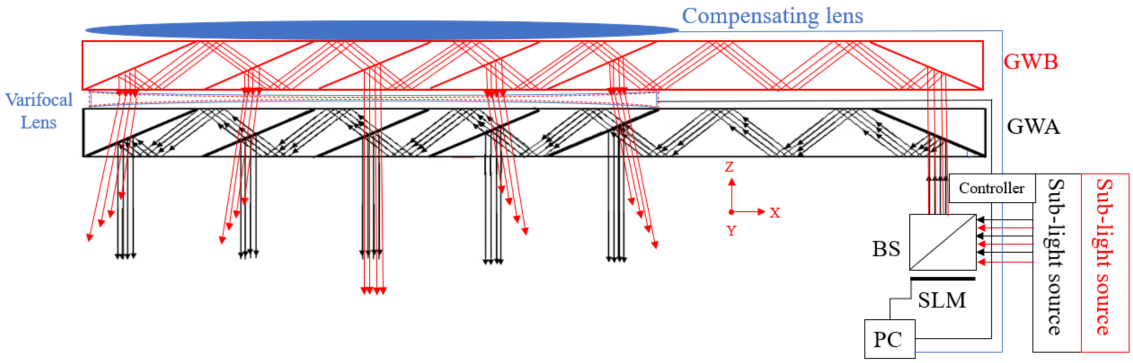

Figure 4. 35 The concept design of varifocal geometrical waveguide display.


0D
1.5D
3D

Figure 4. 36 Liquid lens by Lemnis Technologies [247].

The curvatures of the middle lens can be changed to simulate the continuous depth change of the liquid lens. Following the above stray light elimination strategy, the optimized model is designed and simulated. The simulation result is shown in Figure 4.37. Three typical depths of the virtual images are simulated to represent the focal varying process. Figure 4.37(a) shows the virtual images at 50 mm depth, (b) indicates 200 mm depth and (c) illustrates the 300 mm depth of the virtual images. When the curvature of the middle lens changes, the irradiance received from the exit pupil area also changes accordingly. The irradiance at the exit pupil in Figure 4.37 follows Eq. (4.36). Thus, it can be concluded that the virtual images plane can be shifted by changing the curvature of the middle liquid lens. From the simulation, the combination of varifocal lens and geometrical waveguide realizes focal depth plane change with a thin form factor. The curvature of the compensating lens should also be opposite of the liquid lens's curvature to counteract the aberration, so the real-world information will not change significantly.

Such a varifocal design is potentially more favourable for solving the VAC problem. However, the conflict between motion perception and visual perception could also generate dizziness and vertigo. Any delay in the reaction of the liquid lens which is longer than the resolution of human eyes would result in conflict. The response time of the lens must be as short as possible. Besides, the drift of the optical axis position and the curvature of the lens must be sufficiently precise to meet the continuous depth change.

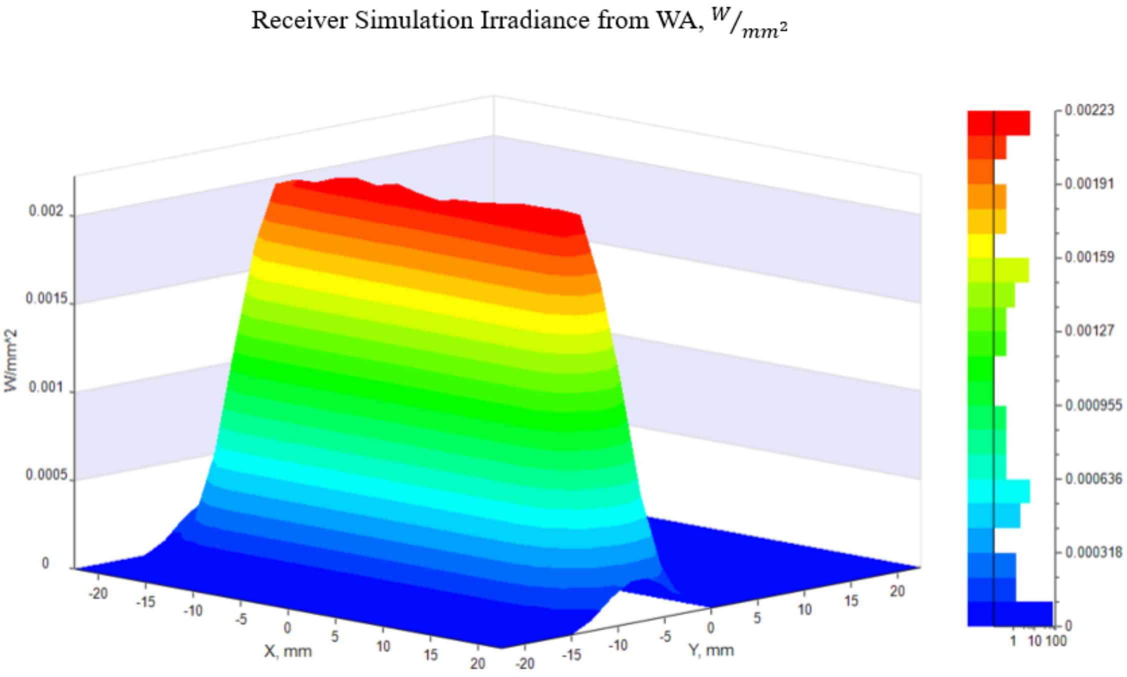

(a) LumViewer irradiance from combined waveguide at 50mm depth

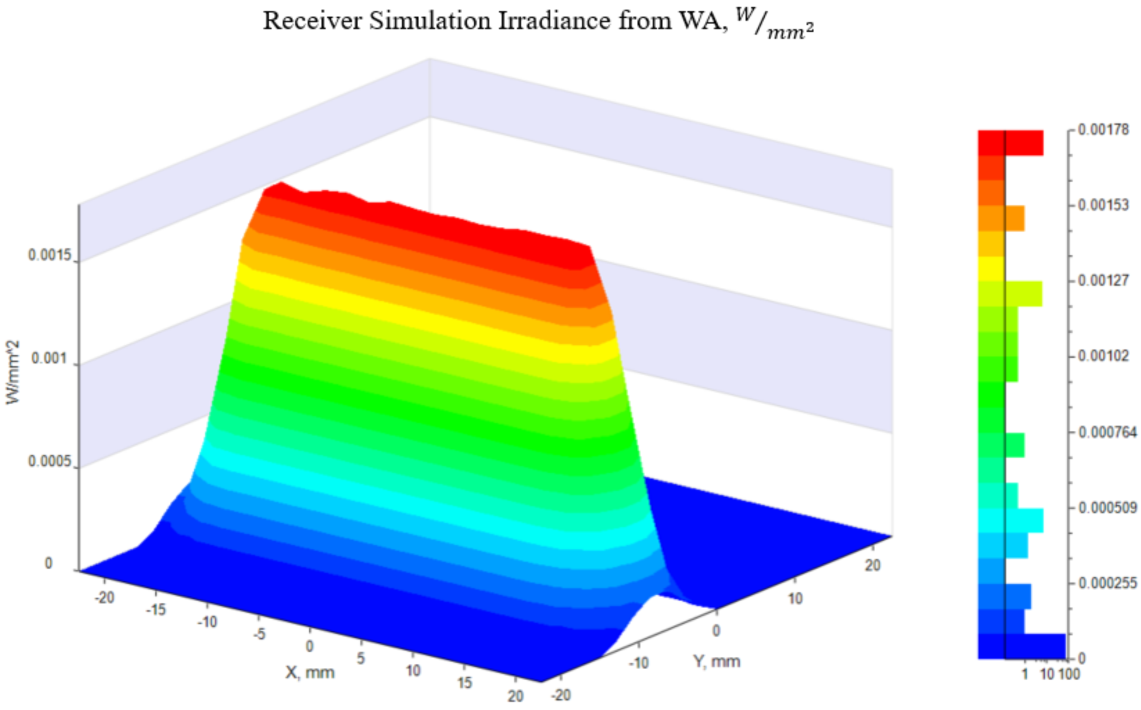

(b) LumViewer irradiance from combined waveguide at 200mm depth

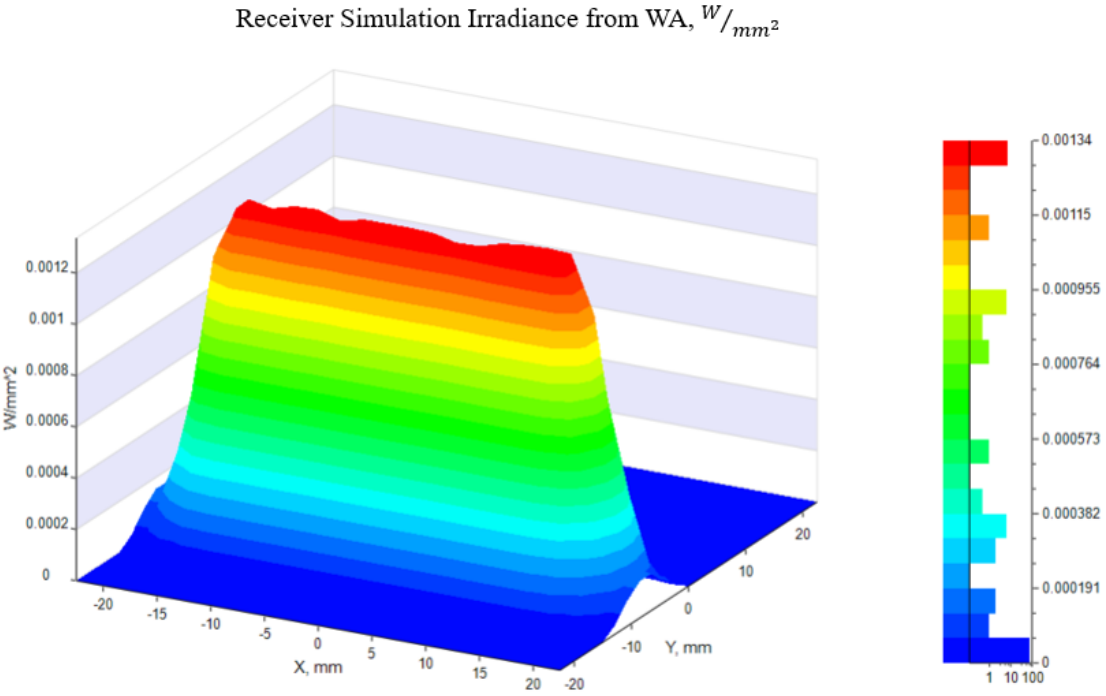

(c) LumViewer irradiance from combined waveguide at 300mm depth

Figure 4. 37 LumViewer irradiance with different curvatures of the middle lens from combined waveguide at the exit pupil.

4.4 Design of varifocal and multifocal systems for AR

4.4.1 Varifocal design

There are two ways to change the depth of virtual information, one is changing the curvature of the liquid lens, and the other is changing the curvature of the spherical mirror. Light information is projected and then reflected by the mirror to the liquid lens working as the convex lens and generates the intermediate images. Afterwards, light passes through the BS and transfers to the spherical mirror. The spherical mirror relays the intermediate image and redirects the light to the eyes of the observer by the BS. When the focal length of the liquid lens is changed, the divergence angle of the light is changed, thus the accommodation distance of virtual images would be changed as shown in 4.38(a). When the spherical mirror with different focal length is changed, the virtual images would be displayed at different depths. When the focal length of the spherical mirror increases (from solid to dashed lines as shown in 4.38(b)), the virtual images would be displayed from near to far distance to change the depths.

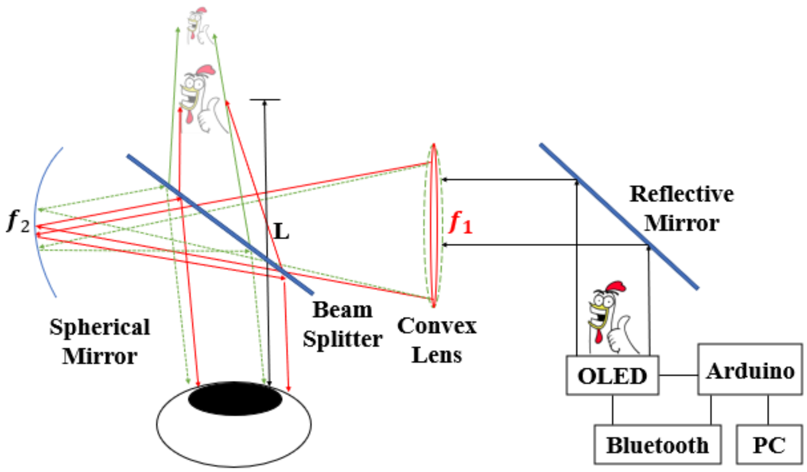

(a) Accommodation distance changed with focal length of liquid lens

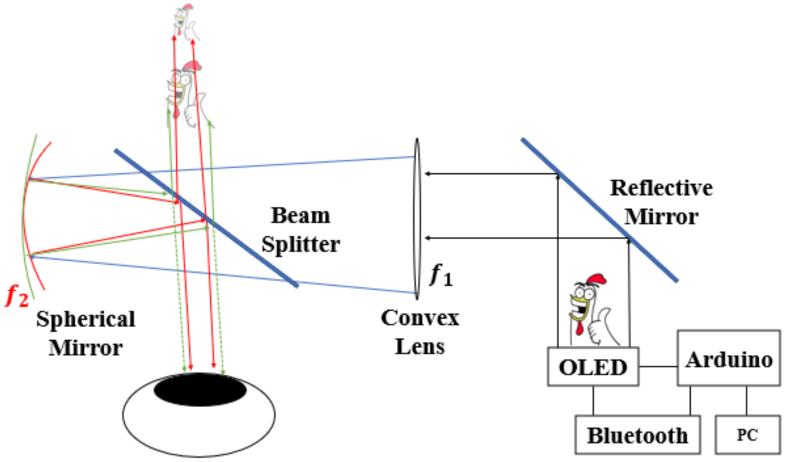

(b) Accommodation distance changed with focal length of spherical mirror

Figure 4. 38 Sketch of the varifocal model.

The system is simulated using LightTools as shown in Figure 4.39. The spherical mirror is a 50.8mm aperture with a focal length of 75 mm, which can reflect all information from previous elements. As shown in Figure 4.40, it presents the accommodation distance as a function of the radius of curvature of the liquid lens. According to Figure 4.40, the virtual images can be displayed to infinity. The curvature of the liquid lens limits the shortest accommodation distance of the virtual distance.

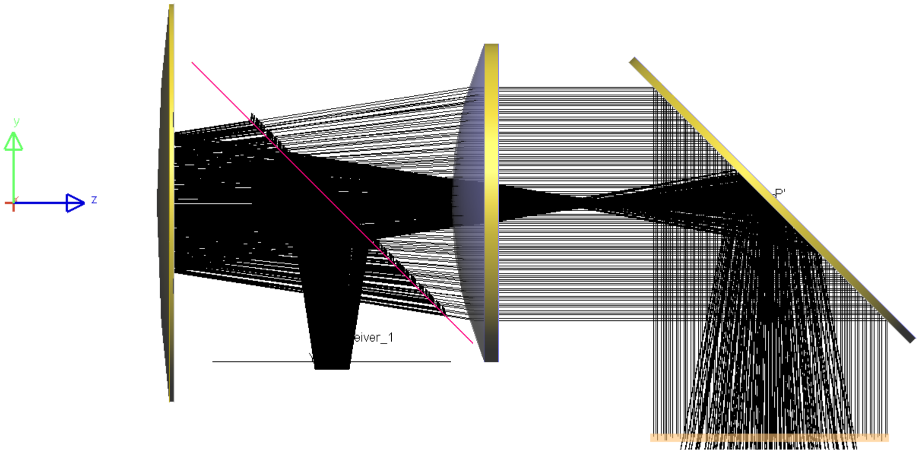

Figure 4. 39 Simulation of the designed system to change the focal depths.

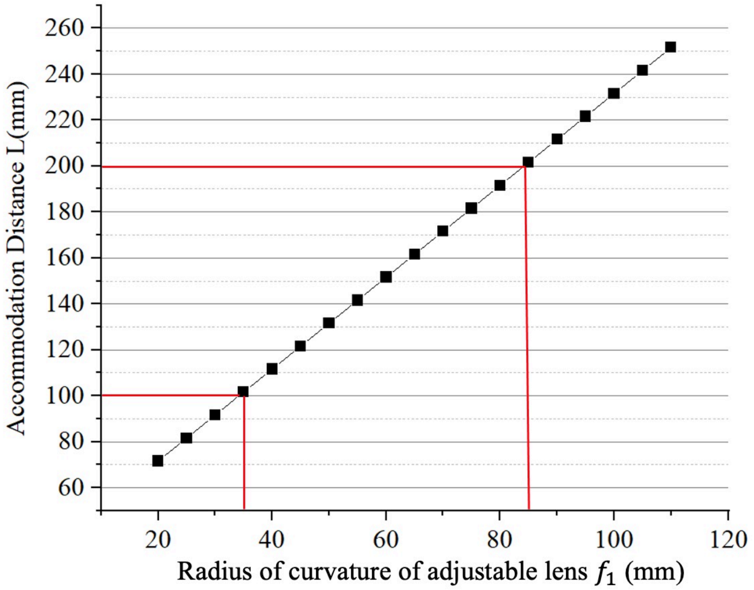

Figure 4. 40 Accommodation distance is constrained by the radius of curvature of liquid lens.

From the simulation analysis, the illuminance results are obtained when the virtual images are projected at different depths, as shown in Figure 4.41. Figure 4.41 (a) is the irradiance received at the human eyes when the virtual image is projected at 100cm and (b) is the irradiance received when the virtual image is 200 cm in depth. The illuminance intensity on a surface is inversely proportional to the square of its distance from the light source and can be expressed as [248]:

$$\mathrm{E} = \frac{\Phi}{\mathrm{d}^2} \tag{4.37}$$

where E is illuminance intensity, unit is lux (lumen/m^2); Φ is the quantity of light emitted by a light source, unit is luminous flux (lumen) and d is the distance from the light source (m). If there is an angle θ between the normal to the plane at the illuminated point and the line connecting the source to the illuminated point as shown in Figure 4.42 The illuminance density can be derived as [249]:

$$\mathrm{E} = \frac{\mathrm{I}_\theta}{\mathrm{d}^2} * \cos\theta \tag{4.38}$$

where I_θ is the luminous intensity of the source in the direction of the illuminated point. When the virtual image is projected at 100m or 200m, the angle θ is the same value. Thus, the relationship between the irradiance ratio and the distance can be derived as

$$\frac{\mathrm{E}_{100\mathrm{cm}}}{\mathrm{E}_{200\mathrm{cm}}} = \frac{\mathrm{d}_{100\mathrm{cm}}}{\mathrm{d}_{200\mathrm{cm}}} \tag{4.39}$$

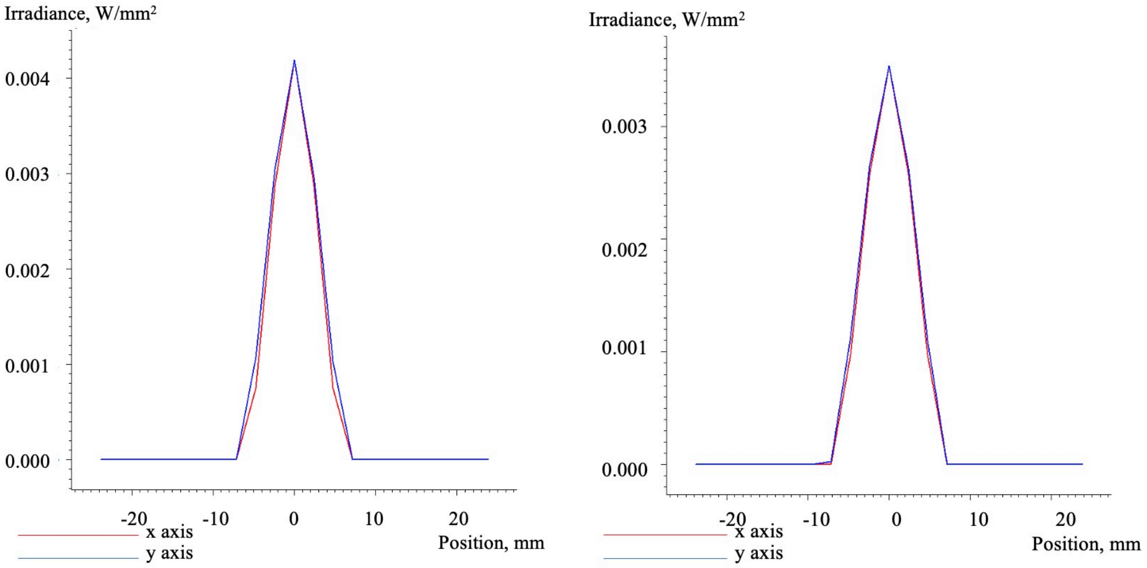

(a) Illuminance when virtual images at 100 cm (b) Illuminance when virtual images at 200 cm

Figure 4. 41 Illuminance results when the virtual images are projected at 100 cm and 200 cm.

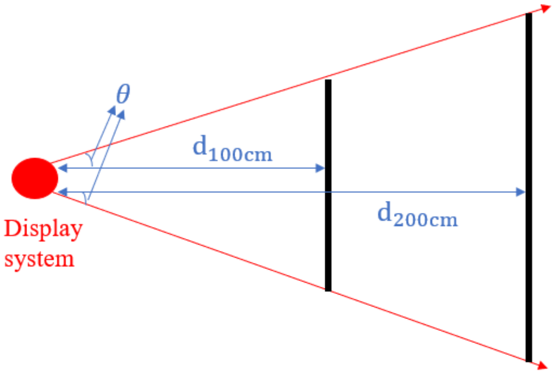

Figure 4. 42 Irradiance from the light source to a surface.

The simulation results of the illuminance and the focal power meet Eq. (4.39). Thus, the virtual accommodation cue can be shifted by changing the focal power of the liquid lens.

4.4.2 Multifocal design

To add one more depth of virtual images, one additional projector is needed. Each has an independent optical path, which may be changeable at object distance or focal length of lens f_1 or spherical mirror f_2, as shown in Figure 4.43. When changing the focal length of the lens f_1, the accommodation distance of virtual images would be changed. When changing the spherical mirror with different focal length, the virtual images would be displayed at different depths. When the focal length increases, the virtual images would be displayed from near to far distance. The projector system consists of two color-OLED displays. There are two ways to project two independent depths as illustrated in Figure 4.43(a) and (b). The virtual images in Figure 4.43 (a) share one lens f_1 by a BS. When the focal length of f_1 is changed, the depths of virtual images from the OLED 1 and OLED 2 are all changed accordingly. And the virtual images in Figure 4.43 (b) have their own lens to change independent depths. The focal lengths of these two lenses of f_1 and f_3 are independent. The depths of each virtual information from OLED 1 or OLED 2 can be changed by changing the corresponding focal length of f_1 or f_3. Then they are all reflected by a spherical mirror to generate the intermediate images. Afterward, the spherical mirror relays the intermediate image and redirects the light to the eyes of the observer by the BS.

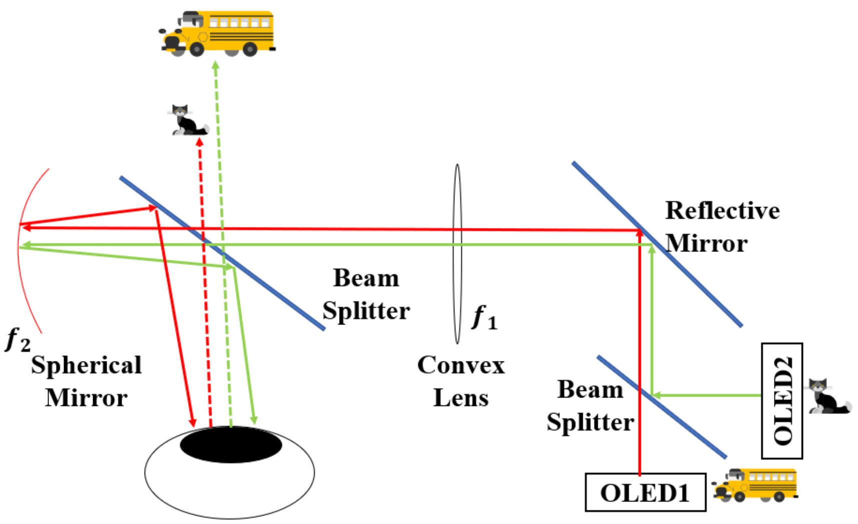

(a) Multifocal display which changes object distance to change the depth of the virtual images

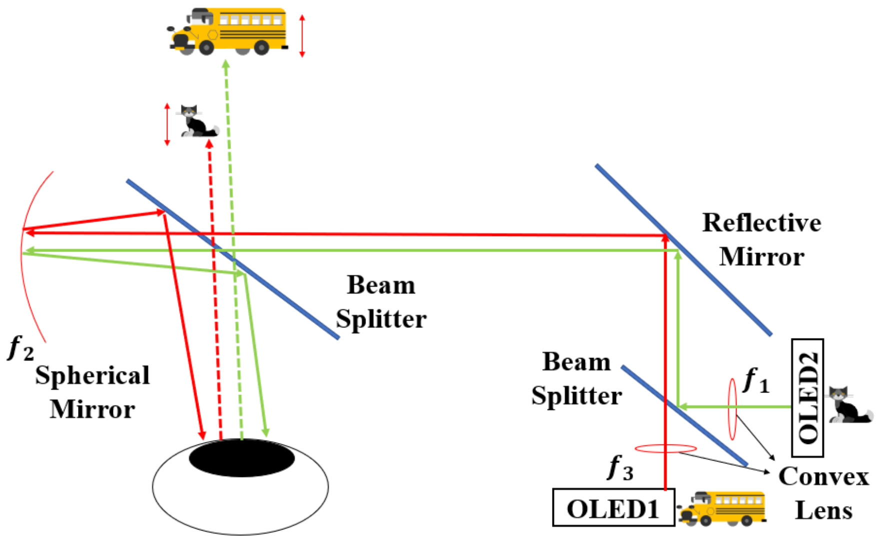

(b) Multifocal display which changes corresponding focal lengths of projectors to change the depth of the virtual images

Figure 4. 43 Multifocal display with different ways to change the depths of virtual images.

4.4.3 System design

The projector system is the light source of the design consisting of a color organic light-emitting diode (OLED) display, an Arduino microcontroller, and a Bluetooth element. An OLED display was chosen due to its small size, thinness, and low power consumption. A Bluetooth module and the OLED display are connected to the microcontroller-Arduino Nano, charged by a battery, as shown in Figure 4.44. Codes and instructions are written into the Arduino nano microcontroller from the PC.

A projector system with a 16-bit color OLED display is connected to the Arduino system and Bluetooth. Any information to be displayed on the OLED can be inputted on PC or smartphone. The screen measures 0.96 inches and has 96 × 64 pixels. This board uses the SSD1331 driver chip, which manages the display and is interfaced using a serial peripheral interface (SPI) (clock, data, chip select, data/command and an optional reset pin). The printed circuit board (PCB) size is 31.5 × 35.5 × 5 mm. To test the chip and projector, the coding in Appendix A is tested.

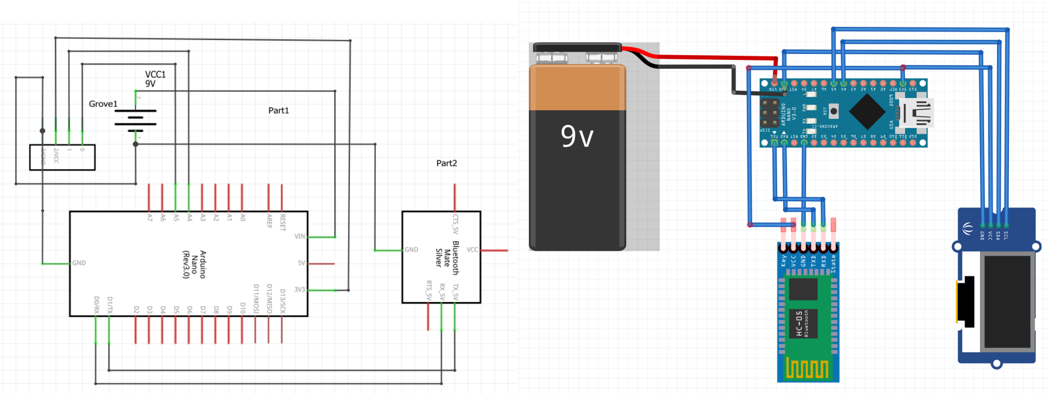

(1) PCB diagram (2) Breadboard diagram

Figure 4. 44 Circuit diagram of the projection system

In the light path, the imaging is divided into two parts. The first is to produce the intermediate image I by the liquid lens which is a varying focal convex lens from the OLED source, and the other is reflected by the spherical mirror which is a concave mirror and produce the virtual image II by the beam splitter (BS), as shown in Figure 4.45. The object distance of the image is p, thus the image distance of the intermediate image q can be derived as:

$$q = \frac{p * f_1}{p - f_1} \tag{4.40}$$

where f_1 is the focal length of the liquid lens. Since the lens is the limiting aperture of the model, the position of the lens is set at the center of the curvature of the spherical mirror. The conjugate exit pupil can be formed by the BS, human eyes should be placed at the conjugate pupil position to observe the virtual images and the real images from the real world clearly. The object distance of the intermediate image is u, the image distance reflected by the spherical mirror can be derived as the following:

$$v = \frac{u * f_2}{u - f_2} \tag{4.41}$$

where f_2 is the focal length of spherical mirror. The relationship between the focal length f_2 and the radius of curvature R of the spherical mirror is:

$$f_2 = \frac{R}{2} \tag{4.42}$$

$$R = q + u \tag{4.43}$$

The distance between the spherical mirror to human eyes in the light path is the same as the curvature of the spherical mirror as R, as shown in 4.39. From the above equations, the image distance can also be derived as:

$$v = \frac{R^2 * p - R^2 * f_1 - R * p * f_1}{R * p - R * f_1 - 2 * p * f_1} \tag{4.44}$$

The accommodation distance L of the virtual image is obtained as:

$$L = v + R = \frac{2 * R^2 * p - 2 * R^2 * f_1 - 3 * R * p * f_1}{R * p - R * f_1 - 2 * p * f_1} \tag{4.45}$$

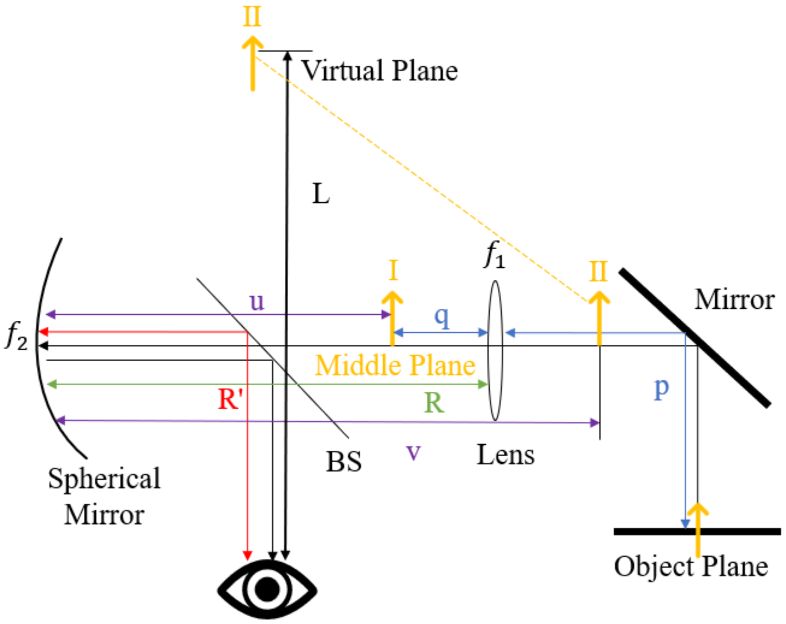

Figure 4. 45 Light path of the optical system.

All the above values are scalars. Except for changing the object distance to change the virtual depth, when the focal length f_1 of the liquid lens or focal length f_2 of the spherical mirror is changed, the accommodation distance would change corresponding. For example, when f_2 is changed to a larger number, the accommodation distance would be larger, which means the virtual images are projected at far depths. In addition, when the object distance p is changed, the accommodation depth would have a great change accordingly, which is hard to move a slight depth. Thus, both the variable focal length of the liquid lens and the radius of curvature of spherical mirror can change the virtual depth. However, there is no changeable curvature spherical mirror device, the liquid lens with a variable focal lens is applied for the experiments. The exit pupil diameter is limited by the size of the BS, which is 25*36mm. The eye relief is set up at 20mm, thus, the diagonal FOV is around 66°. At the exit pupil area, an optical camera is placed as the receiver, which can change the depths of vergence and accommodation.

Based on this design, the varifocal display and multifocal plane can be realized by adding more elements to the projection module.

4.4.4 Experimental verification

In the system, the ratio of reflection and transmission is 50:50. Light is transmitted once and reflected once by the BS, thus there is only 25% light intensity of the original images left. Light contrast may also prevail concerning outdoor contrast requirements which have an impact on brightness and battery life. Here, ambient light can wash out the content and render the image unrecognizable. Under generally accepted guidelines, an Ambient Contrast Ratio (ACR) of 3:1 is required for recognizable images, 5:1 for adequate readability, and 10:1 for appealing quality [250]. The resolution of the eyes is related to the brightness and contrast of the observed object. Because of the chromatic aberration of the eyes and the influence of the spectral components of the illumination light, the resolution under monochromatic light is higher than that with white light. According to actual statistics, the angular resolution of the eye is 60"=1' under good lighting conditions. Therefore, in this optical system, it is necessary to ensure that the output image can reach the resolution of the eye rate. The brightness and resolution of the OLED screen should be high enough.

Based on the system design in Figure 4.38, two same targets at 100 cm and 200 cm away from the camera are set as shown in Figure 4.46. The varifocal design was set up as shown in Figure 4.47. By adjusting the radius of curvature of liquid lens, two different sizes and positions of virtual information are displayed. The accommodation depth was switched according to Figure 4.47. When the virtual information was projected at 100 cm, the camera was focusing on the 100 cm position, the near target and the virtual image were clear, and the far target was blurred. When the virtual information was projected at 200 cm, the camera focused on the 200 cm position, the far target and the virtual image were clear, and the near target was blurred as shown in Figure 4.48. The coding for the projector is shown in Appendix B. The virtual image can be modified to match the physical depth of human eyes. Besides, the virtual image can be adjusted to interact with the real scene to increase the immersive feeling and reduce the VAC problem. However, when the virtual images are presented at near depth, the virtual images would experience a serious distortion. Besides the resolution restriction by the camera, the curvature of the lens would also result in distortion, which is discussed in the next section. The details of the information in the virtual images are provided as shown in Figure 4.49. The area scan camera can capture the virtual images clearly, which has a 2048px*1088px resolution.

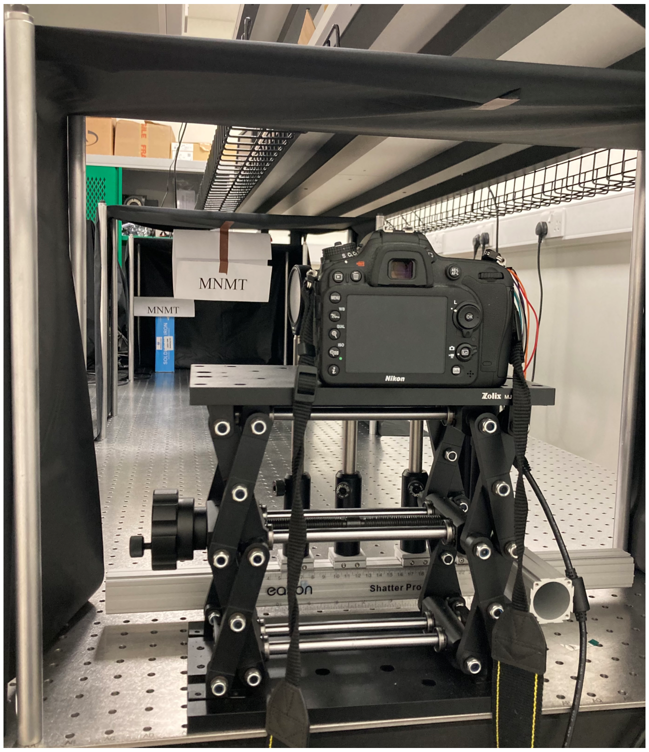

Figure 4. 46 Targets are set in the system for varifocal model. Two same letters are set at 100 cm and 200 cm away from the camera.

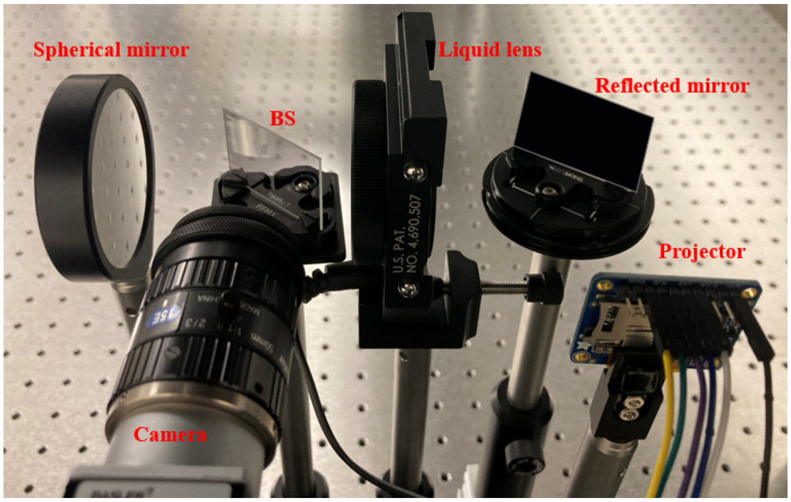

Figure 4. 47 The prototype of the system.

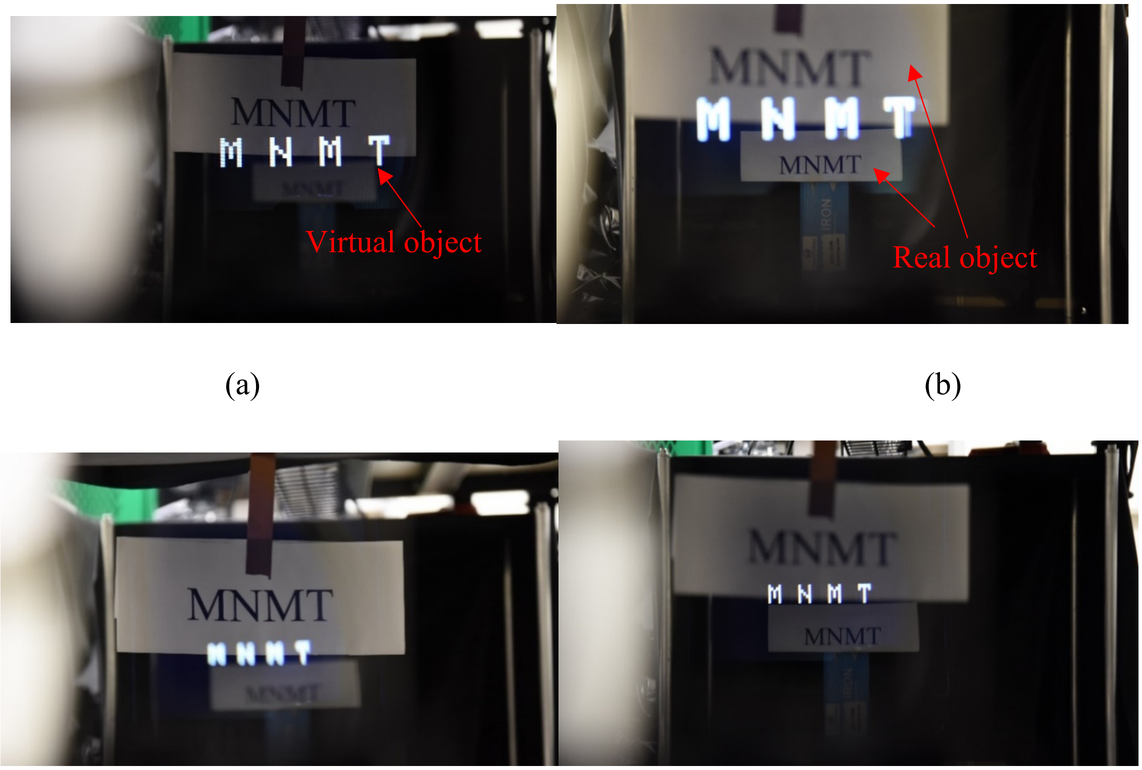

(a) (b)

(c) (d)

Figure 4. 48 Pictures captured by digital camera. Two same real images are set at different distances, 100 cm and 200 cm respectively away from the camera. The camera focuses at 100 cm in (a) and (b) when the virtual image is projected at 100 cm and 200 cm; and at 200 cm in (c) and (d) when the virtual image is set at 100 cm and 200 cm away from the camera.

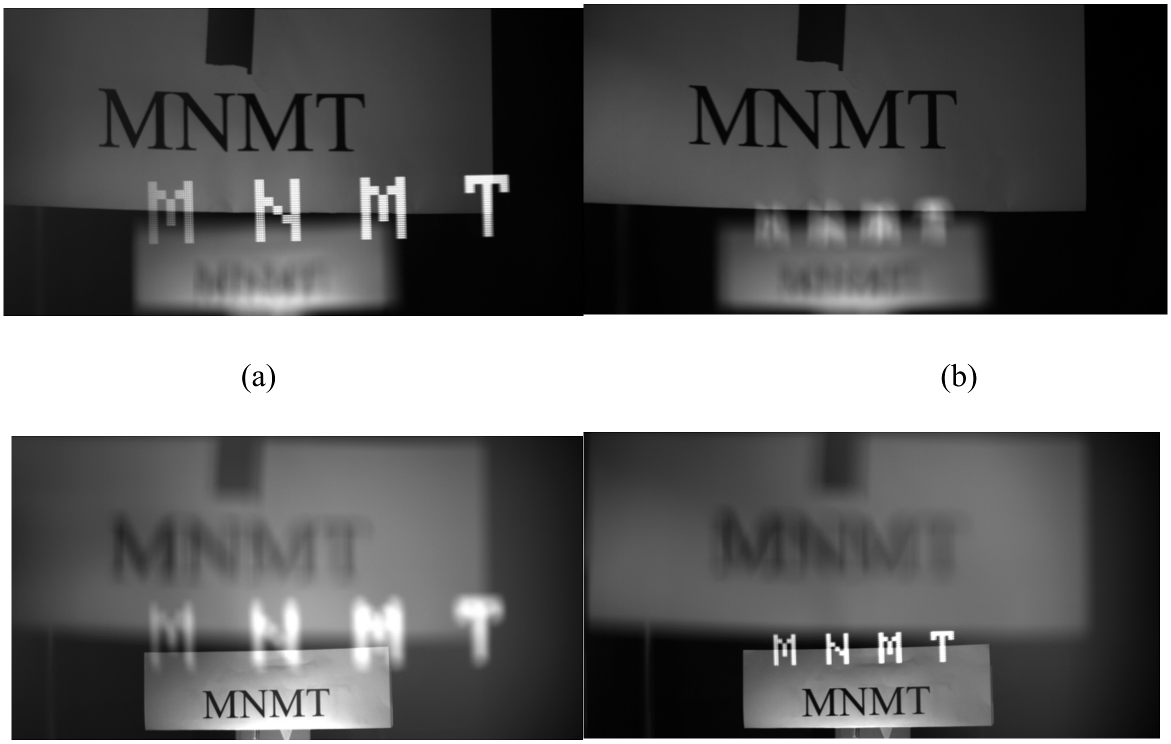

(a) (b)

(c) (d)

Figure 4. 49 Information is captured by the CCD camera. Two same real images are set at different distances, 100cm and 200cm respectively away from the camera. The camera focuses at 100cm in (a) and (b) when the virtual images are projected at 100cm and 200cm respectively; The camera focus at 200cm in (c) and (d) when the virtual images are set at 100cm and 200cm away from the camera.

To add one more virtual depth in the system, two projectors (D1 and D2) are set in the system as shown in Figure 4.50. The vari-multifocal design in Figure 4.50 has the same imaging principle as the varifocal design, as shown in Figure 4.4. There are two projectors applied in the system. One projects white 'MNMT' at 100 cm and the other projects colorful 'MNMTs' at 200 cm away from the camera. From Eq. (4.45), the object distance of the white MNMT is set at 11.8 cm and the colorful MNMTs are set at 12.7 cm. As shown in Figure 4.51, when the camera focused on 100 cm, the white MNMT and the near paper text target were clear and other images were blurred. If the camera focal distance was 200 cm, the result was the opposite as shown in Figure 4.51. However, the initial size of the virtual images from these two projectors should be calculated and set. The relationship between the depth of the virtual images and the size of the virtual images should match the visual requirement of the distance. Thus, two different focal lengths of the liquid lens are used for each optical path of the projectors. Each light path can be adjusted independently for different depths of virtual images. According to the experimental results, the depth information of virtual images was presented as simulated.

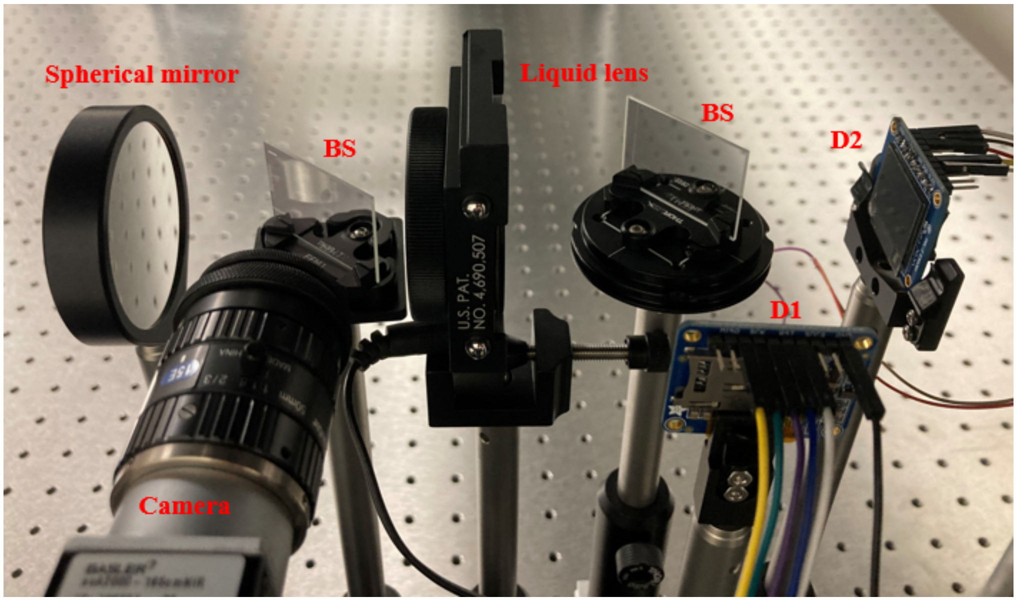

Figure 4. 50 The prototype of the multifocal system

(a) camera focused on 100 cm

(b) camera focused on 200 cm

Figure 4. 51 Pictures captured by digital camera. (a) focuses the images 100 cm away from the camera and (b) focuses the images 200 cm away from the camera.

4.4.5 Discussion

The focal power of the liquid lens is driven by the current from 0 to 250 mA in one direction, as shown in Figure 4.52. The focal power can be switched from -2 diopter to 4 diopter, which is around -500 mm to 250 mm. According to Eq. (4.45), the virtual images can be displayed from 25 cm to infinity. Due to the gravity on liquid and some other factors, the line is not linear. Thus, the image stability of the system would be affected by the focal power. According to Eq. (4.45) and the linear relation between the focal power and the virtual depth, the nonlinear error between the current and the virtual depth can be calculated.

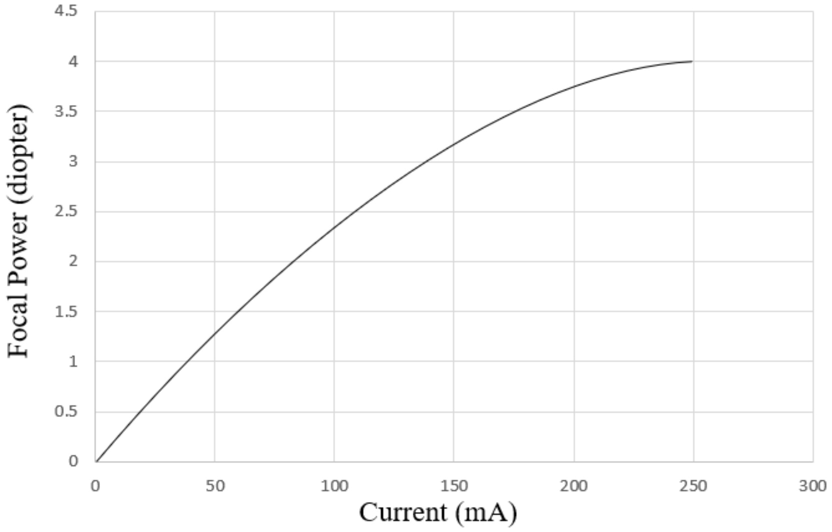

Figure 4. 52 Tunable liquid lens focal power response with current [251]

The response time of the liquid lens is a response stability concern of the system. Usually, a uniform frame rate of around 30 fps is the limit at which the human eye can comfortably view a dynamic picture by the persistence of vision. Thus, if the response time is longer than 33 ms, also known as a critical time, the human eye can sense the delay of the dynamic picture. The response time of the liquid lens is shown in Figure 4.53, which needs around 170 ms to keep stable. The trajectory of the image can still be sensed by human eyes. Thus, the selection of the drive mode, liquid material and temperature are critical to achieving a shorter response time.

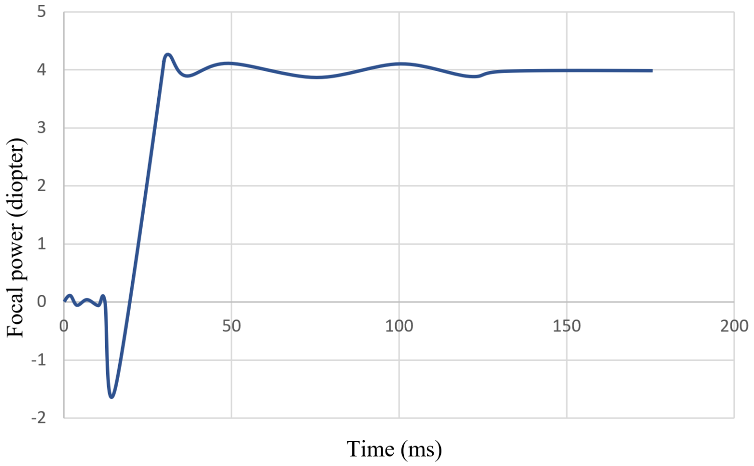

Figure 4. 53 Response time of the liquid lens with focal power

Figure 4.54 shows the calculated slanted-edge modulation transfer function (MTF) of the system at different depths. The MTF values are calculated at 33lps/mm for all the fields. The abscissa represents the distance to the center of the lens, and the ordinate represents the contrast and resolution values. The contrast and resolution of the lens are best on the optical axis, and worse towards the edges. The trend of the MTF lines indicates the image uniformity at the edge and center of the lens, which reflects the loss of the observed images compared with the originally projected images. The MTF lines are also analysed to compare modulation value according to the spatial frequency at different diopters. As shown in Figure 4.54, the loss in the edge is higher than that in the center. The MTF value performs much better at 1 diopter and 2 diopter than 3 diopter and 4 diopter. When the power is at 3 diopter or 4 diopter, the most clear real image surface is not a plane but a curved surface due to the curvature of the field. For the 3 diopter and 4 diopter, there are obvious depressions between 10 mm to 15 mm spatial frequency in a circle as shown in Figure 4.54. There may be the influence of coma due to the gravity, the material refractive index or the capsule of the liquid. Image field curvature refers to the fact that due to the defect of the lens, after the light emitted on the plane is imaged by the lens, the clear and best real image surface is not a plane but a curved surface. The presence of waves means that the image field is bent. The larger the wave, the more serious it is. The actual situation is generally not a big problem, because it can be compensated by software after calculating and simulating the distortion.

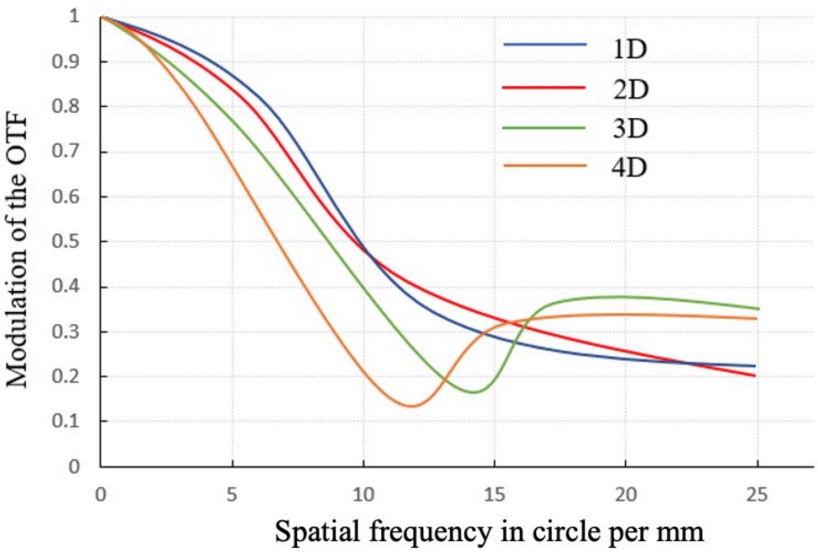

Figure 4. 54 Plotting the average Modulation transfer function (MTF) of the system

According to the experimental results, the depth information of virtual images was presented as simulated. However, there is radial distortion caused by the optical elements. Radial distortion is the distortion distributed along the radial direction of the lens, which is caused by the fact that the light is more curved at the center of the principal lens than near the edge. The distortion at the center of the optical axis of the image is 0 and moves to the edge along the direction of the lens radius, with the distortion becoming more and more serious. The distortion caused by the liquid lens can be described as

$$x_0 = x(1 + k_1 r^2 + k_2 r^4 + k_3 r^6) \tag{4.46}$$

$$y_0 = y(1 + k_1 r^2 + k_2 r^4 + k_3 r^6) \tag{4.46}$$

where (x_0, y_0) is the original position of the distortion point on the image, and (x, y) is the new position after correction. k_1, k_2, k_3 are the radial distortion coefficient, r is the radius of the liquid lens or the spherical mirror. Thus, the distortion coefficient of the liquid lens or the spherical mirror can be calculated by the software algorithm between the actual position and the ideal position of the image through calibration. The images from the projector can be presented by the mapping of the correction.

The system can be layout as a wearable device, such as glass as shown in Figure 4.55 when all elements are integrated into a portable frame. The projector is driven by the Bluetooth module and the virtual images can be displayed at different depths to suppress the VAC problem. Near-eye see-through display is gradually developing in the direction of miniaturization, integration, and intelligence.

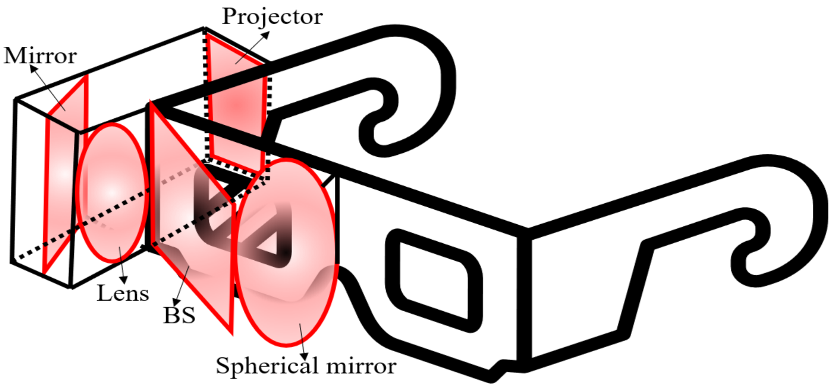

Figure 4. 55 Sketch diagram of the near-eye see-through system

The see-through display is presented with addressable depth cues and a field of view of 66° to reduce dizziness and vertigo problems. The presenting depth of the virtual images can be successfully varied by changing the curvature of the liquid lens from 25 mm to infinity in this design, which can successfully match the accommodation depth range of the human eye. The time response and the MTF are analysed to evaluate the system performance and the method is developed to eliminate the image distortion. For the multifocal display, two focal planes are displayed, and both planes can be adjusted independently. Following this method, it could be extended to a multi-focal display with more focal depths. Great efforts have to be made to achieve the miniaturization, integration and intelligence of the optical elements and electronic device.

4.5 Summary

Most conventional stereoscopic three-dimensional displays have inherent vergence accommodation conflicts problem because they simulate the perception of 3D images by the psychological perception from two-dimensional images, which are not real stereoscopic images. Thus, VAC is produced by the conflicts between binocular parallax and accommodation. In this chapter, the cause of VAC is systematically analysed and the approaches to solve VAC are classified based on the imaging principle. Based on the principle of current display applied for solving VAC, we propose a varifocal and multifocal near-eye see-through display design by applying geometrical waveguide and liquid lens. There are two depth layers, one is at infinity and the other one is movable to match visual perception. The FOV of the system is around 35°. The total thickness of the dual-layer waveguide is around 5.6 mm. The eye relief is set at 20 mm and the eye box is 38.46 mm. The stray light of the system is suppressed under 1.5%. Besides, a new easily achievable varifocal and multifocal design based on plate beam splitter and liquid lens is proposed. The MTF of the system is around 0.3 and the response time of the system is around 170ms to keep virtual depth stable.

Chapter 5 Fabrication of geometric optical waveguide

5.1 Fabrication process

In geometric optical waveguide, the image needs to be reflected into the human eye through the spectral film coating on the out-couplers. To obtain a larger field of view and eye movement range, multiple spectral surfaces (out-couplers) need to be prepared inside the waveguide, and each spectral surface is composed of 25-30 layers of coating, which makes the model design and fabrication extremely difficult. This chapter develops an efficient geometric optical waveguide fabrication process, as shown in Figure 5.1. The coatings are first deposited uniformly on the substrate, then bonded together with high precision by optical adhesive, and cut into slices at a highly parallel angle, they are polished and shaped to obtain the desired waveguide structure. The uniformity of the coating, the transmittance/reflection ratio of the coating surface, the flatness of the substrate, the surface roughness, the optical adhesive, and the cutting accuracy all have a significant impact on the AR display performance. A simple combination of existing processing technologies is difficult to meet such a high manufacturing requirement, thus exploration of more effective and precision manufacturing technologies and process chain is highly desired.

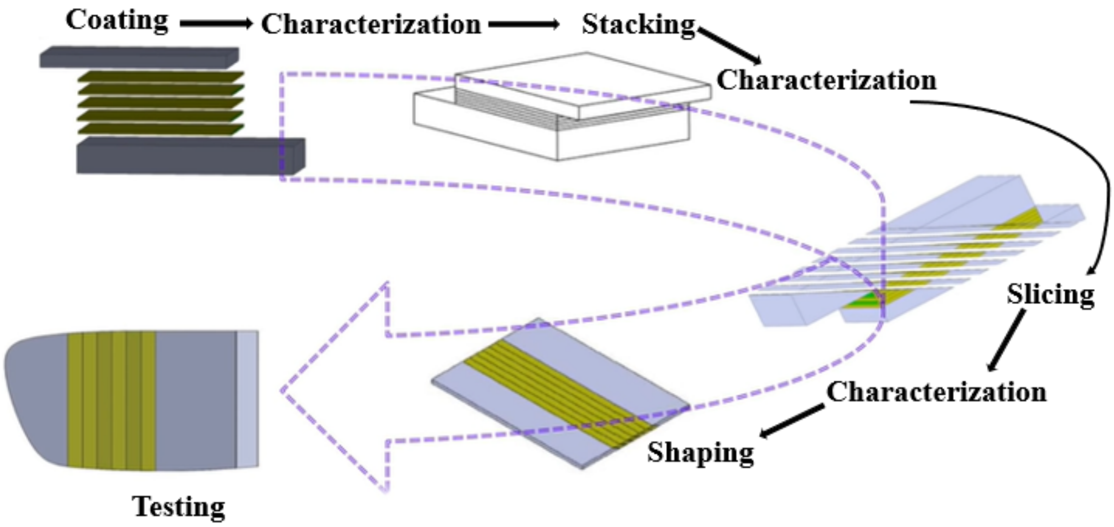

Figure 5. 1 Manufacturing process of geometrical waveguide

5.2 Material selection, coating and gluing

5.2.1 Material selection

For the substrate material selection of the geometrical waveguide, the optical property, physical property, chemical property, and mechanical property are important for the optical performance including transmittance, refractive index, density, optical dispersion etc. The refractive index limits the critical angle of TIR, which affects the FOV of the final component. Thus, higher refractive index, higher transmittance and lower density are the primary objectives. High index glass is one of the limited choices currently for supporting such a high-end technical specification. SCHOTT RealView® 1.9 lightweight show significant advantages in fabricating geometrical waveguide which cuts off 20% of density compared with conventional glasses and keeps a high refractive index. As a suitable glass material for light-weight waveguide, it also features superior mechanical and optical properties. This glass enables significant weight reduction from optical module which means a lighter and more comfortable user experience.

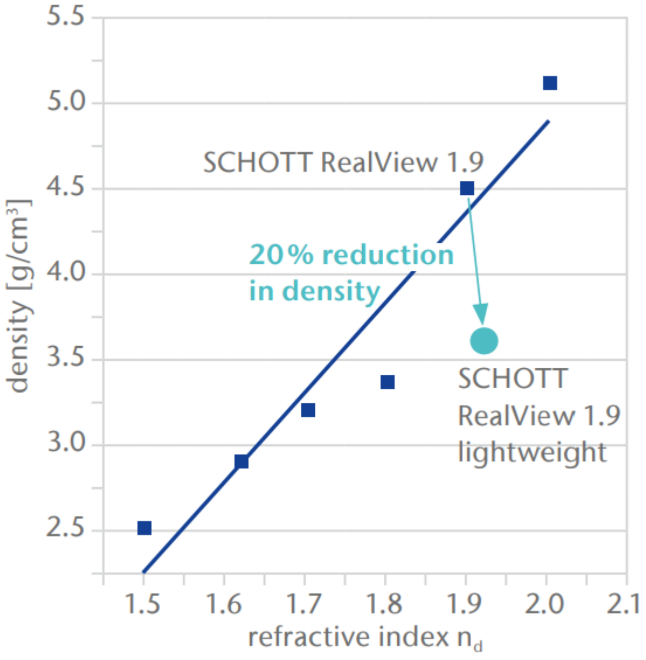

Figure 5. 2 Density with refractive index

5.2.2 Coating, stacking and gluing

After selecting the proper substrate material and setting the thickness of the material, the coating is the next step to be concerned. One side of the substrate is coated with different spectral ratios, which follows Eq. (4.26). According to the visual characteristics of human eyes, the photopic vision and scotopic vision decide the tolerance of the spectral ratio. The sensitivity of the human eye to different wavelengths of light in normal daylight is called the bright visual response, also known as daytime vision, and is described by the bright visual spectral light efficiency function. At this time, it is mainly acted by cone cells, which produce both light and dark sensation and color sensation. When the light is dim to a certain level, only the rod cells act and do not distinguish color, but only reflect the degree of light and darkness, which is called dark vision, also known as night vision, which describes the human eyes at night or in low light sensitivity. The spectral efficiency curves of photopic and scotopic spectral light are shown in Figure 5.3. The visual sensitivity of the human eye to light is different in the state of photopic vision and dark vision, and the visual sensitivity in the visible spectrum range is not uniform. It changes with the wavelength, which is similar to the shape of a parabola. The spectral efficiency requires the brightness and the light efficiency of the AR system. From Figure 5.3, it can be calculated that human eyes require different virtual image brightness at different background brightness.

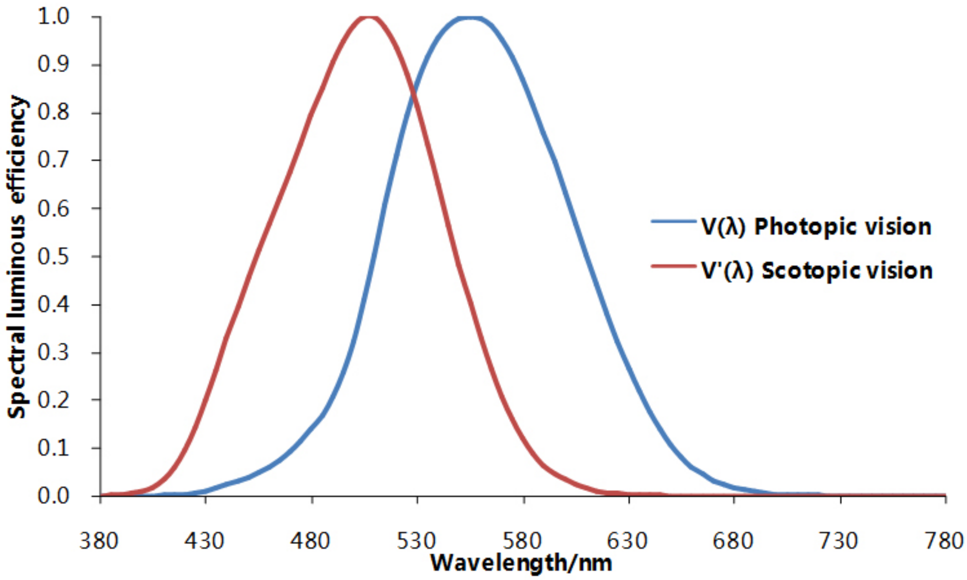

Figure 5. 3 Photopic and scotopic spectral light efficiency curves

The human eye's ability to perceive changes in luminance is limited, and the minimum luminance change that can be perceived varies for different luminance L. ΔL_m is the luminance difference between the central patch and the background when the human eye can just distinguish between them, which is called the visibility threshold, or the luminance discrimination threshold. At a certain luminance L, the minimum relative luminance changes $\Delta L_m / L$ perceptible to the human eye is approximated as a constant, called the relative contrast sensitivity valve or Fechner coefficient, denoted by ξ as expressed below.

$$\xi = \Delta L_m / L \text{ (generally 0.005 to 0.02)} \tag{5.1}$$

The difference in luminance perception of the human eye is determined by the relative luminance change, luminance perception S is linearly related to the logarithm of luminance L, that is, when the luminance perception increases by a factor of 1, the luminance increases to 10 times. This law is called Weber-Fechner Law, that is,

$$S = k \times \log L + k_0 \tag{5.2}$$

In practice, most of the targets are in an inhomogeneous background, and the brightness of the background varies with time and space, in which case the visibility threshold will increase. This phenomenon is called the visual masking effect. Moreover, it is also found that the same luminance, the visual range in which the relative luminance sensation is different. The human eye's brightness perception is relative and is not determined by the absolute luminance. There is no necessity that the brightness of the reproduced image is equal to the actual brightness of the scene. The human eye can get the same subjective brightness feeling as the scene in front of the screen by keeping the contrast C constant between the two scenes. The ratio between maximum luminance L_{max} and minimum luminanceL_{min} is the contrast C. Thus, it should keep contrast and luminance in the same level. It is because of the limited ability of the human eye to perceive luminance difference, that is, the luminance level that the human eye can distinguish is a limited amount, therefore, when digitizing the video signal, the quantization level is decided according to this characteristic. To meet Eq. (5.1) and Eq. (5.2), the tolerance of the reflectance should be smaller than 3%. Based on above, the difference of spectral ratio should make the exit pupil achieve uniform illumination. Thus, the reflectance on each coupler should meets

$$R_i = (1 - R_i) \times R_{i+1} \tag{5.3}$$

where i is the serial number of the out-couplers. The T/R ratio is determined by Eq. (5.3). The coating film is only coated on one side of substrate.

Stacking and gluing are the next step after getting coated substrate. The glued area contains two surfaces, one is fully transparent side of substrate surface, the other one is coated surface of the substrate. The surface roughness of these two surfaces should be within the range which is limited by the resolution of human eyes 60″. Based on Eq. (3.27) and Eq. (3.28), the roughness tolerance should be smaller than 0.667μm in Sa and the thickness of the adhesive should be smaller than 20.21μm. The surface roughness of the uncoated side and coated side of the out-coupler is shown as Figure 5.4 and Figure 5.5 (5 random positions are selected on each surface). Five randomly selected locations on a coupling out board are characterized from one sample. The surface roughness of uncoated side of the substrate is around 4.7nm in Sa and the surface roughness Sa of the coated surface is around 7nm, measured by 3D surface metrology.

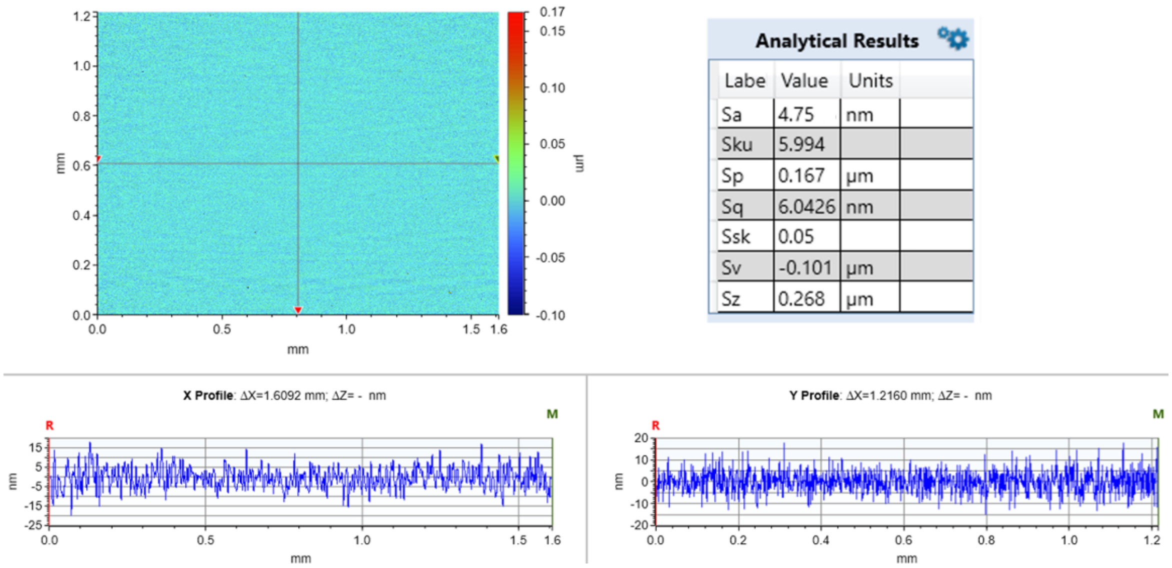

Analytical Results

Labe	Value	Units
Sa	4.75	nm
Sku	5.994	
Sp	0.167	µm
Sq	6.0426	nm
Ssk	0.05	
Sv	-0.101	µm
Sz	0.268	µm

Figure 5. 4 Surface topography of the uncoated side on the out-coupler

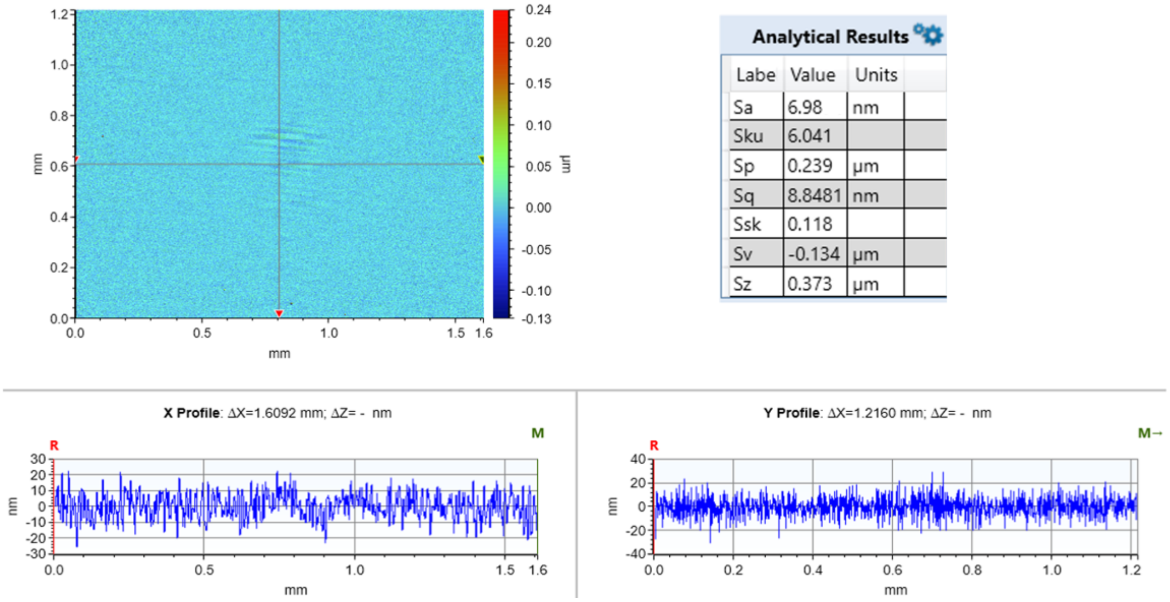

Analytical Results

Labe	Value	Units
Sa	6.98	nm
Sku	6.041	
Sp	0.239	µm
Sq	8.8481	nm
Ssk	0.118	
Sv	-0.134	µm
Sz	0.373	µm

Figure 5. 5 Surface topography of the coating side on the out-coupler

For the properties of the adhesive, the refractive index, and the curing method and the transparency affect the optical performance. The refractive index of adhesive should be the same as the substrate' s ideally. The spin coater is used to disperse the adhesive on the substrate and tries to form a uniform layer in a controlled way. After dropping 0.1ml adhesive on the center of the substrate, start the spin coater with 500 acceleration and 1500rpm in 90 seconds. After spinning the adhesive, the surface roughness is measured around Sa 7.8nm, as shown in Figure 5.6, which are randomly selected from one sample. The thickness of the adhesive is around 7µm by the micrometer. The surface roughness error bar of these three surfaces is shown as Figure 5.7.

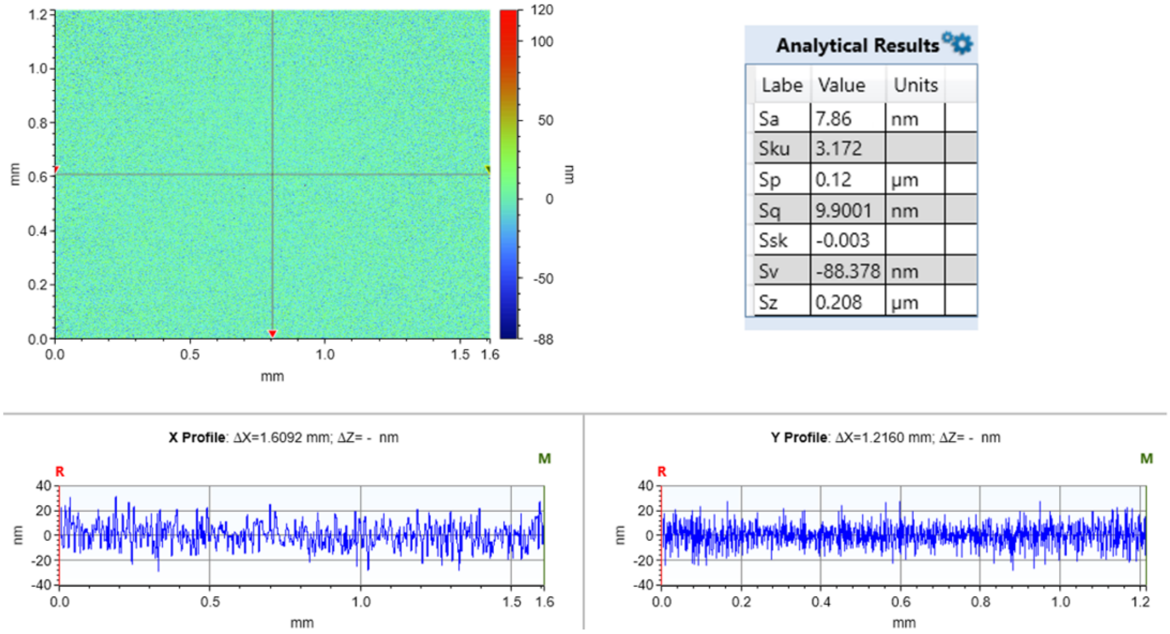

Analytical Results

Labe	Value	Units
Sa	7.86	nm
Sku	3.172	
Sp	0.12	µm
Sq	9.9001	nm
Ssk	-0.003	
Sv	-88.378	nm
Sz	0.208	µm

Figure 5. 6 Surface topography of the adhesive

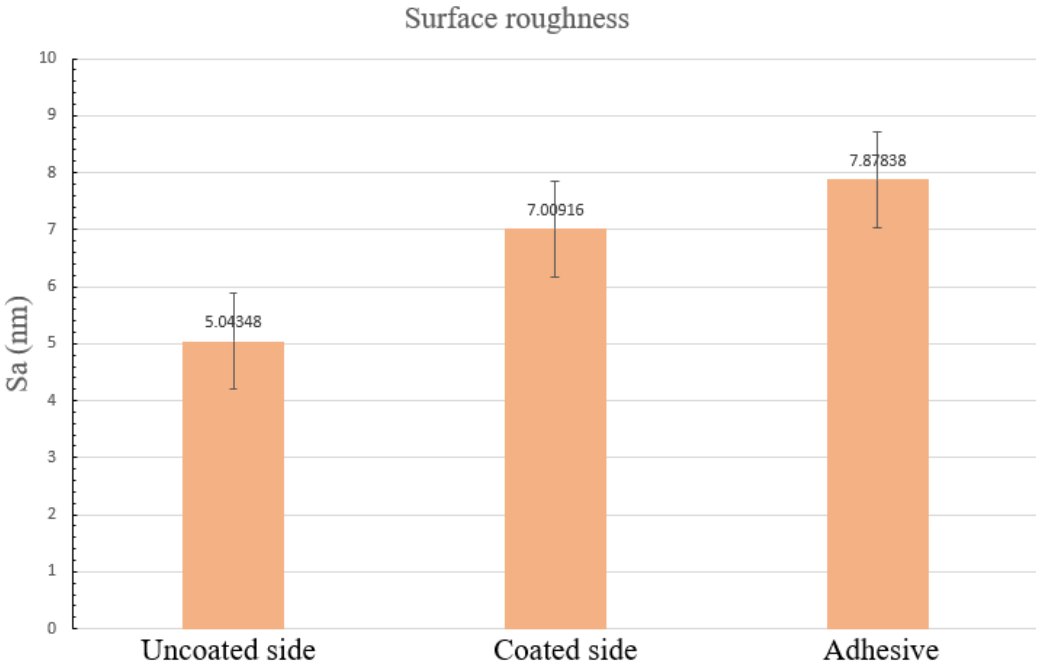

Figure 5. 7 Surface roughness error bar

To stack the substrate materials, the glue can be cured by UV light, as shown in Figure 5.8

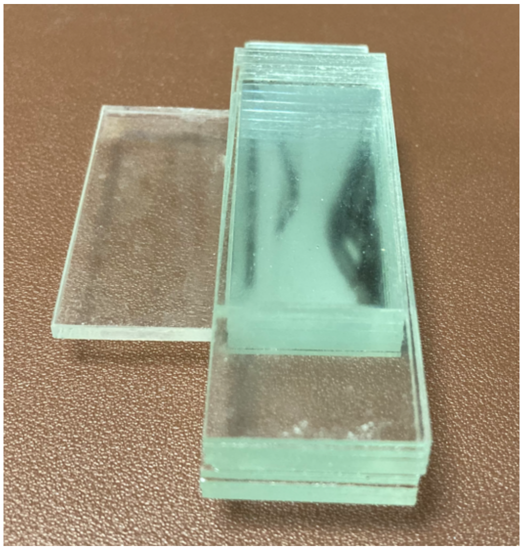

Figure 5. 8 Glued substrate material

5.3 Cutting, polishing and characterization

The wire-electrode cutting method is chosen for slicing the glued glasses and the cross-sectional view of sliced glasses is shown in Figure 5.9. After polishing sequentially by the P240→P320→P600→P1200→P4000-grit silicon carbide abrasive paper (MetPrep Ltd), the morphology of the polished surface is shown in Figure 5.10. Since there is an adhesive layer between two different coating slices, the discontinuity would have a negative impact on the uniformity of the optical performance of finished prototypes. The images from the real world through the glasses can be captured as shown in Figure 5.11. The left side is captured through the glasses and the right side is directly captured by the camera. The captured image demonstrates the prototype still requires optimization in process and design to provide high-fidelity images as the commercial camera lens, the transparency of the prototype is presumably around 70%.

Figure 5. 9 Sliced substrate material

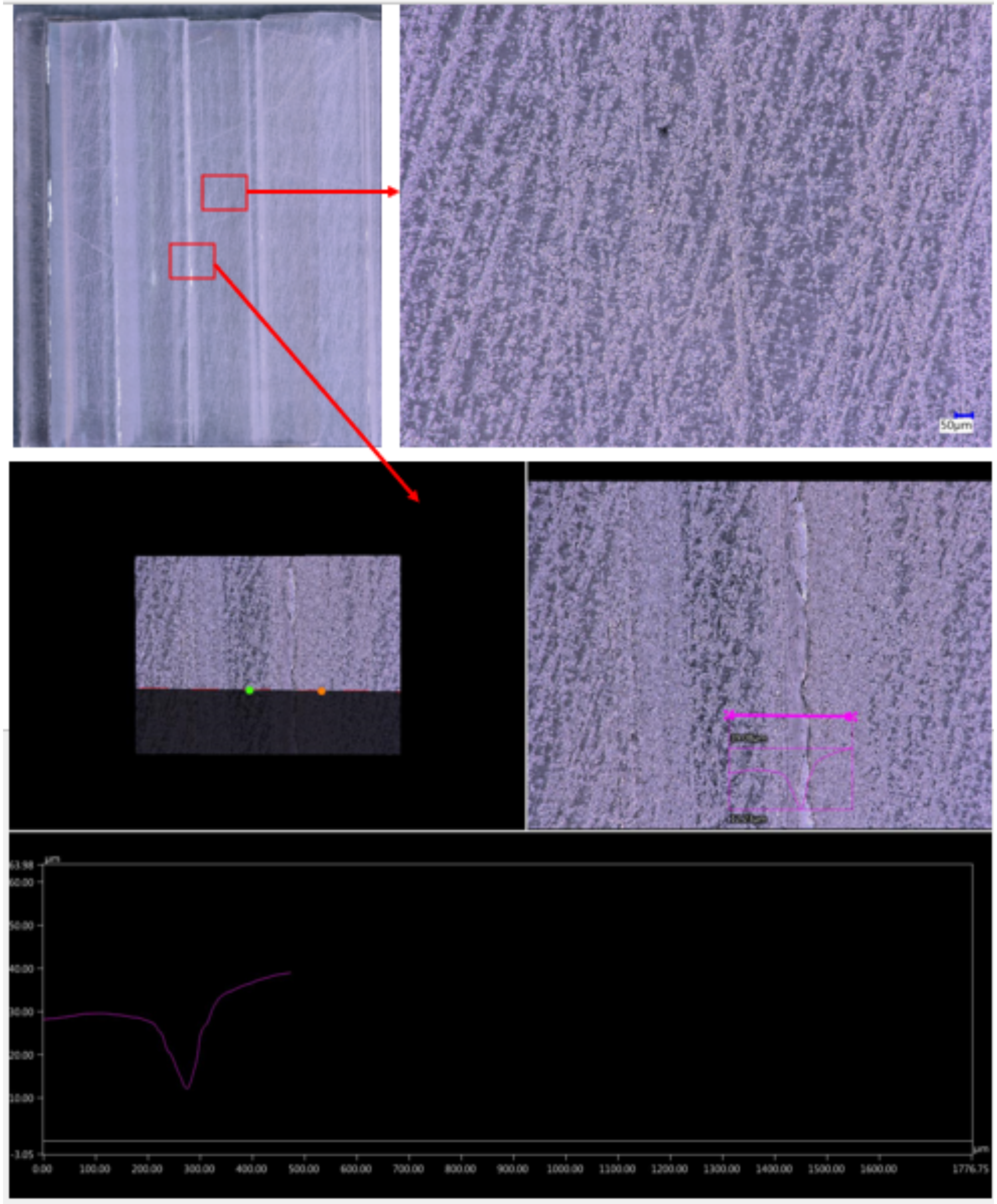

Figure 5. 10 Morphologies of polished glasses surface.

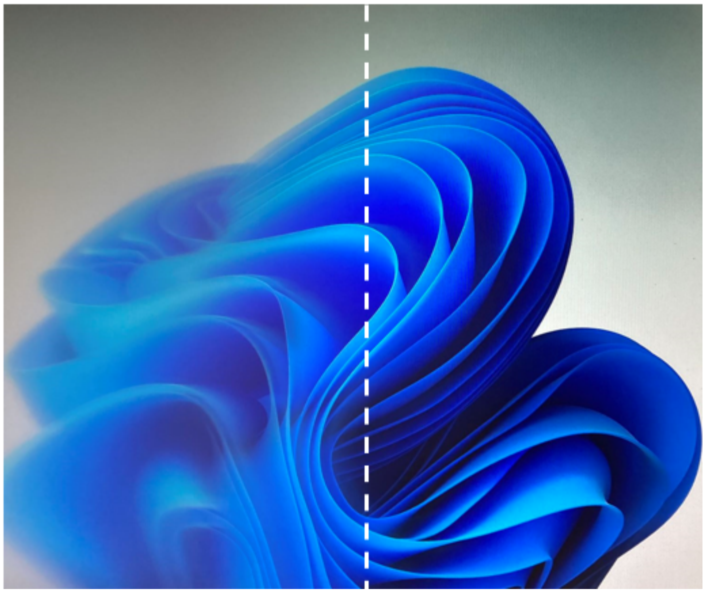

Figure 5. 11 Images captured through the geometrical waveguide. Left side is captured through the glasses and the right side is directly captured by the camera.

The waveguide requires customized collimated micro-projector, which is around 2mm*2mm size. It is hard to find a proper size micro-projector, which need to be customized but extremely expensive. Thus, the red light is used for the light distribution for the waveguide. Figure 5.12 shows the light distribution of the waveguide (polished glasses). The light from the out-coupler is a little bit not uniform, it may be caused by the coating error. The red light can still be seen at the non-functional area, it is caused by the cutting and polishing accuracy, which cannot meet the requirement of TIR. Besides, the light leakage can also be caused by the thickness error of the waveguide due to slicing and polishing accuracy. The light distribution of the Lumus AR glasses is shown in Figure 5.13, it can be seen the light is also not uniform. These problems can be solved when the fabrication and assembly accuracy is guaranteed.

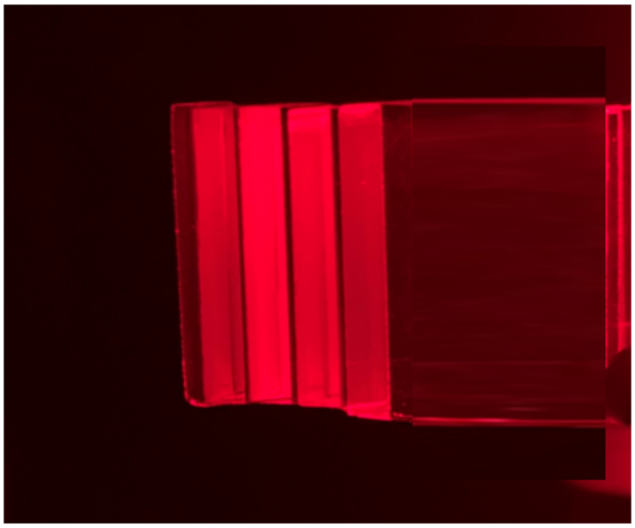

Figure 5. 12 Light distribution of the waveguide

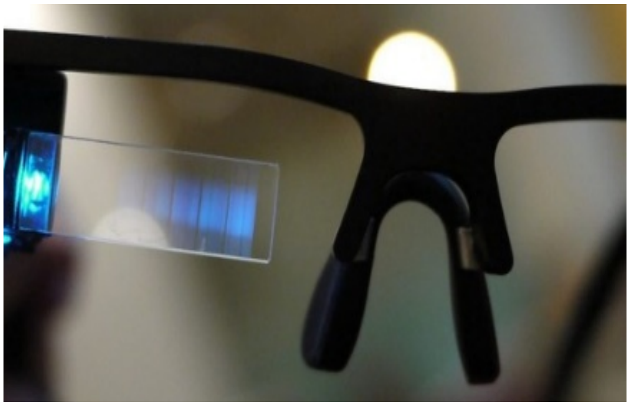

Figure 5. 13 Lumus AR glasses light distribution [46]

In the manufacturing process, the geometric optical waveguide adopts the traditional optical cold processing technology. The advantages are the optical coating, optical cutting, nano-grinding, nano-polishing, fine carving and other processes are very mature, and the optical imaging quality is high, and there is no color cast. The difficulty lies in the lamination and assembly of the mirror array in the outcoupling link. It is necessary to ensure that the processing accuracy of each step is high enough, otherwise light and dark stripes, black stripes, etc. will easily occur. Especially if the traditional glue lamination process is used for lamination, the product yield rate will be very low. Thus, the manufacturing accuracy of each step must be lower than the tolerance to reduce the influence on the imaging quality. At present, the manufacturing of the waveguide in the lab cannot meet the accuracy of each process. The manufacturing cost is extremely high to reach high accuracy of the waveguide.

5.4 Summary

Since the geometric optical waveguide adopts the traditional optical cold processing technology, the market already has mature and complete but independent materials, processes, equipment and other related industrial chains. A simple combination of existing processing technologies is difficult to meet such a high manufacturing requirement, thus exploration of more effective and precision manufacturing technologies and process chain is highly desired. In this chapter, the manufacturing process of the geometrical waveguide is provided. The characterization method and manufacturing tolerance of each step are systematically discussed. Leveraging these manufacturing and characterization methodologies, a high-precision geometrical waveguide is obtained. The light distribution problems can be solved when the fabrication and assembly accuracy is guaranteed. It is then possible to achieve an AR glasses with a combination of such a geometrical waveguide and a high-performance projector.

Chapter 6 Design and application of innovative AR display system

6.1 Design of novel composite optical system

Traditional cameras have significant limitations in calculating the scene depth and thus generally obtain 2D images of the targets. Light field camera (plenoptic camera) solves this problem with depth information. The image focus can be switched and rebuilt computationally after optical information is taken by the camera. The micro-lens array (MLA) between the main lens and the photoreceptor plays a key role in the light field camera as shown in Figure 6.1. Each small lens in this array receives the light from the main lens and transmits the light to the photoreceptor. The photoreceptor records the light information digitally after light focusing and converting. The camera's built-in software operates an expanded depth light field that tracks where each ray of light falls on the image from different distances and digitally refocuses the target depth to recreate the information from the real world. Thus, the light field camera has obvious advantages in angular resolution. The 3D image acquisition of the observed object can be achieved conveniently and quickly, and refocus to form a series of focal stack images by the software selection and calculation [252, 253].

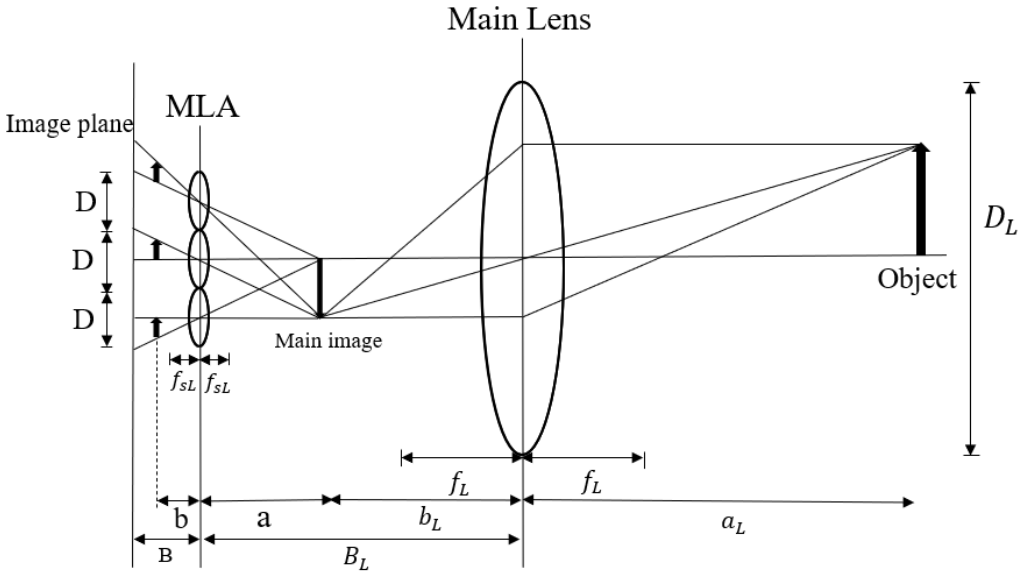

Figure 6. 1 The basic imaging process of plenoptic camera (light field camera)

However, due to its hardware structure, a plenoptic camera cannot avoid some inherent defects such as low spatial resolution, short baseline, and compressed dynamic range by high-dynamic range (HDR) [254]. To obtain a good depth resolution at the larger field-of-view and larger depth-of-field, the micro-lens array needs to be closer to the main lens as reported by Raytrix [255]. In particular, this means that a plenoptic camera in combination with a wide-angle lens can only see depth differences close to the main lens. The plenoptic camera typically works under standard lighting and even a flash, thus it is not competent for difficultly recognized surfaces under a poor lighting environment or without identifiable features, thus a pattern projector is needed which is not the standard configuration of the commercial products. The built-in software required for the 3D image reconstruction imposes challenges on the computational efficiency and data utilization [255, 256]. For the image's reconstruction, the focused target needs to be selected manually, which cannot be identified automatically by the software. Although the image is captured from multiple angles at the same time, the angle difference is subtle, the ability to identify the blocked part is extremely limited, and it is time-consuming. Such drawbacks make it incompetent for some practical applications such as gesture recognition in a daily environment with high noise, complex background, hard-to-identify textures, block of partial objects, poor lighting conditions, the rigorous requirement on real-time response, etc.

Furthermore, at present, the emerging AI methods in academia mainly use the aberration-free ideal data sets of synthetic scenes. However, the real scenes are far more complex and richer than the synthetic scenes, and the image features vary with the change of background scenes. At the same time, the actual scene contains a variety of image noises, and highly reflective target objects, which are hard to be recognized. Compared with the synthesis based on ray tracing, the actual scene is more difficult to acquire and collect, and the necessary label of the dataset is easy to be missing or inaccurate, and some other associated problems. E.g., a demo provided by a commercial plenoptic camera (to avoid the conflict of interest, the brand is not indicated here, and the reference is not provided) for illustrating the gesture recognition is performed under a black background to reduce the background noise. Even so, the finger recognition effect is vague as shown in Figure 6.2, which implies the limitation of the environment [257]. Another brand uses a 40-megapixel lens and a large f/2.0 aperture to improve photo quality. However, the efficiency is just 10%, that's to say, about 10 million pixels of this 11-megapixel sensor are wasted. There is no doubt that this has a great impact on the resolution of the photo, and the stitching algorithm itself will also lose resolution to a certain extent [258, 259]. Therefore, the actual resolution of this 11-megapixel sensor is approximately equal to the level of 500,000 pixels. For a 1/3-inch f/2.0 sensor, using the algorithm of sacrificing time for space, more than 100 distance slices can completely record all the information. But if it is replaced by the current standard 1/2.3-inch sensor, then distance slices will be increased to nearly 200 to record all the information. If the advanced photo system type-C (APS-C) sensor is used, this number can be increased to 3000. Even if there is a continuous shooting speed of 60 frames per second, unlimited cache, and extremely high storage speed, 10 times the data multiplexing rate, it still takes 0.3 to 0.5 seconds to take a photo (covering 3000 distance slices) excluding the calculation time. Based on this real efficiency, if taking a 1-minute shooting and outputting a RAW format file, the size of the file is very large. No matter which scene is selected afterward, a significant part of the captured information would be wasted as only one focus plane will be used in each scene. Obviously, such a way requires longer processing time for image reconstruction and thus is not suitable for some real-time tasks.

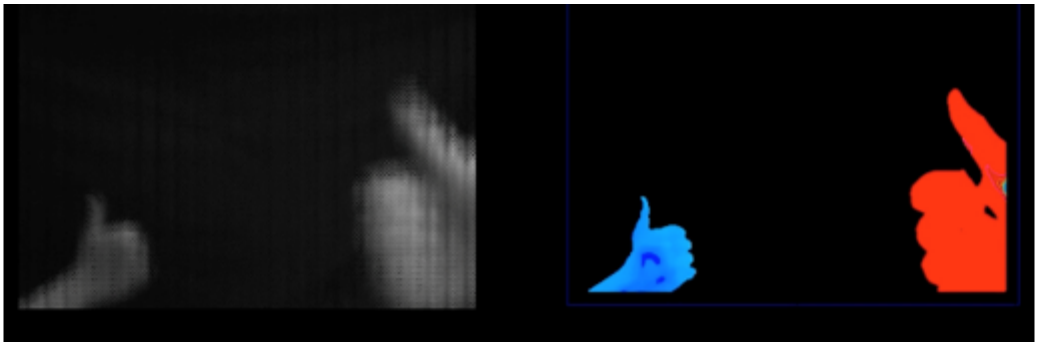

Figure 6. 2 Finger reorganization by commercial plenoptic camera

To solve the above problems, the virtual scaling system could help in a variety of application scenarios, such as gesture recognition. For example, the virtual scales can be projected through the AR system and used to limit the automatic focus range, quickly filter a part of the background, and scope useful information more efficiently. The virtual scale network can set an easily discernible scaling feature that provides accurate quantitative depth information even in poor lighting conditions. Insufficient or too strong lighting, noise, and unclear target characteristics can be effectively compensated through the virtual scaling system. The camera could actively search for such features that real objects intersect with the virtual scales on the focal plane, which helps spotlight the features on the real objects and directly provides a quantitative depth information. A faster computational speed can be achieved for continuous and rapid action by using limited data, as there is no need for reconstructing the full 3D model which contains a large part of useless information, and only valid information scoped by the virtual scales is collected and processed. For the actual use for gesture capturing and recognition, the virtual network can further establish a local coordinate system on hands to identify the pose of the fingers by identifying and incorporating valid virtual and real images. This coordinate system reduces the time for handling invalid resources. Much fewer distance slices need to be captured, which facilitates higher efficiency of data processing.

In this chapter, a virtual scaling system based on the combination of a geometrical waveguide and micro-lens array is designed and simulated for solving the above problems of the plenoptic camera. The working principles of the whole system are described and analyzed schematically. By establishing a geometrical model to quantitatively correlate the synthesizing images and the virtual scale networks, it is proposed a method to calibrate and correct the depth errors caused by the plenoptic cameras. The coefficient of determination R^2 is presented to indicate how closely these two surfaces fit each other. The closer the value of determination is to 1, the less the depth error is, and the more accurate the 3D image is. In this way, the system can achieve depth error correction in real time and with higher precision than conventional plenoptic cameras. Experiments based on this innovative AR system also demonstrated the effective filter of complex backgrounds and rapid scoping of targeted useful information without spending many resources on useless signals for complex 3D modelling, thus it achieves low-latency real-time response more accurately, even under poor lighting conditions.

6.2 Mechanism and system design

The innovative AR system combines optical waveguide and MLA to capture two types of images using two different application modes respectively: 1) the plenoptic camera mode captures the image with depth information as conventionally; 2) the AR mode projects virtual scales first, and then focuses on the specified scales (depth) which simultaneously captures the real objects on the same plane. By comparing these two images, the depth error of the plenoptic camera image can be calibrated and corrected by our proposed algorithm, to reconstruct a more accurate 3D image. Besides, in poor lighting condition or complex background, the object is usually hard to be identified and focused on. The virtual scales facilitate the plenoptic camera to focus on the expected plane and capture the objects more effectively.

To offer the quantitative depth information of the real objects for accurate 3D tracking, the AR system is designed, as Figure 6.3. The main optical system consists of three parts: a projector displaying virtual scales, a waveguide expanding and relaying the virtual scales to a multi-focal MLA, and the MLA projects virtual scales in different depths. The visual scales are projected and collimated into a waveguide through the in-coupler. The light can be totally internally reflected within the waveguide component and coupled out by the partially reflective mirror array (PRMA), which breaks the condition of total internal reflections (TIRs). So, the geometrical waveguide works as an entrance pupil expander. Afterward, the virtual scales from the waveguide passes through the micro-lens array and are present at different depth. A refractive micro-lens array was applied in this system to divide the wavefront into many tiny parts, each of which is focused on a specified focal plane by a corresponding lens pitch. The focal length of each pitch is independent of each other. Thus, the virtual scales corresponding to different depths form a calibration network (virtual scale coordinate system) covering various focal planes. The virtual scales help the image acquisition module to achieve fast and precise positioning of each part of the image. The plenoptic camera could collect both virtual information and real optical information in such an AR mode. Additionally, in the conventional plenoptic camera mode, the sensor could capture the image with depth information by the main lens and MLA and form the auxiliary coordinate system, like the imaging in Figure 6.1. By comparing the coordinates of two images captured by different modes (in the virtual scale coordinate system and auxiliary coordinate system respectively), the depth error can be calculated and corrected quantitatively to synthesize more accurate 3D images.

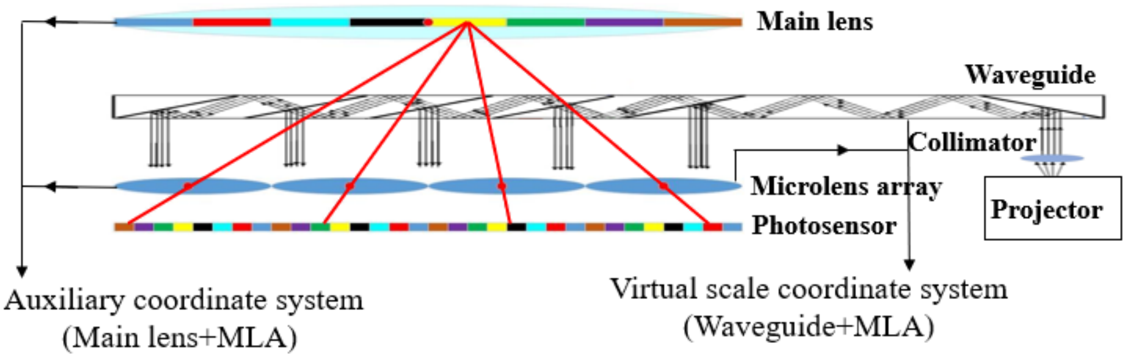

Figure 6. 3 Schematic diagram of the system design

6.2.1 Plenoptic camera

A focused plenoptic camera works as shown in Figure 6.1. The main lens replicates the object to its left as the main image which is then projected by the micro lenses on the image plane. The projection of the main lens follows the lens equation:

$$\frac{1}{f_L} = \frac{1}{a_L} + \frac{1}{b_L} \tag{6.1}$$

where the main lens with focal length f_L projects an image at the position b_L behind the lens of an object at distance a_L. The micro lens array (MLA) is placed at a small distance a in front of or behind the focal plane b_L. The imaging sensor is placed at a distance b behind the MLA. The f-number of the microlens N and the f-number of the main lens N_L follows $N \approx N_L$ since $b \ll D_L$. The object is projected inside the camera by the main lens, then the flipped and depth-discretized image is projected on the image plane by the MLA. The depth of the main images can be calculated by image matching from different homologous points of micro-images. Thus, the depth of the main image in plenoptic camera can be defined as:

$$v = \frac{a}{B} \tag{6.2}$$

where a is the distance between the main image and the MLA and B is the distance between MLA and the imaging sensor. The relationship between object distance and the virtual depth b can be derived as

$$a_L = \left[\frac{1}{f_L} - \frac{1}{B_L - \left(\frac{1}{f_{sL}} - \frac{1}{b}\right)^{-1}}\right]^{-1} \tag{6.3}$$

where f_{sL} is the focal length of the microlens and b is the virtual depth of the virtual images.

The depth error in plenoptic cameras is caused by the inaccuracies in the focusing of the lens array. This is due to the imperfect alignment of the lens components, optical aberration, and misalignment of the imaging planes. Improper alignment of the lens can cause optical distortions in its field of view, which can result in inaccurate calculations in the depth error or inaccuracies in the image sensor's data output. Optical aberrations can affect the depth error of a plenoptic camera by causing distortions in its field of view, which can result in inaccuracies in its calculations. Specifically, chromatic aberrations can cause color fringing and reduce the accuracy of the camera's depth calculation, while spherical aberrations can distort the edges of an image. Other factors that can contribute to depth error in plenoptic cameras include the optical properties of the lenses, the number of lenses used, and the size of the imaging sensors. The number of lenses in a plenoptic camera can affect its depth accuracy because it increases the chances of optical distortion, misalignments between lens elements, and inaccuracies in calculations by the camera. Additionally, more lenses can lead to additional noise and an increase in the size of the camera. Besides, the size of the sensor in a plenoptic camera can affect its depth accuracy by controlling the amount of light entering the camera and controlling the noise. A larger sensor can lead to an increase in resolution, which can help with depth calculations. In contrast, smaller sensors can limit the field of view, leading to an increased amount of parallax errors. Furthermore, motion blur can result in inaccurate depth measurements, particularly for fast-moving objects.

6.2.2 Waveguide

The geometrical waveguide expands the entrance pupil and reduces the thickness of the exit pupil optical elements. The light information comes in the waveguide in parallel and comes out in parallel as shown in Figure 6.3. Thus, the field of view of the waveguide can be derived as Eq. (6.4).

$$\mathrm{FOV} = 2\tan^{-1}\frac{\frac{\mathrm{N}*\mathrm{D}}{\tan\theta} - \mathrm{EPD}}{2\mathrm{ERF}} \tag{6.4}$$

where D is the thickness of the waveguide, θ is the angle between the edge of waveguide and in-coupler (equal to the angle between the out-coupler and the edge of the waveguide), M is the number of out-couplers in the waveguide. Eye relief (ERF) is the distance between the waveguide and MLA. Exit pupil diameter (EPD) is the entrance pupil of the MLA. There may be some stray light generated in the process of expanding light. The suppression methods of the stray light have been discussed by Yao, etc. in [156, 244].

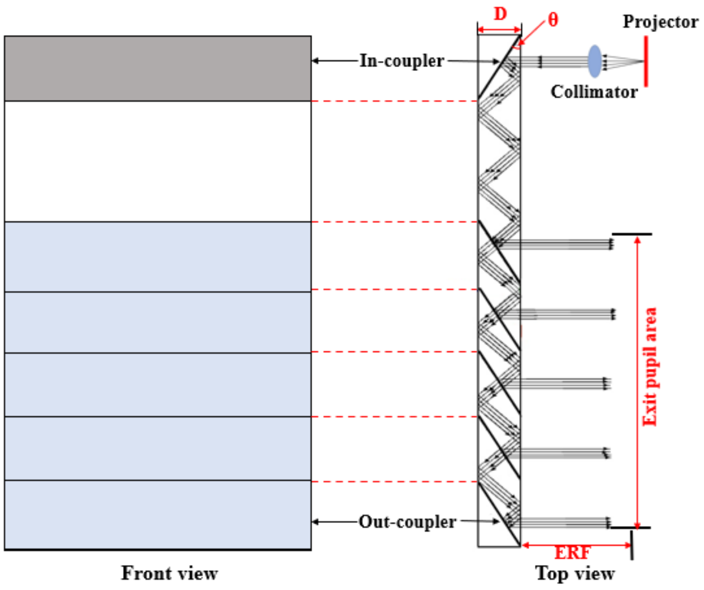

Figure 6. 4 Schematic design of the geometrical waveguide

The light from the waveguide is in parallel and then focused on the image plane by the MLA, as shown in Figure 6.5, The virtual image (scales) is projected behind the image plane, where several different virtual depths can be calculated. The depths of the virtual scales from the waveguide can be derived as:

$$\omega = \frac{f_{sL} \times c}{c - f_{sL}} \tag{6.5}$$

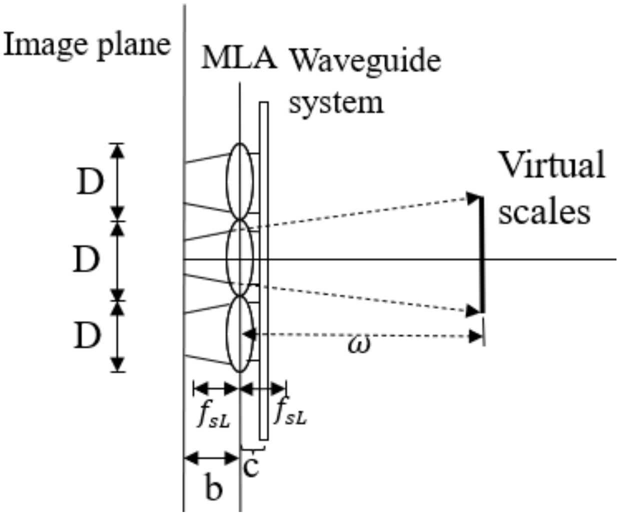

Figure 6. 5 Waveguide-MLA system

6.2.3 MLA

The main function of the micro-lens array is to discretize and decouple the light emitted from the same point on the surface of the object in various directions within a certain angle range. The degree of discretization is determined by the amount, focal lengths and apertures of the micro-lenses and the distance between the micro-lens and the imaging plane. The thickness of the micro-lens array is determined by the curvature and form factor of the sub-lens. As shown in Figure 6, the geometry of the sub-lens is plano-convex square. The curvatures of the sub-lenses can be divided into several groups to convert the light to different depths. The material of the lens array is fused silica. To ensure its accuracy, the micro-lens array must be able to tolerate various external forces or vibrations without deforming or altering its shape and should be able to reach a tolerance of 1/10 of a millimetr or better. Aside from the tolerance and external forces, other important parameters to consider when evaluating a micro-lens array include the number of lenses, their focal length, the size of the lenses, and the size of the image sensor. Additionally, the quality of the lenses themselves will also play an important role in the accuracy and performance of the micro-lens array [260, 261].

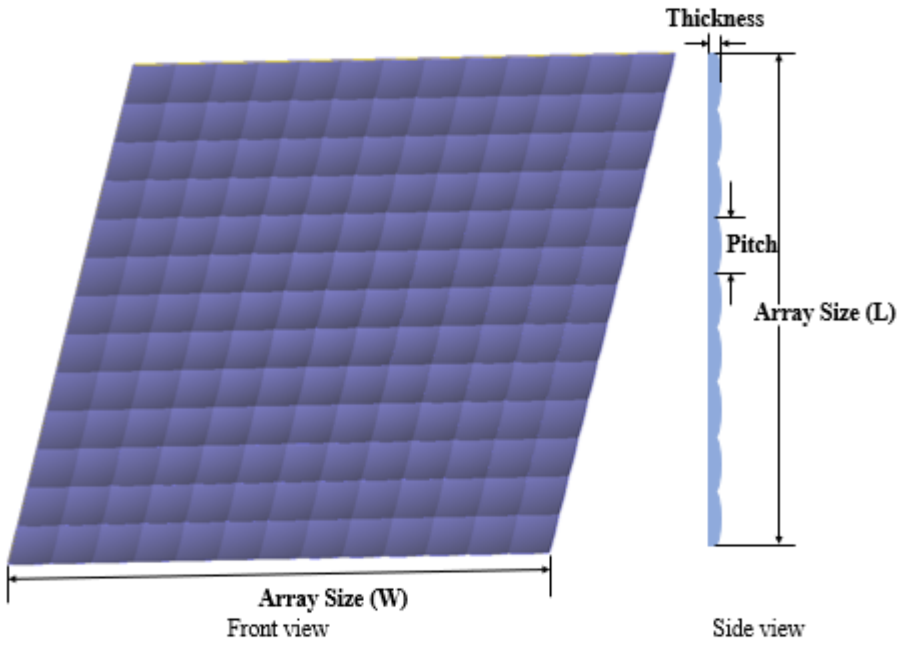

Figure 6. 6 Schematic design of the micro-lens array.

As shown in Figure 6.7, the profile S of the symmetrical plano-convex lens is given by

$$S = \frac{1}{R}\frac{r^2}{1+\sqrt{1-(K+1)\,r^2/R^2}} + \text{higher order terms} \tag{6.6}$$

where R is the radius of curvature, r is the distance to the optical axis and K is the aspherical constant. Thus, the radius of curvature can be derived as

$$R = (K+1)\frac{h}{2} + \frac{r^2}{2h} \tag{6.7}$$

where h is the height at the vertex. When K is 0, the lens is a spherical lens. The focal length of the lens can be derived as

$$f = \frac{R}{n-1} = \frac{h + r^2/h}{2(n-1)} \tag{6.8}$$

The F-number and he diffraction-limited resolution d along the y-axis are given by

$$F/\text{number} = \frac{EFL}{DEP} = \frac{f}{2r} \tag{6.9}$$

$$d \approx \frac{\lambda}{2NA} \tag{6.10}$$

where ERL is the focal length of the lens, DEP is the diameter of the entrance pupil and NA denotes the numerical aperture.

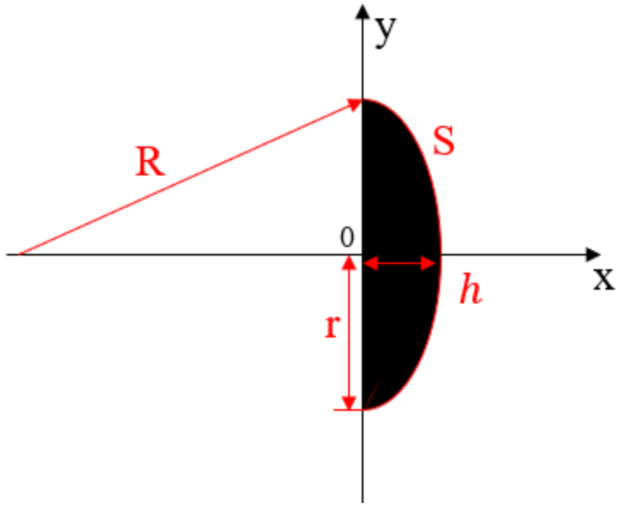

Figure 6. 7 The sub plano-convex lens

The light from the waveguide passes through the MLA and produces virtual scales at the same side of the objects, with different pre-set depths as shown in Figure 6.8. Thus, the image sensor can capture both virtual scales and real objects together, as shown in Figure 6.3.

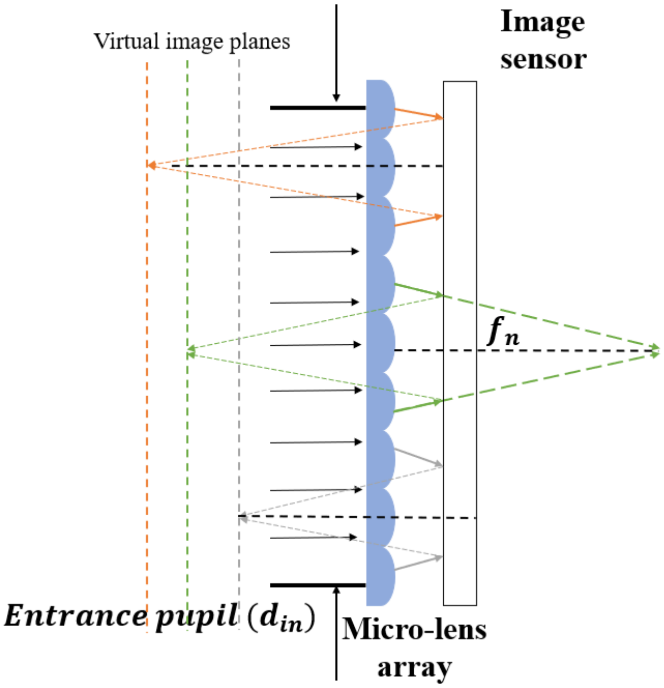

Figure 6. 8 Generation of spatial virtual scales through geometrical waveguide and micro-lens array

6.3 Experiments and discussion

The system is designed and simulated as shown in Figure 6.9. The micro-lens array focuses the virtual scales from the waveguide at different depths. The illumination distribution was captured from the waveguide and micro-lens array respectively by LightTools. The light from the waveguide is illuminated in Figure 6.10. From the ray-tracing analysis, the light distribution is uniform, and the stray light is greatly suppressed. The projected light is expanded several times by the folding and unfolding process. The gap between exit-pupil blocks is below the perceptible resolution of 60" of human eyes [157, 262]. An intact virtual image is displayed by the waveguide. The light illumination distribution passing through the micro-lens array is shown in Figure 6.11. The multi-focal micro-lens array forms 6 different lengths in this simulation, which could be reduced or extended flexibly depending on the requirements. Each depth is labeled using a different color in the figure for clearer illustration. The virtual depth is described as Eq. (6.5).

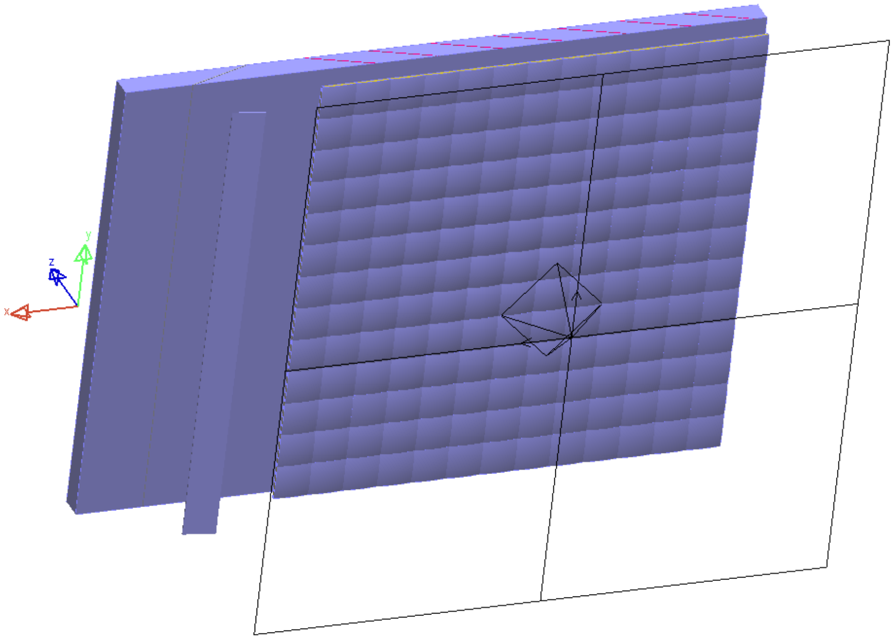

Figure 6. 9 Schematic diagram of waveguide-microlens system

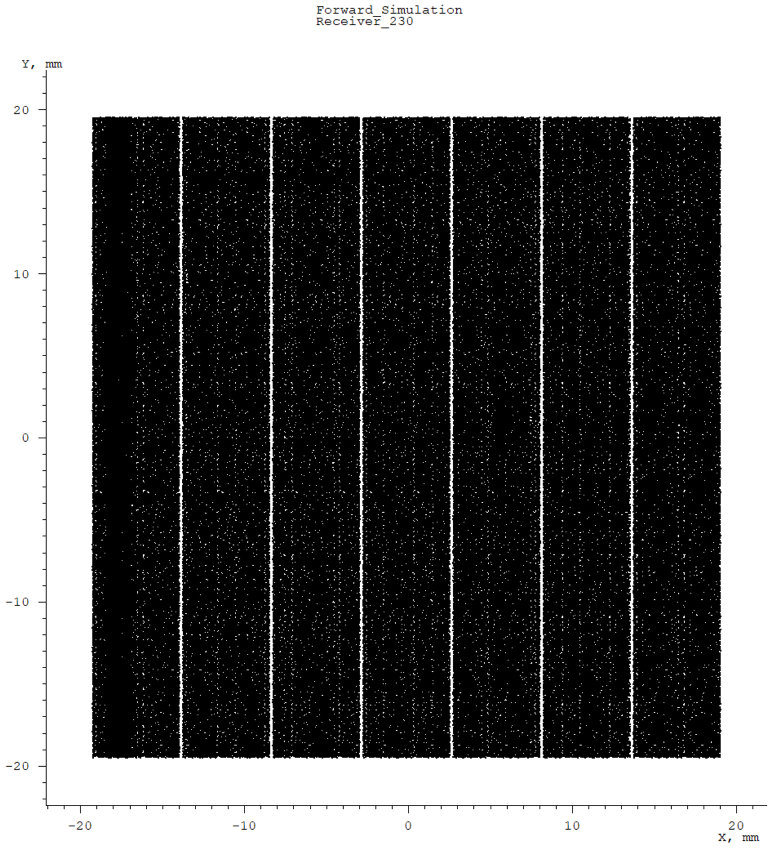

Figure 6. 10 The illumination of the light coupling-out of the waveguide.

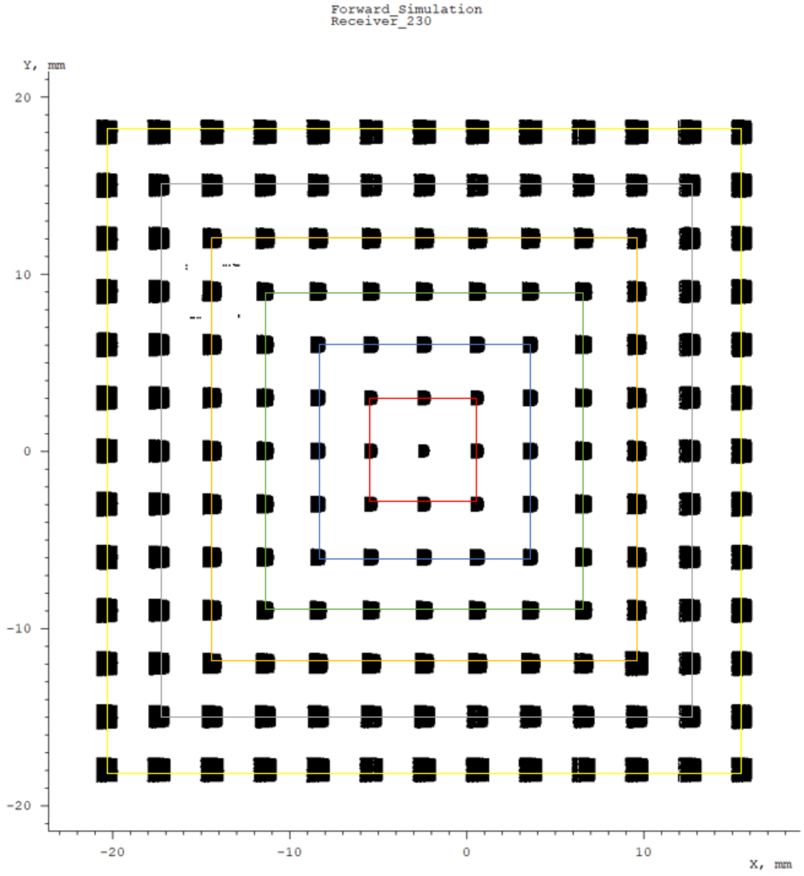

Figure 6. 11 The illumination of the light passing through the micro lens array from the waveguide.

To evaluate the depth of the images generated by a plenoptic camera, image synthetization is necessary. A synthesized image from a plenoptic camera is an image that is created by combining information from multiple micro-lenses. Several adjacent micro-lenses capture the light from their respective angles, creating several images to form one single image with one depth, like P_1, P_2, P_3 in Figure 6.12, They are aligned, corrected for distortion, and adjusted for brightness. This composite image is then used to measure the depth of the scene. Accordingly, an auxiliary coordinate system can be established. Thus, the depth estimation of each pixel in the synthesized images can be made by provided synthesizing algorithm [263]. To calculate the depth v of a plenoptic camera, the commercial synthesizing algorithm should consider the relative distance between the lens array and the image sensor, the size of the imaging sensors, the optical aberrations of the lenses, the number of lenses used, and the amount of light present in the scene. As shown in Figure 6. 12, the synthesizing algorithm is set up in geometry. All the positions of micro-lenses are fixed, thus the pixel positions (x,y,v) of the synthesizing image in the auxiliary coordinate system are quantitatively determined and can be calculated. The final color value is the weighted average of the color values at the pixel locations computed on the image plane. The intensity attenuation from each pixel position on the image plane is essentially a measure of the amount of light being reflected or absorbed at that particular spot. This data can be used to calculate the integral data for a given scene, which refers to the amount of light received from each point in the scene. This integral data helps to assess depth more accurately by considering the different angles at which light is entering the camera's field of view

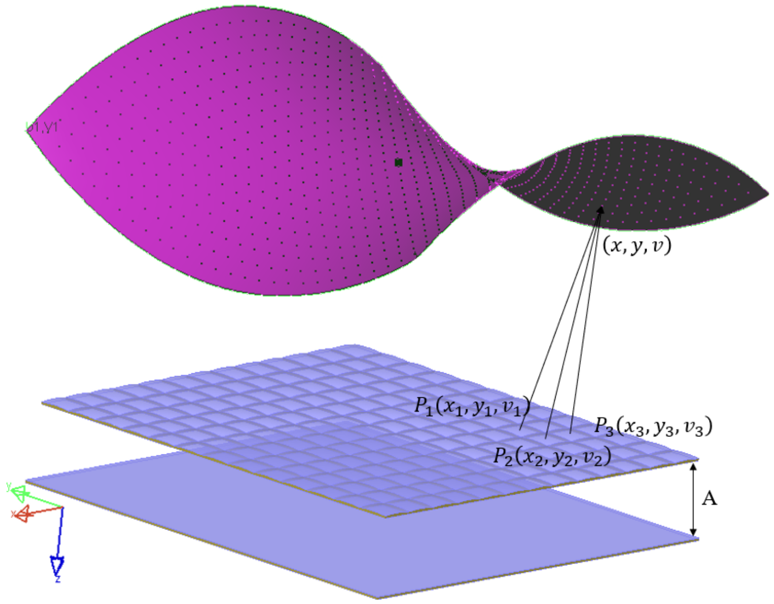

Figure 6. 12 Synthesizing images by the plenoptic camera

The real object captured on the image sensor is established in the auxiliary coordinate system by plenoptic camera, expressed as (x,y,v). The position of the virtual scales from the waveguide and MLA can be calculated in the virtual scale coordinate system. The positions of points in the virtual network can be expressed as $(\mathrm{m}, \mathrm{n}, \mathrm{q})$. The three-dimensional coordinate difference between the auxiliary coordinate system and the virtual scale coordinate system can be expressed as:

$$\Delta \mathrm{x} = \mathrm{M} \pm \frac{\mathrm{d}}{\mathrm{e}} |\mathrm{x} - \mathrm{m}| \tag{6.11}$$

$$\Delta \mathrm{y} = \mathrm{N} \pm \frac{\mathrm{d}}{\mathrm{e}} |\mathrm{y} - \mathrm{n}| \tag{6.12}$$

$$\Delta \mathrm{z} = \mathrm{P} \pm \frac{\mathrm{d}}{\mathrm{e}} |\mathrm{v} - \mathrm{q}| \tag{6.13}$$

where K is the translational shift of the x-axis, Q is the translational shift of the y-axis, P is the translational shift of the z-axis, d is the parallax error and e is the baseline of the system. The length of the baseline is the distance between the optical center of the auxiliary coordinate system and the optical center of the virtual scale coordinate system as shown in Figure 6.13. By comparing the two surfaces (images) captured in these two different coordinate systems, the coefficient of determination R^2 can be calculated based on the equation below which shows how closely these two surfaces fit each other.

$$R^2 = 1 - \frac{\sum_{i=1}^{n} \sigma_i (\omega - v)^2}{\sum_{i=1}^{n} \sigma_i \left(v - \frac{v + \omega}{2}\right)^2} \tag{6.14}$$

where ω is the calibration virtual depths (in the virtual coordinate system), v is the depth in the plenoptic camera (in the auxiliary coordinate system) and σ_i is the weight derived from the standard deviation of the target measurement (σ_i is calculated by taking the square root of the sum of all squared differences between the expected value and the measured value. This value then serves as an indicator of how much variance there is between the expected and measured value, with a higher value indicating more discrepancy). The closer the value of R^2 is to 1, the more accurate the depth information of the synthesizing image in the auxiliary coordinate system is. Thus, in this way, the system can achieve the aberration correction in real-time.

As R^2 can be calculated by correlating the points in the auxiliary coordinate system and virtual scale system, we can use an algorithm to actively search for the condition closest to R^2= 1. E.g., if it is indicated that a point's depth v (in the auxiliary coordinate system) and depth ω (in the virtual coordinate system) has a difference, which can be calculated by Eq. (12), we can correct the depth information of this point quantitatively. By calibrating and correcting the whole surface (not all the points need to be corrected), a new corrected surface (image) can be generated with more accurate depth information. Correspondingly, R^2 is closer to 1. Simultaneously, labels can be created and attached to each point of the original synthesizing image (in auxiliary coordinate system) with a certain depth error indicated.

Even sometimes due to the limited depth slices of plenoptic camera and a limited amount of virtual scales, it is impossible to correct each point to the ideal depth information (e.g. accurate depth is 60cm while in both coordinate systems we only have 61cm and 59cm focal length), by searching for the closest R^2 value to 1, we can still significantly improve the depth accuracy of 3D images to the best extent achievable.

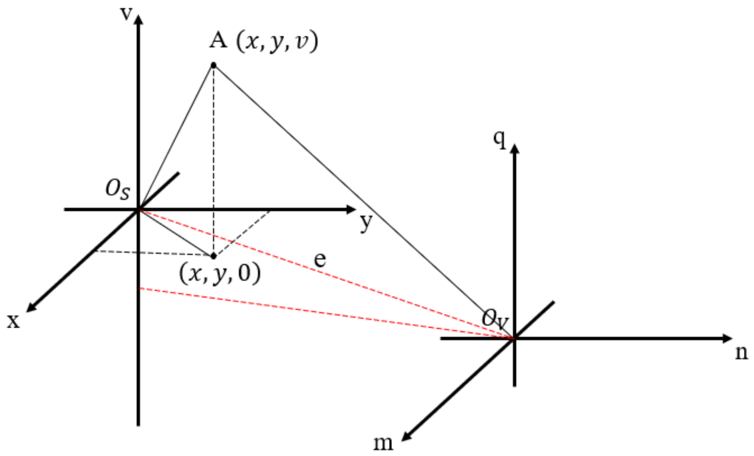

Figure 6. 13 Correction mechanism between the synthesized image system and virtual scale system

Depth estimation is suitable for application scenarios where the target is rich in texture features, that is, there must be a high contrast between the imaged features and the background. Texture features are almost a common requirement for all passive vision measurements, and active vision measurement technologies such as structured light artificially create a delicate and sharp contrast. At the same time, the baseline of the light field camera is relatively short, so the depth resolution of the far field is not good. Thus, the virtual scale network helps to recognise the position of the real item more accurately. The depths of the given virtual scales are pre-set once the optical hardware are installed in place with quantitative depth information feedback [264, 265]. The depths of the observed target can be calculated based on Eq. (6. 3). By calibrating the difference between these two coordinates, the error in depth can be calculated and corrected. Basically, the virtual scales can help achieve the 3D imaging in a faster and more accurate way through the following three mechanisms: 1) filter the complex background by focusing on the targeted real objects; 2) correct the depth errors, especially under high noises or poor lighting environment; 3) rapidly scope the targeted useful information without spending resources on useless signals for complex 3D modelling.

To testify the first mechanism, one meaningful experiment is to prove whether the virtual scales can help filter the complex background and recognise the targeted object as expected. In the experiment, we set a scene with complex background under insufficient light condition (100 nits), as shown in Figure 6.14. Figure 6.14 (a) is captured by plenoptic camera in insufficient light condition and (b) is the side view in normal light condition, which helps to observe the relative positions of the objects in the field of view. The back hand in Figure

6.14 (b) is defined as the hand near the red box, and the front hand is the other far from the box. Captured by plenoptic camera, the depth map can be received as shown in Figure 6.15 (a), which focused on the back hand without virtual scales. We can see although the box is put behind the front hand at a certain distance, there is a vague boundary between the front hand and the box (background) in this depth map. Then, we built virtual scales for the observed targets, one focused on the back hand and the other one focused on the front hand. For both, we first focused on the virtual scales, as the back hand or front hand was placed in the same plane with the pre-set virtual scales, they were simultaneously focused. And only this plane was focused, so the box (and the other patterns in the background) was filtered effectively in the depth map as shown in Figure 6.15 (b) and (c). Comparing Figure 6.15 (a) and (b), they both focused on the same position, but the one with virtual scales can filter the background. The observed target can be recognized more accurately with virtual scales. A significant part of background is quickly filtered, and the useful information is scoped. In the insufficient lighting environment, the scales can be easily identified and provide accurate quantitative depth information. The system could actively search for such features that intersect the virtual scales on the focus plane with real objects.

(a) (b)

Figure 6. 14 Set-up scene (a) front view with complex background in insufficient light condition. (b) is the side view of the captured item in normal light condition.

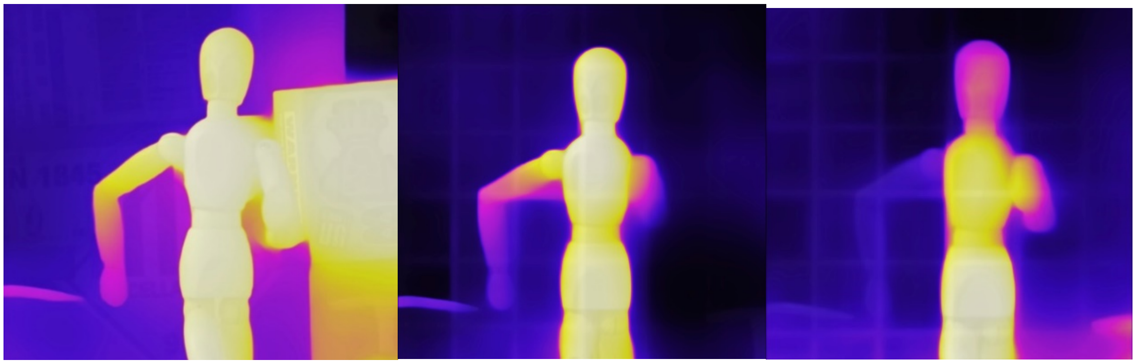

(a) (b) (c)

Figure 6. 15 Depth map of the set-up scene. (a) focusing on back hand without virtual scales; (b) focusing on back hand with virtual scales and (c) on front hand with virtual scales

To find out if there is some difference in the depth information between the captured images with and without virtual scales, Figure 6.15 is transferred to greyscale images as Figure 6.16.

(a) (b) (c)

Figure 6. 16 Brightness greyscale images. (a) is focus on back hand, (b) is focus on back hand with virtual scale and (b) is focus on front hand with virtual scale

Based on Figure 6.14 (b), the distance between the head and the back hand can be measured, which is 8 cm in depth. We set the distance as z-value. Besides, we set the depth map from back hand to front hand as from 0.0 to 1.0. The linearly transform is applied to formalise the z-value within the range [0,1]. The equation transforms the z-value to the depth value as:

$$F_{depth} = \frac{z - d_{front\ hand}}{d_{back\ hand} - d_{front\ hand}} \tag{6.14}$$

The graph can be received as:

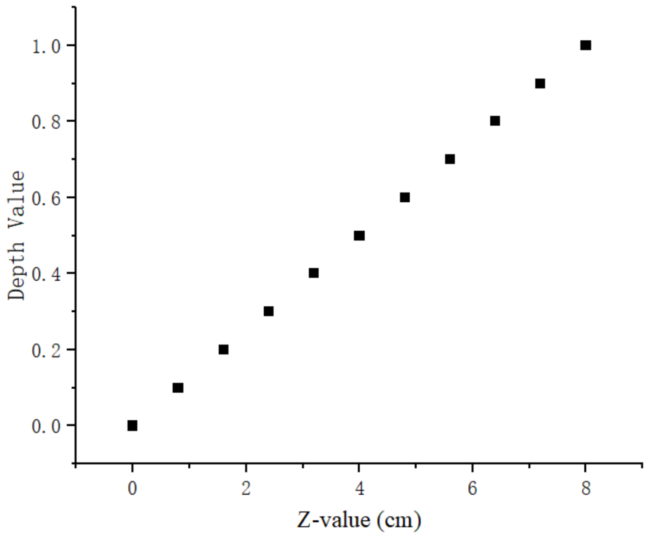

Figure 6. 17 The relation between the z-value and its corresponding depth value.

Based on the grayscale depth and depth value in Figure 6.17, Figure 6.16 (a) and (b) can be converted to Figure 6.18 by standard greyscale value chart. The depth is divided into 8 sections from 0.0 to 1.0. The line recognises the greyscale at each section and export corresponding value. The gradients of these two lines are hard to fit, which means there are errors in depth estimation between these two images. This demonstrates that the image captured by the plenoptic camera produced some error in the depth information so inaccurate 3D models would be generated if such information was adopted. This is not unusual in the daily practice due to the extreme complexity of environment and variable lighting conditions. As the result, it is important to correct the depth error quantitatively for accurate 3D imaging, which is exactly the objective of inventing this virtual-scales technology.

After receiving and processing the data from Figure 6.15 (a) and (b), the data can be calibrated by the algorithm as shown in Figure 6.19. After synthesizing the surfaces with and without virtual scales, the coefficient of determination R^2 can be calculated which shows how closely these two surfaces fit each other. The closer the value of determination is to 1, the less the depth error is. So, we can use the R^2 to evaluate if the depth error is reduced to an acceptable level.

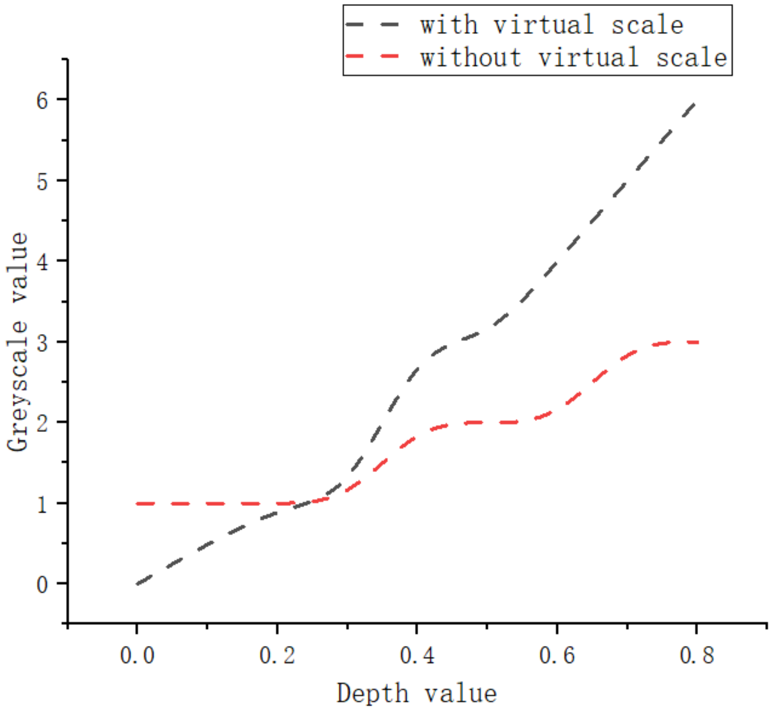

Figure 6. 18 Greyscale depth with depth value

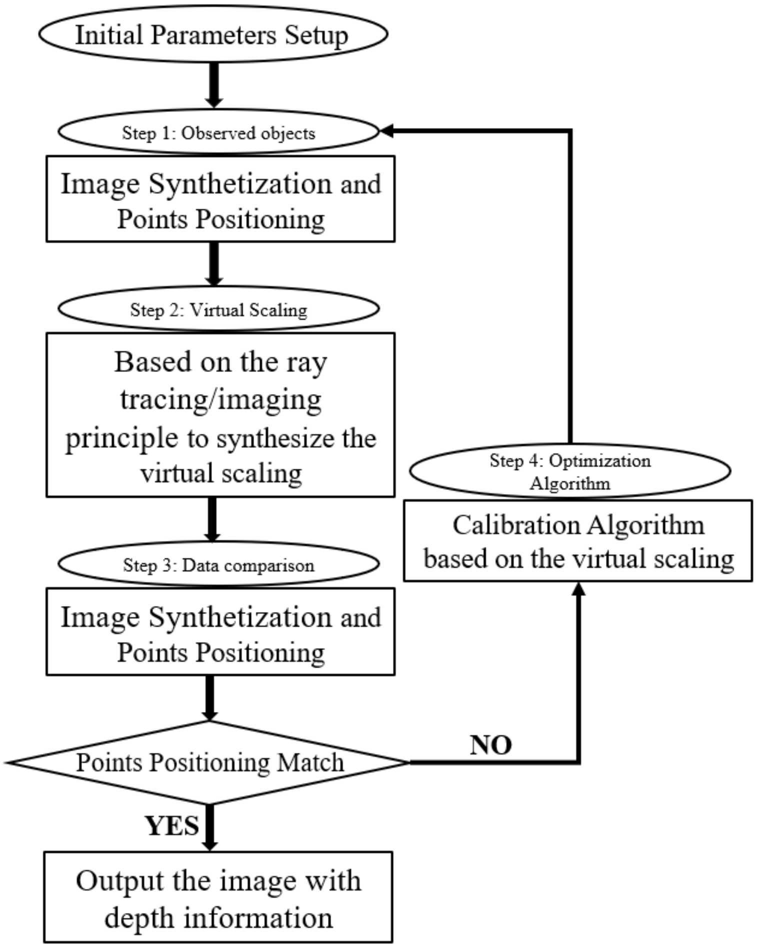

Figure 6. 19 The flow chat of the calibration algorithm of the depth information

Based on Figure 6.16 (b) and (c), the brightness is parsed into image histogram, as shown in Figure 6.20. Figure 6.20 (a) is the image histogram of Figure 6.16 (b) and (b) is the image histogram of Figure 6.16 (c). The horizontal axis represents the brightness level, from 0 (dark tone) on the left to 255 (bright tone) on the right, thus the brightness level of the photo is divided into 256 levels. The vertical axis represents the number of pixels under each brightness level. The higher the value, the greater the number of pixels of the light and shade value, and the larger the area occupied in the screen. Focusing on different positions contain different depth information. More virtual scales can be used to obtain more depth information for the reconstruction of the 3D model. More layers of virtual scales also help to distinguish the space with finer grids so the more accurately that the depth of the original object can be restored. Figure 6.21 shows the reconstructed 3D model based on Figure 6.15 (b) and (c) by the self-developed algorithm of depth-of-field (DOF), it can be seen the background of the scene is filtered out. Besides, virtual scales avoid wasting processing resources on the useless information and significantly save processing time [266, 267], which benefit much to the low-latency response for real-time tasks like gesture recognition.

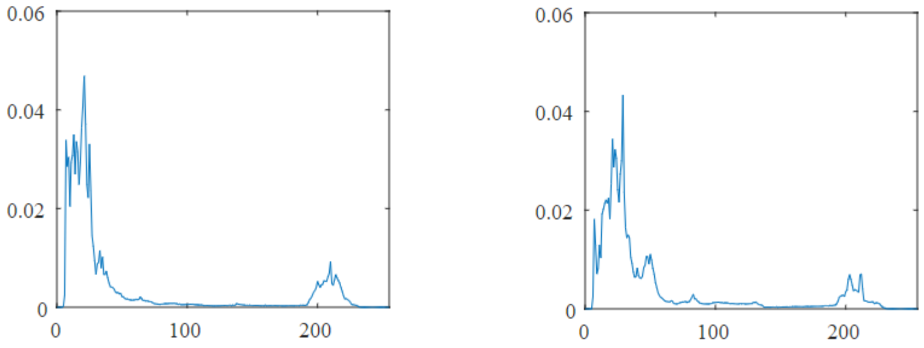

(a) (b)

Figure 6. 20 Depth estimation by AI depth estimation algorithms. (a) is the image histogram of Figure 16 (b) and (b) is the image histogram of Figure 6.16 (c).

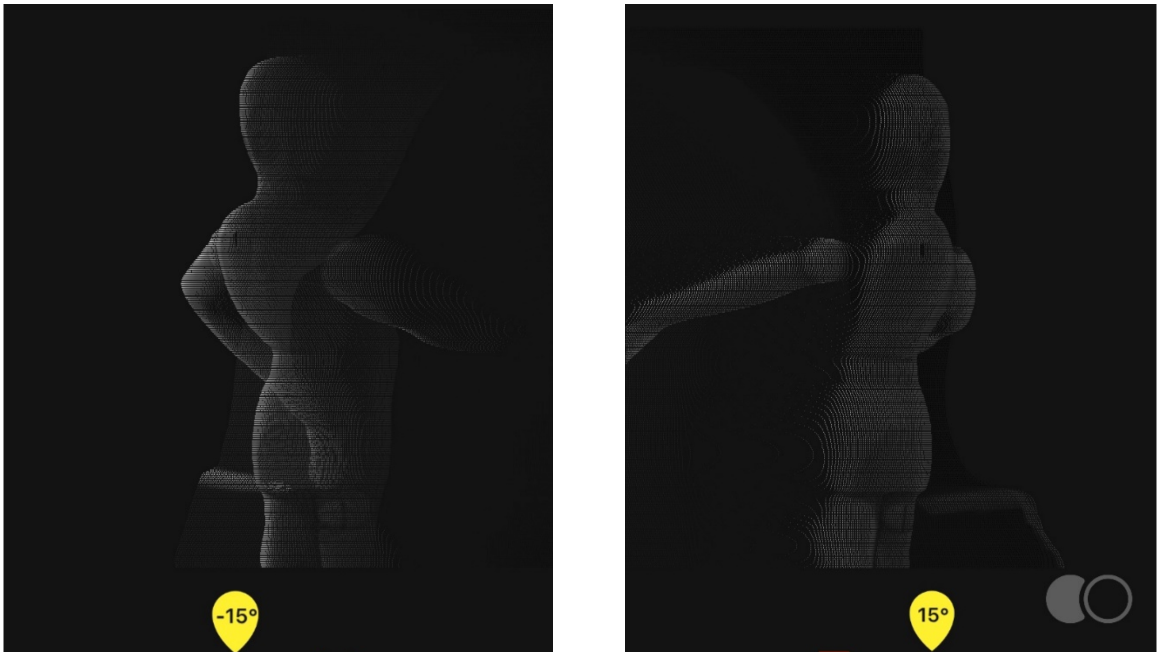

(a) (b)

Figure 6. 21. Depth simulation result by AI. (a) is simulated -15° information and (b) is simulated 15° information restored by AI algorithm.

As discussed above, the observed target can be recognized more easily and quickly with virtual scales. The part of background is quickly filtered, and the useful information is effectively scoped. In the complex or insufficient lighting background, the easily discernible scaling can provide accurate quantitative depth information. The system could actively search for such features of real objects that intersect the virtual scales on the focus plane. More virtual scales help to reconstruct the 3D model with finer depth information, in a faster way than conventional plenoptic cameras. Recalling the gesture recognition shown in Figure 6.2, it is possible to distinguish the fingers using such virtual scales for more accurate recognition and consume less processing time for 3D modelling of the targeted object. This could be extended to more diversified real-time application scenarios and industrial applications for which current plenoptic cameras cannot make an excellent balance between the response time and accuracy.

6.4 Summary

In this chapter, an innovative optical system is developed to utilize the virtual scale networks to measure and correct the depth error produced by the plenoptic cameras. The system combines the geometrical waveguide and micro-lens array to work based on the AR mechanism for scoping the targeted information more effectively and accurately. The experiments proved that virtual scales could filter complex background effectively and focus on the targeted object rapidly. By exploiting the parameter relationship between the images with and without virtual scales, a geometric calibration method was proposed to correct the depth error caused by the plenoptic cameras. The coefficient of determination R^2 is presented to evaluate the depth accuracy of the 3D images. The closer the value of R^2 is to 1, the more accurate the depth information contains in the image. In this way, the system can achieve active calibration and correction of image depth for more accurate 3D imaging than conventional plenoptic cameras. Experiments also demonstrated the rapid scoping of targeted useful information without spending many resources on useless signals for complex 3D modelling, thus achieved low-latency real-time response more accurately, even under poor lighting conditions.

Chapter 7 Conclusion and perspective

7.1 Scientific and technological deliverables

AR technology finds wide applications in the fields of aerospace, medical, educational and entertainment. The AR display is the key device in AR systems, undertaking the simulation of visual information. The thesis is introduced to overcome the challenges in developing a high-performance AR imaging system. The main research outputs can be summarized as follows:

(1) A design model for 2D geometrical waveguide is developed. The optimized model design method based on a large FOV is systematically discussed. The causes of stray light that results in the ghost images are analyzed in detail by means of ray tracing, and correspondingly the method of stray light suppression is proposed in terms of both design and manufacture. The optimized 2D geometrical waveguide successfully achieves 69° × 56° FOV with 22.6mm × 26mm eye box at 20mm eye relief.

(2) A wide-FOV dual-focal geometrical waveguide see-through display with a relatively thin structure is proposed. The causes of stray light in the dual-focal model are systematically analysed based on the non-sequential ray tracing. Correspondingly, a solution is presented to eliminate the stray light and reach uniform illumination at the entire exit pupil area. The achieved illumination uniformity of the dual-depth system reaches 0.83 and the intensity uniformity is over 0.7. The depth cues of the optimized design are at infinity and 100mm with 35° FOV, 38.46mm eye box and 20mm eye relief, which significantly improves the optical performance and reduces the dizziness caused by the VAC problem.

(3) An efficient and cost-competitive high-precision manufacturing process route for the geometrical waveguide component is developed. During the manufacturing process, the uniformity of the coating, the transmittance and reflectance ratio of the coating film, the flatness of the substrate, the surface roughness, the optical glue, and the cutting precision all have a significant impact on the geometric waveguide performance. The characterization methods and the tolerances of each step based on human eye resolution are presented.

(4) A new hybrid optical system is developed combining a geometrical waveguide and micro-lens array to project a virtual scaling network for quantitative depth calibration and fast tracking of targets. Such a methodology based on the AR working principle helps to rapidly track the targeted objects/features without reconstructing the full

range 3D model, significantly saving the processing time for a low- latency response. By establishing a geometrical model to quantitatively correlate the synthesizing images and the virtual scaling networks, it is proposed a method to calibrate and correct the depth error of images caused by the plenoptic cameras. Experiments proved that under complex background or insufficient light, in virtue of the virtual coordinate networks, targets can be effectively identified according to actual depth. The algorithm flow chart of correction of position depth error is given. In this way, the system can achieve faster and more accurate capturing of 3D objects in a real-time manner than conventional plenoptic cameras.

The innovative work of this thesis can be summarized as the following:

(1) Design geometrical waveguide model with a large field of view, and effectively improve the core optical performance indicators such as the FOV, eye box and eye relief through parameter optimization and material selection. Combined with ray tracing simulation and model optimization algorithm, it can effectively suppress the stray light of the optical system, thereby improving the system resolution and imaging quality.

(2) Design multi-focal stray-light-free optical waveguide models and imaging optimization algorithms. By increasing the number of focal planes to meet the 3D vision perception of the human eye and mitigate the VAC, the dizziness problem of long-term use can be reduced.

(3) An innovative optical system is developed by utilizing the virtual scale networks to measure and correct the depth error produced by the plenoptic cameras. The system combines the geometrical waveguide and micro-lens array to work based on the AR mechanism for scoping the targeted information more effectively and accurately.

7.2 Research outlook

(1) The user experience of observers is related to image quality, the weight and even the wearable ability of the device. Thus, the optical design and optical elements are crucial to the system performance. There are many requirements needed for different environment and users. It is hard to identify which specific parameter is most influential, however, the expected applications are always the driving factor in the optical design, including FOV, eye box, eye relief, weight, size, stray light, brightness, contrast, and resolution, etc. The breakthrough in AR technology may

require more than just a few design elements to be optimized. Even if a full-colour Micro LED display is introduced, it will only address the size of the display and will have little impact on the size of the optics. Thus, it is conceivable that it will be a long time before AR glasses with powerful features such as large FOV, small size, high brightness, and suitability for high performance applications.

(2) The AR displays currently on the market do not yet have the ability to render black pixels. Existing active optical technologies can only add color to the optics and do not generate black pixels. Therefore, a layer of LCD screen could be considered to produce black viewing pixels by shading, but this would have the disadvantage of reducing the light transmission of the optical display element by half and would also cause polarized ambient light. Besides, the higher the pixel density of the screen, the higher the requirements for the design of the time waveguide transfer function. Taking 1080p HD screens as an example, a better matched optical waveguide in the transmission path for brightness, picture quality loss degree is smaller, so the optical part of the maximum output of 1080p HD images, and minimize distortion, which for the design and process also put forward high requirements.

(3) Processors for AR-enabling tasks are steadily improving required capabilities for enterprise with optimal form factors. For example, graphics processors must be small, lightweight and highly power efficient in order to be placed within eyewear frames that remain comfortable to wear. Combined with eye-tracking capabilities, reliable voice and gesture recognition, these computational requirements add up, both in terms of battery consumption and heat production, which need to be properly and efficiently managed. Continuously providing AR experiences based on cloud-hosted services and content requires uninterrupted bandwidth and coverage are necessary for wherever customers with AR devices.

As other types of wearables, AR display represents a novel technology whose development and usage are still evolving. Both technological and business challenges are in the process of being addressed so that the displays are generally accepted in future as routine tools and become more recognized for their productivity-enhancing features.

References

[1] K. Lee, "Augmented Reality in Education and Training," *TechTrends,* vol. 56, no. 2, pp. 13-21, 2012.

[2] R. T. Azuma, "A survey of augmented reality," *Presence: teleoperators & virtual environments,* vol. 6, no. 4, pp. 355-385, 1997.

[3] P. Milgram and F. Kishino, "A taxonomy of mixed reality visual displays," *IEICE TRANSACTIONS on Information and Systems,* vol. 77, no. 12, pp. 1321-1329, 1994.

[4] J. P. Rolland, R. L. Holloway, and H. Fuchs, "Comparison of optical and video see-through, head-mounted displays," in *Telemanipulator and Telepresence Technologies*, 1995, vol. 2351: International Society for Optics and Photonics, pp. 293-308.

[5] C. Curran. "Breakthroughs in optics that are reshaping augmented reality." http://usblogs.pwc.com/emerging-technology/breakthroughs-in-optics-that-are-reshaping-augmented-reality/ (accessed.

[6] "Meeting the optical design challenges of mixed reality." https://www.electrooptics.com/analysis-opinion/meeting-optical-design-challenges-mixed-reality (accessed.

[7] K. Akşit, W. Lopes, J. Kim, P. Shirley, and D. Luebke, "Near-eye varifocal augmented reality display using see-through screens," *ACM Transactions on Graphics (TOG),* vol. 36, no. 6, p. 189, 2017.

[8] A. Maimone, A. Georgiou, and J. S. Kollin, "Holographic near-eye displays for virtual and augmented reality," *ACM Transactions on Graphics (TOG),* vol. 36, no. 4, p. 85, 2017.

[9] A. Bauer and J. P. Rolland, "Visual space assessment of two all-reflective, freeform, optical see-through head-worn displays," *Optics express,* vol. 22, no. 11, pp. 13155-13163, 2014.

[10] D. Cheng, Y. Wang, C. Xu, W. Song, and G. Jin, "Design of an ultra-thin near-eye display with geometrical waveguide and freeform optics," *Optics express,* vol. 22, no. 17, pp. 20705-20719, 2014.

[11] H. Benko, E. Ofek, F. Zheng, and A. D. Wilson, "Fovear: Combining an optically see-through near-eye display with projector-based spatial augmented reality," in

Proceedings of the 28th Annual ACM Symposium on User Interface Software & Technology, 2015: ACM, pp. 129-135.

[12] D. Lanman and D. Luebke, "Near-eye light field displays," *ACM Transactions on Graphics (TOG),* vol. 32, no. 6, p. 220, 2013.

[13] A. B. Pratt, "Weapon," ed: Google Patents, 1916.

[14] H. Li, X. Zhang, G. Shi, H. Qu, Y. Wu, and J. Zhang, "Review and analysis of avionic helmet-mounted displays," *Optical Engineering,* vol. 52, no. 11, p. 110901, 2013.

[15] M.-U. Erdenebat, Y.-T. Lim, K.-C. Kwon, N. Darkhanbaatar, and N. Kim, "Waveguide-Type Head-Mounted Display System for AR Application," in *State of the Art Virtual Reality and Augmented Reality Knowhow*: IntechOpen, 2018.

[16] I. E. Sutherland, "A head-mounted three dimensional display," in *Proceedings of the December 9-11, 1968, fall joint computer conference, part I*, 1968: ACM, pp. 757-764.

[17] N. George and G. Morris, "Optical matched filtering in noncoherent illumination," in *Current Trends in Optics*, 1981, p. 80.

[18] Q.-L. Zhao, Z.-Q. Wang, and T.-G. Liu, "Design of optical system for head-mounted micro-display," *Optik,* vol. 118, no. 1, pp. 29-33, 2007.

[19] P. Gilboa and S. Abraham, "Third-generation DASH helmet," *Displays,* vol. 15, no. 2, pp. 106-109, 1994.

[20] J. Carmigniani, B. Furht, M. Anisetti, P. Ceravolo, E. Damiani, and M. Ivkovic, "Augmented reality technologies, systems and applications," *Multimedia tools and applications,* vol. 51, no. 1, pp. 341-377, 2011.

[21] H. Hoshi, N. Taniguchi, H. Morishima, T. Akiyama, S. Yamazaki, and A. Okuyama, "Off-axial HMD optical system consisting of aspherical surfaces without rotational symmetry," in *Stereoscopic Displays and Virtual Reality Systems III*, 1996, vol. 2653: International Society for Optics and Photonics, pp. 234-243.

[22] G. Evans, J. Miller, M. I. Pena, A. MacAllister, and E. Winer, "Evaluating the Microsoft HoloLens through an augmented reality assembly application," in *Degraded environments: sensing, processing, and display 2017*, 2017, vol. 10197: International Society for Optics and Photonics, p. 101970V.

[23] T. Ando and M. Okamoto, "Head-mounted display using a holographic optical element," *Three-Dimensional Television, Video and Display Technologies,* vol. 3293, pp. 183-189, 1998.

[24] J. Horwitz. "Magic Leap One’s field of view leak signals another AR disappointment." https://venturebeat.com/2018/07/31/magic-leap-ones-field-of-view-leak-signals-another-ar-disappointment/ (accessed.

[25] F. Liu. "From off-axis to waveguide technology: Explain the past and the future of AR display." https://www.leiphone.com/news/201703/M65F9oVoURab2qE9.html (accessed.

[26] Microsoft. "Hololens." https://www.microsoft.com/en-us/hololens (accessed.

[27] Lumus. "Waveguide." https://lumusvision.com/technology/ (accessed.

[28] J. E. Melzer and C. Spitzer, "Head-mounted displays," *Digital Avionics Handbook,* 2001.

[29] S. Chi, Y. Yin, G. Yaoyuneyong, and E. Johnson, "Augmented Reality: An Overview and Five Directions for AR in Education," *Journal of Educational Technology Development & Exchange,* vol. 119, no. 4, pp. 119-140, 2011.

[30] S. C.-Y. Yuen, G. Yaoyuneyong, and E. Johnson, "Augmented reality: An overview and five directions for AR in education," *Journal of Educational Technology Development and Exchange (JETDE),* vol. 4, no. 1, p. 11, 2011.

[31] I. Radu, "Augmented reality in education: A meta-review and cross-media analysis," *Personal & Ubiquitous Computing,* vol. 18, no. 6, pp. 1533-1543, 2014.

[32] C. Moro, Z. Štromberga, A. Raikos, and A. Stirling, "The effectiveness of virtual and augmented reality in health sciences and medical anatomy," *Anatomical sciences education,* vol. 10, no. 6, pp. 549-559, 2017.

[33] S.-L. Tang, C.-K. Kwoh, M.-Y. Teo, N. W. Sing, and K.-V. Ling, "Augmented reality systems for medical applications," *IEEE engineering in medicine and biology magazine,* vol. 17, no. 3, pp. 49-58, 1998.

[34] T. Sielhorst, M. Feuerstein, and N. Navab, "Advanced medical displays: A literature review of augmented reality," *Journal of Display Technology,* vol. 4, no. 4, pp. 451-467, 2008.

[35] C. Kamphuis, E. Barsom, M. Schijven, and N. Christoph, "Augmented reality in medical education?," *Perspectives on medical education,* vol. 3, no. 4, pp. 300-311, 2014.

[36] D. I. Han, T. Jung, and A. Gibson, *Dublin AR: Implementing Augmented Reality in Tourism*. Springer International Publishing, 2013.

[37] J. Í. Kysela and P. ?torková, "Using Augmented Reality as a Medium for Teaching History and Tourism," *Procedia - Social and Behavioral Sciences,* vol. 174, pp. 926-931, 2015.

[38] O. Danielsson, M. Holm, and A. Syberfeldt, "Augmented reality smart glasses in industrial assembly: Current status and future challenges," *Journal of Industrial Information Integration,* vol. 20, p. 100175, 2020.

[39] M. A. Livingston *et al.*, "An augmented reality system for military operations in urban terrain," 2002.

[40] M. A. Livingston *et al.*, "Military applications of augmented reality," *Handbook of augmented reality,* pp. 671-706, 2011.

[41] A. Mejías Borrero and J. Andújar Márquez, "A pilot study of the effectiveness of augmented reality to enhance the use of remote labs in electrical engineering education," *Journal of science education and technology,* vol. 21, no. 5, pp. 540-557, 2012.

[42] W. Piekarski and B. Thomas, "ARQuake: the outdoor augmented reality gaming system," *Communications of the ACM,* vol. 45, no. 1, pp. 36-38, 2002.

[43] C. Stapleton, C. Hughes, M. Moshell, P. Micikevicius, and M. Altman, "Applying mixed reality to entertainment," *Computer,* vol. 35, no. 12, pp. 122-124, 2002.

[44] I. Barakonyi and D. Schmalstieg, "Augmented reality agents in the development pipeline of computer entertainment," in *International Conference on Entertainment Computing*, 2005: Springer, pp. 345-356.

[45] Y. Zhou, J. Zhang, and F. Fang, "Advances in the design of optical see-through displays," *Advanced Optical Technologies,* vol. 9, pp. 167-186, 2020.

[46] K. GUTTAG. "“Why is making good AR displays so hard?” Article by Daniel Wagner, the CTO of Daqri." https://kguttag.com/2019/08/09/why-is-making-good-ar-displays-so-hard-article-by-daniel-wagner-the-cto-of-daqri/ (accessed.

[47] S. Park, S. Bokijonov, and Y. Choi, "Review of microsoft hololens applications over the past five years," *Applied Sciences,* vol. 11, no. 16, p. 7259, 2021.

[48] K. GUTTAG. "Magic Leap 2 at SPIE AR/VR/MR 2022." https://kguttag.com/2022/01/31/magic-leap-2-at-spie-ar-vr-mr-2022/ (accessed.

[49] K. GUTTAG. "Magic Leap Review Part 2 – Image Issues." https://kguttag.com/2018/10/01/magic-leap-review-part-2-image-issues/ (accessed.

[50] K. GUTTAG. "Nreal Teardown: Part 3, Pictures Through the Lens." https://kguttag.com/2021/06/07/nreal-teardown-part-3-pictures-through-the-lens/ (accessed.

[51] K. GUTTAG. "Hololens 2 Display Evaluation (Part 6: Microsoft's FUD on Photographs)." https://kguttag.com/2020/09/06/hololens-2-display-evaluation-part-6-microsofts-fud-on-photographs/ (accessed.

[52] J. T. Holladay *et al.*, "Optical performance of multifocal intraocular lenses," *Journal of Cataract & Refractive Surgery,* vol. 16, no. 4, pp. 413-422, 1990.

[53] N. Vlugt, "An Ontological Enquiry into the MagicLeap and Augmented Reality," University of Twente, 2017.

[54] L. Thibos, A. Bradley, D. Still, X. Zhang, and P. Howarth, "Theory and measurement of ocular chromatic aberration," *Vision research,* vol. 30, no. 1, pp. 33-49, 1990.

[55] R. Bedford and G. Wyszecki, "Axial chromatic aberration of the human eye," *JOSA,* vol. 47, no. 6, pp. 564_1-565, 1957.

[56] A. Seidemann and F. Schaeffel, "Effects of longitudinal chromatic aberration on accommodation and emmetropization," *Vision research,* vol. 42, no. 21, pp. 2409-2417, 2002.

[57] S. A. Levin, "Dispersion and population interactions," *The American Naturalist,* vol. 108, no. 960, pp. 207-228, 1974.

[58] P. A. Moreau, E. Toninelli, T. Gregory, and M. J. Padgett, "Ghost imaging using optical correlations," *Laser & Photonics Reviews,* vol. 12, no. 1, p. 1700143, 2018.

[59] K. W. C. Chan, M. N. O'Sullivan, and R. W. Boyd, "Two-color ghost imaging," *Physical Review A,* vol. 79, no. 3, p. 033808, 2009.

[60] K. GUTTAG. "CES 2019 – AR and other Interesting Display Technology." https://kguttag.com/2019/01/24/ces-2019-ar-and-other-interesting-display-technology/ (accessed.

[61] F. L. Kooi and A. Toet, "Visual comfort of binocular and 3D displays," *Displays,* vol. 25, no. 2-3, pp. 99-108, 2004.

[62] M. Lambooij, W. Ijsselsteijn, M. Fortuin, and I. Heynderickx, "Visual Discomfort and Visual Fatigue of Stereoscopic Displays: A Review," *Journal of Imaging Science & Technology,* vol. volume 53, no. 3, pp. 30201-1-30201-14(14), 2009.

[63] M. Charbonneau, A. E. Priot, C. Roumes, and A. Léger, "Comparative effects of vergence/accommodation conflicts with different interocular separation and viewing distances," 2008.

[64] G. Kramida, "Resolving the Vergence-Accommodation Conflict in Head-Mounted Displays," *IEEE Transactions on Visualization & Computer Graphics,* vol. 22, no. 7, pp. 1912-1931, 2016.

[65] Y. Lu, B. Deng, Y. Yan, Z. Qie, J. Li, and J. Gui, "Vergence-accommodation conflict potential solutions in augmented reality head mounted displays," in *AIP Conference Proceedings*, 2019, vol. 2185, no. 1: AIP Publishing, p. 020001.

[66] D. M. Hoffman, A. R. Girshick, K. Akeley, and M. S. Banks, "Vergence–accommodation conflicts hinder visual performance and cause visual fatigue," *Journal of vision,* vol. 8, no. 3, pp. 33-33, 2008.

[67] E. H. Adelson and J. R. Bergen, "The Plenoptic Function and the Elements of Early Vision," *Computational Models of Visual Processing,* vol. 1, pp. 3-20, 1991.

[68] R. Suryakumar, J. P. Meyers, E. L. Irving, and W. R. Bobier, "Vergence accommodation and monocular closed loop blur accommodation have similar dynamic characteristics," *Vision Research,* vol. 47, no. 3, pp. 327-337, 2007.

[69] M. Sungchul, P. Min-Chul, P. Sangin, and W. Mincheol, "SSVEP and ERP measurement of cognitive fatigue caused by stereoscopic 3D," *Neuroscience Letters,* vol. 525, no. 2, pp. 89-94, 2012.

[70] H. Hagura, "Study of asthenopia caused by the viewing of stereoscopic images: measurement by MEG and other devices," in *Electronic Imaging*, 2006.

[71] J. Frey, L. Pommereau, F. Lotte, and M. Hachet, "Assessing the Zone of Comfort in Stereoscopic Displays using EEG," in *Chi 14 Extended Abstracts on Human Factors in Computing Systems*, 2014.

[72] K. Akşit *et al.*, "Varifocal virtuality: a novel optical layout for near-eye display," in *ACM SIGGRAPH 2017 Emerging Technologies*, 2017: ACM, p. 25.

[73] D. Dunn *et al.*, "Wide field of view varifocal near-eye display using see-through deformable membrane mirrors," *IEEE transactions on visualization and computer graphics,* vol. 23, no. 4, pp. 1322-1331, 2017.

[74] H. Davson. "human eye anatomy." https://www.britannica.com/science/human-eye (accessed.

[75] D. Georgiev. "What is the maximum human field of vision?" https://www.quora.com/What-is-the-maximum-human-field-of-vision (accessed.

[76] W. Chao, Y. Liu, W. Meng, Z. Ke, and S. Ma, "Incorporating Non-sequential Behavior into Click Models," in *the 38th International ACM SIGIR Conference*, 2015.

[77] J. Liang, . and D. R. Williams, "Aberrations and retinal image quality of the normal human eye," *Journal of the Optical Society of America A Optics Image Science & Vision,* vol. 14, no. 11, p. 2873, 1997.

[78] H.-W. Chen, J.-H. Lee, B.-Y. Lin, S. Chen, and S.-T. Wu, "Liquid crystal display and organic light-emitting diode display: present status and future perspectives," *Light: Science & Applications,* vol. 7, no. 3, pp. 17168-17168, 2018.

[79] D. Berreman and W. Heffner, "New bistable cholesteric liquid-crystal display," *Applied Physics Letters,* vol. 37, no. 1, pp. 109-111, 1980.

[80] H. Hasebe, H. Takatsu, Y. Iimura, and S. Kobayashi, "Effect of polymer network made of liquid crystalline diacrylate on characteristics of liquid crystal display device," *Japanese journal of applied physics,* vol. 33, no. 11R, p. 6245, 1994.

[81] J. Kalinowski, *Organic Light-Emitting Diodes: Principles, Characteristics & Processes*. CRC press, 2018.

[82] Y.-S. Tyan, "Organic light-emitting-diode lighting overview," *Journal of Photonics for Energy,* vol. 1, no. 1, p. 011009, 2011.

[83] B. Geffroy, P. Le Roy, and C. Prat, "Organic light-emitting diode (OLED) technology: materials, devices and display technologies," *Polymer international,* vol. 55, no. 6, pp. 572-582, 2006.

[84] H. J. Jang *et al.*, "Progress of display performances: AR, VR, QLED, OLED, and TFT," *Journal of Information Display,* vol. 20, no. 1, pp. 1-8, 2019.

[85] L. He *et al.*, "Graphitic C3N4 quantum dots for next-generation QLED displays," *Materials Today,* vol. 22, pp. 76-84, 2019.

[86] T. Moynihan, "What are quantum dots, and why do I want them in my TV," *WIRED. com,* 2015.

[87] Z. Zhang, Z. You, and D. Chu, "Fundamentals of phase-only liquid crystal on silicon (LCOS) devices," *Light: Science & Applications,* vol. 3, no. 10, pp. e213-e213, 2014.

[88] G. Lazarev, A. Hermerschmidt, S. Krüger, and S. Osten, "LCOS spatial light modulators: trends and applications," *Optical Imaging and Metrology: Advanced Technologies,* vol. 1, 2012.

[89] V. Jülch, "Comparison of electricity storage options using levelized cost of storage (LCOS) method," *Applied energy,* vol. 183, pp. 1594-1606, 2016.

[90] D. Vettese, "Liquid crystal on silicon," *Nature Photonics,* vol. 4, no. 11, pp. 752-754, 2010.

[91] J. A. Castellano, "Handbook of display technology," 2012.

[92] D. H. Brainard, D. G. Pelli, and T. Robson, "Display characterization," *Signal Process,* vol. 80, pp. 2,067-2,070, 2002.

[93] D. Matsumoto, S. H. Yoo, S. Hirayama, and G. Petrova, "Development and validation of a measure of display rule knowledge: the display rule assessment inventory," *Emotion,* vol. 5, no. 1, p. 23, 2005.

[94] H. J. Jang, J. Y. Lee, G. W. Baek, J. Kwak, and J.-H. Park, "Progress in the development of the display performance of AR, VR, QLED and OLED devices in recent years," *Journal of Information Display,* vol. 23, no. 1, pp. 1-17, 2022.

[95] D. Ren, T. Goldschwendt, Y. Chang, and T. Höllerer, "Evaluating wide-field-of-view augmented reality with mixed reality simulation," in *2016 IEEE Virtual Reality (VR)*, 2016: IEEE, pp. 93-102.

[96] D. Lanman and D. Luebke, "Near-eye light field displays," *ACM Transactions on Graphics (TOG),* vol. 32, no. 6, pp. 1-10, 2013.

[97] S.-B. Kim and J.-H. Park, "Optical see-through Maxwellian near-to-eye display with an enlarged eyebox," *Optics letters,* vol. 43, no. 4, pp. 767-770, 2018.

[98] P. C. Teo and D. J. Heeger, "Perceptual image distortion," in *Proceedings of 1st International Conference on Image Processing*, 1994, vol. 2: IEEE, pp. 982-986.

[99] D. L. Schacter, S. A. Guerin, and P. L. S. Jacques, "Memory distortion: An adaptive perspective," *Trends in cognitive sciences,* vol. 15, no. 10, pp. 467-474, 2011.

[100] J. I. Nicholls, "The measurement of distortion: theoretical considerations," *The Journal of prosthetic dentistry,* vol. 37, no. 5, pp. 578-586, 1977.

[101] L. Gu, D. Cheng, Q. Wang, Q. Hou, and Y. Wang, "Design of a two-dimensional stray-light-free geometrical waveguide head-up display," *Applied optics,* vol. 57, no. 31, pp. 9246-9256, 2018.

[102] Y. Zhou, J. Zhang, and F. Fang, "Stray light analysis and design optimization of geometrical waveguide," *Advanced Optical Technologies,* vol. 10, no. 1, pp. 71-79, 2021.

[103] J. C. Stevens and S. S. Stevens, "Brightness function: Effects of adaptation," *JOSA,* vol. 53, no. 3, pp. 375-385, 1963.

[104] R. B. Lotto and D. Purves, "The effects of color on brightness," *Nature neuroscience,* vol. 2, no. 11, pp. 1010-1014, 1999.

[105] L. E. Arend and B. Spehar, "Lightness, brightness, and brightness contrast: 1. Illuminance variation," *Perception & Psychophysics,* vol. 54, no. 4, pp. 446-456, 1993.

[106] J.-L. Starck, F. Murtagh, E. J. Candès, and D. L. Donoho, "Gray and color image contrast enhancement by the curvelet transform," *IEEE Transactions on image processing,* vol. 12, no. 6, pp. 706-717, 2003.

[107] R. E. Hendrick and E. Mark Haacke, "Basic physics of MR contrast agents and maximization of image contrast," *Journal of Magnetic Resonance Imaging,* vol. 3, no. 1, pp. 137-148, 1993.

[108] T.-L. Ji, M. K. Sundareshan, and H. Roehrig, "Adaptive image contrast enhancement based on human visual properties," *IEEE transactions on medical imaging,* vol. 13, no. 4, pp. 573-586, 1994.

[109] Y. Zhou, J. Zhang, and F. Fang, "Vergence-accommodation conflict in optical see-through display: review and prospect," *Results in Optics,* p. 100160, 2021.

[110] L. Zhou *et al.*, "See-through near-eye displays enabling vision correction," *Optics Express,* vol. 25, no. 3, pp. 2130-2142, 2017.

[111] S. Lee *et al.*, "Foveated retinal optimization for see-through near-eye multi-layer displays," *IEEE Access,* vol. 6, pp. 2170-2180, 2017.

[112] J.-H. Park and S.-B. Kim, "Optical see-through holographic near-eye-display with eyebox steering and depth of field control," *Optics express,* vol. 26, no. 21, pp. 27076-27088, 2018.

[113] U. Fontana, F. Cutolo, N. Cattari, and V. Ferrari, "Closed–loop calibration for optical see-through near eye display with infinity focus," in *2018 IEEE International Symposium on Mixed and Augmented Reality Adjunct (ISMAR-Adjunct)*, 2018: IEEE, pp. 51-56.

[114] KarlG, "Near-Eye Bird Bath Optics Pros and Cons – And IMMY’s Different Approach," ed, March 3, 2017.

[115] A. Chandra. "Working Principle of Google Glass [Infographic]." http://www.techpuffs.com/38503/working-principle-of-google-glass-infographic (accessed.

[116] KarlG. "Disney-Lenovo AR Headset – (Part 1 Optics)." https://www.kguttag.com/2017/07/18/disney-lenovo-ar-headset-part-1/ (accessed.

[117] F. Fang, X. Zhang, A. Weckenmann, G. Zhang, and C. Evans, "Manufacturing and measurement of freeform optics," *CIRP Annals,* vol. 62, no. 2, pp. 823-846, 2013.

[118] S. Chen, C. F. Cheung, F. Zhang, and M. Liu, "Optimization of Tool Path for Uniform Scallop-Height in Ultra-precision Grinding of Free-form Surfaces," *Nanomanufacturing and Metrology,* vol. 2, no. 4, pp. 215-224, 2019.

[119] K. Tsurutani *et al.*, "65-2: Optical Attachment to Measure Both Eye-Box/FOV Characteristics for AR/VR Eyewear Displays," in *SID Symposium Digest of Technical Papers*, 2017, vol. 48, no. 1: Wiley Online Library, pp. 954-957.

[120] Y. Zhang and F. Fang, "Development of planar diffractive waveguides in optical see-through head-mounted displays," *Precision Engineering,* 2019.

[121] F. Fang, Y. Cheng, and X. Zhang, "Design of freeform optics," *Advanced Optical Technologies,* vol. 2, no. 5-6, pp. 445-453, 2013.

[122] H. Hong and J. Bahram, "A 3D integral imaging optical see-through head-mounted display," *Optics Express,* vol. 22, no. 11, pp. 13484-13491, 2014.

[123] H. Hong and C. Gao, "A compact eyetracked optical see-through head-mounted display," *Proceedings of SPIE - The International Society for Optical Engineering,* vol. 8288, no. 9, p. 46, 2012.

[124] H. Hong, H. Xinda, and G. Chunyu, "A high-resolution optical see-through head-mounted display with eyetracking capability," *Optics Express,* vol. 21, no. 25, p. 30993, 2013.

[125] H. Matsukuma, R. Ishizuka, M. Furuta, X. Li, Y. Shimizu, and W. Gao, "Reduction in Cross-Talk Errors in a Six-Degree-of-Freedom Surface Encoder," *Nanomanufacturing and Metrology,* vol. 2, no. 2, pp. 111-123, 2019.

[126] T. Blalock, K. Medicus, and D. G. Nelson, "Fabrication of freeform optics," in *Spie Optical Engineering + Applications*, 2015.

[127] A. W. Snyder and J. Love, *Optical waveguide theory*. Springer Science & Business Media, 2012.

[128] N. Marcuvitz, *Waveguide handbook* (no. 21). Iet, 1951.

[129] E. Snitzer, "Cylindrical dielectric waveguide modes," *JOSA,* vol. 51, no. 5, pp. 491-498, 1961.

[130] Kore. "Display technologies for Augmented and Virtual Reality." https://medium.com/inborn-experience/isplay-technologies-for-augmented-and-virtual-reality-82feca4e909f (accessed.

[131] KarlG, "Magic Leap Review Part 1 – The Terrible View Through Diffraction Gratings," ed, September 26, 2018.

[132] KarlG. "Magic Leap Review Part 2 – Image Issues." https://www.kguttag.com/2018/10/01/magic-leap-review-part-2-image-issues/ (accessed.

[133] P. Äyräs, P. Saarikko, and T. Levola, "Exit pupil expander with a large field of view based on diffractive optics," *Journal of the Society for Information Display,* vol. 17, no. 8, pp. 659-664, 2009.

[134] I. Vishik. "What is a diffraction grating?" https://www.quora.com/What-is-a-diffraction-grating (accessed.

[135] J. M. Miller, "Synthesis of pulse-width-modulated and inclined binary high-frequency diffractive optical elements," in *Practical Holography X*, 1996, vol. 2652: International Society for Optics and Photonics, pp. 182-187.

[136] N. De Beaucoudrey, J. M. Miller, P. H. Chavel, and J. P. Turunen, "Design and fabrication of high-efficiency inclined binary high-frequency gratings," in *Specification, Production, and Testing of Optical Components and Systems*, 1996, vol. 2775: International Society for Optics and Photonics, pp. 533-537.

[137] J. M. Miller, N. De Beaucoudrey, P. Chavel, J. Turunen, and E. Cambril, "Design and fabrication of binary slanted surface-relief gratings for a planar optical interconnection," *Applied optics,* vol. 36, no. 23, pp. 5717-5727, 1997.

[138] P. Laakkonen and T. Levola, "Method of producing a diffraction grating element," ed: Google Patents, 2012.

[139] L. O'Toole, C. Kang, and F. Fang, "Advances in Rotary Ultrasonic-Assisted Machining," *Nanomanufacturing and Metrology,* pp. 1-25.

[140] Y. Amitai, S. Reinhorn, and A. Friesem, "Visor-display design based on planar holographic optics," *Applied Optics,* vol. 34, no. 8, pp. 1352-1356, 1995.

[141] Y. Amitai, "Polarizing optical system," ed: Google Patents, 2017.

[142] Y. Amitai, "Compact head-mounted display system," ed: Google Patents, 2017.

[143] Y. Takatsuka, H. Yabu, K. Yoshimoto, and H. Takahashi, "Retinal Projection Display Using Diffractive Optical Element," in *Tenth International Conference on Intelligent Information Hiding & Multimedia Signal Processing*, 2014.

[144] B. C. Kress and P. Meyrueis, *Applied digital optics: from micro-optics to nanophotonics*. John Wiley & Sons, 2009.

[145] A. Frommer, "11-3: Invited paper: Lumus optical technology for AR," in *SID Symposium Digest of Technical Papers*, 2017, vol. 48, no. 1: Wiley Online Library, pp. 134-135.

[146] Z. Mu. "Godview Resin MR Glasses." https://www.leiphone.com/news/201808/fbOARlMHlRJsn6AB.html (accessed.

[147] H. Takahashi, S. Suzuki, K. Kato, and I. Nishi, "Arrayed-waveguide grating for wavelength division multi/demultiplexer with nanometre resolution," *Electronics Letters,* vol. 26, no. 2, pp. 87-88, 1990.

[148] "GodView Resin Arrayed Waveguide MR Glasses." https://optics.ofweek.com/2018-08/ART-250003-8110-30256038_2.html (accessed.

[149] J. Zhang, Y. Zhou, and F. Fang, "Advancements in Optical See-through Near-Eye Display," in *Display Technologies*: IntechOpen, 2022.

[150] K. Mirza and K. Sarayeddine, "Key challenges to affordable see through wearable displays: the missing link for mobilearmass deployment," *Internal Technical Paper-OPTINVENT SA,* 2012.

[151] EPSON. "Moverio BT-300." https://www.epson.ie/en_IE/products/smart-glasses/see-through-mobile-viewer/moverio-bt-300/p/20178?cid=ps:google:genexp-pd22-ie:111::&gclid=CjwKCAjw7p6aBhBiEiwA83fGuoCQ684eWl5A6upbnypBRK03o-yKrMGtkPB0nfVpMaYktsYtx_OHvhoCn0wQAvD_BwE&gclsrc=aw.ds (accessed.

[152] Y. Chen, Q. Wang, H. Chen, X. Song, H. Tang, and M. Tian, "An overview of augmented reality technology," in *Journal of Physics: Conference Series*, 2019, vol. 1237, no. 2: IOP Publishing, p. 022082.

[153] M. Born and E. Wolf, *Principles of optics: electromagnetic theory of propagation, interference and diffraction of light*. Elsevier, 2013.

[154] D. Betancourt and C. del Río, "Study of the human eye working principle: an impressive high angular resolution system with simple array detectors," in *Fourth IEEE Workshop on Sensor Array and Multichannel Processing, 2006.*, 2006: IEEE, pp. 93-97.

[155] D. Atchison and G. Smith, "Optics of the Human Eye," *Encyclopedia of Modern Optics,* pp. 43-63, 2000.

[156] Y. Zhou, J. Zhang, and F. Fang, "Stray light analysis and design optimization of geometrical waveguide," *Advanced Optical Technologies,* vol. 9, 2020.

[157] Y. Zhou, J. Zhang, and F. Fang, "Design of a dual-focal geometrical waveguide near-eye see-through display," *Optics & Laser Technology,* vol. 156, p. 108546, 2022.

[158] Z. Zhao, H. Zhang, S. Liu, and X. Wang, "Effective freeform TIR lens designed for LEDs with high angular color uniformity," *Applied Optics,* vol. 57, no. 15, pp. 4216-4221, 2018.

[159] A. J. Schmitt and J. H. Gardner, "Illumination uniformity of laser-fusion pellets using induced spatial incoherence," *Journal of applied physics,* vol. 60, no. 1, pp. 6-13, 1986.

[160] R. Nawrowski, "The use of multiple reflection method for calculation of luminous flux in interiors," *Journal of Light & Visual Environment,* vol. 24, no. 2, pp. 2_45-2_49, 2000.

[161] A. Gershun, "The light field," *Journal of Mathematics and Physics,* vol. 18, no. 1-4, pp. 51-151, 1939.

[162] E. H. Adelson and J. R. Bergen, *The plenoptic function and the elements of early vision*. Vision and Modeling Group, Media Laboratory, Massachusetts Institute of technology, 1991.

[163] G. Wetzstein, I. Ihrke, D. Lanman, and W. Heidrich, "Computational plenoptic imaging," in *Computer Graphics Forum*, 2011, vol. 30, no. 8: Wiley Online Library, pp. 2397-2426.

[164] A. Isaksen, L. McMillan, and S. J. Gortler, "Dynamically reparameterized light fields," in *Proceedings of the 27th annual conference on Computer graphics and interactive techniques*, 2000, pp. 297-306.

[165] D. Van Norren and L. Tiemeijer, "Spectral reflectance of the human eye," *Vision research,* vol. 26, no. 2, pp. 313-320, 1986.

[166] J.-X. Chai, X. Tong, S.-C. Chan, and H.-Y. Shum, "Plenoptic sampling," in *Proceedings of the 27th annual conference on Computer graphics and interactive techniques*, 2000, pp. 307-318.

[167] M. Levoy and P. Hanrahan, "Light field rendering," in *Proceedings of the 23rd annual conference on Computer graphics and interactive techniques*, 1996, pp. 31-42.

[168] P. Moon and D. E. Spencer, "Theory of the photic field," *Journal of the Franklin Institute,* vol. 255, no. 1, pp. 33-50, 1953.

[169] D. Lanman, G. Wetzstein, M. Hirsch, W. Heidrich, and R. Raskar, "Polarization fields: dynamic light field display using multi-layer LCDs," in *Proceedings of the 2011 SIGGRAPH Asia Conference*, 2011, pp. 1-10.

[170] A. Jones, I. McDowall, H. Yamada, M. Bolas, and P. Debevec, "Rendering for an interactive 360 light field display," in *ACM SIGGRAPH 2007 papers*, 2007, pp. 40-es.

[171] F.-C. Huang, G. Wetzstein, B. A. Barsky, and R. Raskar, "Eyeglasses-free display: towards correcting visual aberrations with computational light field displays," *ACM Transactions on Graphics (TOG),* vol. 33, no. 4, pp. 1-12, 2014.

[172] D. Kim, S. Choi, and K. Sohn, "Effect of vergence–accommodation conflict and parallax difference on binocular fusion for random dot stereogram," *IEEE transactions on circuits and systems for video technology,* vol. 22, no. 5, pp. 811-816, 2012.

[173] J. P. Wann, S. Rushton, and M. Mon-Williams, "Natural problems for stereoscopic depth perception in virtual environments," *Vision Research,* vol. 35, no. 19, pp. 2731-2736, 1995.

[174] E. Brunswik, *Perception and the representative design of psychological experiments*. Univ of California Press, 1956.

[175] P. A. McGrath, "Psychological aspects of pain perception," *Archives of Oral Biology,* vol. 39, pp. S55-S62, 1994.

[176] L. A. Zebrowitz and J. M. Montepare, "Social psychological face perception: Why appearance matters," *Social and personality psychology compass,* vol. 2, no. 3, pp. 1497-1517, 2008.

[177] C. V. Hofsten, "The role of convergence in visual space perception," *Vision Research,* vol. 16, no. 2, pp. 193-198, 1976.

[178] H. Hua and B. Javidi, "Augmented Reality: Easy on the Eyes," *Optics & Photonics News,* vol. 26, no. 2, p. 26, 2015.

[179] M. Cao. "Overview of light field technology." https://zhuanlan.zhihu.com/p/47492390 (accessed.

[180] R. MacArthur and R. Levins, "The limiting similarity, convergence, and divergence of coexisting species," *The american naturalist,* vol. 101, no. 921, pp. 377-385, 1967.

[181] K. Hiraoka, "Three-dimensional image display system using binocular parallax," 1989.

[182] M. Braun, U. Leiner, and D. Ruschin, "Evaluating motion and binocular parallax as depth cues for autostereoscopic displays," in *Stereoscopic Displays and Applications XXII*, 2011.

[183] S. Tabata, "Stereoscopic display that controls binocular parallax between two images and controls image reconstitution according to parallax data," ed: US, 2002.

[184] B. Rogers and M. Graham, "Motion parallax as an independent cue for depth perception," *Perception,* vol. 8, no. 2, pp. 125-134, 1979.

[185] M. L. Braunstein, *Depth perception through motion*. Academic Press, 2014.

[186] H. Hong and S. H. Kang, "Measurement of the lens accommodation in viewing stereoscopic displays," *Journal of the Society for Information Display,* vol. 23, no. 1, pp. 19-26, 2015.

[187] A.-L. Engren and A. Behndig, "Anterior chamber depth, intraocular lens position, and refractive outcomes after cataract surgery," *Journal of Cataract & Refractive Surgery,* vol. 39, no. 4, pp. 572-577, 2013.

[188] G. Kramida, "Resolving the vergence-accommodation conflict in head-mounted displays," *IEEE transactions on visualization and computer graphics,* vol. 22, no. 7, pp. 1912-1931, 2015.

[189] M. L. Venturi, C. E. Attinger, A. N. Mesbahi, C. L. Hess, and K. S. Graw, "Mechanisms and clinical applications of the vacuum-assisted closure (VAC) device," *American journal of clinical dermatology,* vol. 6, no. 3, pp. 185-194, 2005.

[190] R. Konrad, E. A. Cooper, and G. Wetzstein, "Novel optical configurations for virtual reality: Evaluating user preference and performance with focus-tunable and monovision near-eye displays," in *Proceedings of the 2016 CHI conference on human factors in computing systems*, 2016, pp. 1211-1220.

[191] T. Inoue and H. Ohzu, "Accommodative responses to stereoscopic three-dimensional display," *Applied optics,* vol. 36, no. 19, pp. 4509-4515, 1997.

[192] C. Vienne, L. Sorin, L. Blondé, Q. Huynh-Thu, and P. Mamassian, "Effect of the accommodation-vergence conflict on vergence eye movements," *Vision research,* vol. 100, pp. 124-133, 2014.

[193] K. J. MacKenzie and S. J. Watt, "Eliminating accommodation-convergence conflicts in stereoscopic displays: Can multiple-focal-plane displays elicit continuous and consistent vergence and accommodation responses?," in *Stereoscopic displays and applications XXI*, 2010, vol. 7524: International Society for Optics and Photonics, p. 752417.

[194] B. Javidi and F. Okano, *Three-dimensional television, video, and display technologies*. Springer Science & Business Media, 2002.

[195] H. M. Ozaktas and L. Onural, *Three-dimensional television: capture, transmission, display*. Springer Science & Business Media, 2007.

[196] D. Dunn, P. Chakravarthula, Q. Dong, and H. Fuchs, "Mitigating vergence-accommodation conflict for near-eye displays via deformable beamsplitters," in *Digital Optics for Immersive Displays*, 2018, vol. 10676: International Society for Optics and Photonics, p. 106760U.

[197] S. Liu, D. Cheng, and H. Hua, "An optical see-through head mounted display with addressable focal planes," in *2008 7th IEEE/ACM International Symposium on Mixed and Augmented Reality*, 2008: IEEE, pp. 33-42.

[198] K. Akşit, W. Lopes, J. Kim, P. Shirley, and D. Luebke, "Near-eye varifocal augmented reality display using see-through screens," *ACM Transactions on Graphics (TOG),* vol. 36, no. 6, pp. 1-13, 2017.

[199] H. Hua and B. Javidi, "A 3D integral imaging optical see-through head-mounted display," *Optics express,* vol. 22, no. 11, pp. 13484-13491, 2014.

[200] M. A. Klug, S. C. Cahall, and H. Chung, "Separated pupil optical systems for virtual and augmented reality and methods for displaying images using same," ed: Google Patents, 2016.

[201] Y. Katsumata, W. Yamada, and H. Manabe, "Optical see-through head-mounted display with deep depth of field using pinhole polarizing plates," in *The Adjunct Publication of the 32nd Annual ACM Symposium on User Interface Software and Technology*, 2019, pp. 102-104.

[202] A. Maimone, D. Lanman, K. Rathinavel, K. Keller, D. Luebke, and H. Fuchs, "Pinlight displays: wide field of view augmented reality eyeglasses using

defocused point light sources," in *ACM SIGGRAPH 2014 Emerging Technologies*, 2014, pp. 1-1.

[203] G. A. Koulieris, K. Akşit, M. Stengel, R. K. Mantiuk, K. Mania, and C. Richardt, "Near-eye display and tracking technologies for virtual and augmented reality," in *Computer Graphics Forum*, 2019, vol. 38, no. 2: Wiley Online Library, pp. 493-519.

[204] A. Wilson and H. Hua, "Design and demonstration of a vari-focal optical see-through head-mounted display using freeform Alvarez lenses," *Optics express,* vol. 27, no. 11, pp. 15627-15637, 2019.

[205] I. M. Erkelens and K. J. MacKenzie, "19-2: Vergence-Accommodation Conflicts in Augmented Reality: Impacts on Perceived Image Quality," in *SID Symposium Digest of Technical Papers*, 2020, vol. 51, no. 1: Wiley Online Library, pp. 265-268.

[206] T. Ueno and Y. Takaki, "Super multi-view near-eye display to solve vergence–accommodation conflict," *Optics express,* vol. 26, no. 23, pp. 30703-30715, 2018.

[207] K. MacKenzie, R. Dickson, and S. Watt, "Vergence and accommodation to multiple-image-plane stereoscopic displays:'Real world'responses with practical image-plane separations?," in *Stereoscopic Displays and Applications XXII*, 2011, vol. 7863: International Society for Optics and Photonics, p. 786315.

[208] R. Narain, R. A. Albert, A. Bulbul, G. J. Ward, M. S. Banks, and J. F. O'Brien, "Optimal presentation of imagery with focus cues on multi-plane displays," *ACM Transactions on Graphics (TOG),* vol. 34, no. 4, pp. 1-12, 2015.

[209] L. Ryana, K. J. MacKenziea, and S. J. Watta, "Multiple-focal-planes 3D displays: A practical solution to the vergence-accommodation conflict?," in *2012 International Conference on 3D Imaging (IC3D)*, 2012: IEEE, pp. 1-6.

[210] N. Matsuda, A. Fix, and D. Lanman, "Focal surface displays," *ACM Transactions on Graphics (TOG),* vol. 36, no. 4, pp. 1-14, 2017.

[211] I. S. Potemin, I. Livshits, D. Zhdanov, A. Zhdanov, and N. Bogdanov, "An application of the virtual prototyping approach to design of VR, AR, and MR devices free from the vergence-accommodation conflict," in *Computational Optics II*, 2018, vol. 10694: International Society for Optics and Photonics, p. 1069404.

[212] H. Davis, D. Buckley, R. E. G. Jacobs, D. A. A. Brennand, and J. P. Frisby, "Accommodation to large disparity stereograms," *Journal of American Association for Pediatric Ophthalmology & Strabismus,* vol. 6, no. 6, pp. 377-384, 2002.

[213] T. Inoue and H. Ohzu, "Accommodative responses to stereoscopic three-dimensional display," *Appl Opt,* vol. 36, no. 19, pp. 4509-4515, 1997.

[214] Y. Zhao and F. Fang, "Measurement of the peripheral aberrations of human eyes: A comprehensive review," *Nanotechnology and Precision Engineering,* vol. 3, no. 2, pp. 53-68, 2020.

[215] Y. Zheng, L. Song, J. Huang, H. Zhang, and F. Fang, "Detection of the three-dimensional trajectory of an object based on a curved bionic compound eye," *Optics letters,* vol. 44, no. 17, pp. 4143-4146, 2019.

[216] K. Pang, F. Fang, L. Song, Y. Zhang, and H. Zhang, "Bionic compound eye for 3D motion detection using an optical freeform surface," *JOSA B,* vol. 34, no. 5, pp. B28-B35, 2017.

[217] K. Pang, L. Song, F. Fang, Y. Zhang, and H. Zhang, "An imaging system with a large depth of field based on an overlapped micro-lens array," *CIRP Annals,* vol. 65, no. 1, pp. 471-474, 2016.

[218] D. H. Shin, S. Tibuleac, T. A. Maldonado, and R. Magnusson, "Thin-film optical filters with diffractive elements and waveguides," *Optical Engineering,* vol. 37, 1998.

[219] Y. Zhang and F. Fang, "Development of planar diffractive waveguides in optical see-through head-mounted displays," *Precision Engineering,* vol. 60, 2019.

[220] S. J. Robbins and I. Nguyen, "COMPACT PROJECTION LIGHT ENGINE FOR A DIFFRACTIVE WAVEGUIDE DISPLAY," ed.

[221] L. Mi, C. P. Chen, Y. Lu, W. Zhang, and N. Maitlo, "Design of lensless retinal scanning display with diffractive optical element," *Optics Express,* vol. 27, no. 15, p. 20493, 2019.

[222] H. Wang, C. J. R. Sheppard, K. Ravi, S. T. Ho, and G. Vienne, "Fighting against diffraction: apodization and near field diffraction structures," *Laser & Photonics Reviews,* vol. 6, no. 3, pp. 354-392, 2012.

[223] X. Chen, J. Liao, H. Gu, C. Zhang, H. Jiang, and S. Liu, "Remote Absolute Roll-Angle Measurement in Range of 180° Based on Polarization Modulation," *Nanomanufacturing and Metrology,* vol. 3, no. 3, pp. 228-235, 2020.

[224] C. Jang, K. Bang, S. Moon, J. Kim, and B. Lee, "Retinal 3D: Augmented Reality Near-Eye Display Via Pupil-Tracked Light Field Projection on Retina," *ACM Transactions on Graphics,* vol. 36, no. 6CD, pp. 190.1-190.13, 2017.

[225] "PinMR™." LetinAR. https://letinar.com/ (accessed.

[226] A. Mohan, G. Woo, S. Hiura, Q. Smithwick, and R. Raskar, "Bokode: imperceptible visual tags for camera based interaction from a distance," in *ACM SIGGRAPH 2009 papers*, 2009, pp. 1-8.

[227] J.-Y. Son, V. V. Saveljev, D.-S. Kim, Y.-M. Kwon, and S.-H. Kim, "Three-dimensional imaging system based on a light-emitting diode array," *Optical Engineering,* vol. 46, no. 10, p. 103205, 2007.

[228] S. J. Watt, K. Akeley, M. O. Ernst, and M. S. Banks, "Focus cues affect perceived depth," *Journal of Vision,* vol. 5, no. 10, pp. 7-, 2005.

[229] R. Konrad, N. Padmanaban, E. Cooper, and G. Wetzstein, "Computational focus-tunable near-eye displays," in *ACM SIGGRAPH 2016 Emerging Technologies*, 2016, pp. 1-2.

[230] G. A. Koulieris, G. Drettakis, D. Cunningham, and K. Mania, "Gaze prediction using machine learning for dynamic stereo manipulation in games," in *2016 IEEE Virtual Reality (VR)*, 2016: IEEE, pp. 113-120.

[231] P. Kellnhofer, P. Didyk, K. Myszkowski, M. M. Hefeeda, H.-P. Seidel, and W. Matusik, "GazeStereo3D: Seamless disparity manipulations," *ACM Transactions on Graphics (TOG),* vol. 35, no. 4, pp. 1-13, 2016.

[232] T. Oskam, A. Hornung, H. Bowles, K. Mitchell, and M. H. Gross, "OSCAM-optimized stereoscopic camera control for interactive 3D," *ACM Trans. Graph.,* vol. 30, no. 6, p. 189, 2011.

[233] S. A. Cholewiak, G. D. Love, P. P. Srinivasan, R. Ng, and M. S. Banks, "ChromaBlur: Rendering chromatic eye aberration improves accommodation and realism," *ACM Transactions on Graphics (TOG),* vol. 36, no. 6, pp. 1-12, 2017.

[234] M. Lambooij, M. Fortuin, I. Heynderickx, and W. IJsselsteijn, "Visual discomfort and visual fatigue of stereoscopic displays: A review," *Journal of imaging science and technology,* vol. 53, no. 3, pp. 30201-1-30201-14, 2009.

[235] S. Mun, M.-C. Park, S. Park, and M. Whang, "SSVEP and ERP measurement of cognitive fatigue caused by stereoscopic 3D," *Neuroscience letters,* vol. 525, no. 2, pp. 89-94, 2012.

[236] J. Frey, A. Appriou, F. Lotte, and M. Hachet, "Classifying EEG signals during stereoscopic visualization to estimate visual comfort," *Computational intelligence and neuroscience,* vol. 2016, 2016.

[237] M.-K. Kang, H. Cho, H.-M. Park, S. C. Jun, and K.-J. Yoon, "A wellness platform for stereoscopic 3D video systems using EEG-based visual discomfort evaluation technology," *Applied ergonomics,* vol. 62, pp. 158-167, 2017.

[238] M. T. Lambooij, W. A. IJsselsteijn, and I. Heynderickx, "Visual discomfort in stereoscopic displays: a review," in *Stereoscopic Displays and Virtual Reality Systems XIV*, 2007, vol. 6490: International Society for Optics and Photonics, p. 64900I.

[239] M.-C. Park and S. Mun, "Overview of measurement methods for factors affecting the human visual system in 3D displays," *Journal of Display Technology,* vol. 11, no. 11, pp. 877-888, 2015.

[240] C. J. Kim, S. Park, M. J. Won, M. Whang, and E. C. Lee, "Autonomic nervous system responses can reveal visual fatigue induced by 3D displays," *Sensors,* vol. 13, no. 10, pp. 13054-13062, 2013.

[241] S. A. A. Naqvi, N. Badruddin, A. S. Malik, W. Hazabbah, and B. Abdullah, "Does 3D produce more symptoms of visually induced motion sickness?," in *2013 35th Annual International Conference of the IEEE Engineering in Medicine and Biology Society (EMBC)*, 2013: IEEE, pp. 6405-6408.

[242] E. Peli, "The visual effects of head-mounted display (HMD) are not distinguishable from those of desk-top computer display," *Vision research,* vol. 38, no. 13, pp. 2053-2066, 1998.

[243] N. Padmanaban, R. Konrad, T. Stramer, E. A. Cooper, and G. Wetzstein, "Optimizing virtual reality for all users through gaze-contingent and adaptive focus displays," *Proceedings of the National Academy of Sciences,* vol. 114, no. 9, pp. 2183-2188, 2017.

[244] Y. Zhou, J. Zhang, and F. Fang, "Design of a large field-of-view two-dimensional geometrical waveguide," *Results in Optics,* vol. 5, p. 100147, 2021.

[245] I. Moreno, "Illumination uniformity assessment based on human vision," *Optics letters,* vol. 35, no. 23, pp. 4030-4032, 2010.

[246] H. R. Blackwell, "Contrast thresholds of the human eye," *Josa,* vol. 36, no. 11, pp. 624-643, 1946.

[247] "Lemnis Demonstrates Latest Varifocal Lens Tech in New VR Headset Prototype." https://www.roadtovr.com/lemnis-demonstrates-latest-varifocal-lens-tech-new-vr-headset-prototype/ (accessed.

[248] D. Carter, R. Sexton, and M. Miller, "Field measurement of illuminance," *Lighting Research & Technology,* vol. 21, no. 1, pp. 29-35, 1989.

[249] D. L. Shealy and D. G. Burkhard, "Analytical illuminance calculation in a multi-interface optical system," *Optica Acta: International Journal of Optics,* vol. 22, no. 6, pp. 485-501, 1975.

[250] E. F. Kelley, M. Lindfors, and J. Penczek, "Display daylight ambient contrast measurement methods and daylight readability," *Journal of the Society for Information Display,* vol. 14, no. 11, pp. 1019-1030, 2006.

[251] S. W. Lee and S. S. Lee, "Focal tunable liquid lens integrated with an electromagnetic actuator," *Applied Physics Letters,* vol. 90, no. 12, p. 1128, 2007.

[252] A. Lumsdaine and T. Georgiev, "The focused plenoptic camera," in *2009 IEEE International Conference on Computational Photography (ICCP)*, 2009: IEEE, pp. 1-8.

[253] T. G. Georgiev and A. Lumsdaine, "Focused plenoptic camera and rendering," *Journal of electronic imaging,* vol. 19, no. 2, p. 021106, 2010.

[254] E. H. Adelson and J. Y. Wang, "Single lens stereo with a plenoptic camera," *IEEE transactions on pattern analysis and machine intelligence,* vol. 14, no. 2, pp. 99-106, 1992.

[255] R. J. Marshall *et al.*, "Improving depth estimation from a plenoptic camera by patterned illumination," in *Videometrics, Range Imaging, and Applications XIII*, 2015, vol. 9528: SPIE, pp. 365-370.

[256] O. Johannsen, C. Heinze, B. Goldluecke, and C. Perwaß, "On the calibration of focused plenoptic cameras," in *Time-of-Flight and Depth Imaging. Sensors, Algorithms, and Applications*: Springer, 2013, pp. 302-317.

[257] H. Ma, Z. Qian, T. Mu, and S. Shi, "Fast and accurate 3D measurement based on light-field camera and deep learning," *Sensors,* vol. 19, no. 20, p. 4399, 2019.

[258] A. Vieira, H. Duarte, C. Perra, L. Tavora, and P. Assuncao, "Data formats for high efficiency coding of lytro-illum light fields," in *2015 international conference on image processing theory, tools and applications (IPTA)*, 2015: IEEE, pp. 494-497.

[259] A. Silva, "Light field processor: a lytro illum imaging application," 2016.

[260] A. T. Vu, S. Gulati, P.-A. Vogel, T. Grunwald, and T. Bergs, "Machine learning-based predictive modeling of contact heat transfer," *International Journal of Heat and Mass Transfer,* vol. 174, p. 121300, 2021.

[261] D. M. Aikens, "Objective measurement of scratch and dig," in *Optical Fabrication and Testing*, 2012: Optica Publishing Group, p. OTu2D. 5.

[262] R. H. Silverman, "High-resolution ultrasound imaging of the eye–a review," *Clinical & experimental ophthalmology,* vol. 37, no. 1, pp. 54-67, 2009.

[263] H. Sardemann and H.-G. Maas, "On the accuracy potential of focused plenoptic camera range determination in long distance operation," *ISPRS Journal of Photogrammetry and Remote Sensing,* vol. 114, pp. 1-9, 2016.

[264] J. S. Pierce, B. C. Stearns, and R. Pausch, "Voodoo dolls: seamless interaction at multiple scales in virtual environments," in *Proceedings of the 1999 symposium on Interactive 3D graphics*, 1999, pp. 141-145.

[265] Z. Choudhary, J. Ugarte, G. Bruder, and G. Welch, "Real-Time Magnification in Augmented Reality," in *Symposium on Spatial User Interaction*, 2021, pp. 1-2.

[266] F. Liu, C. Shen, and G. Lin, "Deep convolutional neural fields for depth estimation from a single image," in *Proceedings of the IEEE conference on computer vision and pattern recognition*, 2015, pp. 5162-5170.

[267] M. Liu, M. Salzmann, and X. He, "Discrete-continuous depth estimation from a single image," in *Proceedings of the IEEE Conference on Computer Vision and Pattern Recognition*, 2014, pp. 716-723.

Appendix A. Program code for projector in 1D model

Appendix A is the program code of the virtual image from the projector in 1D model. In this program, different kinds of colors and images are projected for virtual imaging.

```
#define SCR_WD   240

#define SCR_HT   240

#include <SPI.h>

#include <Adafruit_GFX.h>



#if (__STM32F1__) // bluepill

#define TFT_DC  PA1

#define TFT_RST PA0

//#include <Arduino_ST7789_STM.h>

#else

#define TFT_DC  7

#define TFT_RST 8

#include <Arduino_ST7789_Fast.h>

//#include <Arduino_ST7789.h>

#endif

Arduino_ST7789 tft = Arduino_ST7789(TFT_DC, TFT_RST);

// ------------------------------------------------

unsigned long FillScreenTest()

{

  unsigned long start = millis();

  for(int i=0;i<5;i++) {

    tft.fillScreen(RED);
```

```
    tft.fillScreen(GREEN);
    tft.fillScreen(BLUE);
    tft.fillScreen(YELLOW);
  }
  return millis()-start;
}
// ------------------------------------------------
unsigned long ClearScreenTest()
{
  unsigned long start = millis();
  for(int i=0;i<5*4;i++)
    tft.fillScreen(BLACK);
  return millis()-start;
}
// ------------------------------------------------
const uint16_t imgF[] PROGMEM =
{0xF800,0xF840,0xF8A0,0xF900,0xF960,0xF9C0,0xFA20,0xFA80,0xFAE0,0xFB40,0xF
BA0,0xFC00,0xFC60,0xFCC0,0xFD20,0xFD80,0xFDE0,0xFE40,0xFEA0,0xFF00,0xFF6
0,0xFFC0,0xFFE0,0xEFE0,0xE7E0,0xD7E0,0xCFE0,0xBFE0,0xB7E0,0xA7E0,0x9FE0,
0x8FE0,0x87E0,0x77E0,0x6FE0,0x5FE0,0x57E0,0x47E0,0x3FE0,0x2FE0,0x27E0,0x17E
0,0xFE0,0x7E0,0x7E1,0x7E3,0x7E4,0x7E6,0x7E7,0x7E9,0x7EA,0x7EC,0x7ED,0x7EF,0
x7F0,0x7F2,0x7F3,0x7F5,0x7F6,0x7F8,0x7F9,0x7FB,0x7FC,0x7FE,0x7FF,0x79F,0x73F,
0x6DF,0x67F,0x61F,0x5BF,0x55F,0x4FF,0x49F,0x43F,0x3DF,0x37F,0x31F,0x2BF,0x25
F,0x1FF,0x19F,0x13F,0xDF,0x7F,0x1F,0x81F,0x101F,0x201F,0x281F,0x381F,0x401F,0
x501F,0x581F,0x681F,0x701F,0x801F,0x881F,0x981F,0xA01F,0xB01F,0xB81F,0xC81F
,0xD01F,0xE01F,0xE81F,0xF81F,0xF81F,0xF81D,0xF81C,0xF81A,0xF819,0xF817,0xF
816,0xF814,0xF813,0xF811,0xF810,0xF80E,0xF80D,0xF80B,0xF80A,0xF808,0xF807,0
xF805,0xF804,0xF802,0xF801,
```

```
0xF800,0xF840,0xF8A0,0xF900,0xF960,0xF9C0,0xFA20,0xFA80,0xFAE0,0xFB40,0xF
BA0,0xFC00,0xFC60,0xFCC0,0xFD20,0xFD80,0xFDE0,0xFE40,0xFEA0,0xFF00,0xFF6
0,0xFFC0,0xFFE0,0xEFE0,0xE7E0,0xD7E0,0xCFE0,0xBFE0,0xB7E0,0xA7E0,0x9FE0,
0x8FE0,0x87E0,0x77E0,0x6FE0,0x5FE0,0x57E0,0x47E0,0x3FE0,0x2FE0,0x27E0,0x17E
0,0xFE0,0x7E0,0x7E1,0x7E3,0x7E4,0x7E6,0x7E7,0x7E9,0x7EA,0x7EC,0x7ED,0x7EF,0
x7F0,0x7F2,0x7F3,0x7F5,0x7F6,0x7F8,0x7F9,0x7FB,0x7FC,0x7FE,0x7FF,0x79F,0x73F,
0x6DF,0x67F,0x61F,0x5BF,0x55F,0x4FF,0x49F,0x43F,0x3DF,0x37F,0x31F,0x2BF,0x25
F,0x1FF,0x19F,0x13F,0xDF,0x7F,0x1F,0x81F,0x101F,0x201F,0x281F,0x381F,0x401F,0
x501F,0x581F,0x681F,0x701F,0x801F,0x881F,0x981F,0xA01F,0xB01F,0xB81F,0xC81F
,0xD01F,0xE01F,0xE81F,0xF81F,0xF81F,0xF81D,0xF81C,0xF81A,0xF819,0xF817,0xF
816,0xF814,0xF813,0xF811,0xF810,0xF80E,0xF80D,0xF80B,0xF80A,0xF808,0xF807,0
xF805,0xF804,0xF802,0xF801};

uint16_t img[SCR_WD+16];

unsigned long DrawImageTest()

{

  for(int i=0;i<SCR_WD+16;i++) img[i] = tft.rgbWheel(500L*i/SCR_WD);

  unsigned long start = millis();

  for(int i=0;i<5*4;i++) for(int y=0;y<SCR_HT;y++)
tft.drawImage(0,y,SCR_WD,1,img+(((y>>2)+i)&0xf));

  return millis()-start;

}

// ------------------------------------------------

unsigned long DrawImageFTest()

{

  unsigned long start = millis();

  for(int i=0;i<5*4;i++) for(int y=0;y<SCR_HT;y++)
tft.drawImageF(0,y,SCR_WD,1,imgF+(((y>>2)+i)&0xf));
```

```
  return millis()-start;
}
// -----------------------------------------------
// original Adafruit
unsigned long orig ={ 5872, 5872,
1468292,394696,2938532,132952,121996,4068208,925276,1319512,
1278096,1930524,602080,4649200 };
// pre 18.09.2020 Fast
//unsigned long
orig={2645,3577,661616,114064,579036,56216,49500,1830864,222936,259340,175460,9
03348,138264,1853300};
unsigned long res[14];
void result(int i)
{
  Serial.print(res[i]);
  if(res[i]<1000000) Serial.print("\t");
  Serial.print("\t\t\t");
  Serial.print(100*orig[i]/res[i]);
  Serial.println("%");
}
void setup(void)
{
  Serial.begin(9600);
  Serial.println(F("IPS 240x240 ST7789"));
  //tft.reset();
```

```
  //tft.init(SCR_WD, SCR_HT);
  tft.begin();
  tft.fillScreen(BLACK);
  tft.setCursor(0, 0);
  tft.setTextColor(WHITE);  tft.setTextSize(2);
  tft.println("IPS 240x240 ST7789");
  tft.println("Library Benchmark");
  tft.println("starts in 3s ...");
  delay(3000);
  Serial.println(F("Benchmark                Time (microseconds)"));
  res[0]=FillScreenTest();
  Serial.print(F("FillScreen Mbps          "));
  Serial.println(String(res[0])+"ms  "+String(1000*20.0/res[0])+"fps
"+String(20.0*SCR_WD*SCR_HT*16/res[0]/1000.0)+"
Mbps\t"+100*orig[0]/res[0]+"%");
//for(int i=0;i<100;i++) tft.fillRect(i,i,SCR_WD-i*2,SCR_HT-i*2,tft.rgbWheel(i*10));
delay(1000);


  res[1]=ClearScreenTest();
  Serial.print(F("ClearScreen Mbps         "));
  Serial.println(String(res[1])+"ms  "+String(1000*20.0/res[1])+"fps
"+String(20.0*SCR_WD*SCR_HT*16/res[1]/1000.0)+"
Mbps\t"+100*orig[1]/res[1]+"%");


  res[1]=DrawImageTest();
  Serial.print(F("DrawImage Mbps           "));
```

```
  Serial.println(String(res[1])+"ms  "+String(1000*20.0/res[1])+"fps
"+String(20.0*SCR_WD*SCR_HT*16/res[1]/1000.0)+"
Mbps\t"+100*orig[1]/res[1]+"%");
  res[1]=DrawImageFTest();
  Serial.print(F("DrawImageF Mbps          "));
  Serial.println(String(res[1])+"ms  "+String(1000*20.0/res[1])+"fps
"+String(20.0*SCR_WD*SCR_HT*16/res[1]/1000.0)+"
Mbps\t"+100*orig[1]/res[1]+"%");


  res[2]=testFillScreen();
  Serial.print(F("Screen fill              "));
  result(2);
  delay(500);


  res[3]=testText();
  Serial.print(F("Text                     "));
  result(3);
  delay(3000);


  res[4]=testLines(CYAN);
  Serial.print(F("Lines                    "));
  result(4);
  delay(500);


  res[5]=testFastLines(RED, BLUE);
```

```
Serial.print(F("Horiz/Vert Lines         "));
result(5);
delay(500);

res[6]=testRects(GREEN);
Serial.print(F("Rectangles (outline)     "));
result(6);
delay(500);

res[7]=testFilledRects(YELLOW, MAGENTA);
Serial.print(F("Rectangles (filled)      "));
result(7);
delay(500);

res[8]=testFilledCircles(10, MAGENTA);
Serial.print(F("Circles (filled)         "));
result(8);

res[9]=testCircles(10, WHITE);
Serial.print(F("Circles (outline)        "));
result(9);
delay(500);

res[10]=testTriangles();
```

```
Serial.print(F("Triangles (outline)      "));
result(10);
delay(500);

res[11]=testFilledTriangles();
Serial.print(F("Triangles (filled)       "));
result(11);
delay(500);

res[12]=testRoundRects();
Serial.print(F("Rounded rects (outline)  "));
result(12);
delay(500);

res[13]=testFilledRoundRects();
Serial.print(F("Rounded rects (filled)   "));
result(13);
delay(500);

Serial.println(F("Done!"));
Serial.println(F("Results:"));
for(int i=0;i<14;i++) { Serial.print(res[i]); Serial.print(","); }
Serial.println();
```

```
  int c1=YELLOW, c2=WHITE;
  tft.fillScreen(BLACK);
  tft.setCursor(0, 0);
  tft.setTextSize(2);
  tft.setTextColor(CYAN);
  tft.println("RESULTS:");

  tft.setTextSize(1);
  tft.println();
  tft.setTextColor(GREEN);
  tft.println(F("Benchmark               Time (us)"));
  tft.setTextColor(c1); tft.print(F("FillScreen Mbps        "));
  tft.setTextColor(c2); tft.println(String(res[0])+"ms
"+String(20.0*SCR_WD*SCR_HT*16/res[0]/1000.0)+" Mbps");
  //tft.setTextColor(c1); tft.print(F("ClearScreen Mbps       "));
  //tft.setTextColor(c2); tft.print(String(res[1])+"ms
"+String(20.0*SCR_WD*SCR_HT*16/res[1]/1000.0)+" Mbps");
  tft.setTextColor(c1); tft.print(F("DrawImageF Mbps        "));
  tft.setTextColor(c2); tft.println(String(res[1])+"ms
"+String(20.0*SCR_WD*SCR_HT*16/res[1]/1000.0)+" Mbps");

  tft.setTextColor(c1); tft.print(F("Screen fill            "));
  tft.setTextColor(c2); tft.println(res[3]);
  tft.setTextColor(c1); tft.print(F("Text                   "));
  tft.setTextColor(c2); tft.println(res[4]);
```

```
  tft.setTextColor(c1); tft.print(F("Lines                    "));
  tft.setTextColor(c2); tft.println(res[5]);
  tft.setTextColor(c1); tft.print(F("Horiz/Vert Lines         "));
  tft.setTextColor(c2); tft.println(res[6]);
  tft.setTextColor(c1); tft.print(F("Rectangles (outline)     "));
  tft.setTextColor(c2); tft.println(res[8]);
  tft.setTextColor(c1); tft.print(F("Rectangles (filled)      "));
  tft.setTextColor(c2); tft.println(res[9]);
  tft.setTextColor(c1); tft.print(F("Circles (filled)         "));
  tft.setTextColor(c2); tft.println(res[10]);
  tft.setTextColor(c1); tft.print(F("Circles (outline)        "));
  tft.setTextColor(c2); tft.println(res[11]);
  tft.setTextColor(c1); tft.print(F("Triangles (outline)      "));
  tft.setTextColor(c2); tft.println(res[12]);
  tft.setTextColor(c1); tft.print(F("Triangles (filled)       "));
  tft.setTextColor(c2); tft.println(res[13]);
  tft.setTextColor(c1); tft.print(F("Rounded rects (outline) "));
  tft.setTextColor(c2); tft.println(res[14]);
  tft.setTextColor(c1); tft.print(F("Rounded rects (filled)  "));
  tft.setTextColor(c2); tft.println(res[15]);
  tft.setTextColor(RED); tft.println(F("Done!"));
}
```

Appendix B. Program code for projector in 2D model

Appendix A is the program code of the virtual image from the projector in 2D model. In this program, the virtual image MNMT is projected as the virtual scale.

```
#include <Wire.h>

#include <Adafruit_GFX.h>

#include <Adafruit_SSD1306.h>

#define OLED_RESET     4

Adafruit_SSD1306 display(128, 32, &Wire, OLED_RESET);

void setup() {

  display.begin(SSD1306_SWITCHCAPVCC, 0x3C);

  display.setTextColor(WHITE);

  display.clearDisplay();

  display.setTextSize(1);

  display.setCursor(0, 8);

  display.println("MNMT");

  display.display();

}

void loop() {

  display.startscrollright(0x00, 0x0F);

  delay(5000);

  display.stopscroll();

  display.startscrollleft(0x00, 0x0F);

  delay(1000);

  display.stopscroll();

}
```

Appendix C. Program code for DOF map transfer

Appendix C is the code for DOF map transfer from original picture for chapter 6. DOF map is more easy to extract depth information. Different depth contains different chromatic value.

```
from __future__ import absolute_import, division, print_function
%matplotlib inline


import os
import numpy as np
import PIL.Image as pil
import matplotlib.pyplot as plt


import torch
from torchvision import transforms


import networks
from utils import download_model_if_doesnt_exist
model_name = "mono_640x192"


download_model_if_doesnt_exist(model_name)
encoder_path = os.path.join("models", model_name, "encoder.pth")
depth_decoder_path = os.path.join("models", model_name, "depth.pth")


# LOADING PRETRAINED MODEL
encoder = networks.ResnetEncoder(18, False)
depth_decoder = networks.DepthDecoder(num_ch_enc=encoder.num_ch_enc, scales=range(4))


loaded_dict_enc = torch.load(encoder_path, map_location='cpu')
filtered_dict_enc = {k: v for k, v in loaded_dict_enc.items() if k in encoder.state_dict()}
```

```
encoder.load_state_dict(filtered_dict_enc)

loaded_dict = torch.load(depth_decoder_path, map_location='cpu')
depth_decoder.load_state_dict(loaded_dict)

encoder.eval()
depth_decoder.eval();
image_path = "assets/test_image.jpg"

input_image = pil.open(image_path).convert('RGB')
original_width, original_height = input_image.size

feed_height = loaded_dict_enc['height']
feed_width = loaded_dict_enc['width']
input_image_resized = input_image.resize((feed_width, feed_height), pil.LANCZOS)

input_image_pytorch = transforms.ToTensor()(input_image_resized).unsqueeze(0)
with torch.no_grad():
    features = encoder(input_image_pytorch)
    outputs = depth_decoder(features)

disp = outputs[("disp", 0)]
disp_resized = torch.nn.functional.interpolate(disp,
    (original_height, original_width), mode="bilinear", align_corners=False)

# Saving colormapped depth image
disp_resized_np = disp_resized.squeeze().cpu().numpy()
vmax = np.percentile(disp_resized_np, 95)

plt.figure(figsize=(10, 10))
```

```
plt.subplot(211)
plt.imshow(input_image)
plt.title("Input", fontsize=22)
plt.axis('off')

plt.subplot(212)
plt.imshow(disp_resized_np, cmap='magma', vmax=vmax)
plt.title("Disparity prediction", fontsize=22)
plt.axis('off');
```

Appendix D. Program code for image pixel transfer

Appendix C is the code to transfer the depth map to greyscale value, which is much more easy to identify the depth change.

```
clc;
A1=imread('Depth1.jpg');
B1=rgb2gray(A1);
% imshow(B1);

A2=imread('Depth2.jpg');
B2=rgb2gray(A2);
% imshow(B2);

A3=imread('Depth3.jpg');
B3=rgb2gray(A3);
% imshow(B3);

[count1,x1]=imhist(B1);
[count2,x2]=imhist(B2);
[count3,x3]=imhist(B3);

count1=imhist(B1)/numel(B1)
count2=imhist(B2)/numel(B2)
count3=imhist(B3)/numel(B3)

subplot(3,3,1);
imshow(A1);
subplot(3,3,2);
imshow(A2);
subplot(3,3,3);
imshow(A3);
```

```
subplot(3,3,4);
imshow(B1);
subplot(3,3,5);
imshow(B2);
subplot(3,3,6);
imshow(B3);

subplot(3,3,7);
plot(x1,count1)
xlim([0 255]);
ylim([0 0.06]);
subplot(3,3,8);
plot(x2,count2);
xlim([0 255]);
ylim([0 0.06]);
subplot(3,3,9);
plot(x3,count3);
xlim([0 255]);
ylim([0 0.06]);
```